Journal of Fluids Engineering

Published Monthly by ASME

VOLUME 130 • NUMBER 10 • OCTOBER 2008

FLUIDS ENGINEERING DIVISION
Editor
J. KATZ (2009)
Assistant to the Editor
L. MURPHY (2009)

Associate Editors
M. J. ANDREWS (2009)
S. BALACHANDAR (2008)
A. BESKOK (2008)
S. L. CECCIO (2009)
D. DRIKAKIS (2008)
P. DUPONT (2010)
I. EAMES (2010)
C. HAH (2009)
T. J. HEINDEL (2010)
J. KOMPENHANS (2009)
J. A. LIBURDY (2010)
P. LIGRANI (2008)
R. MITTAL (2009)
T. J. O'HERN (2008)
U. PIOMELLI (2010)
Z. RUSAK (2010)
D. SIGINER (2008)
Y. ZHOU (2008)

PUBLICATIONS COMMITTEE
Chair, **B. RAVANI**

OFFICERS OF THE ASME
President, **THOMAS M. BARLOW**
Executive Director, **THOMAS G. LOUGHLIN**
Treasurer, **T. D. PESTORIUS**

PUBLISHING STAFF
Managing Director, Publishing
P. DI VIETRO
Manager, Journals
C. MCATEER
Production Coordinator
A. HEWITT

RESEARCH PAPERS

Flows in Complex Systems

Fundamental Issues and Canonical Flows

Multiphase Flows

Techniques and Procedures

(Contents continued on inside back cover)

Transactions of the ASME, Journal of Fluids Engineering (ISSN 0098-2202) is published monthly by The American Society of Mechanical Engineers, Three Park Avenue, New York, NY 10016. Periodicals postage paid at New York, NY and additional mailing offices. POSTMASTER: Send address changes to Transactions of the ASME, Journal of Fluids Engineering, c/o THE AMERICAN SOCIETY OF MECHANICAL ENGINEERS, 22 Law Drive, Box 2300, Fairfield, NJ 07007-2300. **CHANGES OF ADDRESS** must be received at Society headquarters seven weeks before they are to be effective. Please send old label and new address.

STATEMENT from By-Laws. The Society shall not be responsible for statements or opinions advanced in papers or ... printed in its publications (B7.1, Par. 3).

COPYRIGHT © 2008 by the American Society of Mechanical Engineers. Authorization to photocopy material for internal or personal use under those circumstances not falling within the fair use provisions of the Copyright Act, contact the Copyright Clearance Center (CCC), 222 Rosewood Drive, Danvers, MA 01923, tel: 978-750-8400, www.copyright.com. Request for special permission or bulk copying should be addressed to Reprints/Permission Department.

Canadian Goods & Services Tax Registration #126148048.

This journal is printed on acid-free paper, which exceeds the ANSI Z39.48-1992 specification for permanence of paper and library materials. ∞™
♲ 85% recycled content, including 10% post-consumer fibers.

Downloaded 03 Jun 2010 to 171.66.16.159. Redistribution subject to ASME license or copyright; see http://www.asme.org/terms/Terms_Use.cfm

Journal of Fluids Engineering **Volume 130, Number 10** **OCTOBER 2008**

TECHNICAL BRIEFS

The ASME Journal of Fluids Engineering is abstracted and indexed in the following:

Applied Science & Technology Index, Chemical Abstracts, Chemical Engineering and Biotechnology Abstracts (Electronic equivalent of Process and Chemical Engineering), Civil Engineering Abstracts, Computer & Information Systems Abstracts, Corrosion Abstracts, Current Contents, Ei EncompassLit, Electronics & Communications Abstracts, Engineered Materials Abstracts, Engineering Index, Environmental Engineering Abstracts, Environmental Science and Pollution Management, Excerpta Medica, Fluidex, Index to Scientific Reviews, INSPEC, International Building Services Abstracts, Mechanical & Transportation Engineering Abstracts, Mechanical Engineering Abstracts, METADEX (The electronic equivalent of Metals Abstracts and Alloys Index), Petroleum Abstracts, Process and Chemical Engineering, Referativnyi Zhurnal, Science Citation Index, SciSearch (The electronic equivalent of Science Citation Index), Shock and Vibration Digest, Solid State and Superconductivity Abstracts, Theoretical Chemical Engineering

The Effect of Reynolds Number on Microaxial Flow Fan Performance

David Quin
Cameron Systems Ireland,
Longford, Ireland
e-mail: david.quin@c-a-m.com

Ronan Grimes
Stokes Research Institute,
Limerick, Ireland
e-mail: ronan.grimes@ul.ie

Microscale axial flow fans were investigated in response to the growing cooling requirements of the electronics industry. The two main challenges of this investigation were manufacture of a fully functional fan at the microscale, and performance reduction due to Reynolds number effect. Manufacture of a fully functional axial microfan complete with three-dimensional blade geometry was proven possible using microelectrodischarge machining techniques. Experimental performance measurements proved that Reynolds number effect was not prohibitive at the microscale, and dimensional analysis thereof derived a novel linear scaling method, which quickly and accurately predicted the Reynolds number effect at any fan scale. [DOI: 10.1115/1.2953300]

Keywords: air, axial, British standards, cooling, EDM, fan, flow rate, laminar, micro, pressure, Reynolds

Introduction

In 1965, Moore [1] observed that the density of semiconductor transistors on planar integrated circuits doubled at approximately regular intervals, and famously speculated that the trend would continue. Moore's law became a self-fulfilling prophecy of transistor miniaturization [2], the standard of continuous improvement that chip designers followed to remain competitive [3]. For ten years, transistor density doubled at intervals of 12 months and since 1975 at intervals of 18 months [2]. The subsequent exponential growth in computing power gave vast functionality improvements in consumer products.

Unfortunately, this increase in transistor density caused a simultaneous increase in the amount of waste heat being generated per unit chip area [4–6], and the accompanying increase in component temperatures had adverse effects on product performance, reliability [7,8], and user comfort [9,10]. The continual growth of computing power stipulated by Moore's law was permitted by the evolution of cooling solutions [11,12], and macroscale fans of approximately 60 mm size became the most widespread method of exhausting waste heat to ambient air [13].

Analogous to semiconductors, fan cooling performance can be improved through reducing unit size. An array of small axial fans would give the same pressure and flow rate performance as a single large axial fan while occupying a much smaller fraction of the volume and weight, a principle applied in the cooling of large server cabinets [14,15]. Single miniature fans could direct airflow at hot spots on the chip surface, which can produce heat power per unit area at three times the total surface average [15]. Other potential markets for miniaturized fan technology are shown through the microfan patents of Refs. [16–32]. This paper therefore investigates the viability of axial flow fans at the microscale, as a continuation of the macroscale investigation of Refs. [33,34]. There existed two main challenges to microfan viability, namely, manufacture and Reynolds number effect, which are addressed in this paper.

Manufacturing challenges to miniaturization were the production of microscale blade geometry and reaching an acceptable rotational speed. The microfan blade geometry mimicked that of a typical commercial axial flow cooling fan, which was of variable section and twisted in the spanwise direction. Due to reduction in geometric scale, the airfoil sections were on the order of 2.4 mm chord, 92 μm camber, and 112 μm section thickness; therefore, production of the microscale geometry required an extremely accurate and gentle process. Microscale tip radii required high angular speeds on the order of 60,000 rpm to reach an acceptable tip speed, raising concerns for dynamic balance, wear [35], and sourcing of a capable microscale motor. Addressing the aforementioned microfan manufacturing issues required considerable experience and capability in microscale engineering; hence, microfan manufacture was a collaborative effort between the Stokes Research Institute (SRI) and the Institut für Mikrotechnik Mainz GmbH (IMM). Successive attempts proved microfan manufacture possible.

Aerodynamic challenge to miniaturization arose from the operational principle of an axial flow fan. The fan operates by imparting momentum to the air; unfortunately, by making physical contact with the air, it creates viscous friction. The ratio of momentum forces to viscous forces is defined as *Reynolds number* [36], and operating turbomachinery at lower Reynolds numbers causes a decrease in pressure-flow performance known as *Reynolds number effect* [37–39]. These effects are observed in oil pumps operating with more viscous fluids [40,41] and jet engines operating at higher altitudes [42–44]. Unfortunately, decreasing fan size from the macro- to the microscale causes a reduction in Reynolds number and thus a corresponding reduction in performance. No scaling formulas existed which accurately predicted the Reynolds number effect on a microscale axial flow fan, and therefore it could not be deduced a priori if the performance losses were acceptable. Hence, fan pressure-flow performance measurements were carried out at macro-, meso-, and microfan scales to determine the Reynolds number effect. The effect of Reynolds number on fan performance is shown, and linear trends are discovered therein, which allow determination of fan performance at any geometric scale analytically.

Reynolds Number

The importance of Reynolds number in fan scaling was shown theoretically by Smith [45] through consideration of the continuity equation (1) and Navier–Stokes equation (2), which govern the Newtonian incompressible flow through a fan.

$$\nabla \cdot \mathbf{V} = 0 \tag{1}$$

$$\rho \frac{D\mathbf{V}}{Dt} = -\nabla(P + \rho g z) - \mu \nabla \times \nabla \times \mathbf{V} \tag{2}$$

The dimensionless form of these equations contained only normalized variables [45], with the exception of the term $\rho UL/\mu$,

---

Contributed by the Fluids Engineering Division of ASME for publication in the JOURNAL OF FLUIDS ENGINEERING. Manuscript received October 6, 2007; final manuscript received May 11, 2008; published online September 2, 2008. Assoc. Editor: Chunill Hah.

thereby proving that similar fans would have to be operated at the same Reynolds number to share the same flow properties (i.e., for the governing flow equations to be identical); otherwise, a Reynolds number or scale effect would occur. This derivation is shown in Ref. [46].

Fan miniaturization causes a reduction in Reynolds number through reduction in the characteristic length L; hence, in this experimental investigation, the Reynolds number effect was expected to alter fan performance as the microscale was reached. The reduction in Reynolds number increased the magnitude of the viscous forces relative to the momentum forces; hence, the effect on fan performance was expected to be negative [47]. The effect was not solvable analytically because of the nonlinear nature of the Navier–Stokes equation (2) [45,48]; hence, Reynolds number effect was investigated experimentally.

Reynolds number Re was defined using blade midspan values for reference length and speed in Eq. (3), and thus Re was reduced during experiments by decreasing fan geometric scale and rotational speed incrementally. The use of blade midspan rotational velocity U_{mid} as reference speed made this definition of Reynolds number independent of the fan operating point. Subsequently, Re held a constant value as the fan was throttled, which allowed practical categorizing of experimental results. The Reynolds number range covered in the experimental investigation was sufficiently low to ensure laminar flow within the blade passage [46]. Experimental results at very low Reynolds numbers $\mathrm{Re} \leq 850$ required consideration of the actual velocity of the freestream flow over the blade surface, and hence the fan operating point, to explain the observed physical phenomena.

$$\mathrm{Re} = \frac{\rho U_{\mathrm{mid}} c_{\mathrm{mid}}}{\mu} \tag{3}$$

Test Fans

Three geometrically similar fans were manufactured for experimentation, a datum fan of 120 mm diameter representing the macro scale, a 1/3 scale fan of 40 mm diameter representing the mesoscale, and a 1/20 scale fan of 6 mm diameter representing the microscale, as shown in Fig. 1. Datum blade geometry was taken from a typical axial flow fan for electronics cooling, a Papst 4184 NGX. The chord length of the datum rotor was 47 mm at blade midspan and 52 mm at the tip. Nominal tip speed of 16.4 m/s was also taken from the Papst fan; therefore, the nominal rotating speeds of the datum, 1/3, and 1/20 scale fans were 2800 rpm, 8400 rpm, and 56,000 rpm, respectively.

Datum fan rotor was taken directly from a Papst 4184 NGX. 1/3 scale fan rotor was manufactured by computer numerically controlled (CNC) milling, at an approximate tolerance of 0.05 mm (which was 0.3% of the chord). Attempts at manufacturing rotors at scales below 1/6 via CNC milling failed, as the force of the cutting tool destroyed the fragile blades during manufacture. Hence, the 1/20 scale fan was manufactured by microelectrodischarge machining (μEDM) techniques. This manufacturing process was almost forceless as there was no physical contact between the cutting tool and the workpiece, an important factor given the fragile nature of the 1/20 scale fan geometry (e.g., the trailing edge thickness was 15 μm). The microfan components were eroded from steel workpieces by two μEDM processes: wire μEDM and die-sinking μEDM.

- Wire μEDM used 50 μm diameter zinc plated brass wire electrodes. Dielectric fluid was de-ionized water. This process cut out two-dimensional shapes, and was therefore utilized to form the rotor outline, as shown in Fig. 2. The 250 μm diameter hole for the motor shaft was eroded with a tungsten carbide electrode.
- Die-sinking μEDM used three-dimensional tungsten copper electrodes. Dielectric fluid was oil based. The tungsten copper electrodes were three-dimensional negatives of the desired blade geometry and were manufactured by micro-CNC milling. During the die-sinking μEDM process, the electrodes eroded the curved pressure and suction surfaces of each blade from the workpiece, as shown in Fig. 2. Due to electrode erosion, multiple copies of the cutting tool were required to finish the workpiece.

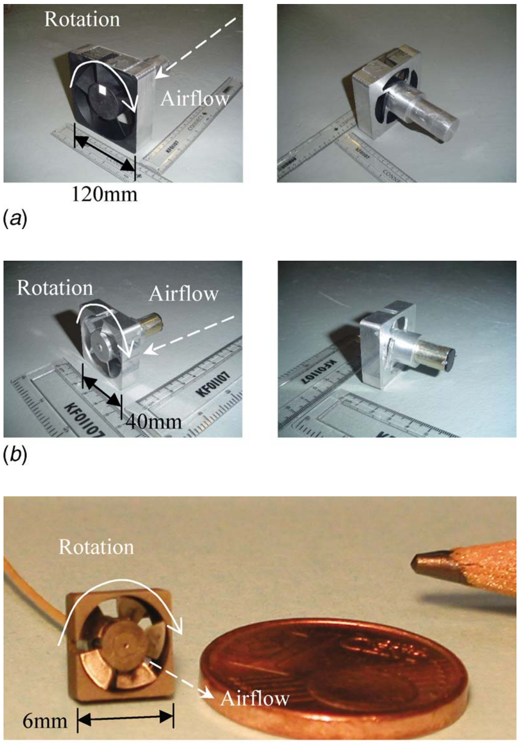

Fig. 1 Test fans. (*a*) Datum fan. 30 cm rulers included for scale. (*b*) 1/3 scale fan. 30 cm rulers included for scale. (*c*) 1/20 scale fan. Pencil tip and European 1 cent coin (Ø16 mm) included for scale.

The parameters for roughing and finishing μEDM processes are given in Table 1. Microscope examination showed the surface finish to be satisfactory. μEDM manufacturing tolerance for the 1/20 scale rotor was approximately 3 μm, which was 0.1% of the chord.

The microfan assembly consisted of four components: a rotor, keyway, motor, and housing, as shown in Fig. 3. Based on their experience in successfully manufacturing the axial microfan, the IMM stated that manufacture by injection molding was possible [49]. Reducing geometric scale would also increase strength to weight ratio and thus allow use of softer and cheaper materials that are easier to form than steel.

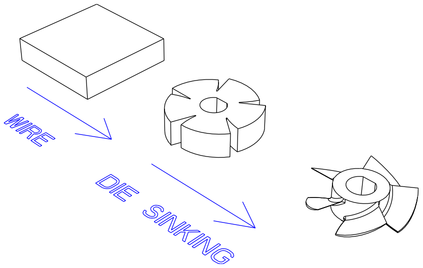

Fig. 2 μEDM of the 1/20 scale rotor

Table 1 Settings for the μEDM process

	Electrode polarity	Workpiece polarity	Voltage (V)	Current (A)	Pulse duration
Roughing cut	Positive	Negative	120–180	20–80	0.5–1.4 μs
Finishing cut	Negative	Positive	60–100	1–2	50–100 ns

Rotational imbalance in the rotor caused the 244 μm diameter motor shaft to bend. At 60,000 rpm, the deflection was sufficient to cause the rotor tips to scrape against the fan housing, thereby preventing the fan from operating at higher rotational speeds. In future designs, the maximum rotational speed can be increased by supporting the rotor at the fan outlet with a second bearing or manufacturing the rotor from a material lighter than steel.

Pressure-Flow Characteristics

The effect of Reynolds number on the performance of each fan was determined by pressure-flow characteristic tests. Each scale fan had its own experimental rig of corresponding size. All fan tests were carried out according to Ref. [50]; thus, the experimental rigs shared the same generic design, as shown in Fig. 4. Air entered the rig through an orifice plate, used for flow rate measurement and coarse control of the test fan operating point. The auxiliary fan provided a means for fine-tuning the operating point of the test fan. Vanes were fitted to ensure swirl-free flow entering and leaving the auxiliary fan. The static pressure rise of the test fan was measured via a settling chamber, which contained mesh screens to ensure parallel flow over the pressure tappings. The width of the settling chamber was at least 2.5 times the test fan diameter; therefore, any boundary layers present on the settling chamber walls did not influence the test fan inlet.

Experimental uncertainty was calculated for each rig using the method of Kline et al. [51]; the results are shown in Table 2.

The experimental results in Fig. 5 show that fan performance was insensitive to Reynolds number reduction until Re=1980 was reached, whereupon further reductions in Reynolds number caused a progressive reduction in fan performance. Neustein [53] noted a similar insensitivity to Reynolds number reduction until 2000 was reached. The reduction in dimensionless flow rate with Reynolds number was corroborated by the observations of Refs. [45,54,55], and similarly the reduction in dimensionless pressure rise was corroborated by the observations of Refs. [44,56,57].

$$\psi = \frac{P_s}{\rho U_{\mathrm{mid}}{}^2} \tag{4}$$

$$\phi = \frac{Q}{U_{\mathrm{mid}} A_2} \tag{5}$$

Scrutiny of the 1/20 scale fan measurements showed that the complex performance characteristic curve could be decomposed into three lines by adjusting the power of the flow rate axis Q, as shown in Fig. 6. These three lines were each defined as separate operating regimes to enable their use as analytical tools. The abrupt stall, progressive stall $\{Q^{0.2}\}$, and normal operating regime $\{Q^2\}$ notation of Ref. [37] was adopted, as shown in Fig. 7, with each linear trend defined by Eqs. (6)–(8), respectively. The linear trend described by Eq. (8) was similar to that found by Ref. [58].

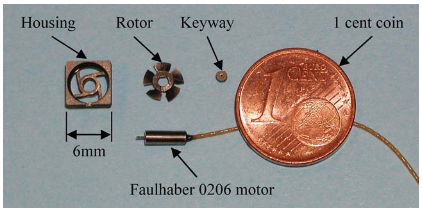

Fig. 3 1/20 scale fan components. European 1 cent coin included for scale

$$P_s = P_{s_{\max}} \tag{6}$$

$$P_s = R_L - S_L Q^{0.2} \tag{7}$$

$$P_s = R_H - S_H Q^2 \tag{8}$$

There was an absence of measurement points in the center of the abrupt stall regime in Fig. 6(*b*) despite the deliberate experimental policy of collecting a greater density of measurements at lower flow rates. This absence may have been due to the onset of full-span stall at the stall point, which would have prevented the fan from producing a flow rate in the abrupt stall regime.

It was possible to generate the performance characteristic of the 1/20 scale fan at any rotational speed ω by relating $P_{s_{\max}}$, R_L, S_L, R_H, and S_H to ω. This analysis has been carried out in Ref. [46].

In accordance with the recommendations of Ref. [59], the analysis for the rest of this investigation will be focused on the normal operating regime, as it is the most useful regime to a potential axial fan designer. The normal operating regimes of the larger 1/3 and datum scale fans contained the linear trend described by Eq. (8), as shown in Figs. 8 and 9, respectively. This linear trend was subsequently present in the dimensionless plot of fan performance, as shown in Fig. 10. Therefore, the normal operating regime linear trend could be used to analyze Reynolds number effect.

The dimensionless form of Eq. (8) was derived by Ref. [46] as Eq. (9) using the method of Refs. [60–62];

$$\psi = R_H{}^* - S_H{}^* \phi^2 \tag{9}$$

where $R_H{}^*$ and $S_H{}^*$ were derived as Eqs. (10) and (11), respectively.

$$R_H{}^* = \frac{R_H}{\rho U_{\mathrm{mid}}{}^2} \tag{10}$$

$$S_H{}^* = \frac{S_H A_2{}^2}{\rho} \tag{11}$$

The effect of Reynolds number on fan performance could now be analyzed through its effect on the dimensionless ordinate intercept $R_H{}^*$ and slope $S_H{}^*$. The variation of $R_H{}^*$ with Reynolds number is shown in Fig. 11. The average value of $R_H{}^*$ for the datum fan was 0.337 for the 1/3 scale fan 0.335 and for the 1/20 scale fan 0.291. These average results alone suggested that $R_H{}^*$ decreased with Reynolds number. However, closer inspection of the 1/20 scale fan results in Fig. 11(*b*) showed $R_H{}^*$ oscillating around 0.291 rather than reducing monotonically with Reynolds number. Therefore, $R_H{}^*$ was independent of Reynolds number, and the lower values of $R_H{}^*$ measured for the 1/20 scale fan were due to an unfortunate discrepancy in experimental rig or model similarity. Therefore, the empirical correlation selected for $R_H{}^*$ was the average of all measurements, 0.307, as follows:

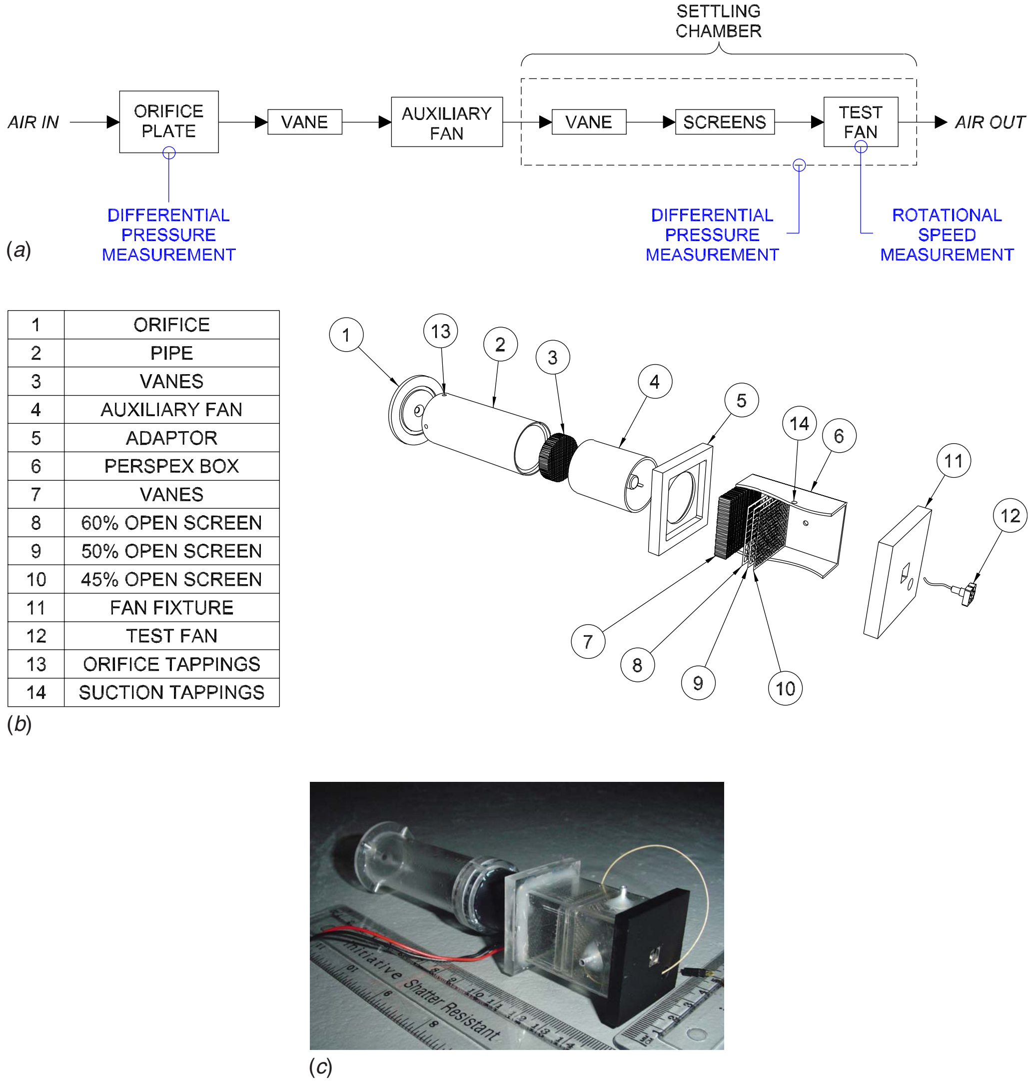

Fig. 4 Fan characterization rigs. (*a*) Schematic of fan characterization rigs. (*b*) Exploded view of microfan characterization rig. (*c*) Assembled microfan characterization rig. 30 cm rulers included for scale.

$$R_H{}^* = 0.307 \tag{12}$$

The experimental results in Fig. 12 show that $S_H{}^*$ increased rapidly at low Reynolds numbers (<2000) and converged towards a constant value at high Reynolds numbers ($>10{,}000$). This behavior seemed asymptotic, with one (viscous) asymptote placed at $\mathrm{Re}=0$ and another (inviscid) asymptote placed at $S_H{}^*=2.3$. Such asymptotic behavior implied a zero flow coefficient ϕ at zero Reynolds number (viscous asymptote) and a maximum flow coefficient $\phi_{\max}$ as Reynolds number tended towards infinity (inviscid asymptote). This asymptotic behavior correctly described the trend of the Reynolds number effect; therefore, the empirical correlation (Eq. (13)) created for $S_H{}^*$ obeyed the asymptotes while also following the experimental data.

Table 2 Uncertainty for characterization rigs

Rig scale	P (Pa)	Q (m^3 s)	Re
Datum	± 0.021	$\pm 1.01\times 10^{-4}$	± 14
1/3	± 0.05	$\pm 8.81\times 10^{-5}$	± 5
1/20	± 0.05	$\pm 1.17\times 10^{-6}$	± 2

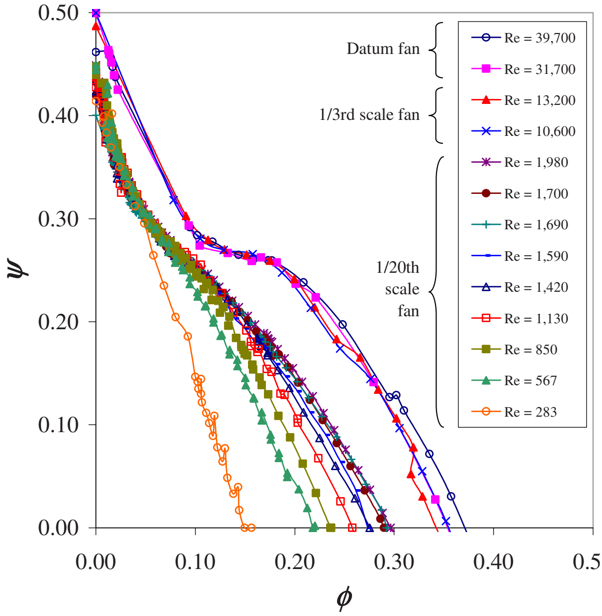

Fig. 5 Dimensionless fan performance. Ψ and ϕ are defined by Eqs. (4) and (5), respectively.

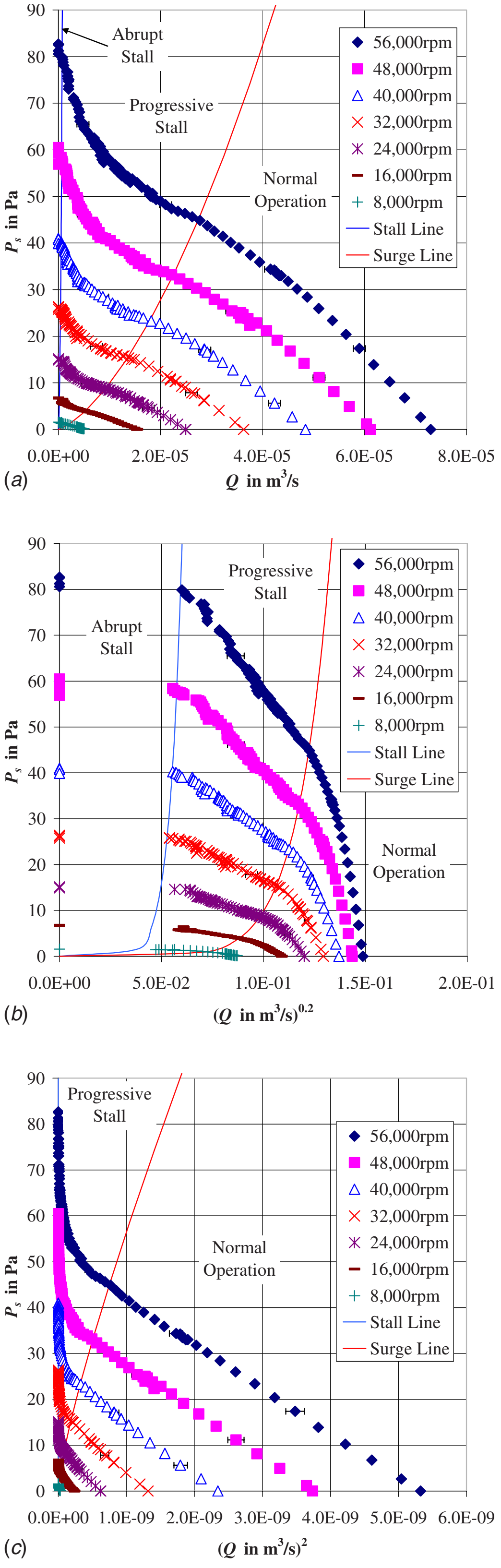

Fig. 6 Static performance characteristics for the 1/20 scale fan; power of the flow rate axis *Q* has been adjusted to decompose the performance characteristic into three lines. (*a*) Static performance characteristics for the 1/20 scale fan. (*b*) Flow rate axis raised to the power of 0.2 to linearize the progressive stall regime. (*c*) Flow rate axis raised to the power of 2 to linearize the normal operating regime.

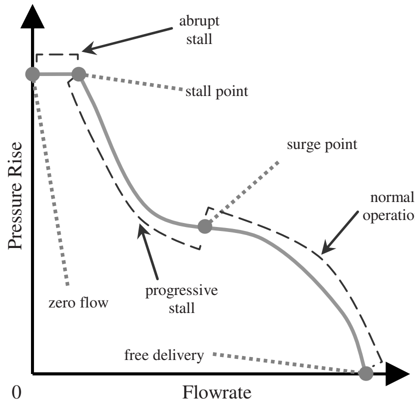

Fig. 7 Pressure flow characteristic, divided into three operating regimes (abrupt stall, progressive stall, and normal operation)

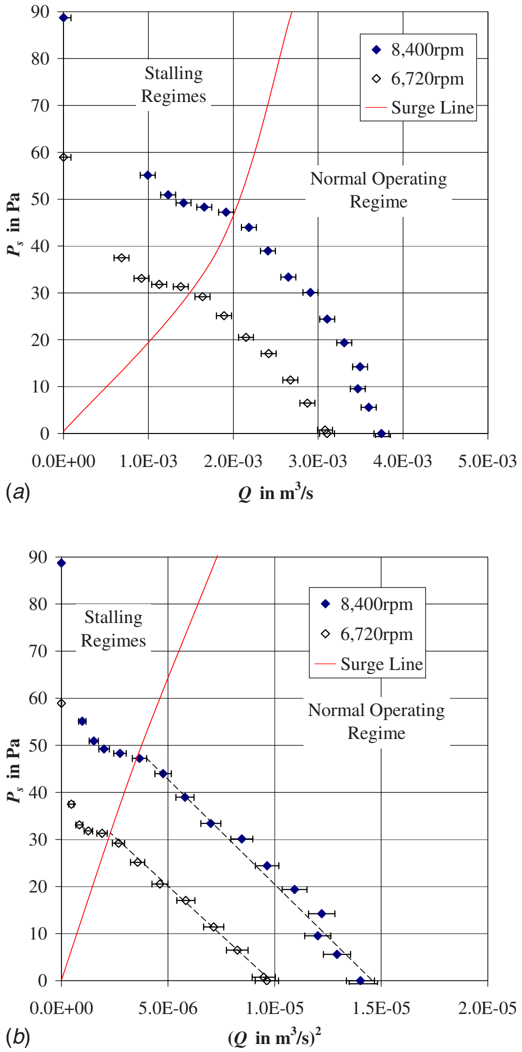

Fig. 8 Linear trend in the normal operating regime of the 1/3 scale fan. (*a*) Static performance characteristics for the 1/3 scale fan. (*b*) Flow rate *Q* axis raised to the power of 2 to linearize the normal operating regime.

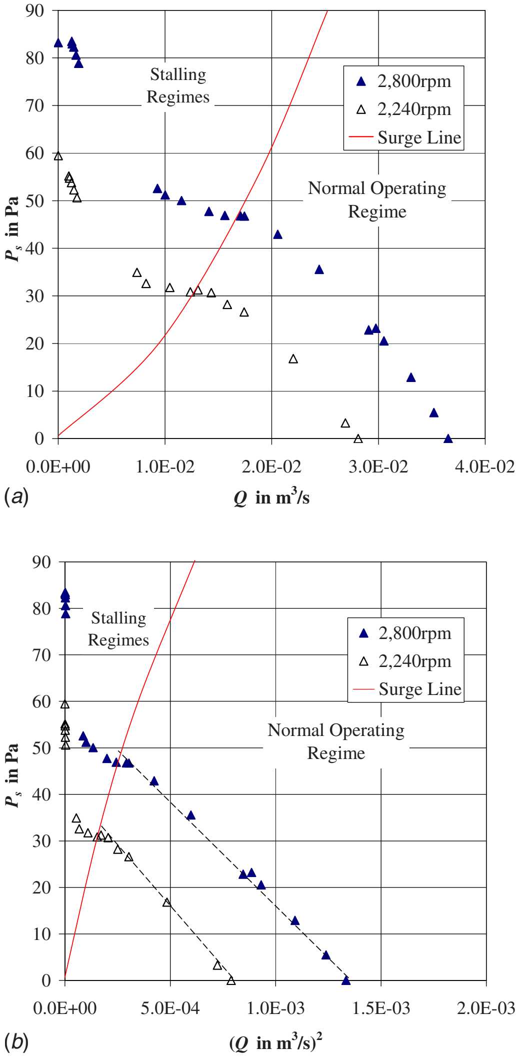

Fig. 9 Linear trend in the normal operating regime of the datum scale fan. (*a*) Static performance characteristics for the datum fan. (*b*) Flow rate *Q* axis raised to the power of 2 to linearize the normal operating regime.

$$S_H{}^* = 2.3 + \underbrace{\frac{2860}{\text{Re}}}_{\text{viscous term}} \tag{13}$$

The maximum flow coefficients $\phi_{\max}$ were calculated from Eqs. (9), (12), and (13) and compared with experimental values in Fig. 13. This plot was not an attempt to "verify" the correlation from the same set of experimental data that it was borne from, but to demonstrate the use of the aforementioned linear method in quantifying the viscous loss and predicting the fan performance at any Reynolds number.

Viscous Dominance

The 1/20 scale fan performance characteristics became progressively linear in appearance as Reynolds number was reduced from 850 to 283, as shown in Fig. 14, without any adjustment of the power of the abscissa ϕ. This self-linearization can be explained through consideration of the definition of the Reynolds number Re (Eq. (3)) and the empirical correlation for $R_H{}^*$ (Eq. (12)) and $S_H{}^*$ (Eq. (13)), which reveal an analogy with the Hagen–Poiseuille formula for laminar pipe flow (Eq. (20)).

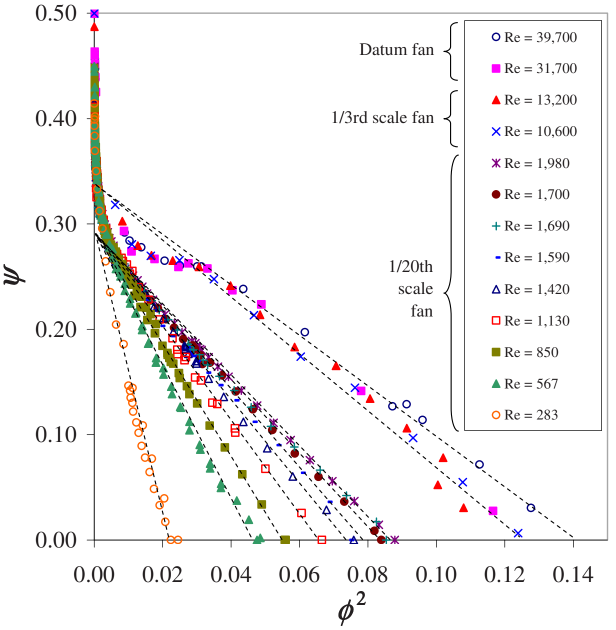

Fig. 10 Dimensionless fan performance; ϕ axis has been raised to the power of 2 to display linear trends

As previously discussed, the fan pressure-flow performance (in the desired normal operating regime) could be determined by substituting the empirical correlations for $R_H{}^*$ (Eq. (12)) and $S_H{}^*$ (Eq. (13)) into the linear dimensionless equation (9), giving

$$\psi = \underbrace{0.307 - 2.3\phi^2}_{\text{inviscid performance}} - \underbrace{\frac{2860}{\text{Re}}\phi^2}_{\text{viscous loss}} \tag{14}$$

Substituting in ψ Eq. (4) and ϕ Eq. (5) gave an expression for fan static pressure rise P_s (Eq. (15)). The viscous loss term in Eq. (15) bore a close resemblance to Darcy's equation for laminar pipe flow [63]. The significance of the "curve" and "line" designations will be explained later in Eq. (21).

$$P_s = \underbrace{0.307\rho U_{\text{mid}}{}^2 - 2.3\overbrace{\frac{\rho Q^2}{A_2{}^2}}^{\text{curve}}}_{\text{inviscid performance}} - \underbrace{\overbrace{\frac{2860}{\text{Re}}\frac{\rho Q^2}{A_2{}^2}}^{\text{line}}}_{\text{viscous loss}} \tag{15}$$

The definition of Reynolds number in Eq. (3) used blade speed U_{mid} as reference speed. This was a necessary and reasonable approximation for experimentation; however, a more accurate definition of Reynolds number would have involved the velocity of the actual freestream flow over the blade surface. To explain the self-linearization of characteristic shape, it was necessary to adopt this more accurate definition of Reynolds number Re_a (Eq. (16)), which is based on the actual flow velocity relative to the blade W_∞;

$$\text{Re}_a = \frac{\rho W_\infty c_{\text{mid}}}{\mu} \tag{16}$$

Substituting Re_a (Eq. (16)) into Eq. (15) gave

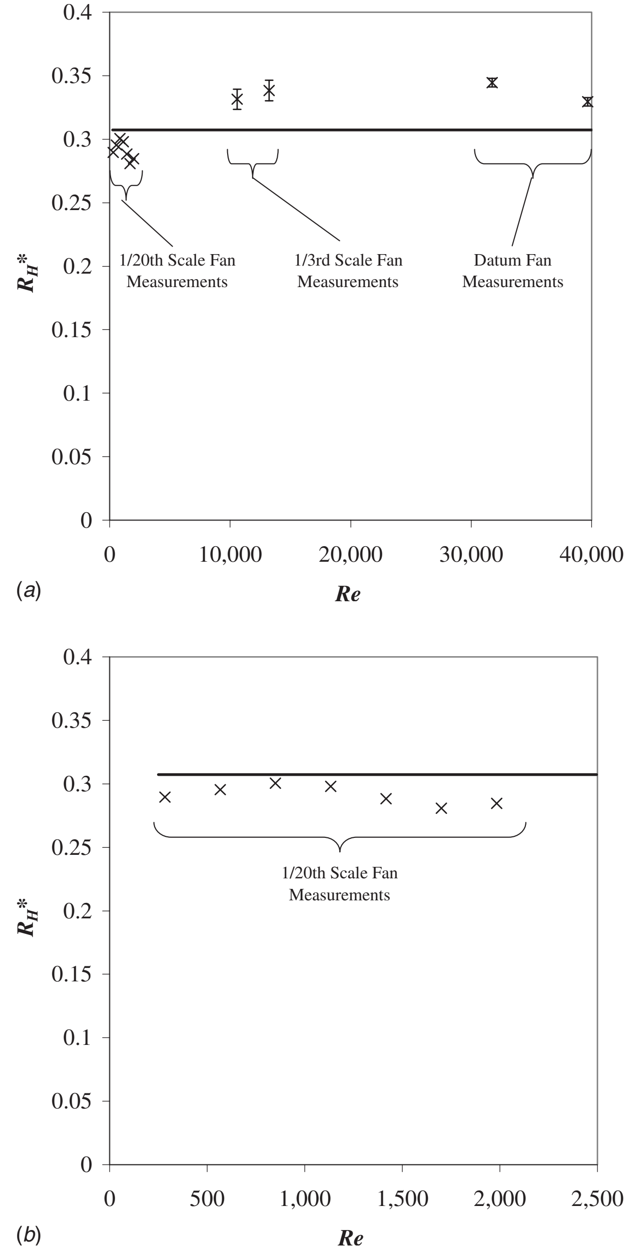

Fig. 11 Plot of R_H^* against the Reynolds number. The points represent measurements and the continuous line represents empirical correlation (Eq. (12)). The results for all fan scales are shown in (*a*) and the results for the 1/20 scale fan are shown more clearly in (*b*).

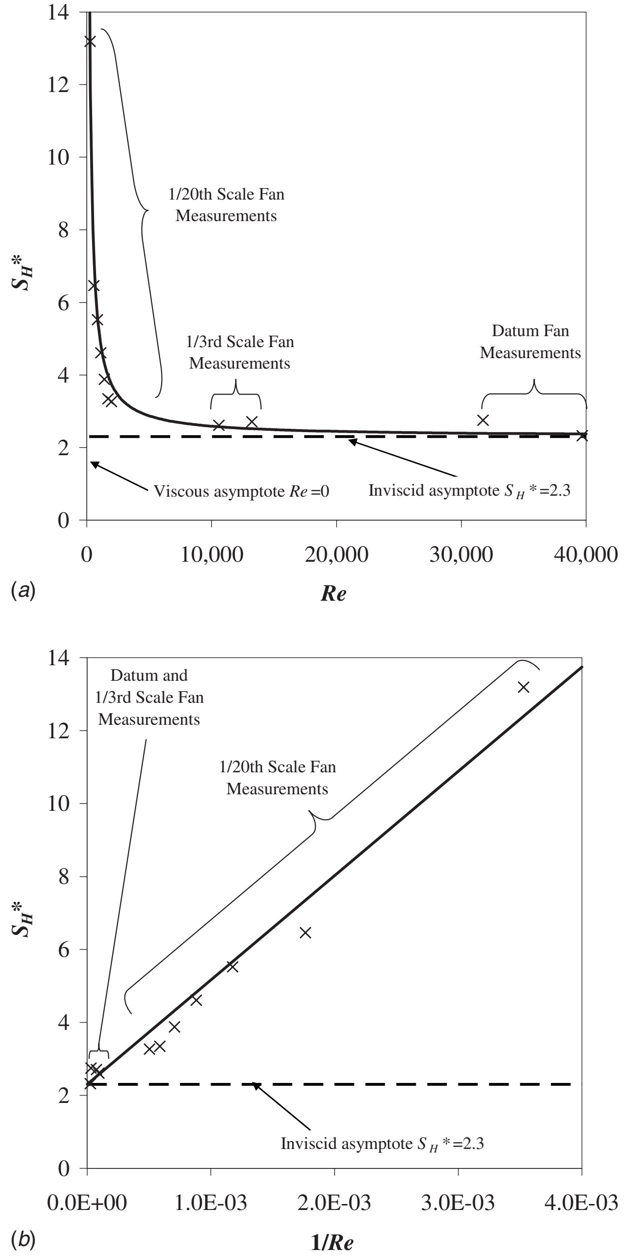

Fig. 12 Plot of S_H^* against the Reynolds number. The points represent measurements and the continuous line represents empirical correlation (Eq. (13)). The results for all fan scales are shown in (*a*) and the results for the 1/20 scale fan are shown more clearly in (*b*).

$$P_s = \underbrace{0.307\rho U_{\text{mid}}^2 - 2.3\frac{\rho Q^2}{A_2^2}}_{\text{inviscid performance}} - \underbrace{2860\frac{\mu}{W_\infty c_{\text{mid}}}\frac{Q^2}{A_2^2}}_{\text{viscous loss}} \tag{17}$$

The flow velocity relative to the blade W_∞ was directly proportional to the mean outlet velocity; thus,

$$W_\infty = k\frac{Q}{A_2} \tag{18}$$

Substituting W_∞ (Eq. (18)) into Eq. (17) gave

$$P_s = \underbrace{0.307\rho U_{\text{mid}}^2 - 2.3\frac{\rho Q^2}{A_2^2}}_{\text{inviscid performance}} - \underbrace{2860\frac{[\mu Q]}{k c_{\text{mid}} A_2}}_{\text{viscous loss}} \tag{19}$$

In comparison, the Hagen–Poiseuille equation (20) for static pressure loss P_{loss} for laminar flow in a pipe of length L_p and diameter d_p was [63]

$$P_{\text{loss}} = \frac{128 L_p}{\pi d_p^4}[\mu Q] \tag{20}$$

Hence, the analogy, the viscous loss term in the fan characteristic equation (19), and the Hagen–Poiseuille equation (20) were both proportional to the product of the dynamic viscosity μ and volumetric flow rate Q. The coincidence was understandable as lami-

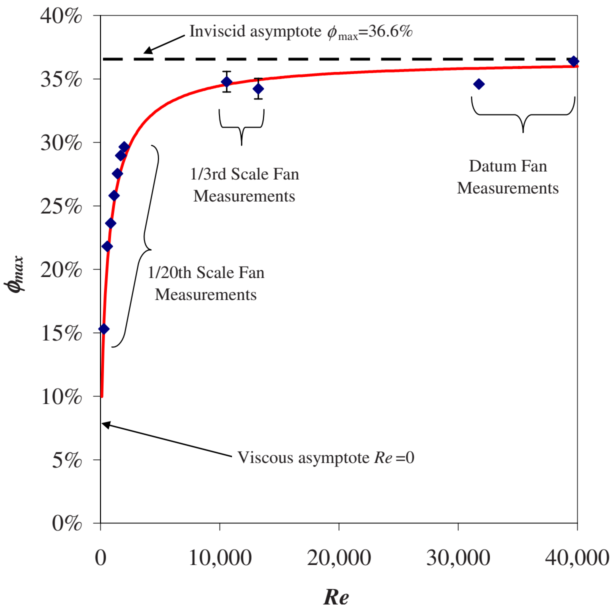

Fig. 13 Plot of the maximum flow coefficient ϕ_{max} against the Reynolds number. The points represent measurements and the continuous line represents empirical correlation.

nar flow was present in both cases, the only difference being that the Hagen–Poiseuille equation (20) governed flow through a simple circular cross section, whereas the fan characteristic equation (19) governed the relative flow through the complex curved cross section presented by the blade geometry. The intersection $[\mu Q]$ between both formulas implied that the linear scaling method applied in this investigation was not a mere curve fit to data, but also correctly described the observed viscous physical phenomenon, and therefore holds for laminar Reynolds numbers outside the experimental range covered.

The form of Eq. (15) explained the transition in characteristic shape from a curve to a line as Reynolds number was reduced. The ratio between the curve and line terms was

$$\frac{\text{line term}}{\text{curve term}} = \frac{2860}{2.3\,\text{Re}} \tag{21}$$

Therefore, reducing Reynolds number Re caused the line term in the previous equation (Eq. (21)) to become stronger relative to the curve term, thus causing the appearance of the pressure-flow characteristic to alter from the traditional curved shape to a line. Similar line characteristics were measured by Ref. [40] while decreasing Reynolds number (i.e., increasing kinematic viscosity ν) in large scale centrifugal pumps. The similarity between both Reynolds number investigations indicates that this viscous physical phenomenon was not confined to axial flow fans and therefore may apply to future microscale turbomachinery such as those manufactured by Ref. [64,65].

Conclusions

Manufacture. This investigation proved that axial flow fans can be manufactured and operated at the microscale. CNC milling techniques were initially investigated but found to be incapable of manufacturing rotors below 1/6 scale, as the contact force of the cutting tool destroyed the fragile blades. The noncontact nature of the μEDM process was the principal factor in its success in manufacturing the microscale rotors intact.

The maximum rotational speed of the microfan was limited to 60,000 rpm because of tip scraping caused by rotor imbalance. This speed limit can be surpassed in future designs by addition of a second bearing at the fan outlet. Speed can also be increased by manufacturing the rotors from lighter plastic materials.

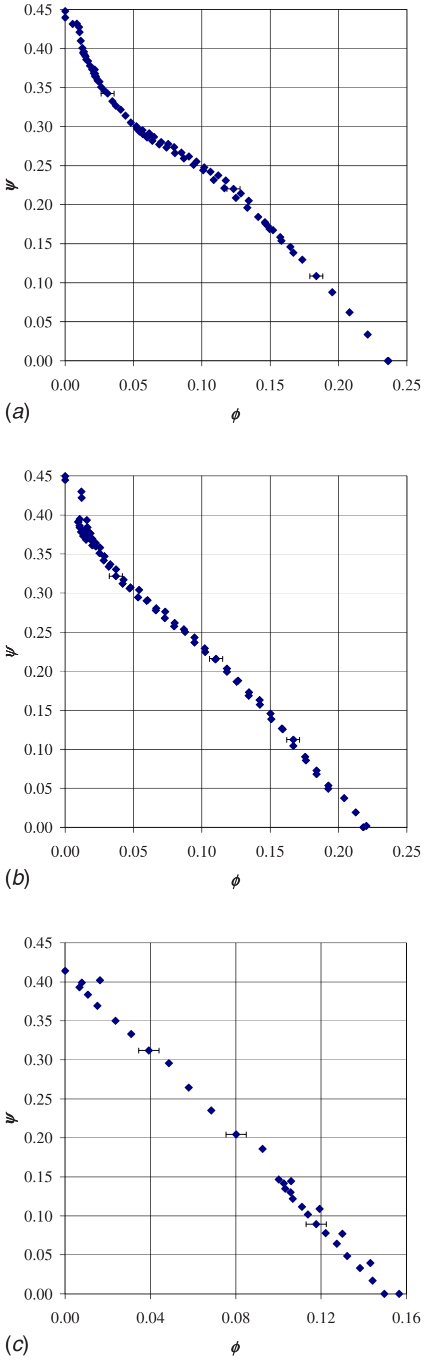

Fig. 14 Dimensionless 1/20 scale fan performance characteristics at low Reynolds number, showing distortion of the characteristic shape. (*a*) Re=850. (*b*) Re=567. (*c*) Re=283.

Pressure-Flow Characteristics. There was a significant decrement in pressure-flow performance as geometric size was reduced towards the microscale (6 mm diameter); however, this decrement was not of sufficient magnitude to prohibit the use of axial microfans in electronics cooling applications.

The complex curves formed by the axial fan pressure-flow characteristics were decomposed into constructions of three lines, with each line forming a different operating regime. These linear trends provided a mathematical foothold (through a slope and ordinate intercept) on the fan performance characteristics. In this investigation, the mathematical foothold was exploited to investigate Reynolds number effect. In future investigations, it may be used to quantify other aerodynamic effects or to provide a quick and accurate method for determining fan performance across a range of parameters (e.g., rotational speed, diameter, fluid density, and viscosity).

Analysis of the normal operating regime yielded novel dimensionless parameters for ordinate intercept R_H^* and slope S_H^*. Applying a similar analysis to the linear trend observed in the progressive stall regime would yield more novel dimensionless parameters. Empirical correlations for R_H^* and S_H^* determined dimensionless fan performance in the normal operating regime at any laminar rotational speed and casing diameter, and hence determined the Reynolds number effect. R_H^* was found to be a constant value, independent of Reynolds number, and dependent only on fan geometric design, whereas S_H^* was found to be dependent on Reynolds number, tending towards infinity as Re tended towards zero, and tending towards a finite positive value as Re tended towards large (laminar) values. Such asymptotic behavior implied zero flow at zero Reynolds number, and convergence towards a finite flow coefficient as Reynolds number tended towards infinity.

The use of blade rotational speed as reference velocity in the definition of Reynolds number sufficed for $\mathrm{Re} \geq 850$. Below this limit, the fan performance characteristics became progressively linear in appearance without any adjustment of the abscissa power. In order to explain this self-linearization, it was necessary to change the definition of Re so that the reference velocity was the actual freestream velocity of the fluid relative to the blade surface. The fan static pressure loss due to Reynolds number effect was subsequently found to be similar to the Hagen–Poiseuille static pressure loss in pipe flow. This was understandable as although the blade passage was a more complex shape than a simple circular cross section, the flow in both cases was laminar, and therefore the static pressure losses due to viscous action varied in a similar manner with Reynolds number. Furthermore, the progressive self-linearization of the fan performance characteristics was found to be due to the dominance of the viscous loss relative to the inviscid performance. Similar experimental measurements in centrifugal pumps indicate that this viscous physical phenomenon is common to very low Reynolds number turbomachinery.

Acknowledgment

The authors wish to acknowledge the support of Enterprise Ireland, the University of Limerick, and the Institut für Mikrotechnik Mainz GmbH, who made this research possible.

Nomenclature

Symbol

A = fan area, m^2
c = blade chord length, m
d = diameter, m
g = acceleration due to gravity, $\mathrm{m/s}^2$
k = proportionality constant, 1
L = length, m
P = static pressure, $\mathrm{N/m}^2$
Q = volumetric flow rate, m^3
R = ordinate intercept, $\mathrm{N/m}^2$
Re = Reynolds number, 1
S = slope (for S_H), $\mathrm{kg\,m}^{-7}$ (for S_L), $\mathrm{kg\,m}^{-1.6}\,\mathrm{s}^{-1.8}$
t = time s
U = speed, m/s
V = absolute airspeed, m/s
W = airspeed relative to blade, m/s
z = Elevation, m

Greek Symbols

ϕ = flow coefficient, 1
μ = dynamic viscosity, kg/m s
ν = kinematic viscosity, m^2/s
ρ = density, $\mathrm{kg/m}^3$
ω = rotational speed, rad/s
ψ = static pressure coefficient, 1

Subscripts

2 = fan outlet
a = accurate
H = normal operating regime
L = progressive stall regime
loss = static pressure loss
max = maximum
mid = blade midspan
p = circular pipe
s = fan static pressure rise
∞ = freestream

Superscripts

$*$ = dimensionless parameter, 1

References

[1] Moore, G. E., 1965, "Cramming More Components Onto Integrated Circuits," Proc. IEEE, **86**(1), pp. 82–85.
[2] Schaller, R. R., 1997, "Moore's Law: Past, Present, and Future," IEEE Spectrum, **34**(6), pp. 52–59.
[3] Azar, K., 2000, "Power Consumption and Generation in the Electronics Industry—A Perspective," *Proceedings of the 16th IEEE SEMI-THERM Symposium*, pp. 201–212.
[4] Moore, G. E., 2003, "No Exponential is Forever: But "Forever" Can Be Delayed!," *Plenary Session 1 of the 2003 IEEE International Solid-State Circuits Conference*.
[5] Ellsworth, M. J., 2004, "Chip Power Density and Module Cooling Technology Projections for the Current Decade," *Proceedings of the 2004 Inter Society Conference on Thermal Phenomena*, pp. 707–708.
[6] Krishnan, S., Garimella, S. V., Chrysler, G. M., and Mahajan, R. V., 2005, "Toward a Thermal Moore's Law," *IPACK2005-73409, Proceedings of the ASME InterPACK '05*, San Francisco, CA.
[7] MIL-HDBK-217F, 1991, *Military Handbook, Reliability Prediction of Electronic Equipment*, Department of Defense, Washington, D.C.
[8] Paik, P., Pamula, V. K., and Chakrabarty, K., 2004, "Thermal Effects on Droplet Transport in Digital Microfluidics With Applications to Chip Cooling," *Proceedings of the IEEE 2004 Inter Society Conference on Thermal Phenomena*, pp. 649–654.
[9] Reinikainen, T., Rantala, J., Dalton, T., Newport, D., Punch, J., and Grimes, R., 2001, "Thermal Roadmap of Portable Products," Nokia Mobile Phones / University of Limerick Research Programme, Stokes Research Institute.
[10] Punch, J., 2005, private communications.
[11] Bergles, A. E., 2003, "Evolution of Cooling Technology for Electrical, Electronic, and Microelectronic Equipment," IEEE Trans. Compon. Packag. Technol., **26**(1), pp. 6–15.
[12] Gillan, P. A., 2002, "Fresh Air—Natural Asset," *Proceedings of the INTELEC 24th Annual International Telecommunications Energy Conference 2002*, pp. 470–477.
[13] Biswas, R., Agarwal, R. B., Goswami, A., and Mansingh, V., 1999, "Evaluation of Airflow Prediction Methods in Compact Electronic Enclosures," *Proceedings of the 15th IEEE SEMI-THERM Symposium*, pp. 48–53.
[14] Turner, M., 1995, "Fan Considerations in Enclosure Cooling," Electronic Packaging and Production, **35**, pp. 44–47.
[15] Wei, J., and Suzuki, M., 2005, "Thermal Management of Fujitsu High-End Unix Servers," *IPACK2005-73313, Proceedings of ASME InterPACK '05*, San Francisco, CA.
[16] Fuji Xerox Co. Ltd., 1989, "Image Reader," Patent No. JP1053677.
[17] Fujikura Ltd., IBM, 2004, "Cooling Device for Electronic Element," Patent No. JP2004015024.
[18] Hitachi Ltd., 1994, "Semiconductor Sealing Package and Cooling Method Thereof," Patent No. JP6013512.
[19] Hitachi Ltd., 1995, "Semiconductor Sealing Package and Cooling Method Thereof," Patent No. JP7030026.
[20] IBM, 1994, "Cooling Microfan Arrangements and Process," Patent Nos. US5326430 and US5296775.
[21] Mitsubishi Electric Corp., 1994, "Integrated Circuit," Patent No. JP6177298.
[22] Nippon Keiki, Fujikura Ltd., 1998, "Cooling System Having Cooling Fan," Patent No. JP10197172.
[23] Papst-Motoren GmbH, 2003, "Miniature Fan or Micro Fan," International Publication No. WO 03/058796 A1, International Patent Classification No. H02K 29/08, International File References PCT/EP02/13822.
[24] Samsung, 1999, "Micro Fan," Patent No. CA2276504.
[25] Samsung, 2000, "Micro Fan," Patent No. KR2000006187.

[26] Samsung, 2001, "Micro Fan," Patent No. TW457842B.
[27] Samsung, 2002, "Micro-Fan," Patent No. US2002127113.
[28] Sharp, 1989, "Air Suction Type Sheet Material Conveying Device," Patent No. JP1064937.
[29] Sony Corp., 1996, "Optical Head Device," Patent No. JP8129771.
[30] Sumitomo Metal Industries Ltd., 2001, "Apparatus for Cooling Electronic Component and Manufacture Thereof," Patent No. JP2001015661.
[31] Sunonwealth Electrical Machine Industry Co., 2004, "Minisize Brushless DC Fan," Patent No. CN1523736.
[32] Yongdeji Lighting Electric Co., 2003, "High Power Compact Energy Saving Lamp With Micro Electric Fan," Patent No. CN2580297Y.
[33] Grimes, R., 2001, "On Air Flow and Heat Transfer in Fan Cooled Electronic Systems," Ph.D. thesis, University of Limerick, Ireland.
[34] Grimes, R., and Davies, M., 2001, "Aerodynamic and Thermal Investigation Into Axial Flow Fan Cooling of Electronic Systems, Part 1: Measurement Techniques and Steady Flow Measurements," 35th National Heat Transfer Conference.
[35] Spearing, M., 2001, "Micropropellers to Keep Your Chips Cool," New Scientist, 20 January, Issue No. 2274.
[36] Schlichting, H., and Gersten, K., 2000, *Boundary Layer Theory*, 8th ed., Springer-Verlag, Berlin, Germany.
[37] Cumpsty, N. A., 1989, *Compressor Aerodynamics* Longman Scientific and Technical, Essex, England.
[38] Hill, P. G., and Peterson, C. R., 1992, *Mechanics and Thermodynamics of Propulsion*, 2nd ed., Addison-Wesley, Wokingham, England.
[39] Saravanamuttoo, H. I. H., Rogers, G. F. C., and Cohen, H., 2001, *Gas Turbine Theory*, 5th ed., Pearson Education, London, England.
[40] Ippen, A. T., 1946, "The Influence of Viscosity on Centrifugal-Pump Performance," Trans. ASME, **68**, pp. 823–838.
[41] Davis, H., Kottas, H., and Moody, A. M. G., 1950, "The Influence of Reynolds Number on the Performance of Turbomachinery," Trans. ASME, **73**, pp. 499–509.
[42] Wallner, L. E., and Fleming, W. A., 1949, "Reynolds Number Effect on Axial-Flow Compressor Performance," NACA Report No. RM E9G11.
[43] Pinnes, R. W., 1957, "A Simple Method of Estimating the Reynolds Number Effect on Aircraft Gas-Turbine Engines Operating at High Altitudes," Trans. ASME, Paper No. 57—A-157, pp. 1–8.
[44] Sievers, G. K., Geye, R. P., and Lucas, J. G., 1958, "Investigation of Reynolds Number Effect on Performance of an Eight-Stage Axial-Flow Research Compressor With Long and Medium-Chord Lengths in the Two Transonic Inlet Stages," NACA Report No. RM E57J30.
[45] Smith, L. H, Jr., 1964, "Some Comments on Reynolds Number," ASME J. Eng. Power, **86**, pp. 225–226.
[46] Quin, D., 2006, "Micro Scale Axial Flow Fans," Ph.D. thesis, University of Limerick, Ireland.
[47] Sohn, R. L., 1956, "An Analysis of the Performance of an Axial-Flow Compressor at Low Reynolds Number," J. Aeronaut. Sci., **23**, pp. 741–746.
[48] White, F. M., 1986, *Fluid Mechanics* 2nd ed., McGraw-Hill, London, England.
[49] Kunz, S., 2003, meeting between the SRI and the IMM.
[50] BSi, 1997, *Fans for General Purposes, Part1, Performance Testing Using Standardized Airways*, BS 848, London, England.
[51] Kline, S. J., and McClintock, F. A., 1953, "Describing Uncertainties in Single-Sample Experiments," Mech. Eng. (Am. Soc. Mech. Eng.), **75**, pp. 3–8, cited from Ref. [52].
[52] Holman, J. P., 1989, *Experimental Methods for Engineers*, 5th ed., McGraw-Hill, London, England.
[53] Neustein, J., 1964, "Low Reynolds Number Experiments in an Axial Flow Turbomachine," ASME J. Eng. Power, **86**(3), pp. 257–295.
[54] Geye, R. P., and Lucas, J. G., 1957, "Investigation of Effects of Reynolds Number on Over-All Performance of an Eight-Stage Axial-Flow Research Compressor With Two Transonic Inlet Stages," NACA Report No. RM E56L11A.
[55] Heidelberg, L. J., and Ball, C. L., 1972, "Effect of Reynolds Number on Overall Performance of a 3.7 Inch Diameter Six Stage Axial Flow Compressor," NASA Report No. TN D6628.
[56] Koch, C. C., 1981, "Stalling Pressure Rise Capability of Axial Flow Compressor Stages," ASME J. Eng. Power, **103**, pp. 645–656.
[57] Schulze, W. M., Erwin, J. R., and Ashby, G. C., Jr., 1957, "NACA 65-Series Compressor Rotor Performance With Varying Annulus-Area Ratio, Solidity, Blade Angle, and Reynolds Number and Comparison With Cascade Results," NACA Report No. TN 4130 (supersedes NACA Report No. RM L52L17).
[58] Venter, S. G., and Kröger, D. G., 1992, "The Effect of Tip Clearance on the Performance of an Axial Flow Fan," Energy Convers. Manage., **33**(2), pp. 89–97.
[59] Bell, E. B., 1941, "Test of a Single-Stage Axial-Flow Fan," NACA Report No. TR 729.
[60] Dalton, T. M., and Davies, M. R. D., 1997, *Convection Dimensional Analysis*, University of Limerick, Ireland.
[61] Davies, M. R. D., and Dalton, T. M., 1997, *Teaching Thermofluids Dimensional Analysis*, University of Limerick, Ireland.
[62] Davies, M. R. D., and Dalton, T. M., 1998, "A New Approach to Teaching Thermofluids Dimensional Analysis," Int. J. Mech. Eng. Educ., **28**(2), pp. 174–184.
[63] Massey, B., and Smith, J. W., 1998, *Mechanics of Fluids*, 7th ed., Stanley Thornes Ltd., Cheltenham, U.K.
[64] Epstein, A. H., 2004, "Millimetre-Scale, Micro-Electro-Mechanical Systems Gas Turbine Engines," Trans. ASME: J. Eng. Gas Turbines Power, **126**, pp. 205–226.
[65] Hanly, K., Grimes, R., Walsh, E., Rodgers, B., and Punch, J., 2005, "The Effect of Reynolds Number on the Aerodynamic Performance of Micro Radial Flow Fans," *Proceedings of the 2005 ASME Summer Heat Transfer Conference*, San Francisco, CA, Paper No. HT2005-72514.

Computational Towing Tank Procedures for Single Run Curves of Resistance and Propulsion

Tao Xing
Ph.D.
Assistant Research Scientist
e-mail: tao-xing@uiowa.edu

Pablo Carrica
Ph.D.
Associate Professor Research Engineer
e-mail: pablo-carrica@uiowa.edu

Frederick Stern
Ph.D.
Professor Research Engineer
e-mail: frederick-stern@uiowa.edu

IIHR-Hydroscience and Engineering,
C. Maxwell Stanley Hydraulics Laboratory,
The University of Iowa,
Iowa City, IA 52242-1585

A procedure is proposed to perform ship hydrodynamics computations for a wide range of velocities in a single run, herein called the computational towing tank. The method is based on solving the fluid flow equations using an inertial earth-fixed reference frame, and ramping up the ship speed slowly such that the time derivatives become negligible and the local solution corresponds to a quasi steady-state. The procedure is used for the computation of resistance and propulsion curves, in both cases allowing for dynamic calculation of the sinkage and trim. Computational tests are performed for the Athena R/V model DTMB 5365, in both bare hull with skeg and fully appended configurations, including two speed ramps and extensive comparison with experimental data. Comparison is also performed against steady-state points, demonstrating that the quasisteady solutions obtained match well the single-velocity computations. A verification study using seven systematically refined grids was performed for one Froude number, and grid convergence for resistance coefficient, sinkage, and trim were analyzed. The verification study concluded that finer grids are needed to reach the asymptotic range, though validation was achieved for resistance coefficient and sinkage but not for trim. Overall results prove that for medium and high Froude numbers the computational towing tank is an efficient and accurate tool to predict curves of resistance and propulsion for ship flows using a single run. The procedure is not possible or highly difficult using a physical towing tank suggesting a potential of using the computational towing tank to aid the design process. [DOI: 10.1115/1.2969649]

Keywords: computational towing tank, resistance, propulsion, ship flow

1 Introduction

Since William Froude (ca. 1850) ship design is based on towing tank tests, which have been standardized beginning in 1933 by procedures developed under the auspices of the International Towing Tank Conference (ITTC) at its tri-annual meetings, e.g., recent proceeding of the 24th ITTC (2005). The advent of computer technology and computational fluid dynamics (CFD) methods offers an alternative to the traditional build and test design approach, i.e., simulation based design (SBD). It has been conjectured that SBD will offer innovative approaches to design and out-of-the box concepts with improved performance.

CFD for ship hydrodynamics is well developed with advanced capabilities for resistance and propulsion, seakeeping, and maneuvering as evidenced by the ship hydrodynamics CFD workshops, most recently CFD Tokyo (2005), and bi-annual Office of Naval Research (ONR) Symposiums on Naval Hydrodynamics (SNH), most recently SNH 2006. One of the leading ship hydrodynamics CFD codes and of present interest is CFDSHIP-IOWA, which has been developed under ONR support at the Iowa Institute of Hydraulics Research (IIHR) over the past 20 years (most recently version 4 [1]). The capabilities of ship hydrodynamics CFD codes have largely been demonstrated mimicking typical towing tank tests using the experimental data for validation of the simulations, including both global and local flow variables (see, e.g. Ref. [2]). Once validated, CFD thus far has largely been used for design analysis, but with its current interdisciplinary capability including global optimization methods [3] and emerging multidisciplinary capability it assures in short time the reality of SBD. Recently, CFD has shown its usefulness for conceptual design for high-speed sealift concepts [4].

Herein, the concept of a computational towing tank is implemented to show that CFD and SBD have a potential to aid the design process. The idea of a numerical towing tank is not new, as the name has been used for an annual European workshop, most recently Numerical Towing Tank Symposium (NUTTS) (2006); however, herein we demonstrate different possibilities and the full potential of the concept. It will be shown that both resistance and propulsion tests can be conducted in a unique and efficient manner not possible or highly difficult using a physical towing tank whereby the resistance and propulsion curves can be predicted in single computer runs, which cover the entire Froude number (Fr) range of interest. To achieve a computational towing tank for resistance, propulsion, and other applications, absolute inertial earth-fixed coordinates are applied. Most previous CFD simulations for resistance [5], propulsion [6], seakeeping [7], steady maneuvering [8], and dynamic maneuvering [9] applied relative inertial coordinates or noninertial ship-fixed coordinates [10].

2 Computational Method

The general-purpose solver CFDSHIP-IOWA-V.4 [1] solves the unsteady Reynolds averaged Navier–Stokes (RANS) or detached eddy simulation (DES) equations in the liquid phase of a free surface flow. CFDSHIP-IOWA-V.4 is briefly summarized with focus on application of the absolute inertial earth-fixed coordinates for development and implementation of the concept of the computational towing tank.

2.1 Modeling. *Governing differential equations*. The governing differential equations (GDEs) of motion are derived and solved in absolute inertial earth-fixed coordinates (X,Y,Z) for an arbitrary moving but nondeforming control volume and solution domain, respectively. As shown in Fig. 1, the control volume is

---

Contributed by the Fluids Engineering Division of ASME for publication in the JOURNAL OF FLUIDS ENGINEERING. Manuscript received January 22, 2008; final manuscript received June 8, 2008; published online September 8, 2008. Assoc. Editor: Paul Durbin.

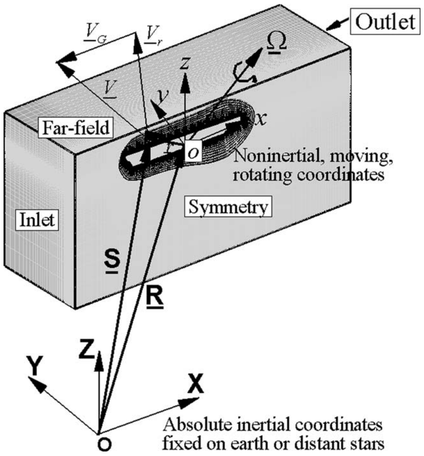

Fig. 1 Definition of absolute inertial earth-fixed coordinates (*X*, *Y*, *Z*) and noninertial ship-fixed coordinates (*x*, *y*, *z*)

for either the ship in black or background in gray. Both black and gray control volumes form the solution domain. (x,y,z) are noninertial ship-fixed coordinates whose origin o is located at the center of gravity of the ship with position vector $\underline{R}$ in (X,Y,Z). $\underline{r}$ and $\underline{S}=\underline{R}+\underline{r}$ are the instantaneous position vectors of any point in (x,y,z) and (X,Y,Z), respectively. The ship translation velocity is $\dot{\underline{R}}=\partial\underline{R}/\partial t=u_i\hat{i}_0+v_i\hat{j}_0+w_i\hat{k}_0$, where $\hat{i}_0$, $\hat{j}_0$, and $\hat{k}_0$ are the unit vectors of X, Y, and Z axes, respectively, and u_i, v_i, and w_i are the surge, sway, and heave velocities of the ship with respect to (X,Y,Z). The ship rotates with angular velocity $\underline{\Omega}=\Omega_X\hat{i}_0+\Omega_Y\hat{j}_0+\Omega_Z\hat{k}_0$ of (x,y,z) in (X,Y,Z). The velocity of the control volume is defined by

$$\underline{V}_G=\dot{\underline{R}}+\underline{\Omega}\times\underline{r} \tag{1}$$

The black control volume performs up to six degrees of freedom (6DOF) motions (surge, sway, heave, roll, pitch, and yaw). The gray control volume performs up to 3DOF (surge, sway, and yaw) motions copied from the corresponding degrees of freedom of the ship's motions. Any number of degrees of freedom can be imposed and the rest is predicted by the 6DOF solvers, which results in captive, free, or semicaptive motions.

The Reynolds transport theorem [11] for incompressible flow with an arbitrary nondeforming control volume moving at $\underline{V}_G$ (shown in Fig. 1) is applied with the velocity relative to the control volume defined by

$$\underline{V}_r=\underline{V}-\underline{V}_G \tag{2}$$

where $\underline{V}$ is the absolute velocity in (X,Y,Z). The flux term is transformed to a volume integral using the Gauss divergence theorem. Taking the limit for elemental control volume for which the integrand is independent of the volume and dividing by the volume, the differential form per unit volume is obtained. Conservation of mass gives the continuity equation for $\underline{V}_r$ as follows:

$$\nabla\cdot\underline{V}_r=0 \tag{3}$$

Substitution of Eq. (2) into Eq. (3) with $\nabla\cdot\underline{V}_G=0$ for a nondeforming control volume results in

$$\nabla\cdot\underline{V}=0 \tag{4}$$

Conservation of momentum using the divergence operator expansion and the continuity equation, and expressing the body and surface forces per unit volume give the momentum equation

$$\rho\left[\frac{\partial\underline{V}}{\partial t}+(\underline{V}-\underline{V}_G)\cdot\nabla\underline{V}\right]=-\nabla(p+\gamma Z)+\frac{1}{\mathrm{Re}}\nabla^2\underline{V} \tag{5}$$

which is nondimensionalized using a reference velocity U_0^* (generally the maximum speed of the ship), the ship length L^*, the water density ρ^*, and viscosity μ^*. When the control volume is limited to a point, the physical meaning of $\underline{V}_G$ is the local grid velocity.

Equation (5) can be transformed into the relative inertial coordinates (X',Y',Z') translating at a constant velocity $\underline{V}_C$ relative to (X,Y,Z) by replacing $\underline{V}$ with $\underline{V}_r'+\underline{V}_C$ and $\underline{V}_G$ with $\underline{V}_G'+\underline{V}_C$, where $\underline{V}_r'$ and $\underline{V}_G'$ are the fluid and control volume velocities in (X',Y',Z'), respectively. The time derivatives in the two inertial coordinates are the same. Since the gradient, divergence, and Laplacian operators in Eq. (5) are frame invariant, the governing equations in terms of $\underline{V}_r'$ in (X',Y',Z') are obtained as follows:

$$\rho\left[\frac{\partial\underline{V}_r'}{\partial t}+(\underline{V}_r'-\underline{V}_G')\cdot\nabla\underline{V}_r'\right]=-\nabla(p+\gamma Z)+\frac{1}{\mathrm{Re}}\nabla^2\underline{V}_r' \tag{6}$$

Equation (5) can also be transformed into the noninertial ship-fixed coordinates by replacing $\underline{V}$ with $\underline{V}_r+\underline{V}_G$ and $\underline{V}_G$ with $\dot{\underline{R}}+\underline{\Omega}\times\underline{r}$. For any vector, the time derivative $\partial/\partial t$ in (X,Y,Z) is related to its time derivative $\tilde{\partial}/\partial t$ in (x,y,z) by [12]

$$\frac{\partial}{\partial t}=\frac{\tilde{\partial}}{\partial t}+\underline{\Omega}\times \tag{7}$$

Again, since the gradient, divergence, and Laplacian operators in Eq. (5) are frame invariant, the governing equations in terms of $\underline{V}_r$ in (x,y,z) are obtained, which have a similar form to the Navier–Stokes equations for a fixed control volume in absolute inertial coordinates (standard NS equations hereinafter), i.e., Eq. (5) with $\underline{V}_G=0$, except with an additional body-force term [11]

$$\rho\left[\frac{\tilde{\partial}\underline{V}_r}{\partial t}+\underline{V}_r\cdot\nabla\underline{V}_r\right]=\underbrace{-\rho\underline{a}_r}_{\text{body force}}-\nabla(p+\gamma z)+\frac{1}{\mathrm{Re}}\nabla^2\underline{V}_r \tag{8}$$

$$\underline{a}_r=\ddot{\underline{R}}+2\underline{\Omega}\times\underline{V}_r+\underline{\Omega}\times(\underline{\Omega}\times\underline{r})+\dot{\underline{\Omega}}\times\underline{r} \tag{9}$$

The GDEs for continuity and momentum in (X,Y,Z) and (X',Y',Z') are transformed from the physical domain in Cartesian coordinates (X,Y,Z,t) to the computational domain in nonorthogonal curvilinear coordinates (ξ,η,ζ,τ) using the chain rule without involving grid velocity for the time derivative transformation [5]

$$\frac{1}{J}\frac{\partial}{\partial\xi^j}(b_i^jU_i)=0 \tag{10}$$

$$\frac{\partial U_i}{\partial\tau}+\frac{1}{J}b_j^k(U_j-U_{Gj})\frac{\partial U_i}{\partial\xi^k}=-\frac{1}{J}b_i^k\frac{\partial p}{\partial\xi^k}+\frac{1}{J}\frac{\partial}{\partial\xi^j}\left(\frac{b_i^jb_i^k}{J\,\mathrm{Re}_{\mathrm{eff}}}\frac{\partial U_i}{\partial\xi^k}\right)+\frac{b_j^k}{J}\frac{\partial\nu_t}{\partial\xi^k}\frac{b_i^l}{J}\frac{\partial U_j}{\partial\xi^l}+S_i \tag{11}$$

Equations (10) and (11) are identical to Warsi [13], who transformed the standard NS equations in (X,Y,Z,t) to a fixed computational domain (ξ,η,ζ,τ) with the inclusion of the grid velocity $\partial X_i/\partial\tau$ in the time derivative transformation. In the present derivation of Eqs. (5) and (6) the solution domain and control volume are coincident with each other, which conceptually better shows the relationship between the moving but nondeforming control volume and solution domain and additionally provides the continuous $\underline{V}_G/\underline{V}_G'$ form of the NS equations. Compared with Eq. (6), Eq. (5) allows nonconstant $\underline{V}_C$. When $\underline{V}_C=0$, Eq. (6) reduces to Eq. (5). Transformation of the continuous $\underline{V}_G$ form of the NS equations in (X,Y,Z) into (x,y,z) clearly shows the difference of

GDEs using the absolute inertial earth-fixed or noninertial ship-fixed coordinate systems. Compared with Eq. (8), application of Eq. (5) simplifies the specification of boundary conditions, saves computational cost by reducing the solution domain size, and can be easily applied to simulate multi-objects such as ship-ship interactions. In general, implementation of Eq. (5) to simulate captive, semicaptive, or full 6DOF ship motions is straightforward.

Turbulence and free surface modeling. The turbulent kinetic energy k is computed using a blended $k-\omega/k-\varepsilon$ model [14]. A single-phase level set method is used [1]. The location of the free surface is given by the zero level set of the level set function Φ, set to the positive distance to the free surface in water and negative in air. Since the free surface is a material surface, the equation for the level set function is

$$\frac{\partial \Phi}{\partial t} + (U_j - U_{Gj})\frac{\partial \Phi}{\partial x_j} = 0 \tag{12}$$

The jump conditions for velocity and the dimensionless piezometric pressure at the free surface are given by Eqs. (15) and (18) in Ref. [1], respectively. Transport of the level set function with Eq. (12) does not guarantee that Φ remains a distance function as the computation evolves. To resolve this difficulty, an implicit extension is performed every time Φ is transported. The first neighbors to the free surface are reinitialized geometrically. The rest of the domain is reinitialized using an implicit transport of the level set function.

Propeller model. For propelled simulations, a simplified body-force model is used to prescribe axisymmetric body force with axial and tangential components [15]. The radial distribution of forces is based on the Hough and Ordway circulation distribution, which has zero loading at the root and tip. A vertex-based search algorithm is used to determine which grid-point control volumes are within the actuator cylinder. The force and torque of each propeller are projected into the noninertial ship-fixed coordinates and used to compute an effective force and torque about the center of rotation, which is coincident to the center of gravity in this study.

Calculations and transformations of forces and moments. The dynamic pressure force $\underline{F}_{pi}$ and the hydrostatic pressure (buoyancy) force $\underline{B}_i$ in the absolute inertial earth-fixed coordinates for the ship are computed from

$$\underline{F}_{pi} = -\int_{S_w} p\, d\underline{a} \tag{13}$$

$$\underline{B}_i = \int_{S_w} \frac{Z}{\mathrm{Fr}^2} d\underline{a} \tag{14}$$

where $\underline{a}$ is the outward pointing area vector and S_w is the wetted surface area. The friction forces are computed using the velocity in the absolute inertial earth-fixed coordinates

$$\underline{F}_{fi} = \frac{1}{2\,\mathrm{Re}}\int_{S_w} (\nabla \underline{V} + \nabla \underline{V}^T) \cdot d\underline{a} \tag{15}$$

Thus the total force is

$$\underline{F}_i = \underline{F}_{fi} + \underline{F}_{pi} + \underline{B}_i \tag{16}$$

The total moments are found from integrating the elemental forces with the distance to the center of gravity $\underline{r}_{\mathrm{CG}}$ as

$$\underline{M}_i = \int_{S_w} \underline{r}_{\mathrm{CG}} \times \left\{ \left[\left(\frac{\nabla \underline{V} + \nabla \underline{V}^T}{2\,\mathrm{Re}} \right) - \left(p - \frac{Z}{\mathrm{Fr}^2} \right) \underline{I} \right] \cdot d\underline{a} \right\} \tag{17}$$

$\underline{F}_i$ and $\underline{M}_i$ are then projected into the noninertial ship-fixed coordinates (x,y,z) using

$$\underline{F}_b = \underline{J}_1(\underline{F}_i)$$

$$\underline{M}_b = \underline{J}_1(\underline{M}_i) \tag{18}$$

The matrix $\underline{J}_1$ transforms any vector in (X,Y,Z) to a vector in (x,y,z) as follows:

$$\underline{J}_1 = \begin{bmatrix} \cos\psi\cos\theta & \sin\psi\cos\theta & -\sin\theta \\ -\sin\psi\cos\phi + \sin\phi\sin\theta\cos\psi & \cos\psi\cos\phi + \sin\phi\sin\theta\sin\psi & \sin\phi\cos\theta \\ \sin\theta\sin\psi + \cos\phi\sin\theta\cos\psi & -\sin\phi\cos\psi + \cos\phi\sin\theta\sin\psi & \cos\theta\cos\phi \end{bmatrix} \tag{19}$$

where ϕ, θ, and ψ are the Euler angles for roll, pitch, and yaw, respectively. The three components of $\underline{F}_b = (\underline{F}_{bx}, \underline{F}_{by}, \underline{F}_{bz})$ are the surge, sway, and heave forces, respectively. The three components of $\underline{M}_b = (\underline{M}_{bx}, \underline{M}_{by}, \underline{M}_{bz})$ are the roll, pitch, and yaw moments, respectively.

6DOF module. The evolution of the location and the attitude of the ship are computed solving the rigid body equations in (x,y,z). The translation of the ship is described by $\underline{V}_b = (u_b, v_b, w_b)$, where u_b, v_b, and w_b are the surge, sway, and heave velocities of the ship with respect to (x,y,z). The ship rotation is described using the Euler angles $\sigma = (\phi, \theta, \psi)$, whose rates of change are computed using $\underline{\Omega}_b = (\Omega_x, \Omega_y, \Omega_z)$, where Ω_x, Ω_y, and Ω_z are the three angular velocity components with respect to (x,y,z) due to roll, pitch, and yaw, respectively.

$$\dot{\sigma} = \underline{J_2 \Omega_b} = \begin{bmatrix} 1 & \sin\phi\tan\theta & \cos\phi\tan\theta \\ 0 & \cos\phi & -\sin\phi \\ 0 & \sin\phi/\cos\theta & \cos\phi/\cos\theta \end{bmatrix} \underline{\Omega_b} \tag{20}$$

The rigid body equations are

$$m(\tilde{\partial} u_b/\partial t - v_b\Omega_z + w_b\Omega_y) = F_{bfx} + F_{bpx} + B_{bx} + W_{bx} + P_{bx} - \mathrm{SFC}_{bx} \tag{21}$$

$$m(\tilde{\partial} v_b/\partial t - w_b\Omega_x + u_b\Omega_z) = F_{bfy} + F_{bpy} + B_{by} + W_{by} + P_{by} - \mathrm{SFC}_{by} \tag{22}$$

$$m(\tilde{\partial} w_b/\partial t - u_b\Omega_y + v_b\Omega_x) = F_{bfz} + F_{bpz} + B_{bz} + W_{bz} + P_{bz} - \mathrm{SFC}_{bz} \tag{23}$$

$$I_x\tilde{\partial}\Omega_x/\partial t + (I_z - I_y)\Omega_y\Omega_z = M_{bfx} + M_{bpx} + M_{bBx} + M_{bPTx} + M_{bPQx} \tag{24}$$

$$I_y\tilde{\partial}\Omega_y/\partial t + (I_x - I_z)\Omega_x\Omega_z = M_{bfy} + M_{bpy} + M_{bBy} + M_{bPTy} + M_{bPQy} \tag{25}$$

$$I_z\tilde{\partial}\Omega_z/\partial t + (I_y - I_x)\Omega_x\Omega_y = M_{bfz} + M_{bpz} + M_{bBz} + M_{bPTz} + M_{bPQz} \tag{26}$$

where m is the mass of the ship. $\underline{B}_b=(B_{bx},B_{by},B_{bz})$, $\underline{W}_b=(W_{bx},W_{by},W_{bz})$, and $\underline{P}_b=(P_{bx},P_{by},P_{bz})$ are the buoyancy, gravity, and propeller thrust forces in (x,y,z), respectively. $\underline{\mathrm{SFC}_b}=(\mathrm{SFC}_{bx},\mathrm{SFC}_{by},\mathrm{SFC}_{bz})$ is the skin friction correction in self-propulsion simulations. The moments and motions due to SFC_b are considered by subtracting SFC_b from the propeller thrust. I_x, I_y, and I_z are the moments of inertial with respect to the principal axes of rotation, which are assumed to be coincident to the x, y, and z coordinates. $\underline{M}_{bB}=(M_{bBx},M_{bBy},M_{bBz})$, $\underline{M}_{bPT}=(M_{bPTx},M_{bPTy},M_{bPTz})$, and $\underline{M}_{bPQ}=(M_{bPQx},M_{bPQy},M_{bPQz})$ are the moments caused by the buoyancy, the propeller thrust force, and the propeller torque in (x,y,z), respectively. It is assumed that the center of rotation and the towing point coincide with the center of gravity. Thus the moments caused by the towing force and gravity are zero. Any number of degrees of freedom can be imposed and the rest is predicted, which results in captive, free, or semicaptive motions. CFDSHIP-IOWA-V.4 only solves rigid body equations for the predicted degrees of freedom using a predictor/corrector implicit approach. The prescribed motions for position, translation velocity, and Euler angles are specified as functions of time in the absolute inertial coordinates and read into CFDSHIP-IOWA-V.4 as a data file.

Integration of Eqs. (21)–(26) provides $\underline{V}_b$ and $\underline{\Omega}_b$. $\underline{V}_b$ and $\underline{\Omega}_b$ are transformed back to $\underline{V}_i=(u_i,v_i,w_i)$ and $\underline{\Omega}_i=(\Omega_X,\Omega_Y,\Omega_Z)$ in the absolute inertial earth-fixed coordinates using

$$\dot{\underline{R}} = \underline{V}_i = \underline{J}_1^{-1}(\underline{V}_b) \tag{27}$$

$$\underline{\Omega}_i = \underline{J}_1^{-1}(\underline{\Omega}_b) \tag{28}$$

New positions of the ship are obtained by integrating $\underline{V}_i$ and $\dot{\sigma}$ with respect to time. The position vectors and grid velocity are computed by

$$\underline{R} = \underline{R}_{\text{initial}} + \int_0^T \underline{V}_i dt \tag{29}$$

$$\underline{V}_G = \underbrace{\dot{\underline{R}}}_{\underline{V}_i} + \underline{\Omega} \times \underline{r} \tag{30}$$

Implementation of Eq. (30) is not straightforward. By taking advantage of the absolute inertial earth-fixed coordinates (X,Y,Z), $\underline{V}_G$ is alternatively computed by

$$\underline{V}_G = \dot{X}\hat{i}_0 + \dot{Y}\hat{j}_0 + \dot{Z}\hat{k}_0 \tag{31}$$

The time derivative is computed using Euler second-order backward differences

$$\partial\varphi/\partial\tau = 1/\Delta\tau(1.5\varphi^n - 2\varphi^{n-1} + 0.5\varphi^{n-2}) \tag{32}$$

For a ship at the hydrostatic condition, all the left-hand-side terms of Eqs. (21)–(26) and the right-hand-side terms of Eqs. (24)–(26) are zero. The right-hand-side terms of Eqs. (21)–(23) are simplified to

$$\underline{B}_b + \underline{W}_b = 0 \tag{33}$$

which provides the ship weight, and

$$M_{bBy} = 0 \tag{34}$$

is used to compute the X-location of the center of gravity.

2.2 Numerical Methods. A second-order upwind scheme is used to discretize the convective terms of the momentum equations. Viscous terms in Eq. (5) are discretized using second-order central differences. Similar numerical schemes are used to discretize the turbulence equations. The time derivatives for momentum and turbulent models are discretized using Eq. (32). The mass conservation is enforced using the pressure Poisson equation

$$\frac{\partial}{\partial\xi^j}\left(\frac{b_i^j b_i^k}{Ja_{ijk}}\frac{\partial p}{\partial\xi^k}\right) = \frac{\partial}{\partial\xi^j}\frac{b_i^j}{a_{ijk}}\left(\sum_{nb} a_{nb}U_{i,nb} - S_i\right) \tag{35}$$

2.3 Solution Strategy. The overall solution strategy using absolute inertial earth-fixed coordinates is illustrated in Fig. 2. The grids for the ship and background are read and split according to user directives for domain decomposition parallelization. Once all the variables are initialized, SUGGAR [16] is called for the first time to obtain the initial overset interpolation information. A nonlinear loop is used to converge the flow field and motions within each time step. At the beginning of each nonlinear iteration, the overset information is read from a binary file produced by SUGGAR, the grids are moved according to the motions resulting from the 6DOF predictor/corrector steps, and the transformation metrics and grid velocity are computed. Then the $k-\omega$ equations are solved implicitly followed by the level set function transport and reinitialization. With the new location of the free surface the pressure gradient is computed and the pressure-implicit split-operator (PISO) [17] method is used to enforce a divergence free velocity field where the pressure Poisson equation (Eq. (35)) is solved using the PETSc toolkit [18]. Once the velocity field is obtained, the forces and moments are weighted with coefficients provided as a preprocessing step by USURP [19] used to properly compute area and forces on overlap regions for a ship hull with appendages.

Then the residuals of the nonlinear iterations are evaluated. If the residuals of all variables drop to 10^{-3} indicating converged for that time step, the motions are predicted for the next time step using Eq. (21) in Ref. [7]. SUGGAR is called to compute the interpolation given the new location of the moving grids. If the nonlinear iteration is not converged, then the motions are corrected using Eq. (22) in Ref. [7]. SUGGAR is called, and a new nonlinear iteration starts.

A message passing interface (MPI)-based domain decomposition approach is used. Two to five nonlinear iterations are required for convergence of the flow field equations within each time step. Convergence of the pressure equation solver is reached when the residual imbalance of the Poisson equation drops six orders of magnitude. All other variables are assumed converged when the linear iteration residuals drop to 10^{-5}.

3 Implementation of Absolute Inertial Coordinates for Resistance and Propulsion

3.1 Single Fr Resistance and Propulsion. For a single Fr resistance simulation, the ship is towed at a speed based on the Fr, i.e., $u_i=V_C=\mathrm{Fr}\sqrt{gL}$. The rigid body equations (21)–(26) are simplified to

$$u_b = (w_b \sin\theta + V_C)/\cos\theta \tag{36}$$

$$v_b = 0 \tag{37}$$

$$m(\tilde{\partial}w_b/\partial t - u_b\Omega_y) = F_{bfz} + F_{bpz} + B_{bz} + W_{bz} \tag{38}$$

$$0 = M_{bfx} + M_{bpx} + M_{bBx} \tag{39}$$

$$I_y\tilde{\partial}\Omega_y/\partial t = M_{bfy} + M_{bpy} + M_{bBy} \tag{40}$$

$$0 = M_{bfz} + M_{bpz} + M_{bBz} \tag{41}$$

The position vectors and grid velocity are computed by

$$\underline{R} = \underline{R}_{\text{initial}} + V_C T\hat{i}_0 + \int_0^T w_i\hat{k}_0 dt \tag{42}$$

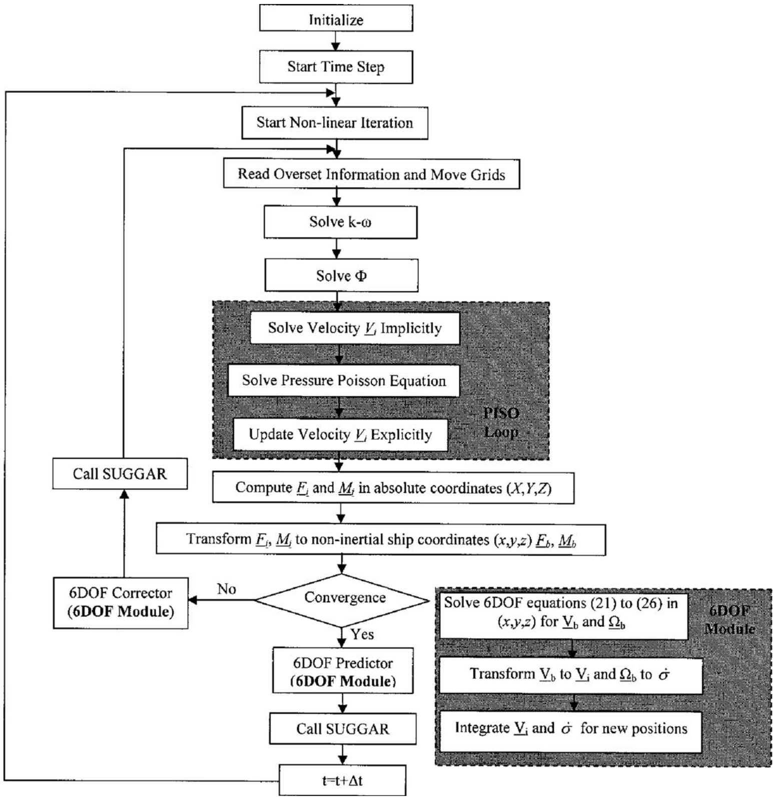

Fig. 2 Solution strategy using absolute inertial earth-fixed coordinates

$$\underline{V}_G = \dot{X}\hat{i}_0 + \dot{Z}\hat{k}_0 \tag{43}$$

The simulation converges when the resistance coefficients reach asymptotic values, after which $\tilde{\partial} w_b/\partial t = \Omega_y = 0$ results from the force and moment balances. The position vectors and grid velocities are further simplified by $w_i = \dot{Z} = 0$. The background grid is prescribed to surge at the same speed of the ship but without sinkage or trim.

The traditional way for a self-propulsion simulation is to mimic the experiment using a root finder module to determine the propeller revolution per second (RPS) [6]. However, this approach is disadvantageous from a numerical simulation point of view. First, even for a fixed RPS, the computations of the sinkage and trim are slow to converge. A root finder that can change RPS above and below the self-propelled point is needed and results in a very expensive computation; secondly and most important, this approach can only be used for a single Fr, which requires many runs if a large range of Fr is of interest, and local features on the resistance curve may be lost if points were not chosen at those specific speeds. Herein, self-propulsion simulation using the absolute inertial earth-fixed coordinates is used to mimic a real self-propelled ship. For a typical steady-state computation, the ship speed is initially set to zero. When the propeller is turned on, the ship accelerates until it reaches a constant speed when the resistance force balances the thrust force from the propeller. The RPS is specified based on the target Fr. The self-propelled Fr, resistance coefficient, sinkage, and trim are all predicted.

A. Set RPS based on the target Fr.
B. Estimate wake factor $1-wt$ from instantaneous velocity U_{ship}.
C. Compute instantaneous advance coefficient $J = U_{\text{ship}}(1-wt)/(nD_P)$.
D. Get thrust coefficient K_T and torque coefficient K_Q from J based on the open water curve.
E. Compute the weight that needs to be added for the instantaneous U_{ship}; this weight is subtracted from the thrust force. This step is necessary if model-scale simulations will be used to predict full-scale conditions or if the experimental data to be simulated followed the same procedure.
F. Since K_T and K_Q are maximum for $J=0$, the ship will accelerate.
G. Go to step B, repeat the above procedure until the final ship velocity is achieved.

The rigid body equations are simplified to

$$m(\tilde{\partial} u_b/\partial t + w_b\Omega_y) = F_{bfx} + F_{bpx} + B_{bx} + W_{bx} + P_{bx} - \text{SFC}_{bx} \tag{44}$$

$$0 = F_{bfy} + F_{bpy} + B_{by} + W_{by} + P_{by} - \text{SFC}_{by} \tag{45}$$

$$m(\tilde{\partial} w_b/\partial t - u_b\Omega_y) = F_{bfz} + F_{bpz} + B_{bz} + W_{bz} + P_{bz} - \text{SFC}_{bz} \tag{46}$$

$$0 = M_{bfx} + M_{bpx} + M_{bBx} + M_{bPTx} \tag{47}$$

$$I_y\tilde{\partial}\Omega_y/\partial t = M_{bfy} + M_{bpy} + M_{bBy} + M_{bPTy} + M_{bPQy} \tag{48}$$

$$0 = M_{bfz} + M_{bpz} + M_{bBz} + M_{bPTz} \tag{49}$$

Note that the net moments caused by the two propellers' torque along the x and z axes are zero since the propellers are symmetric about the center plane (i.e., x-z plane) with counter-rotating directions. The position vector is computed as

$$\underline{R}=\underline{R}_{\text{initial}}+\int_0^T (u_i\hat{i}_0+w_i\hat{k}_0)dt \tag{50}$$

with the grid velocity computed as in Eq. (43). The self-propulsion simulation converges when $\widetilde{\partial u_b}/\partial t=\Omega_y=w_b=\dot{Z}=0$.

The disadvantage of performing single Fr simulations is that to achieve a wide range of flow conditions will require many runs that are very time-consuming in terms of CPU and case setup.

3.2 Full-Fr Curves of Resistance and Propulsion. To increase the flexibility on diagnosing flow physics for a large range of flow conditions, this study develops a computational towing tank procedure that allows a single run for the prediction of resistance and propulsion curves using the absolute inertial earth-fixed coordinates. The basic assumption is that at every instant the flow field is in a quasi steady-state, by virtue of imposing a very small acceleration so as to cover the desired velocity range during the computation. From the mathematical point of view, this means that the time derivatives of GDEs are negligible in a time-average sense. In many situations the ship transom is wet for low speeds and there is continuous vortex shedding from the ship transom corner, which forms naturally unsteady flows.

The shedding of the vortices may induce ship motions, oscillations of forces and moments, and deformation of the free surface. An unsteady constant speed computation can capture all these phenomena. The computational towing tank, being an unsteady solution of an accelerating ship, can also capture these effects as long as the characteristic times of these phenomena are much smaller than the characteristic ship acceleration time. This condition is easy to meet for vortex shedding and the free surface fluctuations, being high-frequency phenomena, but may be difficult for ship motions that have a long period. In summary, the computational towing tank can be regarded as basically a controlled transient calculation method.

The procedure starts with an appropriate choice of a reference velocity to nondimensionalize the equations of motion. For convenience we choose to use the ship speed at the point of maximum Fr to be achieved in the computation; thus

$$\text{Fr}_{\max}=\frac{U_{\max}}{\sqrt{gL}} \tag{51}$$

and thus the instantaneous ship Fr is

$$\text{Fr}=U_{\text{ship}}/\sqrt{gL} \tag{52}$$

Then the following has been carried out.

A. Specify the ramp time T_R for either the ship speed (resistance curve) or the RPS of the propeller (powering curve) to control the acceleration of the ship. The ramp function could be a linear, quadratic, or other continuous smooth function. A linear function is used herein for the ship speed changing from 0 to 1 as follows:

$$V_C=U_{\text{ship}}=\frac{t}{T_R}=\frac{\text{Fr}}{\text{Fr}_{\max}} \tag{53}$$

and the propeller RPS as

$$\text{RPS}=\text{RPS}_{\min}+\frac{t}{T_R}(\text{RPS}_{\max}-\text{RPS}_{\min}) \tag{54}$$

B. Specify the time-step size based on T_R, acceptable error, and computational cost.

C. Perform computation (note V_C in Eq. (42) needs to be inside the integral as it is a function of time).

D. Report the resistance curve, powering curve, and ship motions during the computation.

E. Estimate the total distance traveled and the time needed. For a linear ramp function the total dimensional distance the ship travels can be computed from

$$D^*=L^*\int_0^{T_R}U_{\text{ship}}dt=L^*\int_0^{T_R}\frac{t}{T_R}dt=\frac{T_RL^*}{2} \tag{55}$$

The total dimensional time T^* required for conducting such an experiment can be estimated by

$$T^*=\frac{T_RL^*}{U^*_{\max}}=\frac{T_R}{\text{Fr}_{\max}}\sqrt{\frac{L^*}{g^*}} \tag{56}$$

F. Analyze the free surface wave elevation, ship motions, forces and moments, and other flow details at any Fr of interest.

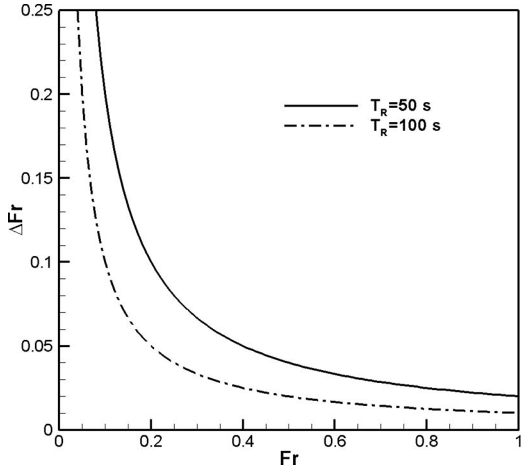

Fig. 3 **The change of Fr to cover one ship length as a function of Fr**

The optimum T_R involves a trade-off between computation speed and accuracy. The characteristic times of the main unsteady processes related to the acceleration of the ship are the time necessary to develop the boundary layer and the Kelvin wave pattern in the vicinity of the ship. Based on the authors' previous CFD simulations, these two times are in the order of the time needed to cover one ship length. So during this time we would like the change of ship speed to be small, to obtain essentially constant speed values of resistance coefficient, sinkage, and trim. If the acceleration to the full speed ($U_{\max}=1$ corresponds to $\text{Fr}_{\max}$) is linear as in Eq. (53), then to cover one ship length the ship needs to travel a time Δt obtained from

$$1=\int_{t-\Delta t/2}^{t+\Delta t/2}t/T_Rdt=\frac{t}{T_R}\Delta t \tag{57}$$

and using Eqs. (53) and (57) we obtain the change in Fr while the ship traveled one ship length

$$\Delta\text{Fr}=\frac{\text{Fr}^2_{\max}}{T_R\text{Fr}} \tag{58}$$

which shows that the change in the Fr while the ship travels one ship length is proportional to the inverse of T_R and the instantaneous Fr. Figure 3 shows ΔFr as a function of Fr for the two ramp times used in the resistance simulation. It clearly demonstrates that the single-curve procedure will not work for very low Fr ($\text{Fr}<0.1$), unless an impractically large T_R is used. This conclusion may be misleading since at low Fr the near-field wave pattern will develop faster than in one ship length. In addition, since we are slowly increasing the ship speed, the solution is only changing slightly when the ship travels one ship length, and thus the characteristic time adopted for this analysis may be too long. Figure 3 also shows that T_R has little effect for $\text{Fr}>0.4$. Further discussion on the subject is presented in the next sections.

Table 1 Simulation conditions

Geometry	Re (M)	Fr	Model	T_R (dimensionless second)		Ship length	Δt	Motions	Propeller
Athena bare hull with skeg	0–46	0–1	URANS	U_{ship}	50	25	0.01	Predicted sinkage and trim for ship grid; static background grid	No
					100	50	0.02		
Fully appended Athena	0–31.3	0–0.84	URANS	PRS	100	56	0.02	Predicted surge, sinkage and trim for ship, appendages, and wake refinement grids; predicted surge for refinement and background grids	Yes

4 Validation for High-Speed Transom Ship

Following the procedure of computational towing tank, single-run full-Fr curves for resistance and self-propulsion are performed for the Athena bare hull with a skeg (BH hereinafter) and a fully appended twin-screw Athena (AH hereinafter), respectively. As shown in Table 1 for BH, two ramp times are used to investigate the sensitivity of different ramp times on the prediction of resistance coefficients and motions, with the long ramp time twice the short one. For the long ramp, a larger time step is used to make the whole curve run at an affordable computational cost. For AH, the long ramp time is used to slowly increase the propeller RPS that will accelerate the ship for a whole range of speeds ($\text{Fr} = 0-1$). The ship lengths that the ship travels for each simulation are also summarized and compared in Table 1 discussed later.

4.1 Experimental Data and Simulation Conditions. Towing tank experiments for resistance of the high-speed transom stern ship Athena with a skeg were conducted on a 1/8.25-scale model by Jenkins [20]. Measurements of resistance, wave resistance, sinkage and trim, and wave elevation along the hull and at several stations were made for Fr ranging from 0.28 to 1.00. The same model but appended with twin rudders, stabilizers, skeg, shafts, and struts was used to measure resistance and powering characteristics [21]. Experimental data include sinkage and trim at 17 different Fr ranging from 0.336 to 0.839, open water curves for the propellers (model 4710), with the corresponding propeller RPS, thrust deduction, and wake factors. Details of the simulation conditions are summarized in Table 1.

4.2 Domain, Grid Topology, and Boundary Conditions. Figures 4 and 5 show the grid topologies for the BH and AH cases, respectively. Body-fitted "O" or "double-O" type grids are generated for the ship hull and appendages, with extensive use of overset grids. Cartesian background grids are used to better specify the boundary conditions from the ship hull and refined near the free surface to resolve the wave field. To resolve the wake, a Cartesian refinement block is included. Though shown in full domain in Fig. 5, only half domain has been computed taking advantage of the symmetry of the problem about the center plane $y=0$. Pitch and heave motions are allowed to predict the final sinkage and trim. Only the grids attached to the hull move in these two degrees of freedom, but all grids move with the surge speed of the ship, following the forward motion. The boundary conditions for all the variables are shown in Table 2.

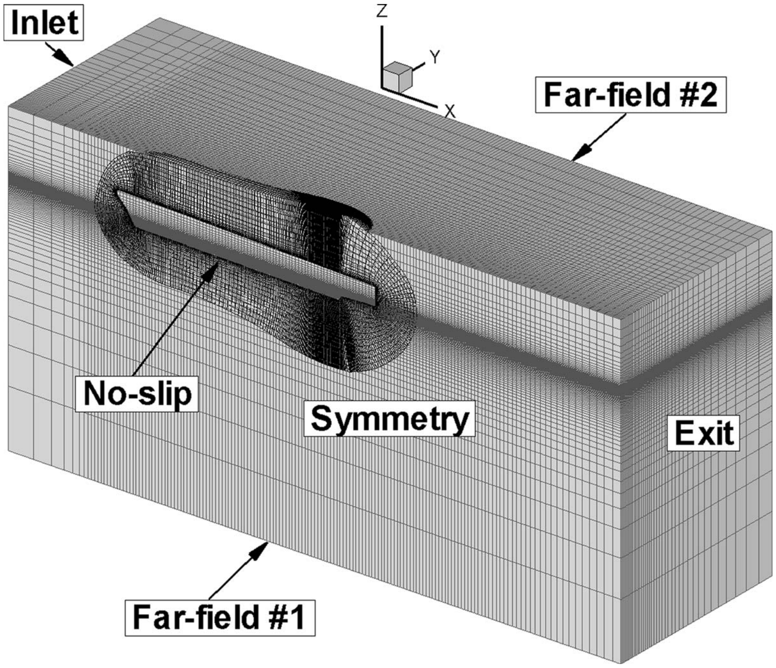

Fig. 4 Simulation domain, grids, and boundary conditions for Athena bare hull with skeg

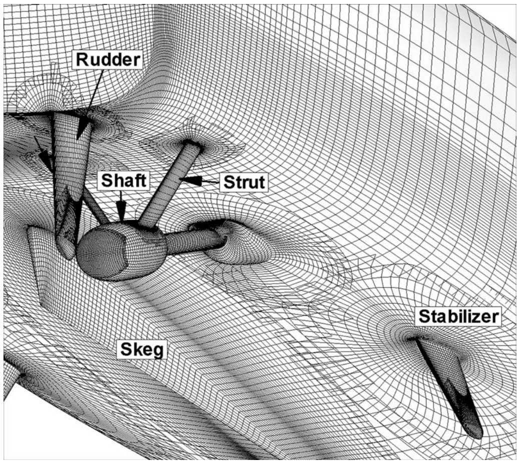

Fig. 5 Grid design for a fully appended Athena

5 Verification and Validation

A verification and validation (V & V) study is conducted for the towed BH for resistance coefficient, sinkage, and trim at Fr $=0.48$. The V & V methodology and procedures follow Stern et al. [22] with an improved correction factor formula for grid/time-step uncertainty estimates [23]. The simulation numerical uncertainty U_{SN} is composed of iterative U_I, grid U_G, and time-step U_T errors

$$U_{\mathrm{SN}}^2 = U_I^2 + U_G^2 + U_T^2 \tag{59}$$

The comparison error E is defined by the difference between the data D and simulation S values as follows:

$$E = D - S \tag{60}$$

The validation uncertainty is defined as

$$U_V = \sqrt{U_{\mathrm{SN}}^2 + U_D^2} \tag{61}$$

where U_D is the uncertainty of the experimental fluid dynamics (EFD) data. When E is within $\pm U_V$, solutions are validated at the intervals of U_V. Validation of the full-Fr curves for resistance coefficient, sinkage, and trim for BH is conducted by assuming that the same interval of U_G based on the grid study for BH at Fr$=0.48$ is valid for the whole Fr range.

Table 3 summarizes all the grids used for V & V for BH at Fr$=0.48$, with y_1^+ of the first grid point away from the wall. The primary objective of this study is full-Fr curves of resistance and propulsion. To maintain an affordable computational cost with a reasonable accuracy, grid 5 is picked for most of the results. Investigation of the issue of approaching the asymptotic range is conducted by systematically refining grid 5 to grid 1 and coarsening grid 5 to grid 7 with a grid refinement ratio $r_G = 2^{1/4}$. This allows nine sets of grids for verification including five sets with $r_G = 2^{1/4}$, three sets with $r_G = 2^{1/2}$, and one set with $r_G = 2^{3/4}$.

For AH, a total of 2.2×10^6 grid points are split into 24 blocks with an average of 90,891 grid points per processor.

5.1 Iterative and Statistical Convergence. Parametric studies on the nonlinear iterations for each time step ensure iterative convergence at each time step. The simulation is then advanced to the next time step. Results show that by increasing the nonlinear iterations from 4 to 5, the difference for the resistance coefficient $C_{TX} = C_{fX} + C_{pX}$ is less than 1%. Simulations used five nonlinear iterations. The distribution of iterative errors $0.1\% S_{\mathrm{fine}} \leq U_I \leq 0.6\% S_{\mathrm{fine}}$ for grids 1 to 7 is shown in Figs. 6(*b*) and 6(*d*) for resistance coefficients and motions of BH, respectively. U_I are of the same order of magnitude for all grids, which suggests that it is mainly determined by the iterative method applied and independent of grid resolutions. The criterion for statistical convergence of C_{TX} is that the oscillations/fluctuations of the running mean are less than 0.4% of the mean value, ensured for all cases run.

Table 2 Boundary conditions for all the variables using absolute inertial earth-fixed coordinates at a single Fr

		Φ	p	k	ω	U	V	W
Inlet	Resistance	$\Phi=-Z$	$\frac{\partial p}{\partial n}=0$	$k_{fs}=10^{-7}$	$\omega_{fs}=9$	$U=0$	$V=0$	$W=0$
	Self-propulsion	$\Phi=-Z$	$\frac{\partial p}{\partial n}=0$	$k_{fs}=10^{-7}$	$\omega_{fs}=9$	$U=0$	$V=0$	$W=0$
	Exit	$\frac{\partial \Phi}{\partial n}=0$	$\frac{\partial p}{\partial n}=0$	$\frac{\partial k}{\partial n}=0$	$\frac{\partial \omega}{\partial n}=0$	$\frac{\partial^2 U}{\partial n^2}=0$	$\frac{\partial^2 V}{\partial n^2}=0$	$\frac{\partial^2 W}{\partial n^2}=0$
	Far-field No. 1	$\frac{\partial \Phi}{\partial n}=0$	0	$\frac{\partial k}{\partial n}=0$	$\frac{\partial \omega}{\partial n}=0$	$U=0$	$V=0$	$W=0$
	Far-field No. 2	$\frac{\partial \Phi}{\partial n}=0$	$\frac{\partial p}{\partial n}=0$	$\frac{\partial k}{\partial n}=0$	$\frac{\partial \omega}{\partial n}=0$	$U=0$	$V=0$	$W=0$
	Symmetry	$\frac{\partial \Phi}{\partial n}=0$	$\frac{\partial p}{\partial n}=0$	$\frac{\partial k}{\partial n}=0$	$\frac{\partial \omega}{\partial n}=0$	$\frac{\partial U}{\partial n}=0$	$V=0$	$\frac{\partial W}{\partial n}=0$
	No slip (ship hull)	$\frac{\partial \Phi}{\partial n}=0$	Eq. (35)	$k=0$	$\omega=\frac{60}{\beta \mathrm{Re}\,\Delta y_1^2}$	$U=U_{G1}$	$V=0$	$W=0$

Table 3 Grids used for verification for Athena bare hull with skeg (Fr=0.48)

Grids	7	6	5	4	3	2	1
Ship	$111\times29\times56$ $=180{,}264$	$132\times34\times66$ $=296{,}208$	$157\times41\times79$ $=508{,}523$	$187\times49\times94$ $=861{,}332$	$222\times58\times112$ $=1{,}442{,}112$	$264\times69\times133$ $=2{,}422{,}728$	$314\times82\times158$ $=4{,}068{,}184$
Background	$111\times29\times56$ $=180{,}264$	$132\times34\times66$ $=296{,}208$	$157\times41\times79$ $=508{,}523$	$187\times49\times94$ $=861{,}322$	$222\times58\times112$ $=1{,}442{,}112$	$264\times69\times133$ $=2{,}422{,}728$	$314\times82\times158$ $=4{,}068{,}184$
Total	360,528	592,416	1,017,046	1,722,644	2,884,224	4,845,456	8,136,368
y_1^+	4.26	3.58	3.06	2.56	2.15	1.80	1.52

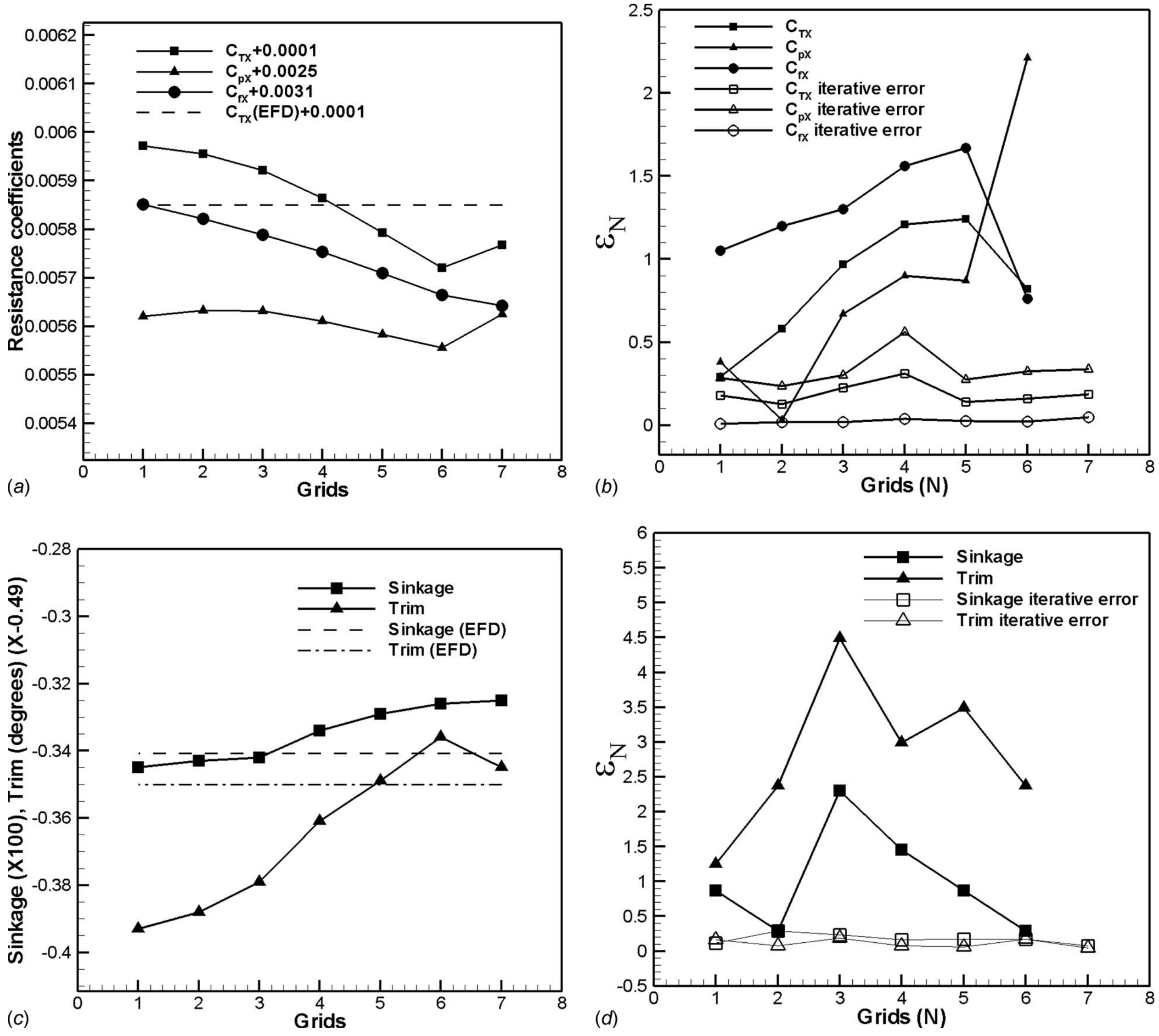

Fig. 6 Verification for resistance coefficients and motions for Athena bare hull with skeg (Fr=0.48): (*a*) resistance coefficients, (*b*) relative change $\varepsilon_N=|(S_N-S_{N+1})/S_1|\times 100$ and iterative errors for resistance coefficients, (*c*) sinkage and trim, and (*d*) relative change ε_N and iterative errors for sinkage and trim

5.2 Verification, Validation, and Discussion of Integral Variables at Fr=0.48. Tables 4 and 5 show verification and validation studies for monotonically converged solutions for C_{TX} and ship motions, respectively. R_G is defined as the ratio of solution changes for medium-fine and coarse-medium solutions, which defines the convergence conditions. C_G is the correction factor and P_G is the observed order of accuracy. $1-C_G$ indicates how far the solution is from the asymptotic range where $C_G=1$.

C_{TX} monotonically converges on grids (2,4,6), (1,3,5), (4,5,6),

Table 4 Verification and validation study for integral resistance coefficient C_{TX} of Athena bare hull with skeg (Fr=0.48). U_G is %S_1, %S_2, %S_3, or %S_4. Others are %EFD (C_{TX}=0.00575); C_{TX} is based on the static wetted area; factor of safety for GCI is 1.25.

Grids	Refinement ratio	R_G	P_G	$1-C_G$	U_G (%) Correction factor	U_G (%) GCI	E (%)	U_V (%)	U_D (%)
2, 4, 6	$\sqrt{2}$	0.63	1.32	0.42	4.90	3.34	1.83	5.21	1.5
1, 3, 5	$\sqrt{2}$	0.40	2.66	−0.51	3.59	0.72	2.10	3.96	1.5
4, 5, 6	$\sqrt[4]{2}$	0.97	0.16	0.93	125.2	52.7	0.24	125.5	1.5
3, 4, 5	$\sqrt[4]{2}$	0.80	1.27	0.41	7.23	4.98	1.23	7.47	1.5
2, 3, 4	$\sqrt[4]{2}$	0.60	2.98	−0.64	8.73	1.07	1.83	9.02	1.5
1, 2, 3	$\sqrt[4]{2}$	0.50	4.00	−1.42	1.11	0.58	2.10	1.88	1.5

Table 5 Verification and validation study for motions of Athena bare hull with skeg ($Fr = 0.48$). U_G is %S_1, %S_2, or %S_4. Others are %EFD (sinkage is −0.00341 and trim is 0.7105 deg).

Parameter	Grids	Refinement ratio	R_G	P_G	$1-C_G$	U_G (%)	E (%)	U_V (%)	U_D (%)
Sinkage	1, 3, 5	$\sqrt{2}$	0.31	3.4	−1.25	1.80	1.5	29.4	29.3
Sinkage	2, 3, 4	$\sqrt[4]{2}$	0.13	12	−15.92	1.37	0.6	29.3	29.3
Trim	1, 3, 5	$\sqrt{2}$	0.48	2.13	−0.09	4.67	13	9.66	8.1
Trim	4, 5, 6	$\sqrt[4]{2}$	0.86	0.89	0.60	42.87	3.7	45.2	8.1
Trim	2, 3, 4	$\sqrt[4]{2}$	0.53	3.69	−1.16	8.91	12	12.81	8.1
Trim	1, 2, 3	$\sqrt[4]{2}$	0.53	3.71	−1.18	4.64	13	9.65	8.1

(3,4,5), (2,3,4), and (1,2,3), oscillatorially diverges on grids (5,6,7), and monotonically diverges on grids (3,5,7) and (1,4,7). All the monotonically or oscillatorially diverged solutions involve the coarsest grid 7, which is likely due to the insufficient grid resolution. As shown in Fig. 6(*a*), C_{TX} and C_{pX} for grid 7 do not follow the trend as shown for grids 6–1. Compared to resistance coefficients, sinkage and trim are more difficult to converge in grid. Sinkage monotonically converges on grids (1,3,5) and (2,3,4) and monotonically diverges on all other grid studies. Trim monotonically converges on grids (1,3,5), (4,5,6), (2,3,4), and (1,2,3), monotonically diverges on grids (1,4,7), (3,5,7), (2,4,6), and (3,4,5), and oscillatorially diverges on grids (5,6,7).

As shown in Table 4, solutions for C_{TX} are far away from the asymptotic range as $1-C_G$ oscillates within a large range of values $-1.42 \leq 1-C_G \leq 0.93$. Grid study (3,4,5) is closest to the asymptotic range. Excluding the highest U_G on the coarse grids (4,5,6) and the lowest U_G on the finest grids (1,2,3), the average U_G is 6.11% and 2.53% for the correction factor and the grid convergence index (GCI) method, respectively. As shown in Fig. 6(*b*), when grids are refined from 5 to 1, the relative solution change between two successive grids ε_N systematically decreases for C_{TX} with 0.28% between grids 2 and 1. U_I remains almost constant with an average at 0.18%. Similar to C_{TX}, the solutions of C_{pX} are far away from the asymptotic range but with a larger oscillation of $1-C_G$ and a smaller average U_G (1.36%). Figure 6(*b*) shows that ε_N of C_{pX} oscillatorially decreases when the grid is refined with 0.4% between grids 1 and 2, which is likely due to the same order of magnitude of the iterative error U_I on grids 1 and 2, which are 0.28% and 0.25%, respectively. Compared to C_{TX} and C_{pX}, oscillations of $1-C_G$ of C_{fX} is much smaller but the average U_G (36.1%) is much larger. Figure 6(*b*) shows that ε_N of C_{fX} linearly decreases when the grid is refined from 5 to 1 with 1.05% between grids 1 and 2. Compared to C_{TX} and C_{pX}, U_I of C_{fX} is smaller with an average at 0.015%.

Table 5 shows the monotonically converged solutions for sinkage and trim. Sinkage only converges on grids (1,3,5) and (2,3,4) with a larger magnitude of $1-C_G$ for the latter but a larger U_G for the former. The average U_G of sinkage is 1.59%. As shown in Fig. 6(*d*), ε_N of sinkage shows linear increase and oscillatory decrease for grids coarser and finer than grid 3, respectively. ε_N between grids 1 and 2 is 0.85% and the average U_I is 0.15%. The oscillatory decrease of sinkage is likely due to the same order of magnitude of U_I on grid 2. Compared with sinkage, oscillation of $1-C_G$ for trim is smaller ($-1.18 \leq 1-C_G \leq 0.6$), but with larger grid uncertainties $4.64\% \leq U_G \leq 42.87\%$ with an average 15.27%. Grids (1,3,5) are closest to the asymptotic range with almost the smallest U_G. As shown in Fig. 6(*d*), ε_N of trim shows oscillatory increase and linear decrease for grids coarser and finer than grid 3, respectively. ε_N between grids 1 and 2 is 1.2% and the average U_I is 0.12%.

Validation is conducted for C_{TX} and ship motions in Tables 4 and 5, respectively. For C_{TX}, the comparison error E between the fine grid solution and the EFD data is increasing from 0.24% to 2.10% of EFD when grid is refined from 4 to 1. Except for grid 4, the average E between the fine grid solution and the EFD data is about 2% and is insensitive to the grid refinement while the average U_V is 5.5%. C_{TX} is validated ($E < U_V$) on grids (2,4,6), (1,3,5), (4,5,6), (3,4,5), and (2,3,4). (1,2,3) is not validated as the verification procedure [22] predicted unreasonable small U_G for $C_G > 1$ (shown in the table) and the improved verification procedure [23] is invalid for $C_G > 2$. Sinkage is validated on grids (1,3,5) and (2,3,4) with E and U_V at the intervals of 1.05% and 29.4%, respectively. Further grid refinement does not reduce the interval of validation since $U_{SN} \ll U_D$. Although trim has a larger U_G, E (10.43% on average) is much larger than that of sinkage and trim is only validated on grids (4,5,6) and (2,3,4) at an average interval of 29% for U_V.

5.3 Validation of Full-Fr Resistance Curve Simulations. Figure 7 shows resistance coefficient, sinkage, and trim BH predictions using the single-run approach with ramp times of 50 and 100 dimensionless seconds, and experimental data for $0 < Fr < 1$. Analysis of Eq. (58) shows that the error on the Fr evaluation is larger at lower speeds. As mentioned earlier, it is reasonable to think that since the ship is accelerated slowly, the solution at any speed starts from a solution that is very close, and thus the one ship length necessary for the boundary layer and wave field to develop evaluated using Eq. (58) may be largely overestimated. This appears to be confirmed by Fig. 7. It shows that for the acceleration ramp time of 100 dimensionless seconds the solution is close to that obtained through steady-state computations and experimental data except for $0.4 < Fr < 0.55$. Beyond $Fr = 0.55$, there is no noticeable difference of resistance coefficient between the two ramps. As shown in Fig. 7, the sinkage matches the experimental data very well for both ramps with the long ramp a little closer. For $Fr < 0.35$, the trim predicted by the long ramp agrees very well with the EFD data. For $Fr > 0.35$, all trim values are underpredicted by 10%, possibly due to the different levels of convergence compared with steady-state computations as the latter agrees well with the EFD data. Since no experimental information was available, the authors used $Z_{CG} = 0.00664$ for the center of gravity, which is chosen by testing a range of Z_{CG} values for $Fr = 0.48$ and comparing resistance coefficient, sinkage, and trim with experimental data. Y_{CG} equals to zero as the geometry is symmetric with respect to the center plane $y = 0$. $X_{CG} = 0.5688$ is calculated based on the balance of pitching moment for static conditions. Two steady-state cases for BH at $Fr = 0.48$ and $Fr = 0.8$ are computed by towing the ship at a constant speed and predicting resistance coefficient, sinkage, and trim. In addition, six steady-state solutions are available in literature [24] computed fixing sinkage and trim to experimental values. Predictions of these CFD computations agree very well with the EFD data.

Distributions of the comparison errors and validation uncertainties ($E, \pm U_V$) versus Fr are shown in Fig. 8 for C_{TX}, sinkage, and trim for the two different T_R. The average comparison errors $|\overline{E}|$, average validation uncertainties $\overline{U_V}, U_D$ [20], U_{SN}, and U_{SN}/U_D are presented in Table 6. U_G of grids (3,4,5) and (1,3,5) are selected for resistance coefficient and motions, respectively. With

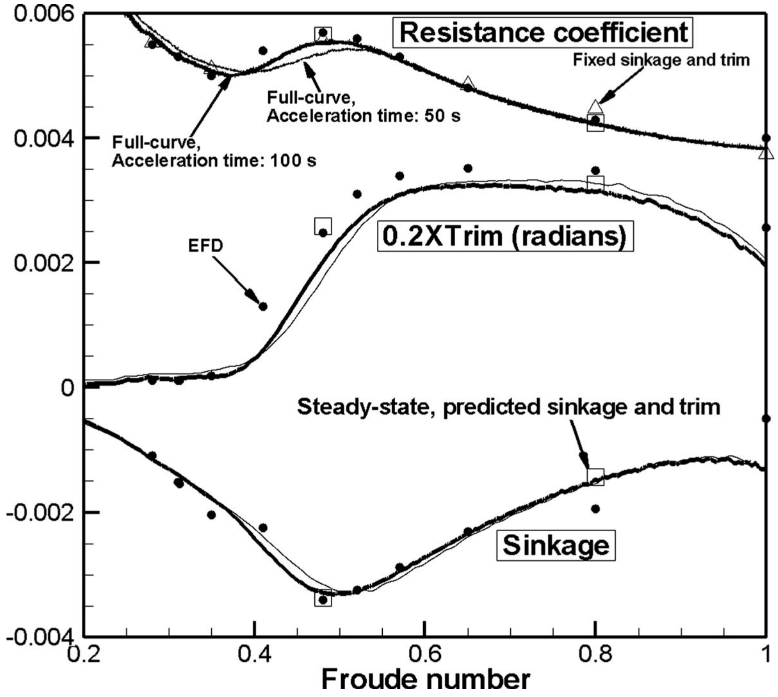

Fig. 7 Resistance coefficient, sinkage, and trim for a slow acceleration of Athena bare hull with skeg (grid 5). Solid circles: experimental data; open triangles: resistance coefficient predictions for fixed experimental sinkage and trim [24]; open squares: steady-state computation of resistance coefficient, sinkage, and trim; lines: predictions.

the increase of Fr, the resistance coefficient E shifts from −5% to +5% and remains small for $\mathrm{Fr} > 0.6$. The sinkage E shows oscillations around zero with the maximum at $\mathrm{Fr} = 1$. The smallest E for trim is for $\mathrm{Fr} < 0.4$. It reaches the maximum 20% at $\mathrm{Fr} = 0.4$ followed by a decrease for $0.41 < \mathrm{Fr} < 0.65$ and a gradual increase for $\mathrm{Fr} > 0.65$. Compared to the short ramp time, the long ramp time helps reduce $|\bar{E}|$ by 34.4%, 4.9%, and 8.6% for resistance coefficient, sinkage, and trim, respectively. For both ramp times, resistance coefficient and sinkage are validated for the whole Fr range at $\overline{U_V}$ 8.5% and 34.3% of the EFD data, respectively. Trim is only validated for $\mathrm{Fr} < 0.4$ at $\overline{U_V}$ of 7.0%. U_{SN}/U_D are 5.6, 0.026, and 0.54 for resistance coefficient, sinkage, and trim, respectively.

For the long ramp time at $\mathrm{Fr} = 0.48$, $|E|$ and U_V for C_{TX} are 2.9% and 7.5%, respectively, compared with the smaller average $|E|$ (2%) and U_V (5.5%) for a single Fr V & V. $|E|$ and U_V for sinkage are 4% and 34.3%, respectively, compared with the smaller average $|E|$ (1.05%) and U_V (29.4%) for a single Fr V & V. $|E|$ and U_V for trim are 13.7% and 7.0%, respectively, compared to a smaller average $|E|$ (10.43%) and a much larger U_V (29%) for a single Fr V & V. E and U_V for C_{TX} are computed based on the EFD data. However, to avoid misleading values for E and U_V due to very small magnitudes for high Fr sinkage and low Fr trim, all percentages of the sinkage and trim for the full-Fr curve are computed based on their dynamic range, of which U_D for sinkage is large due to the small dynamic range.

Using Eq. (55), the total distance the ship travels are 25 and 50 ship lengths for the ramp times of 50 and 100 dimensionless seconds, respectively. The length of the model Athena R/V is $L = 5.69$ m. To run 25 and 50 ship lengths in experiments will require 142.25 m and 284.5 m, respectively. Using Eq. (56) and noting $\mathrm{Fr}_{\max} = 1.0$ for BH, the total time required for conducting such an experiment are 38.1 s and 76.2 s for the CFD ramp times of 50 and 100 dimensionless seconds, respectively. In addition, a variably controlled speed would be necessary for the carriage, which may be cumbersome.

A typical single Fr number run takes 51 wallclock hours on an IBM P4 using 24 processors. If simulations are conducted at all the Fr where EFD data are available for BH, the time saved using a single run is 68.6%.

Figure 9 shows the free surface wave field predicted at $\mathrm{Fr} = 0.43$ using a ramp time of 100 dimensionless seconds. Compared with the unsteady RANS computation for Athena bare hull at $\mathrm{Fr} = 0.43$ [25], the overall flow pattern is similar except for the breaking bow wave, due to the insufficient discretization on the coarse grid applied.

5.4 Validation of Full-Fr Propulsion Curve Simulation. Figure 10 shows the whole powering curve for the AH using a ramp time of 100 dimensionless seconds. The independent variable is the propeller RPS, which is slowly increased as a function of time (Eq. (54)). All the dependent variables, including the resistance coefficient, Fr, and sinkage and trim are predicted. It is observed that overall both the computational towing tank approach and the steady-state computations agree well with the EFD data. Predicted Fr are 2.6% lower than the EFD data, which may be caused by the simplified body-force propeller model applied and the uncertainties of the EFD data. The predicted ship sinkage and trim agree well with EFD for a low-speed range ($\mathrm{Fr} < 0.45$) but are overpredicted for $0.45 < \mathrm{Fr} < 0.83$, the magnitude of the overprediction increasing with increasing Fr. This is likely due to the complexity of the wave splashing and breaking, bubble entrainment, and free surface turbulence for high-speed ship flows, which are not modeled herein. Predicted resistance coefficient agrees very well with EFD, except for $\mathrm{RPS} < 13.6$ ($\mathrm{Fr} < 0.37$), where the difference between CFD and EFD is up to 13%. The nondimensional propeller thrust force is higher than the resistance coefficient within this range, which suggests that the very slow ship speed at the beginning of the whole powering curve simulation does not provide sufficient time for the wave pattern and boundary layer to be fully developed.

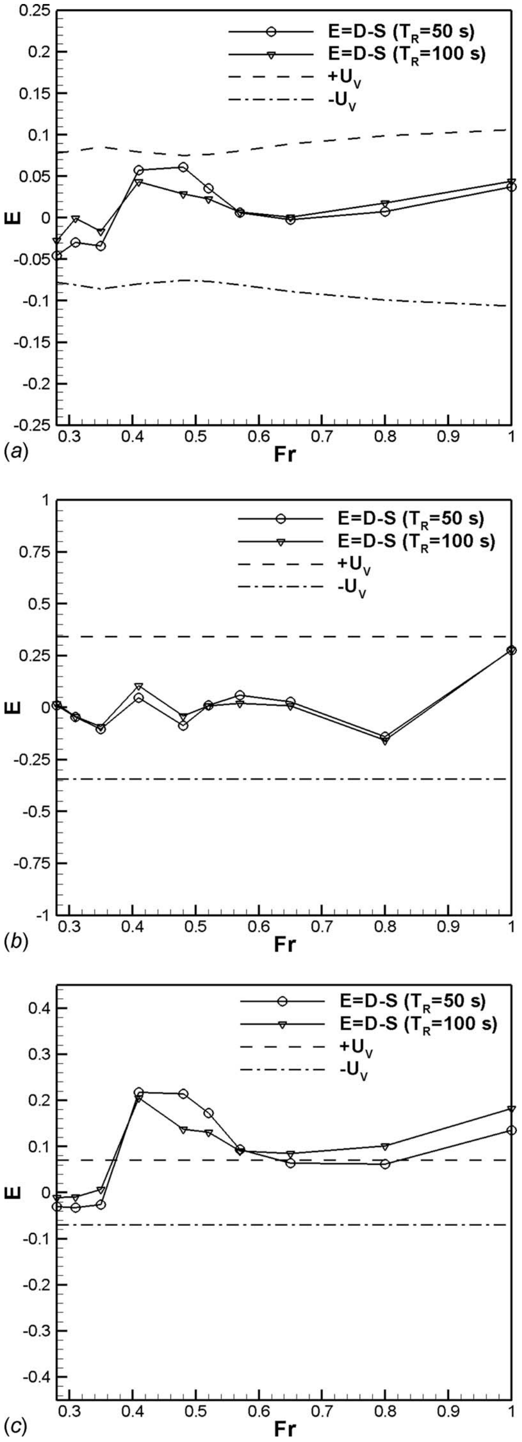

Fig. 8 Validation of Athena bare hull with skeg: (*a*) resistance coefficient, (*b*) sinkage, and (*c*) trim

Three steady-state points were simulated for Fr=0.432, 0.575, and 0.839 and compared with the EFD data (Table 7). The thrust, torque, and advance coefficients of the propeller are computed based on the target Fr. When the resistance force balances the total thrust force from the propeller minus the skin friction correction, the acceleration of the ship equals zero and the ship speed becomes a constant. This self-propelled speed (thus Fr) and the predicted sinkage and trim were then compared with the target values (EFD data). The predictions of the self-propelled Fr are within 2.1% of the EFD values. Sinkage and trim differences are less than 11% for all Fr, with the exception of the very low sinkage observed at the highest Fr, for which the relative error is misleading since the absolute value is properly predicted by CFD.

Table 6 Summary of validation of full-Fr resistance curve simulations. %EFD for C_{TX} and %EFD dynamic range for sinkage and trim.

Parameters		$\lvert\bar{E}\rvert$ (%)	$\overline{U_V}$ (%)	U_D (%)	U_{SN} (%)	U_{SN}/U_D
T_R=50 s	C_{TX}	3.2	8.5	1.5	8.4	5.6
	Sinkage	8.1	34.3	34.3	0.9	0.026
	Trim	10.5	7.0	5.9	3.2	0.54
T_R=100 s	C_{TX}	2.1	8.5	1.5	8.4	5.6
	Sinkage	7.7	34.3	34.3	0.9	0.026
	Trim	9.6	7.0	5.9	3.2	0.54

6 Conclusions and Future Work

The implementation of absolute inertial earth-fixed coordinates (X, Y, Z, t) in the RANS/DES solver CFDSHIP-IOWA allows devel-

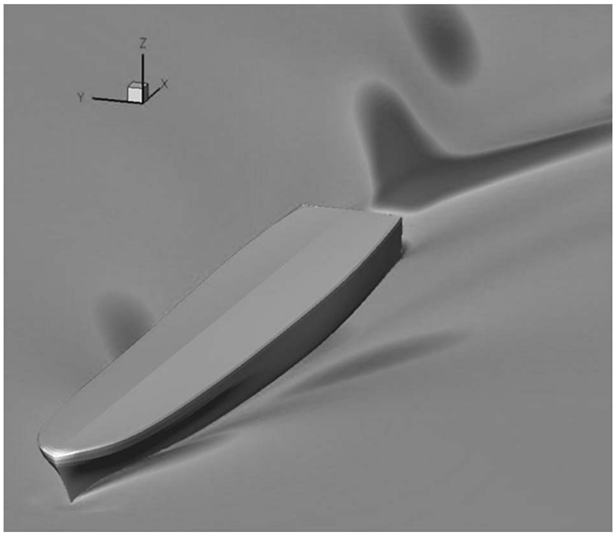

Fig. 9 Free surface wave fields for Athena bare hull with skeg at Fr=0.43

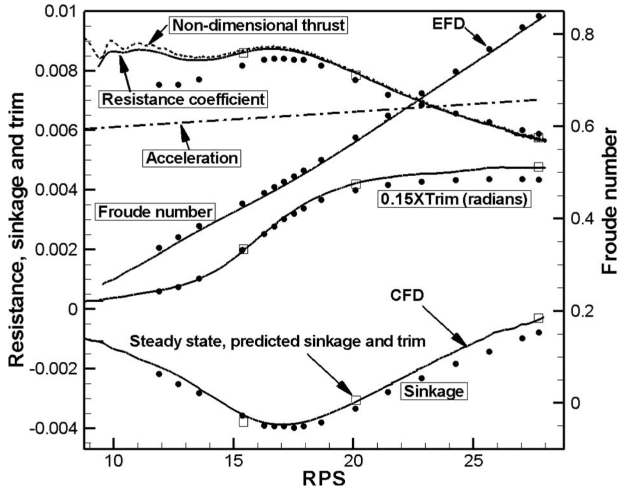

Fig. 10 Whole powering curve for a slow acceleration of a fully appended Athena as a function of RPS. Solid circles: experimental data; open squares: steady-state computation of resistance coefficient, sinkage, and trim; lines: predicted quantities.

Table 7 Steady-state computations for the self-propelled fully appended Athena. %EFD for Fr and %EFD dynamic range for sinkage and trim.

	Fr	Sinkage	Trim (deg)
EFD	0.432	−0.0036	0.73
CFD	0.423	−0.0038	0.74
$\lvert E \rvert$	2.1%	6.2%	0.7%
EFD	0.575	−0.00335	1.46
CFD	0.567	−0.00305	1.54
$\lvert E \rvert$	1.4%	9.4%	5.6%
EFD	0.839	-8.0×10^{-4}	1.60
CFD	0.830	-3.0×10^{-4}	1.75
$\lvert E \rvert$	1.1%	15.6%	10.5%

opment of the computational towing tank procedures to calculate the full Froude number curves for resistance and propulsion for Athena R/V Model 5365 with a skeg and fully appended, respectively. Compared to the relative inertial and noninertial ship coordinates, application of GDEs in (X,Y,Z,t) simplifies the specification of boundary conditions, saves computational cost by reducing the solution domain size, and can be easily applied to simulate multi-objects such as ship-ship interactions. In general, implementation of the absolute inertial earth-fixed coordinates to simulate captive, semicaptive, or full 6DOF ship motions is straightforward.

A verification study is conducted for seven systematically refined grids ranging from 360,528 to 8.1×10^6 grid points, which allows nine sets of grid studies with three different refinement ratios. C_{TX} monotonically converges for six sets of grids except those with the coarsest grid 7 involved whereas motions are more difficult to converge. $1-C_G$ shows a large range of oscillations indicating that the solutions are far from the asymptotic range. The average grid uncertainties U_G are 6.11%, 1.59%, and 15.27% for C_{TX}, sinkage, and trim, respectively. The relative solution changes ε_N between the two finest grids are 0.28%, 0.85%, and 1.2% for C_{TX}, sinkage, and trim, respectively. The average iterative errors U_I are 0.18%, 0.15%, and 0.12% for C_{TX}, sinkage, and trim, respectively, which indicates that separating U_I and U_G for fine grids is problematic. Implementation of more accurate and efficient iterative methods to speed up the convergence (e.g., multigrid) will be necessary.

Sensitivity study of the ramp time conducted for a full-Fr resistance curve shows that C_{TX} and ship motions predicted using the long ramp time are closer to the EFD data than the short one. This is consistent with the validation of the full-Fr resistance curve, which shows that the long ramp time reduces the average comparison errors $|E|$ by 34.4%, 4.9%, and 8.6% for C_{TX}, sinkage, and trim, respectively, compared to the use of the short ramp time. For both ramp times, validation is achieved at intervals of validation (U_V) 8.5% and 34.3% for C_{TX} and sinkage, respectively, but not achieved for trim except for $\mathrm{Fr} < 0.4$ at U_V of 7.0%.

The overall intervals of $|E|$ for resistance coefficient, sinkage, and trim are consistent with previous studies [4,7,26]. For C_{TX}, overall results of the 2005 and 2000 workshop results indicate that the interval of $|E|$ is 4% [26]. Other typical values for $|E|$ is 8% for High Speed Sealift (HSSL)-Delft [4] and 4.3% for 5512 [7]. For sinkage, $|E|$ is 23% for HSSL-Delft and 7.4% for 5512. For trim, $|E|$ is 17% for HSSL-Delft and 10.4% for 5512. U_{SN} for C_{TX} is at the same interval as other studies while U_{SN} for ship motions are rarely evaluated by previous studies.

Overall results prove that for medium and high Froude numbers the computational towing tank is an efficient and accurate tool to predict curves of resistance and propulsion for ship flows using a single run, including time savings on case setup and CPU hours compared to multiple runs and accuracy and flexibility on diagnosing flow physics. The procedure is not possible or highly difficult using a physical towing tank suggesting a potential of using the computational towing tank to aid the design process. However, a full curve simulation for low Fr can be very expensive in terms of computational time due to the long ramp time needed to accelerate the ship and resolve the unsteadiness of the flow.

Future work is to investigate the effects of different ramp time functions and initial conditions and improve the propeller model using a more complex propeller model (for instance, the Yamazaki model [27]) that accounts for the interaction between ship hull and propeller.

Acknowledgment

The Office of Naval Research under Grant Nos. N00014-01-1-0073 and N00014-06-1-0420, administered by Dr. Patrick Purtell, sponsored this research. We would like to thank Professor Yasuyuki Toda from Osaka University for his input and help in setting up the self-propulsion simulation.

References

[1] Carrica, P. M., Wilson, R. V., and Stern, F., 2007, "An Unsteady Single-phase Level Set Method for Viscous Free Surface Flows," Int. J. Numer. Methods Fluids, **53**(2), pp. 229–256.

[2] Longo, J., Shao, J., Irvine, M., and Stern, F., 2007, "Phase-Averaged PIV for the Nominal Wake of a Surface Ship in Regular Head Waves," ASME J. Fluids Eng., **129**(5), pp. 524–540.

[3] Campana, E. F., Peri, D., Tahara, Y., and Stern, F., 2006, "Shape Optimization in Ship Hydrodynamics Using Computational Fluid Dynamics," Comput. Methods Appl. Mech. Eng., **196**(1–3), pp. 634–651.

[4] Stern, F., Carrica, P. M., Kandasamy, M., Gorski, J., O'Dea, J., Hughes, M., Miller, R., Hendrix, D., Kring, D., Milewski, W., Hoffman, R., and Gary, C., 2006, "Computational Hydrodynamic Tools for High-Speed Cargo Transports," Soc. Nav. Archit. Mar. Eng., Trans., **114**, pp. 55–81.

[5] Carrica, P. M., Wilson, R. V., and Stern, F., 2006, "Unsteady RANS Simulations of the Ship Forward Speed Diffraction Problem," Comput. Fluids, **35**(6), pp. 545–570.

[6] Tahara, Y., Wilson, R. V., Carrica, P. M., and Stern, F., 2006, "RANS Simulation of a Container Ship Using a Single-Phase Level-Set Method With Overset Grids and the Prognosis for Extension to a Self-Propulsion Simulator," J. Mar. Sci. Technol., **11**, pp. 209–228.

[7] Carrica, P. M., Wilson, R. V., Noack, R. W., and Stern, F., 2007, "Ship Motions Using Single-Phase Level Set With Dynamic Overset Grids," Comput. Fluids, **36**(9), pp. 1415–1433.

[8] Simonsen, C. D., and Stern, F., 2005, "Flow Pattern Around an Appended Tanker Hull Form in Simple Maneuvering Conditions," Comput. Fluids, **34**, pp. 169–198.

[9] Broglia, R., Muscari, R., and Mascio, A. D., 2006, "Numerical Analysis of Blockage Effects in PMM Tests," *the 26th Symposium on Naval Hydrodynamics*, Rome, Italy, Sept. 17–22, pp. 17–30.

[10] Yamasaki, J., Miyata, H., and Kanai, A., 2005, "Finite-Difference Simulation of Green Water Impact on Fixed and Moving Bodies," J. Mar. Sci. Technol., **10**, pp. 1–10.

[11] White, F., 2008, *Fluid Mechanics*, 6th ed., McGraw-Hill, New York.

[12] Greenwood, D. T., 1988, *Principles of Dynamics*, 2nd ed., Prentice-Hall, Englewood Cliffs, NJ.

[13] Warsi, Z. U. A., 2005, *Fluid Dynamics, Theoretical and Computational Approaches*, 3rd ed., Taylor & Francis, London.

[14] Menter, F. R., 1994, "Two Equation Eddy Viscosity Turbulence Models for Engineering Applications," AIAA J., **32**(8), pp. 1598–1605.

[15] Stern, F., Kim, H. T., Patel, V. C., and Chen, H. C., 1998, "A Viscous-Flow Approach to the Computation of Propeller-Hull Interaction," J. Ship Res., **32**(4), pp. 246–262.

[16] Noack, R., 2005, "SUGGAR: A General Capability for Moving Body Overset Grid Assembly," AIAA Paper No. 2005-5117.

[17] Issa, R. I., 1985, "Solution of the Implicit Discretised Fluid Flow Equations by Operator Splitting," J. Comput. Phys., **62**, pp. 40–65.

[18] Balay, S., Buschelman, K., Gropp, W., Kaushik, D., Knepley, M., Curfman, L., Smith, B., and Zhang, H., 2002, PETSc User Manual, ANL-95/11-Revision 2.1.5, Argonne National Laboratory, Argonne, IL.

[19] Boger, D. A., and Dreyer, J. J., 2006, "Prediction of Hydrodynamic Forces and Moments for Underwater Vehicles Using Overset Grids," AIAA Paper No. 2006-1148.

[20] Jenkins, D., 1984, "Resistance Characteristics of the High Speed Transom Stern Ship R/V Athena in the Bare Hull Condition Represented by DTNSRDC Model 5365," David W. Taylor Naval Ship Research and Development Center, Report No. DTNSRDC-84/024.

[21] Crook, L. B., 1981, "Powering Predictions for the R/V Athena (PG 94) Represented by Model 4950-1 With Design Propellers 4710 and 4711," David W. Taylor Naval Ship Research and Development Center, Report No. DTNSRDC/SPD-0833-05.

[22] Stern, F., Wilson, R., and Shao, J., 2006, "Quantitative Approach to V&V of CFD Simulations and Certification of CFD Codes," Int. J. Numer. Methods

Fluids, **50**, pp. 1335–1355.
[23] Xing, T., and Stern, F., 2008, “Improvement of the Correction Factor Verification Method for Industrial Applications,” ASME J. Fluids Eng., in preparation.
[24] Miller, R., Gorski, J., Xing, T., Carrica, P., and Stern, F., 2006, “Resistance Predictions of High Speed Mono and Multi-Hull Ships With and Without Water Jet Propulsors Using URANS,” *Proceedings of the 26th Symposium on Naval Hydrodynamics*, Rome, Italy, Sept. 17–22.
[25] Wilson, R. V., Carrica, P. M., and Stern, F., 2006, “URANS Simulations for a High-Speed Transom Stern Ship With Breaking Waves,” Int. J. Comput. Fluid Dyn., **20**(2), pp. 105–125.
[26] Stern, F., 2007, “Quantitative V&V of CFD Solutions and Certification of CFD Codes,” *Symposium on Computational Uncertainty (Incertitude de Calcul)*, NATO AVT-147, Athens, Greece, Dec. 3–7.
[27] Yamazaki, R., 1968, “On the Propulsion Theory of Ships on Still Water Introduction,” Mem. Fac. Eng., Kyushu Univ., **27**(4), pp. 187–220.

Numerical Analysis on the Start-Up Flow Past a Resonant Cavity

Antonio Filippone
School of Mechanical, Aerospace and Civil Engineering,
The University of Manchester,
Manchester M60 1QD, UK

This paper presents the results of a computational analysis on a three-dimensional unsteady flow inside a resonant cavity. The cavity was fully immersed in a channel flow, had a squared cross section, and a spanwise aspect ratio equal to 3. It was partly closed to the inflow by slits upstream and downstream. The lid was 1/4 of the cavity length. The Reynolds number was Re = 8000 based on the freestream velocity. The numerical simulations were carried out for flow times up to 380 units. Results are presented for a symmetric cavity with respect to the normal to the freestream. The analysis shows complex three-dimensional vortex structures, with Taylor–Görtler-type vortices, filament vortices, and other secondary vortices, some having a relatively short life-span. It is shown that the flow is substantially symmetric, with small spanwise instabilities. It is further shown that there is an asymptotic tendency to an unsteady flow with large wavelengths. A primary vortex establishes at the center of the cavity. Most vortex regions disappear and that they depend on the type of geometry and the state of the boundary layer at the inlet. [DOI: 10.1115/1.2969271]

1 Introduction

The present study deals with the flow entrained by an external channel on a cavity. An impulsive flow at a laminar Reynolds number is considered. The cavity is immersed in a channel and partly occluded by slits, necks, and other means that can be placed upstream, downstream, or at both locations. The arrangement discussed is sometimes called *resonant cavity*.

Fluid is set in motion by the shear layer at the lid, as indicated in the sketch of Fig. 1. The incoming boundary layer creates shear forces large enough to create vertical currents in the downstream edge, and thence a global circulation, vortices of various nature and time-span, and a mixing of fluid in most areas. The state of the boundary layer at the lid is extremely important. An unstable (perhaps already separated) boundary layer is a source of unstable forcing at the lid.

The aims of the present study were threefold: (1) to investigate the start-up of the flow, the mechanism of flow entrainment, and the mass flow exchange between the cavity and the channel; (2) to investigate the dynamic behavior of the vortex structures and (3) to investigate the long term flow behavior of the cavity flow.

Flow trapped in resonant cavities is of importance in all problems dealing with the mixing of fluids, the diffusion of pollutants, and the spreading of fires. Other applications include indoor ventilation, panel joints in aerospace and automotive engineering, open bays and gaps of various nature that create drag and forced vibrations. The relative width of the lid h/L in some cases can be as low as $1/10$ (L is the length of the cavity). As the relative lid size decreases, the flow entrainment also decreases, and the characteristic times become quite large. Changes in the aspect-ratio of the cavity lead to substantial changes in the flow characteristics.

A number of basic three-dimensional (3D) features of classical cavity flows are known to exist, as proved by Rhee et al. [1] and Migeon [2]. These are corner vortices, spanwise currents, and counter-rotating Taylor–Görtler-like (TGL) vortices. Corner vortices may be thought of as extensions of the secondary vortices in the lower corners of the ideal two-dimensional cavity. They were first shown by Moffatt [3]. In particular, it was proved analytically that an infinite series of diminishing counter-rotating vortices would appear in a corner flow. Koseff and Street [4,5] contended that the corner vortices were extensions of those secondary vortices because a vortex cannot simply end at a surface. The corner vortices are generated by the interaction of the primary vortex and the end-wall condition [6].

The fluid in a cavity flow is not confined to one spanwise plane, but currents of fluid exist that transfer fluid from the end-walls to the center, and back again. The end-walls are known to be responsible for this particular flow feature, as proved by experimental studies (Koseff and Street [5]), involving cavities of different spanwise aspect ratios. According to Bernoulli's principle, a velocity gradient will also generate a pressure gradient, so the pressure at the cavity's end-walls becomes slightly higher than at its center. The result of this is that the fluid in the primary vortex core tends to spiral toward the cavity center, following the pressure gradient. To satisfy the law of conservation of mass, however, there must be an equal amount of fluid flowing back to the end-walls, and this occurs inside the secondary vortices.

Because both end-walls cause this effect, the spanwise flow pattern inside a driven cavity is symmetrical, with the inward-moving flow in the primary vortex traveling toward the center from both end-walls. These two flows collide in the middle of the cavity, and this is the reason why the primary vortex strength in the cavity's center is diminished. It is therefore possible to trace the spanwise recirculation within cavity flow: Fluid is transported to the cavity's center in the core of the primary vortex, and at the center-plane it is transferred to the secondary vortices. They transport it back toward the end-walls, where the corner vortices transfer it back to the primary vortex.

TGL vortices have been noted in almost all experimental studies of cavity flows, and they are still a subject of interest. They consist of small pairs of counter-rotating vortices that exist along the boundary of the primary vortex, aligned with the direction of fluid motion. They exist because fluid flowing over a concave boundary tends to become destabilized because of centrifugal forces acting on it. This instability leads to the formation of TGL vortices. Conversely, fluid flowing over a convex boundary tends to be more stable than "flat" flow, for a given Reynolds number [7]. In the case of cavity flow, the concave boundary that leads to TGL vortex formation is the boundary of the primary vortex, al-

---

Contributed by the Fluids Engineering Division of ASME for publication in the JOURNAL OF FLUIDS ENGINEERING. Manuscript received January 24, 2007; final manuscript received June 3, 2008; published online August 26, 2008. Assoc. Editor: Ye Zhou.

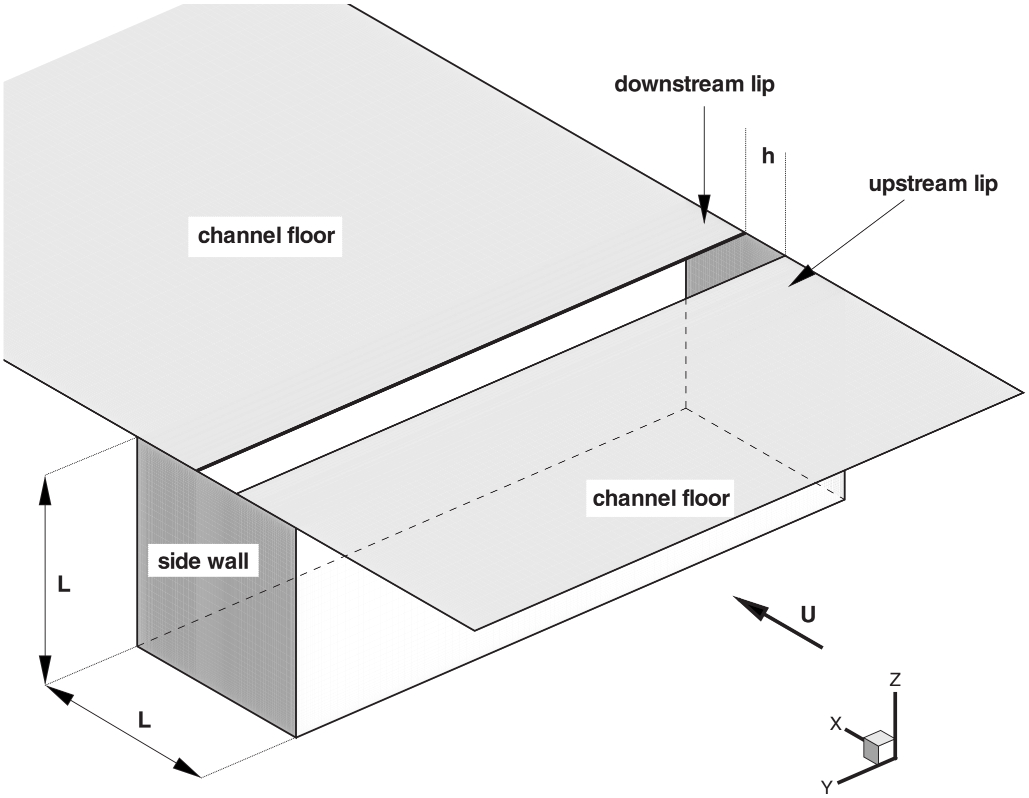

Fig. 1 Three-dimensional view of the cavity (computational model)

though this has been a cause of debate in the past. Initially, the separation of the primary vortex's boundary from the cavity walls at the corners, to go around the secondary vortices, was thought to be the generation trigger [4]. However, more recent studies seem to indicate that it is merely the concavity alone that causes TGL vortex formation and that a separation point is not required, as reported in Ref. [2].

There are four stages to TGL vortex formation [2], and they progress with the increasing Reynolds number. To begin with, an oscillatory undulation forms in the boundary between the primary vortex and one of the secondary vortices; this is followed by a converged-streamline structure forming, which in turn begins to oscillate. Finally, this develops into the counter-rotating motion characteristic of TGL vortices. Disagreement exists as to whether they are generated at the corner vortices or in the center of the cavity. Some studies such as that of Freitas [6] seem to implicate the rotational action of the corner vortices. However, other researchers such as Chiang and Sheu [8] point to the undulations in the primary vortex's boundary, being spawned from the cavity's center. This study also found that TGL vortices are known to burst from regions of local maximum kinetic energy formed by the interaction of the vortex and secondary vortices.

A large number of scientific and technical publications address cavity problems, some of which are of marginal relevance to the present study. From the numerical point of view, we mention the work of Drikakis et al. [9] on multigrid convergence, Gilmanov and Sotiropoulos [10] for the simulation of bodies immmersed in cavities, and Peng et al. [11] with the Boltzmann lattice method. We limit the following discussion to results that are of relevance to the present investigations. A suitable review on the subject is the one of Shankar and Deshpande [12]. Guermond et al. [13] investigated start-up flows in the lid-driven cavity and correlated simulation and experimental data at Re=1000. Their detailed study pointed at the importance of the boundary conditions, and concluded that correlation between data is difficult over long flow times when the two sets of data tend to diverge. Prasad and Koseff [14] investigated the effect of the cavity's spanwise aspect-ratio and the Reynolds number on the development of the TGL vortices for a lid-driven cavity flow and concluded that both parameters affect the flow development and instability. In fact, a low aspect-ratio confines the flow between two end-walls and tends to reduce the velocity fluctuations, which are ultimately due to residual TGL vortices.

2 Computational Flow Model

The computational model consisted of a finite-volume Navier–Stokes solver and a multiblock mesh. The solver is written in general curvilinear coordinates and is well documented in other publications, for example Refs. [15–17]. The code uses simple variables (u, v, w, and p) in a collocated storage arrangement. Rhie [18] interpolation is used to avoid odd/even pressure decoupling. The convective terms are discretized using a second-order total variation diminishing (TVD) upwind scheme, implemented using a deferred correction approach. Central differences are used for the viscous terms, where only the normal terms are treated fully implicit, while the terms from nonorthogonality and the variable viscosity terms are treated explicitly.

For incompressible flow, no equation of state exists for the pressure. The necessary pressure and velocity coupling is obtained through the SIMPLE algorithm of Patankar and Spalding [19]. This method is based on deriving an equation for the pressure or pressure correction by combining the continuity equation with the momentum equations.

The equations are solved iteratively. First, the momentum equations are used as a predictor step to advance the solution in time. At this point in the computation the resulting flow field will not fulfill the continuity equation. The rewritten continuity equation (the so called pressure correction equation) is used as a corrector, making the predicted flow field satisfy the continuity constraint.

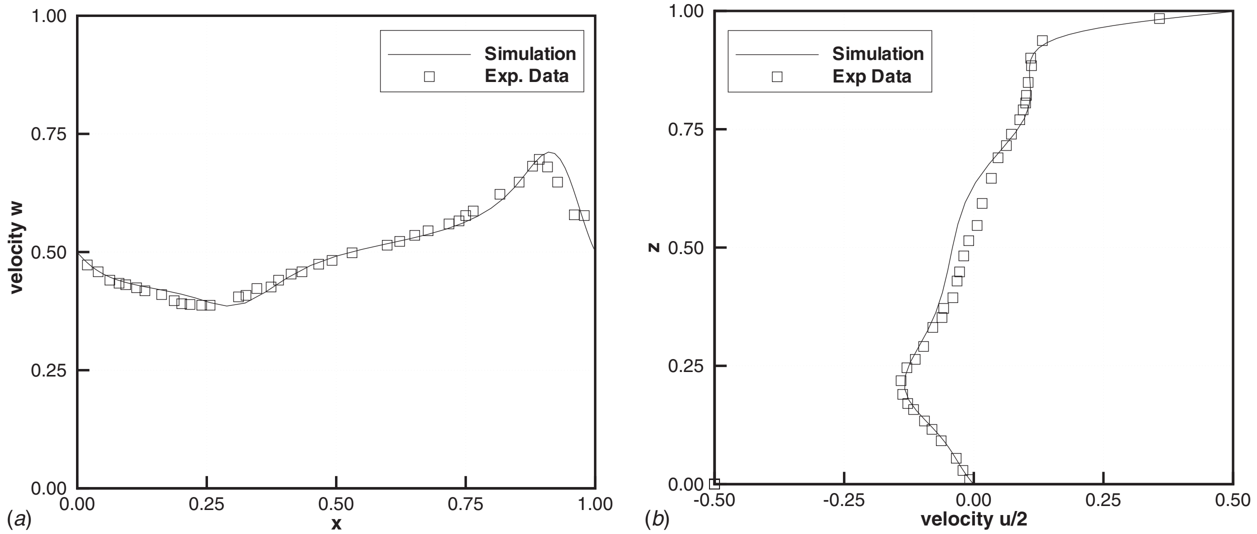

Fig. 2 Comparisons between the present model and the case presented by Guermond et al. [13], flow time $\tau=12$

This two-step procedure corresponds to a single iteration or pseudo-time-step; the process is repeated until convergence is obtained.

The three momentum equations are solved decoupled using a red/black Gauss–Seidel point solver. The solution of the elliptic Poisson system arising from the pressure correction equation is accelerated using a multigrid method. A three-level grid sequence and local time stepping are used. The solver uses message passing interface (MPI) for parallelization on distributed memory.

2.1 Validation of the Model. We have performed numerical studies over a wide range of Reynolds numbers for both lid-driven and shear driven cavity flows. For the validation of the numerical technique no data were available on similar models. Therefore, we have chosen some lid-driven cavity problems that are well documented in literature.

The first case is a lid-driven flow as described by Guermond et al. [13]. In this test case the cavity has spanwise aspect-ratio (SAR)=2:1. It is set into a vertical motion from rest in a rig that is described in that paper. The Reynolds number was Re=1000, and the time step was $\Delta t=0.005$, for a grid made of a single cubic block $68\times68\times68=314,432$ cells. This compares with a time step of $\Delta t=0.004$ and a grid size of about 300,000 tetrahedra in the half-cavity of the reference data. Both experiments and numerical simulations seemed to prove that the flow tends asymptotically to a steady state after a flow time $\tau=12$. It was also proved that the flow is symmetric with respect to the midsectional plane.

Figure 2 shows the comparison between velocity components at the symmetry cross section at a flow time $\tau=12$. One graph is the *w*-velocity component on the horizontal line through the center of the cavity, and the other graph is the *u*-component on the vertical line through the center. We considered this correlation satisfactorily.

The second case is a lid-driven cavity flow as described by Arnal et al. [20] and Kost et al. [21]. This is a cavity of SAR =3:1, at a Reynolds number Re=3200. This case is referred to as completely symmetric, as the previous case. The mesh topology, size, and time step were the same as for the case of Re=1000. Reference data are available at various flow times. We have chosen a relatively large one, $\tau=50$, since correlations between numerical simulations and experimental data tend to degrade over time. Comparisons were made at the symmetry section, as in the previous case. The results are shown in Fig. 3. The distribution of *w*-velocity component shows a flat plateau around the upstream vertical wall, perhaps due to interpolation errors. The other data are in fairly good agreement. With these interim results, we proceeded to simulate the model of Fig. 1.

3 Computational Model of the Cavity

The reference system is orthogonal, with the *x*-axis in the streamwise direction, the *y*-axis in the spanwise direction, and the *z*-axis in the vertical direction. The length of the cavity is *L* and its depth is *h*. The cavity has a squared cross section, a lid equal to $h/L=1/4$, and a span of $b=3L$. The upstream channel flow was 1.5*L*; the height of the channel (not shown in the figure) was 2*L*. Wall boundary conditions were set at the vertical channel sides as well as the channel floor. The lid had a very small thickness to reduce skewness in the grid at the inlet and to ease the grid generation. However, also parametric cases (not shown here) with a thicker lid were investigated. Details of this configuration are shown in Fig. 4. The difference between these grids is limited to a thickness parameter. Then the grid is generated in the same way.

The Reynolds number, based on the freestream velocity and on the cavity's length, was Re=8000. We note that this Reynolds number characterizes the channel flow, while the cavity flow is dominated by the Reynolds number based on the length of the inlet (1/4*L*). If we take into account the fact that the driving shear force at the inlet is actually lower than the freestream, due to the upstream boundary layer, the Reynolds number is even lower. From the calculations we estimated a long-term streamwise speed at the center of the cavity inlet $u\sim0.195$. With this speed the cavity Reynolds number is estimated at Re$\sim$400—by all means a laminar Reynolds number.

The flow solver was run on 36 processors on a Linux cluster. The computational grid for the results presented was made of 36 cubic blocks $n\times n\times n$, where $n=40$ was the number of cells in each direction. This arrangement optimizes the parallel performance of the flow solver, and the orthogonal arrangement minimizes errors due to the metrics. A total of 160 spanwise cells was used on the model, and each plane contained 9600 cells. The number of cells in the cavity was 1,535,000, out of a total 2,304,000.

The simulations shown were carried out up to flow time $\tau=380$. We defined the normalized flow time $\tau=tu/L$. The time step of these calculations was $\Delta t=0.005$, which corresponds to 200 time steps per unit of flow time, for a speed $u=1$ (normalized value).

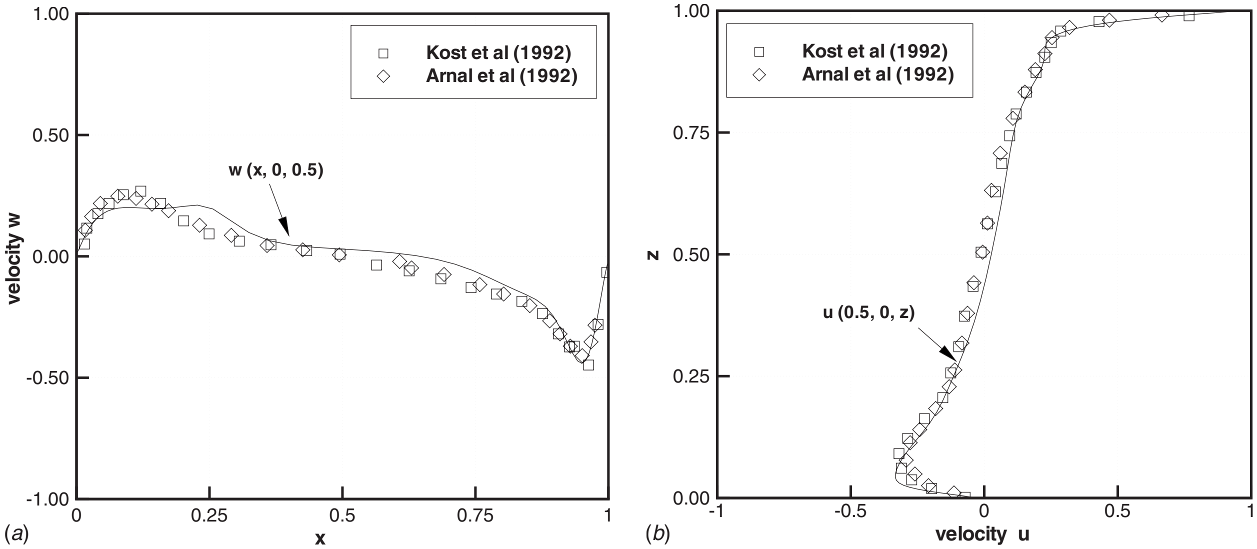

Fig. 3 Comparisons between the present model and the experimental results of Arnal et al. [20] and Kost et al. [21], flow time $\tau=50$

For clarity, we will refer to the upstream/downstream portion of the cavity and the corresponding flow as that region in the first/second half of the cavity, respectively. This terminology will be used throughout the discussion of the results.

4 Description of Results

Due to the complexities of the flow physics within the cavity, a number of different analyses can be carried out by taking cross sections along appropriate planes. These are essentially cuts along the x, y, and z axes. For slices along $y=\text{const}$, the features close to the end-walls are of most interest, as the symmetry plane reveals characteristics of known flow features, similar to the 3D lid-driven cavity. For slices along $z=\text{const}$, a plane at the center of the cavity and a plane close to the floor of the cavity can be considered. Finally, a number of crosswise sections $x=\text{const}$ can be taken, though we limit the discussion on planes at the center of the cavity, for comparisons with similar studies on the lid-driven open cavity. In fact, most vortex structures can be visualized at those stations, as they gradually disappear moving closer to the upstream and downstream walls.

The analysis of fully 3D effects requires refined graphic tools. The results presented include the main aspects of flow unsteadiness, spanwise and vertical currents, floor currents, and filaments. Other effects, perhaps secondary, not fully described for brevity, include periodic secondary vortices, end-wall vortices, and additional effects due to the cavity's geometry.

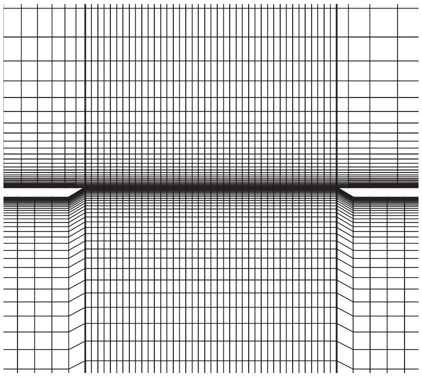

Fig. 4 Cavity model with thick lid

4.1 Flow Unsteadiness.

The time-dependence of the flow structures such as vortices, descending and ascending currents, and near-wall flow features is difficult to capture because of different time scale involved. Short-lived and small vortex structures have to be captured during a short time frame. On the other hand, the tendency to an asymptotic state is rather slow. In order to visualize the flow features in a compact form we have chosen a number of points inside the cavity and stored the velocity components, pressure, and vorticity as the simulation proceeded. This strategy allowed some analysis of the breakdown in flow symmetry and the main frequencies of oscillations. The coordinates of some of these points are given in Table 1. Point P_1 was about half a cavity length from the symmetry plane; point P_2 was close to the sidewall. Both points are just below the inlet.

For the baseline cavity geometry, a plot of v- and w-components is shown in Fig. 5 as a function of time for $\tau<360$. After an impulsive start, small differences in the velocity components due to the numerics failed to amplify and the flow remains substantially symmetric. As a consequence, the large vortex structures had a symmetric arrangement with respect to the plane $y=0$.

The distribution of velocities shows that the flow tends to a stationary state, or an unsteady state with long wavelengths, after 300 flow units. By comparison, the lid-driven cavity of Guermond et al. reached an asymptotically steady state after a time estimated between 12 and 18 units. One reason for such a different time scale is the limited flow entrainment through the lid and the effect of the upstream boundary layer that limit the effective Reynolds number *seen* by the fluid inside the cavity by a factor of 20.

4.2 Spanwise Currents.

The analysis of spanwise flows reveals that the start-up mechanism creates strong currents from the

Table 1 Selected reference points inside the cavity; b=width of the cavity

Point	x/L	$2y/b$	z/L
P_1	0.525	0.3548	−0.034149
$-P_1$	0.525	−0.3548	−0.034149
P_2	0.525	0.97813	−0.034149
$-P_2$	0.525	−0.97813	−0.034149

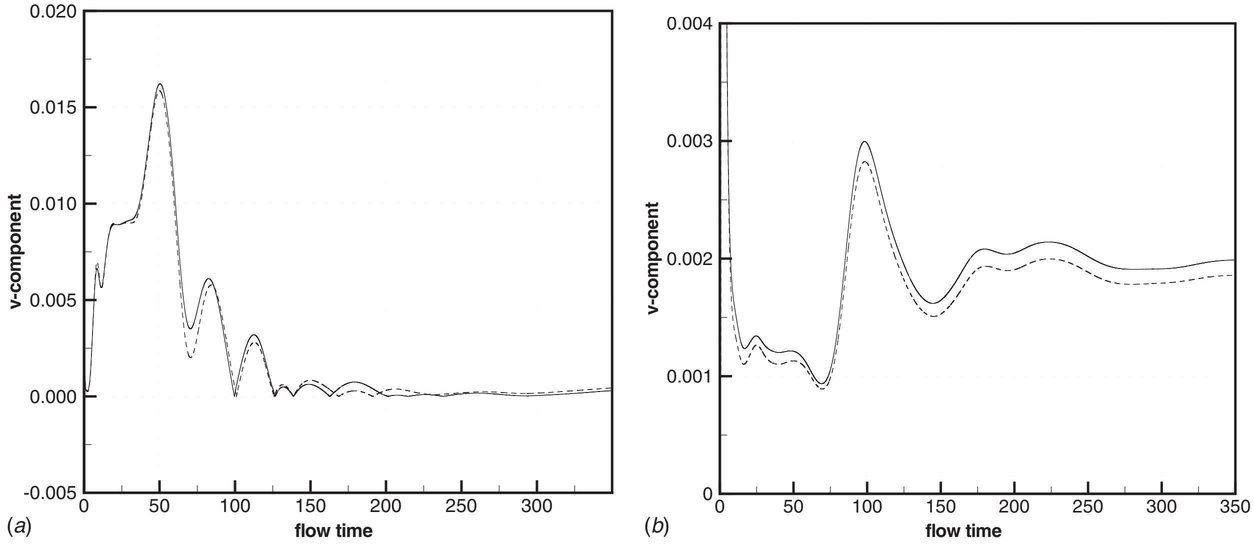

Fig. 5 Tracking of *v*-velocity components over time: (*a*) point P_1 and its symmetric and (*b*) point P_2 and its symmetric

periphery toward the center of the cavity. These currents affect areas located right below the downstream lip. This region slowly expands to involve most of the cavity, including the upstream section; then it contracts to the point of disappearing. In fact, only the strong currents are diffused. While this process takes place, slower spanwise currents with more complex topology are established.

The loci of zero spanwise velocity, $v=0$, are of great complexity, both at the start-up and for the fully developed cavity flow. These loci are of interest in the identification of the boundaries of

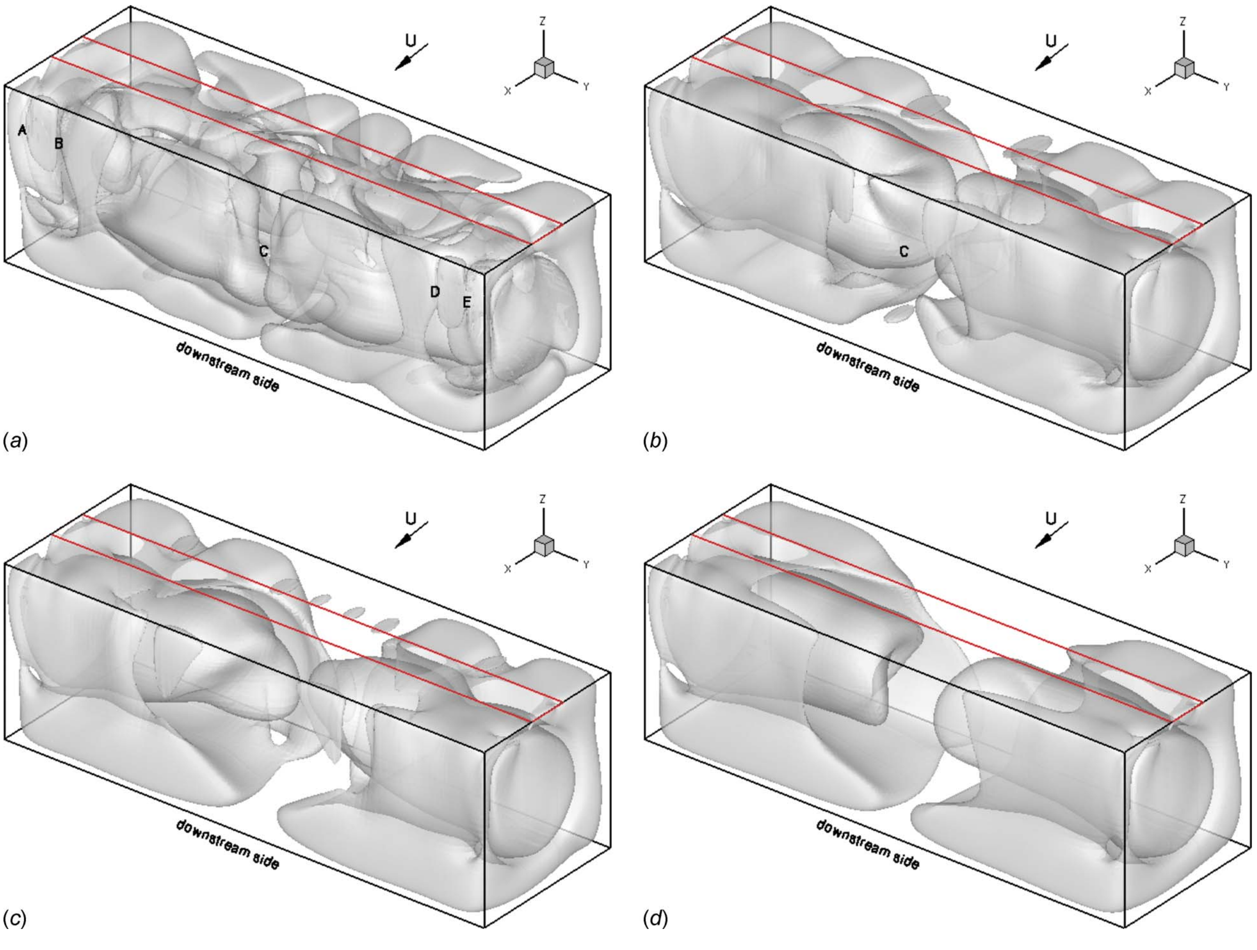

Fig. 6 Isosurface of spanwise velocity *v*, with value $v=10^{-3}$, at the times indicated; three-dimensional view from the downstream side

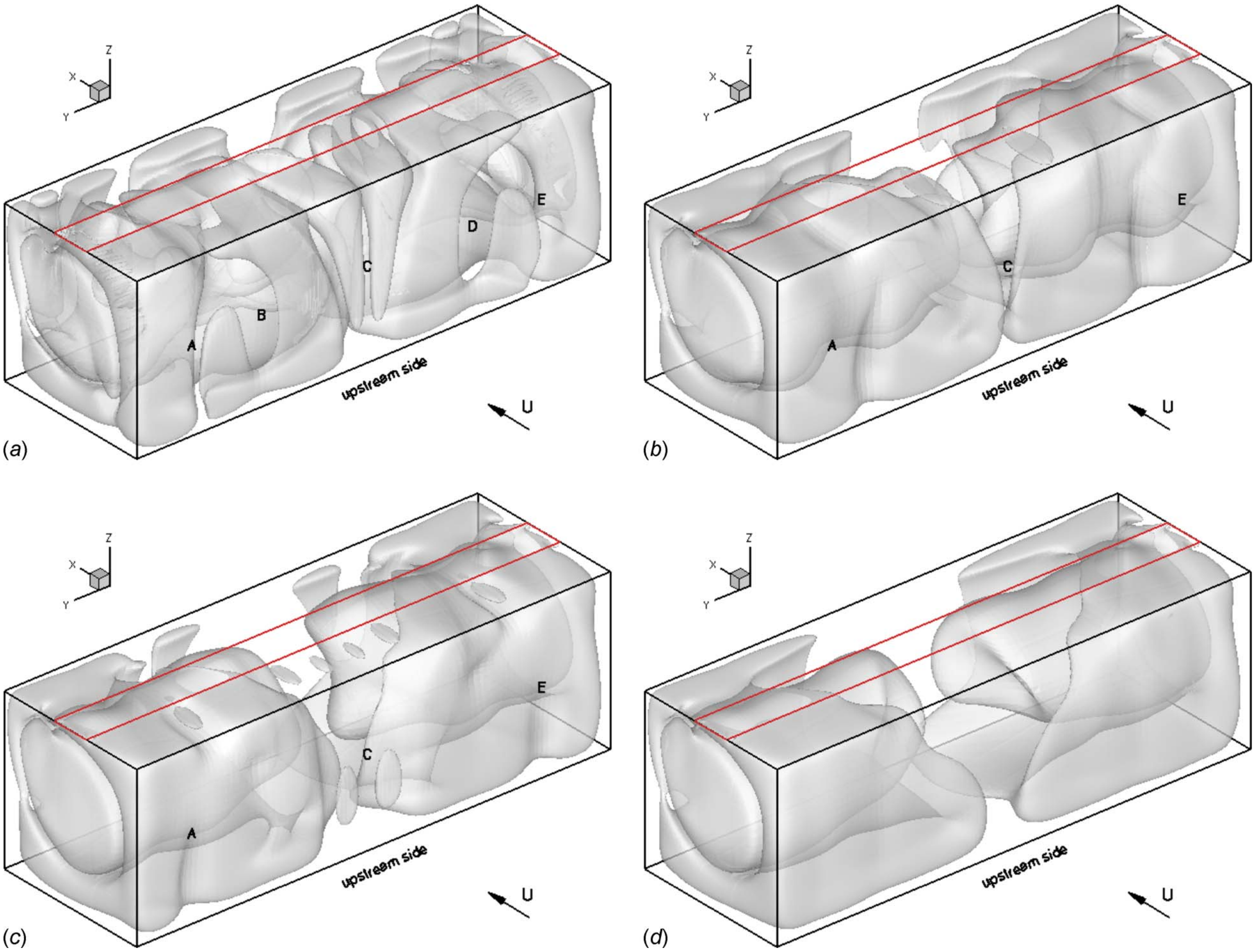

Fig. 7 Isosurface of spanwise velocity *v*, with value $v=10^{-3}$, at the times indicated; three-dimensional view from the upstream side

currents flowing toward the end-walls and back.

As a broad generalization, velocity magnitudes in the spanwise direction are largest around the 3/4 spanwise section on both sides and reduce to nearly zero at the symmetry section. This implies that flow is expelled from the cavity or pushed toward the floor at that point (as it will be clarified separately). The earliest time after which these currents are established is estimated at 3 flow units.

The isosurface $v=10^{-2}$ is widely extended after the initial transient; after an initial expansion (as shown in the figure), it gradually decreases in size, while reducing in complexity. Eventually, it ends in isolated patches of slower moving particles when the flow has settled from the initial transient. Some of the isolated patches of the isosurface denote the presence of alternate flows and are a mark of the presence of spanwise vortices.

The figure also shows a single streamtrace, created by seeding a particle in the vortex core at the periphery of the cavity (coordinates $P=\{0.85,1.4,-0.5\}$). Due to the strong pull toward the center, the particle orbits around the isosurface; eventually it is ejected and moves toward a settling area, where it becomes engulfed.

The particle traces that are shown in the same figure follow a spiral movement. Their path clearly depends on the point of release. A particle released in the periphery of the vortex core is pulled toward the center after a number of orbital turns; as it is pushed out of the primary vortex it travels back to the periphery, where it eventually becomes engulfed. Particles released at nearby points can escape the cavity. This process changes over time and is presumed to become more complex. More orbital turns are usually due to smaller amount of centrifugal pull—which happen when the flow has settled to a (nearly) steady state. However, there are locally stronger centrifugal pulls, and the streamtraces change characteristics altogether.

Figures 6 and 7 show isosurfaces for a later flow time, as indicated. In these cases, 3D views are provided. The value of the spanwise velocity is reduced by half, $v=5\times10^{-3}$, since the isosurface at the previous value $v=10^{-2}$ has disappeared. As time advances, even these isosurfaces smooth out and dissipate. In particular, consider the time $\tau=100$ units (upstream and downstream views). There are a number of structures formed near the vertical walls. These structures delimit interstices of relatively high spanwise velocity from regions of minor spanwise velocity and are denoted as A–E. Some of these structures are concentrated in the upper regions of the wall. They are an indication of the presence of either vertical currents or stagnation areas. They dissipate in a relatively short time, and only the central structure denoted by C remains.

The number of wall-bounded structures, in fact, varies from 5 to 11, depending on time. The interstices between the surface boundaries are regions of relatively low spanwise currents and high vertical currents. Mixing occurs according to a 3D recirculation process with spanwise and vertical currents that continue all the way to the wall.

The downstream view shows that a relatively strong spanwise current exists at the upstream floor of the cavity. Over time also these structures disappear and leave room only to the most stable vortices in the spanwise direction. These are a primary vortex, two lower/upper downstream secondary vortices, and two lower/upper

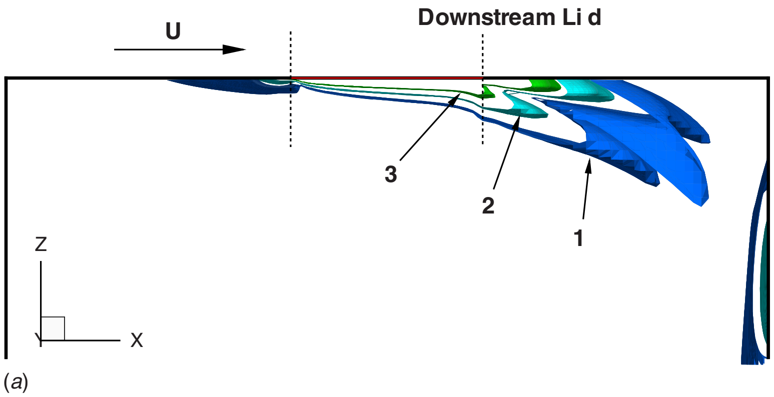

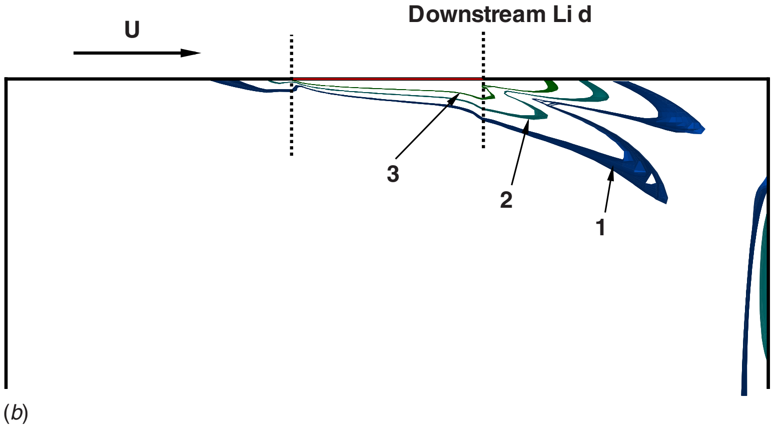

Fig. 8 Isosurfaces of total vorticity; two-dimensional view in the *x*-*z* plane

upstream secondary vortices, as in the lid-driven cavity flow.

From this analysis, we estimate the start-up process to end at about 100 time units. The spanwise currents remain but with a more limited magnitude of the mass flow. As a result, particle traces seeded from the same point tend to orbit around longer without ever reaching the cavity center. If they are moving from the very periphery of the cavity, they may never leave and remain trapped.

4.3 Vertical Currents. Descending currents are mostly concentrated below the downstream lip of the cavity; ascending flows are upstream. If one looks at a time series of the w-velocity component isosurfaces, this is a generalization. However, it describes in broad terms the mechanism by which mass flow is exchanged between the cavity and the outside channel.

A first line of investigation consists in looking at vorticity contours. Suitable contours at the inlet give an indication of how the flow is entrained in the cavity. Figure 8 shows three vorticity contour levels near the lid at flow time $\tau=100$ and 200. Increasing numbers indicate increasing levels of vorticity. There is some spanwise effect although most of the strain occurs at the end walls. The contours show some waves below the downstream lid, which is an indication of flow forcing itself into the cavity. The vorticity effects below the upstream lid are of little consequence.

Figure 9 shows two-dimensional views of isosurfaces of the w-component of the velocity. The values chosen, $w=\pm 0.015$, are relatively high velocities that decrease over time. These plots define the global vertical circulation and do not show the smaller eddies at the floor of the cavity and the upstream and downstream walls.

The vertical currents are two complicated isosurfaces, initially entangled. This fact expresses the notion that at the start-up both ascending and descending currents develop below the downstream lip, while the upstream regions remain stagnant. This conclusion is coherent with the behavior of the spanwise currents. From the central regions fluid travels spanwise in the lower cavity, then arises at the periphery, and is expelled from the upstream regions of the lid. Numerical data shown in Fig. 9 indicate that both spanwise and vertical currents are involved.

As the flow settles to a fully developed state, most of the cavity flow is set into motion, with the exception of some stagnant areas that have peculiar characteristics. The other main effect is that the vertical currents become more regular in the spanwise direction and gradually separate from each other. This is indicated in the graphics at the bottom of the same figure (flow time $\tau=50$ and 100). At these times the graphs show the presence of a well developed primary vortex across the cavity.

A closer analysis of the w-velocity component at the lid, past the start-up transient, suggests that the inflow is concentrated to a tiny portion, adjacent to the downstream edge. The outflow occurs at relatively low speeds and involves at least three-quarters of the lid. Therefore, inflow is fast through a small area and outflow is slow through a large area. As a further demonstration of this fact, the plot of streamtraces at the crosswise plane cut $x/L=0.5$ reveals streamtraces rising above the lid, bending and traveling spanwise toward the symmetry plane. This is further discussed with the Taylor–Görtler vortices in Sec. 4.8.

In the numerical simulation, the splitting of the flow at the sharp lid is smooth, and no outbursts of in- and outflows are encountered in the numerical simulation. This effect may well be different in laboratory observations if the lid has a finite thickness. Another feature of the vertical currents is seen at the inlet, where the w-component of the velocity shows a number of waves, growing over time from 2 to 6. Once the start-up phase has ended, these waves disappear, as most other vortical features.

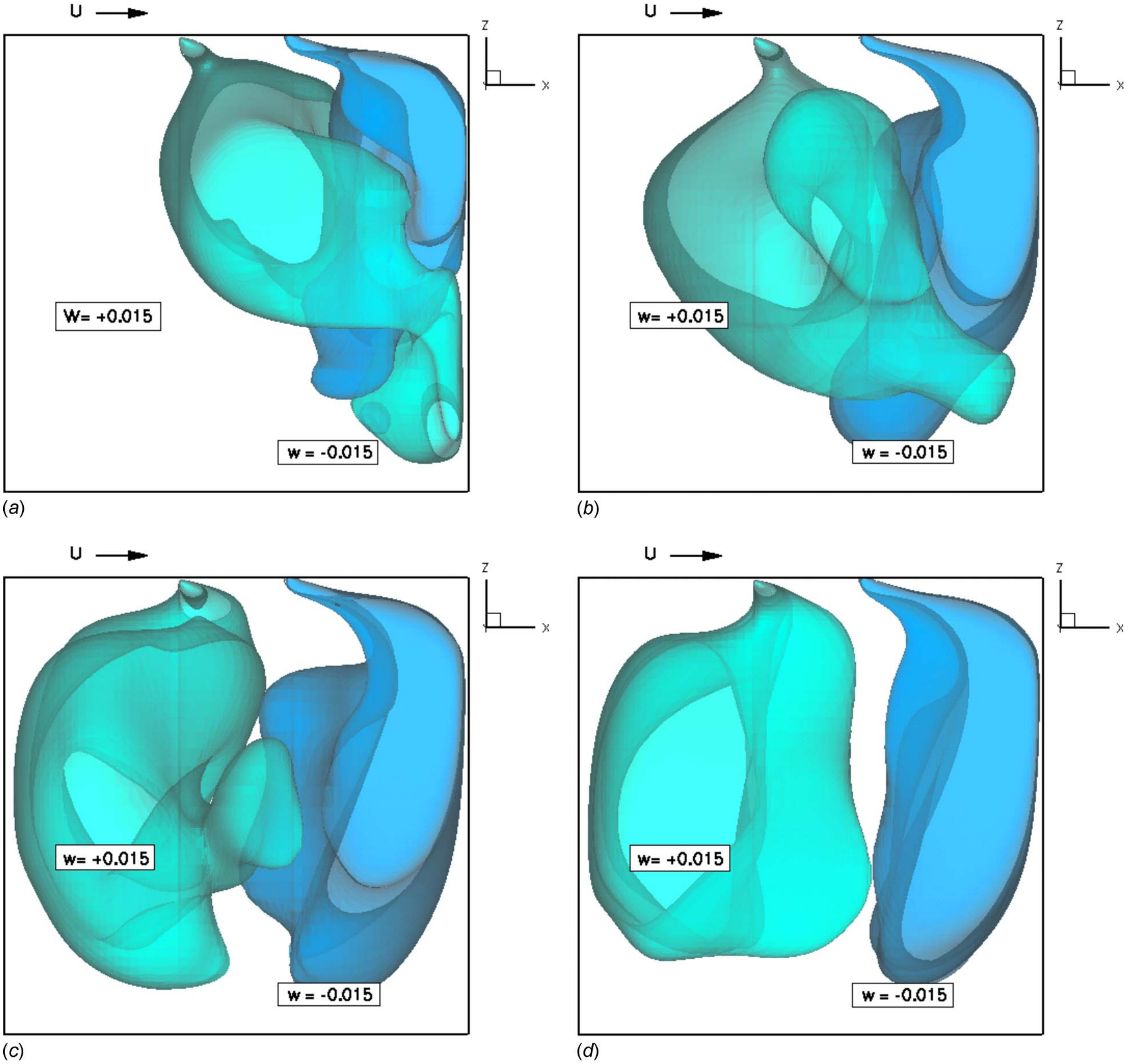

Fig. 9 Isosurfaces of vertical velocity *w*, ascending and descending flows, with values $w=\pm 0.015$, at the times indicated; two-dimensional view in the *x*-*z* plane

4.4 Floor Currents. Like any other feature, the pattern of flow separation, attachment, and vortex development depends on the flow time. Once the flow is fully established there is a long attachment and separation line, running spanwise at about 1/4 and 3/4 cavity lengths. Vertical flows start from these lines. The start-up phase shows different patterns and, in particular, at one time frame, $\tau=50$, indicates that at some points the shear forces draw fluid from the cavity floor and create a vertical filament.

4.5 Filament Vortices. Some qualitative laboratory visualizations indicated that in nearly every condition that generates a primary vortex, the flow is accompanied by vertical filaments of dye in the middle of the cavity. The filaments rise almost vertically from the floor. The evolution of these structures suggests that they are drawn up by shear forces created between counter-rotating vortices. The fact that these are filaments and not sheets of dye suggests that a cell of vortices or a ring is responsible.

The filaments appear to be generated at random, usually after the primary vortex flow has been established in the cavity. Their lifetime ranges between 5 min and 10 min, depending on the Reynolds number. Initially, the structure rises vertically. At about half the cavity depth the tip of the vortex begins to curl in one direction or another. Meanwhile, the rest of the filament begins to lean in the opposite direction, and eventually it bends in this direction, with the original tip diffusing. Finally, the whole filament diffuses. Filaments are most commonly generated from the edges of patches of dye on the cavity floor. Given the remarkable coherence of the filaments' structure, it is possible that they trace out the cores of thin vertical vortices. Filaments also seemed to be generated from concentration points in the primary vortex as well as rising up the sidewalls of the cavity and tracing out the primary vortex before they were fully visible. Filaments were also generated at the cavity walls, apparently by the primary vortex, and these filaments would rise further up the walls than the primary vortex itself, before finally curling inward at a greater height. This confirmed speculations that the flow at the cavity walls was essentially traveling uniformly upward and that this flow extends all the way to the lid. Some evidence was even seen of flow traveling further, along the underside of the lid right up to the neck. The flow in the upper half of the cavity is not well understood because the dye rarely penetrated that far upward.

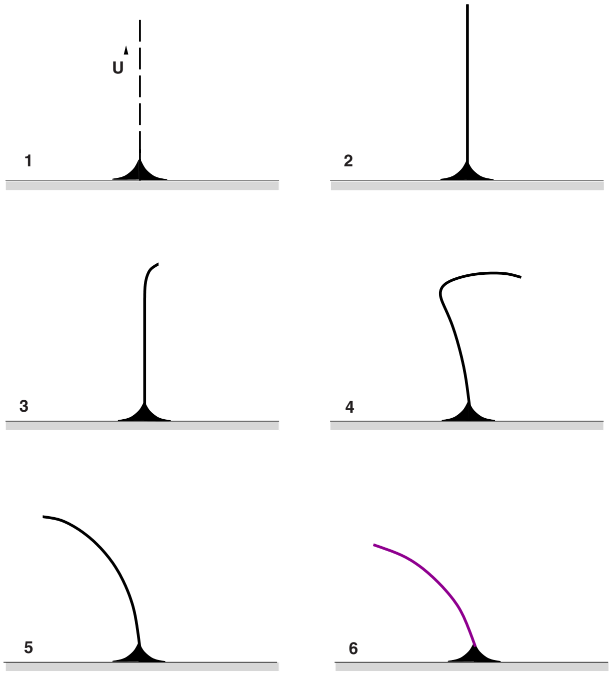

Fig. 10 Phases in the development of the vertical filament vortex

Filaments were also generated at the end-walls. These filaments were of a different type to the midfloor or dye-edge filaments, although there are similarities with the filaments generated within the side-wall main vortices. It is likely that the end-wall filaments are associated with the end-wall main vortices in the same way. Interestingly, if the dye had reached both end-walls, the end-wall filaments often appeared at both end-walls simultaneously and symmetrically, suggesting a cavity-wide coherence to the flow structure.

The process by which these filaments arise is relatively simple and is illustrated in Fig. 10: A filament grows vertically to reach almost half the cavity depth; then the head of the vortex curls in one direction or another, while the leg begins to lean in the opposite direction; eventually the leg bends toward the head and the tip begins diffusing. Diffusion gradually expands to the leg of the filament. The presence of this vortex was found also in the numerical solution, although it admittedly has a much shorter time-span. In the laboratory the life-span of the filament can be of the order of a minute, while in the simulations it was of the order of a few time units.

The numerical simulation showed another mechanism. The vortex filament starts as a much larger horseshoe vortex that included a horizontal section through the cavity symmetry plane. In brief, this vortex starts at the floor of the cavity, rises to above half the cavity depth, turns at a right angle, and heads for the symmetry. As the flow develops, the vertical leg of the vortex breaks down due to instability, and the horizontal leg reaches up to the end-walls, thereby creating the core of the primary vortex in the fully established cavity flow.

4.6 Vortex Cores. The analysis of the vortex cores within the cavity and the topology of the eddies depends on the time scale of the eddies. The definition of vortex cores has been given in the past by several authors, and here we just mention the work of Chong et al. [22] and Perry and Chong [23]. An analysis of vortex cores suggests that the primary vortex is more or less established after a flow time $\tau=50$. The primary vortex has a complex evolution. It starts from the cavity floor and it spirals around to reach the upper levels of the cavity. It turns in the spanwise direction and points toward the center of the cavity in a spiral shape. Over time it levels up and becomes almost a straight line from one end-wall to the other. The vertical legs of this vortex separate and form what we believe is a vertical filament vortex, described in Sec. 4.5. We also believe that this is only one of the mechanisms that create a filament.

A level of complication is reached at $\tau \sim 40$. The primary vortex

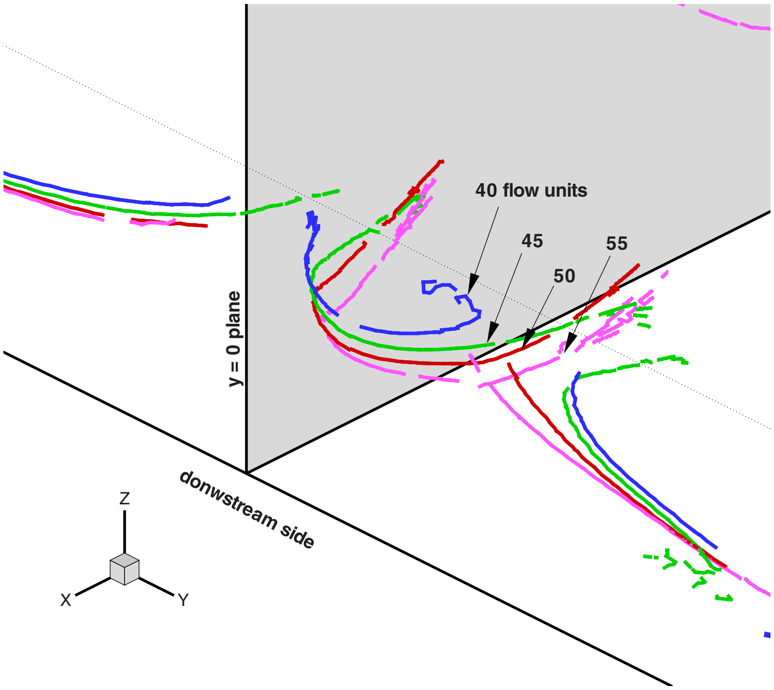

Fig. 11 Hairpin vortex at the cavity center, time series with flow times as indicated

is a spiral from one end-wall to the other and pierces the symmetry plane $y=0$ below the downstream lid (point V_1). Another large scale vortex running along the horizontal line arises from the cavity floor, spirals in the opposite direction of the main vortex, and is dissipated before reaching the symmetry plane. Three main filament vortices are present at the cavity floor, in addition to two other lower upstream vortices of smaller size around $y=0$. Finally, there is a lower (spiral) corner vortex and a smaller upper vortex at each side of the cavity.

For the primary vortex flow to be established one has to wait until a flow time $\tau\sim 100$. The lower downstream vortex takes some time to develop and starts as a set of vortices below the floor of the cavity. Three major vortices develop. First, a central vortex that evolves into a large U-shaped vortex (horseshoe) against the direction of the freestream. This vortex decays rapidly and joins up with the two lateral vortices at the cavity floor. This vortex evolves into a hairpin at flow times $\tau\sim 25$ (Fig. 11). The lateral vortices are on either side of the symmetry plane, exactly planar with the central vortex. Over time they relax and straighten up. When the flow is fully established, three vortices have joined together to form an almost linear configuration at the downstream floor of the cavity.

We also noted that the hairpin is centered in the cavity well upstream, between two linear vortices at the lower upstream of the cavity, with its heads turning back. As the time progresses, the vortex straightens out; instead of dissolving, it merges with the two linear vortices to form a large lower upstream vortex that is quite stable.

4.7 Primary and Secondary Vortices. As shown in the analysis of the previous section, after the initial start-up process, a primary vortex is established in the cavity. This is shown in Fig. 12. The primary vortex is located centrally within the cavity cross section. The formation point of this vortex is not static but moves, tracing out a spiral; it firstly spirals outward, and then returns inward to the end-wall center—always rotating in the same direction as the vortex. This vortex formation point comes about by the meeting of four end-wall bound filament vortices. A filament vortex is formed from this point and grows perpendicularly from the end-wall toward the centerline, while rotating with the cavity. The vortex is formed at the two end-walls and travels toward the center, meeting and growing in diameter to a maximum at the cavity centerline. The primary vortex rotates such that layers of fluid contacting with the freestream flow move in the same direction, i.e., the flow rotates downstream along the lid, down the downstream wall, upstream along the floor, and up the upstream wall.

There are three permanent (stable) secondary vortices present in the cavity. They are located in the upstream top, upstream bottom, and downstream bottom corners. These secondary vortices rotate in the opposite direction to the primary vortex. They are corner bound and significantly smaller than the primary vortex.

4.8 Taylor–Görtler Flows. TGL vortex has been noted in many experimental and numerical investigations on cavity flows, and their features continue to stir interest. They consist of a pair of counter-rotating vortices and exist because of the flow instability over a concave boundary. In this instance, the concave boundary is replaced by the primary vortex; therefore one may argue that the presence of the TGL vortices is not noted until the primary vortex itself is fully established. It has also been proved (for example, Ref. [24]) that there is a correlation between the maximum kinetic energy and the onset of laminar instabilities, which leads to the conclusion that TGL vortices are likely to appear in regions of large kinetic energy.

There are some stages in the development of the TGL vortices. To begin with, an oscillatory undulation forms at the boundary between the primary vortex and a secondary vortex; this is followed by a structure consisting in a converging streamline. Finally, this structure begins to oscillate and develops into the counter-rotating structure known as TGL vortex. An analysis of these vortex structures is shown in Fig. 13. The analysis is done in the $x=0.5$ plane cut through the center of the cavity. We have found that this is one of the best positions for the extent of these vortices, which totally disappear at $1/4$ and $3/4$ cavity lengths. The view is from the downstream wall (e.g., the freestream has a direction out of the page). The position of the vortex centers in this figure is found on lines of zero spanwise flow, $v=0$, and zero vertical flow, $w=0$. Therefore, these centers lie on points having an essentially streamwise flow velocity.

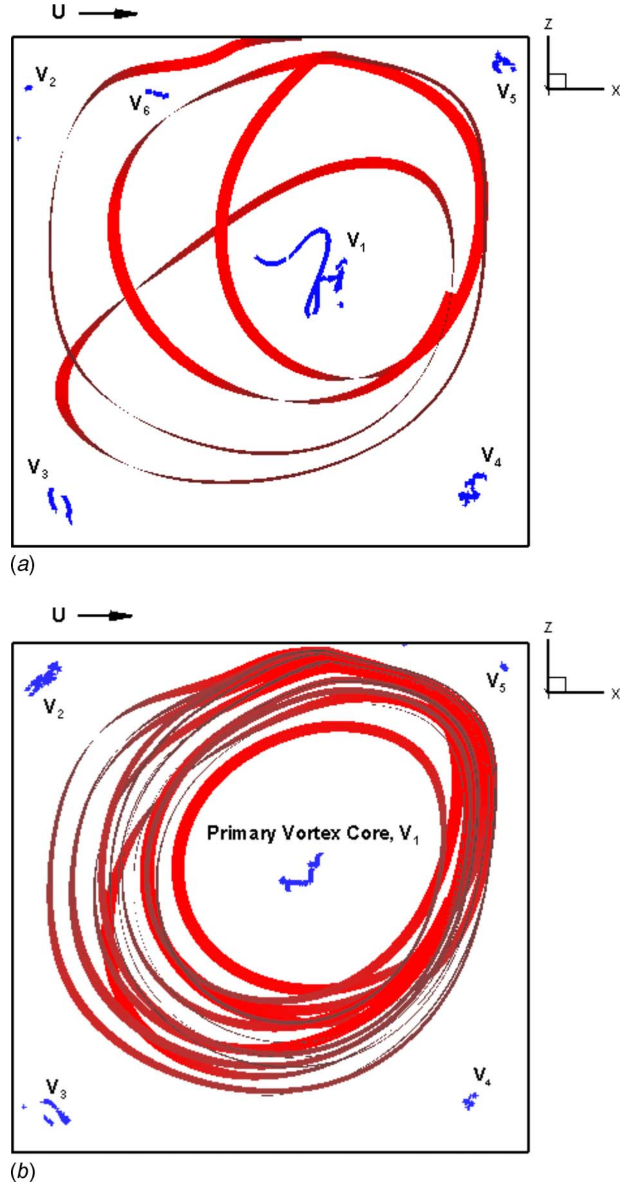

Fig. 12 Primary vortex core and secondary vortices after the initial transient

The counter-rotating vortex pairs appear at a flow time of about 30 and disappear completely before $\tau=200$. They are most developed at times $\tau=35-70$, as it is indicated in the figure. A suitable time scale for analyzing these structures is $\Delta\tau\simeq 5$ or less. There are up to five pairs of counter-rotating vortices, each with a different lifetime.

Consider the time frame at $\tau=50$. One pair is positioned at a symmetric position with respect to $y=0$. These central TGL vortices rise directly from the cavity floor, and once fully established, creep upward and grow in the process. The pair next to the central TGL vortices (on either side) are arranged as to always have a

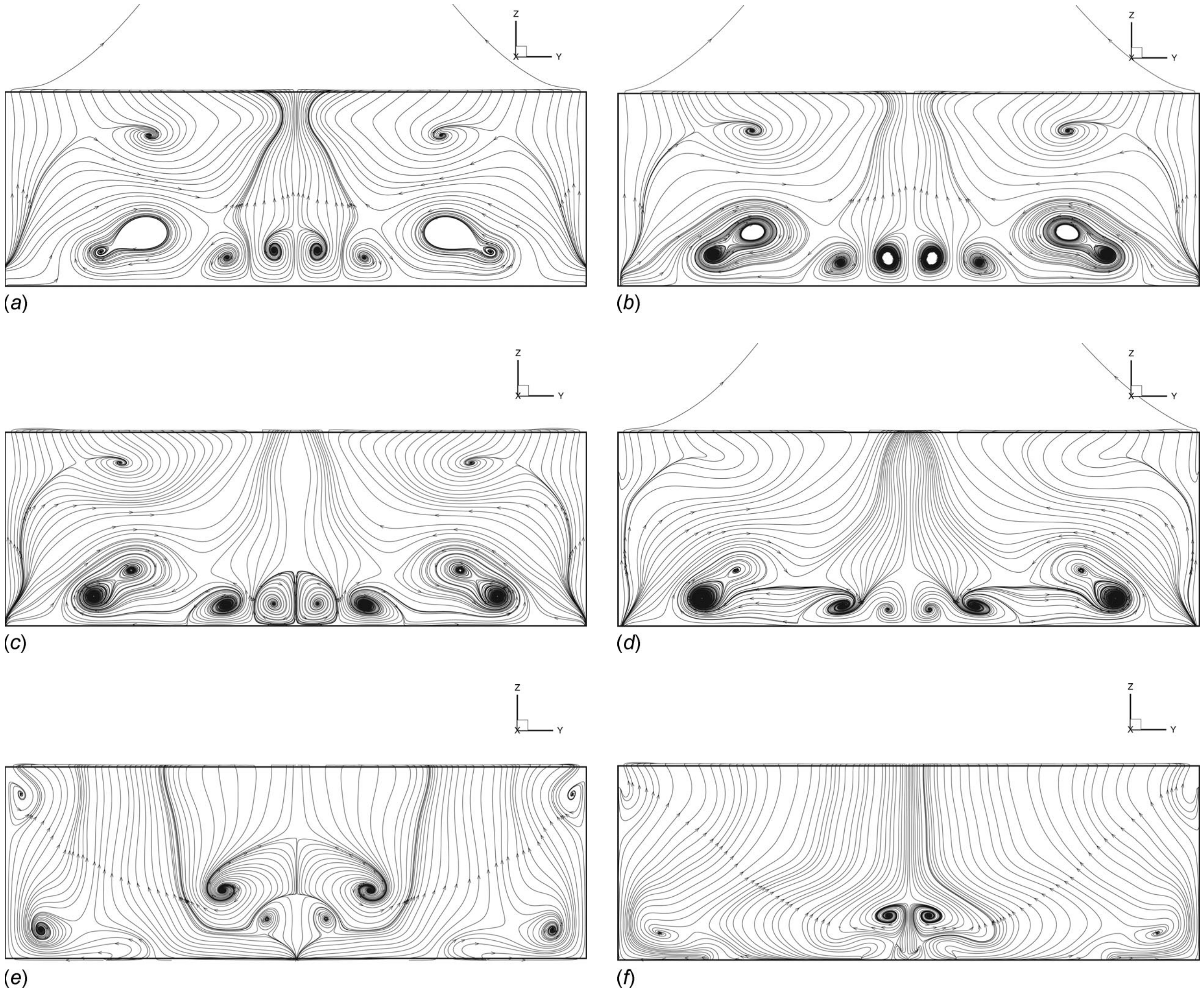

Fig. 13 Streamtraces on plane cut $x=0.5$ (middle of the cavity) at the times indicated; plots show evolution of counter-rotating vortices

sequence of counter-rotating vortices. As the first pair creeps upward, this pair takes their place by moving spanwise toward the center of the cavity.

A particular event is found at time $\tau \sim 100$ when a pair of counter-rotating vortices sits on top of another pair. In the process, the second pair of vortices evolves from a spiraling streamtrace to a mushroom shape—characteristic of this type of vortices—while the first pair opens up. However, the first pair outlasts the second pair, which dissipates and leaves streamtraces moving around a large TGL central vortex. Eventually, also this vortex disappears, and from $\tau \sim 200$ note that the main diffusion process consists in a straightening of the streamtraces, leading to a large more regular primary vortex, with characteristics similar to the lid-driven cavity flow.

The third and fourth pairs of counter-rotating vortices consist of vortices on the same side with respect to the symmetry plane. These vortices are stronger and less prone to dissipation, being the last ones to disappear. They draw a large mass of fluid around their cores. If we consider one pair, the more internal vortex is the first to smear out and leaves the other vortex moving spanwise, away from the center, while opening up.

On the upper part of the cavity the fifth pair is made of vortices on either side of the symmetry plane; these vortices travel spanwise from the center to the periphery and stop at the end-walls, creating stable end-wall vortices. Two corner vortices establish at the end-walls and are responsible for some faster outflow, as indicated by two streamtraces moving upward, away from the cavity.

5 Conclusions

The study of the start-up flow at a laminar Reynolds number has shown that a number of vortex structures are created and then dissipated. The numerical instabilities never amplified and led to an asymptotically stable flow. After a long transient, the flow evolves into a vortex flow similar with the lid-driven cavity. In particular, we have evidenced the presence of a primary central vortex that establishes when the flow has reached a fully developed state in the cavity, some TGL vortices, and stable upstream and downstream secondary vortices. In addition to the above, the presence of short-lived vortex filaments, descending vortex jets, and wall-bounded vortices at the upstream and downstream cavity walls have peculiar characteristics. The start-up flow takes up about 100 time units. The flow reaches a steady state after 250–300 time units.

The through-flow at the neck of the cavity shows coherent waves, but inflow is mostly concentrated at the downstream edge, and outflow is at the downstream edge. A great deal of mixing occurs at this location because of the incoming flow meeting outgoing flow. Inflow is concentrated on a lower lid area; the outflow dominates the lid area although the exit speed is relatively low.

It is possible that a thick or streamlined neck yields a different flow pattern. Therefore, we conclude that the baseline case is an idealized cavity flow, showing a number of vortex features that are unstable and depending on the geometry of the arrangement and on the state of the boundary layer at the lid.

After the slow start-up process, the flow reaches a state that can be considered steady. The primary vortex formation is nearly complete after 200 time units. Finally, the findings of the numerical analysis are accurate at moderate flow times. Qualitative laboratory visualizations indicated that the flow does not reach either a steady state or a fully symmetric structure. The reasons for this are attributed to instability in the upstream boundary layer and to the thickness of the downstream lip.

References

[1] Rhee, H. S., Koseff, J. R., and Street, R. L., 1984, "Flow Visualization of a Recirculating Flow by Rheoscopic Liquid and Liquid Crystal Techniques," Exp. Fluids, **2**, pp. 57–64.

[2] Migeon, C., 2002, "Details on the Start-Up Development of the Taylor-Görtler-Like Vortices Inside a Square-Section Lid-Driven Cavity for 1,000 $<\mathrm{Re}<3{,}200$," Exp. Fluids, **33**(4), pp. 594–602.

[3] Moffatt, H. K., 1964, "Viscous and Resistive Eddies Near a Sharp Corner," J. Fluid Mech., **18**(1), pp. 1–18.

[4] Koseff, J. R., and Street, R. L., 1984, "The Lid-Driven Cavity Flow: A Synthesis of Qualitative and Quantitative Observations," ASME J. Fluids Eng., **106**, pp. 390–398.

[5] Koseff, J. R., and Street, R. L., 1984, "On End-Wall Effects in a Lid-Driven Cavity Flow," ASME J. Fluids Eng., **106**, pp. 385–389.

[6] Freitas, C. J., Street, R. L., Findikakis, A. N., and Koseff, J. R., 1994, "Numerical Simulation of Three-Dimensional Flow in a Cavity," Int. J. Numer. Methods Fluids, **5**, pp. 561–575.

[7] Koseff, J. R., and Street, R. L., 1984, "Visualization Studies of a Shear-Driven Three-Dimensional Recirculating Flow," ASME J. Fluids Eng., **106**, pp. 21–29.

[8] Chiang, T. P., and Sheu, W. H., 1997, "Numerical Prediction of Eddy Structure in a Shear-Driven Cavity," Comput. Mech., **20**, pp. 379–396.

[9] Drikakis, D., Iliev, O. P., and Vassileva, D. P., 1998, "A Nonlinear Multigrid Method for the Three-Dimensional Incompressible Navier–Stokes Equations," J. Comput. Phys., **146**(1), pp. 301–321.

[10] Gilmanov, A., and Sotiropoulos, F., 2005, "A Hybrid Cartesian/Immersed Boundary Method for Simulating Flows With 3d, Geometrically Complex, Moving Bodies," J. Comput. Phys., **207**(2), pp. 457–492.

[11] Peng, Y., Shu, C., and Chew, Y. T., 2004, "A 3D Incompressible Thermal Lattice Boltzmann Model and its Application to Simulate Natural Convection in a Cubic Cavity," J. Comput. Phys., **193**(1), pp. 260–274.

[12] Shankar, P. N., and Deshpande, M. D., 2000, "Fluid Mechanics in the Driven Cavity," Annu. Rev. Fluid Mech., **32**, pp. 93–136.

[13] Guermond, J. L., Migeon, C., Pineau, G., and Quartapelle, L., 2002, "Start-Up Flows in a Three-Dimensional Rectangular Driven Cavity of Aspect Ratio 1:1:2 at $\mathrm{Re}=1000$," J. Fluid Mech., **450**, pp. 169–199.

[14] Prasad, K., and Koseff, J. R., 1989, "Reynolds Number and End-Wall Effects on a Lid-Driven Cavity Flow," Phys. Fluids A, **1**, pp. 208–218.

[15] Michelsen, J. A., 1994, "Block Structured Multigrid Solution of 2D and 3D Elliptic PDE's," Department of Mechanical Engineering, Technical University of Denmark, Technical Report No. AFM 94-06.

[16] Sørensen, N. N., 1995, "General Purpose Flow Solver Applied Over Hills," Risø National Laboratory, Technical Report No. RISØ-R-827-(EN).

[17] Sørensen, N. N., 1995, "General Purpose Flow Solver Applied Over Hills," RISØ National Laboratory, Technical Report No. RISØ R-827-(EN).

[18] Rhie, C. M., 1981, "A Numerical Study of the Flow Past an Isolated Airfoil With Separation," Ph.D. thesis, University of Illinois, Urbana-Champaign, IL.

[19] Patankar, S. V., and Spalding, D. B., 1972, "A Calculation Procedure for Heat, Mass and Momentum Transfer in Three-Dimensional Parabolic Flows," Int. J. Heat Mass Transfer, **15**, pp. 1787–1806.

[20] Arnal, M., Lauer, O., Lilek, Z., and Peric, M., 1992, "Prediction of Three-Dimensional Lid Driven Cavity Flow," *GAMM Workshop*, M. Deville , T. H. Le, and Y. Morchoisne, eds., pp. 13–24.

[21] Kost, A., Mitra, N. K., Fiebig, M., and Bochum, R. U., 1992, "Numerical Simulation of Three Dimensional Unsteady Flow in a Cavity," *GAMM Workshop*, M. Deville, T. H. Le, and Y. Morchoisne, eds., Vol. 36, pp. 79–80.

[22] Chong, M. S., Soria, J., Perry, A. E., Chacin, J., Cantwell, B. J., and Na, Y., 1998, "Turbulent Structures of Wall-Bounded Shear Flws Using DNS Data," J. Fluid Mech., **357**, pp. 225–247.

[23] Perry, A. E., and Chong, M. S., 1987, "Description of Eddying Motions and Flow Patterns Using Critical-Point Concepts," Annu. Rev. Fluid Mech., **19**, pp. 125–155.

[24] Chiang, T. P., Sheu, W. H., and Hwang, R. R., 1997, "Three-Dimensional Vortex Dynamics in a Shear-Driven Rectangular Cavity," Int. J. Numer. Methods Fluids, **8**, pp. 201–214.

Aytac Arikoglu
Faculty of Aeronautics and Astronautics,
Aeronautical Engineering Department,
Istanbul Technical University,
Maslak, TR-34469 Istanbul, Turkey

Guven Komurgoz
Faculty of Electric and Electronics,
Istanbul Technical University,
Maslak, TR-34469, Istanbul, Turkey

Ibrahim Ozkol[1]
Faculty of Aeronautics and Astronautics,
Aeronautical Engineering Department,
Istanbul Technical University,
Maslak, TR-34469 Istanbul, Turkey
e-mail: ozkol@itu.edu.tr

Effect of Slip on the Entropy Generation From a Single Rotating Disk

In this study, it is the first time that the effect of slip on the entropy generation is investigated for the flow over a rotating single free disk. The problem is considered for steady and axially symmetrical case in a Newtonian ambient fluid. The classical approach introduced by Von Karman is followed to reduce nonlinear flow and heat field equations to ordinary differential equations. Then these equations are solved by using differential transform method. Entropy generation equation for this system is then derived and nondimensionalized. This equation, which has never been introduced for such a geometry and boundary conditions before in open literature, is interpreted for various physical cases by using nondimensional parameters of fluid and heat fields. It is observed that the effects of slip are to reduce the magnitude of entropy generation and to reduce the total energy in the system by reducing velocities and velocity gradients. Also, while entropy generation reduces, Bejan number converges to 1 with increasing slip factor.
[DOI: 10.1115/1.2953301]

Keywords: *entropy generation, slip flow, rotating disk*

1 Introduction

The flow fields due to rotating disks are chosen since these type flow fields are of great interest in many practical and engineering aspects. Mainly the requirement of high temperatures in the turbine stage of a gas turbine engine to achieve high thermal efficiencies, the cooling of air is essential to ensure long lifetime for turbine disk and blades. For such type rotary systems thermal efficiencies may not only be functions of temperature. The reason for that is the complexity of the flow and thermal fields and not having implicit analytical expressions for each field. It is vital to know how the flow and the thermal fields are at every stage for a safe and effective work life in the operation of the rotary type machine systems. For accurate determination of temperature distribution, the flow field must be solved as precisely as possible [1]. Since the governing equations, namely, the momentum equations, are highly nonlinear and coupled, it is hard to obtain an exact-analytical solution. Therefore, in many cases numerical or seminumerical-analytical solutions are carried out.

The second law of thermodynamics has recently been used for prediction of performance of the engineering processes. For the efficiency calculations of such complex systems, the loss of available energy must be considered. However, calculations using the second law of thermodynamics, which is related to entropy generation and efficiency calculation, are more reliable than first law-based calculations because the latter make no reference to the best possible performance, namely, to the minimization of the irreversibilities present in the physical process, and thus may be misleading.

The usage of the method of the second law of thermodynamics as a measure of the system performance was introduced by Bejan [2]. Since then, many studies on the second law of thermodynamics, the entropy generation rates, and the irreversibility for the basic arrangements have been published in literature.

Hitherto, though, there are numerous studies on second law analysis for flow field and heat transfer problems [3–5]; none of them consider the effect of slip on the entropy generation. Erbay et al. [6] studied the effect of the motion of the bottom plate, in the case of two parallel plates, on the entropy generation. In a similar study of Mahmud and Fraser [7], the mechanism of entropy generation as well as its distribution through flow field for basic channel geometries including one fixed and the other moving plates are carried out by considering simplified or approximate analytical expressions. In another study, Yilbas [8] determined the heat transfer characteristics and the resulting entropy generation across annuli with rotating outer cylinder for the case of linear velocity distribution. Entropy generation due to laminar mixed convection from an isothermal rotating cylinder was calculated numerically by Abu-Hijleh et al. [9].

The slip over a moving surface is mainly caused by two effects, surface roughness and rarefaction of the fluid. This type of flow is commonly encountered in many engineering aspects such as high-altitude flight, micromachines, vacuum technology, aerosol reactors, etc. In this study we will consider the effect of slip as a result of rarefied fluid flow; however, the numerical results evaluated in this study can also be adapted to the other case, surface roughness. The slip regime for the Knudsen number (Kn) lies between the range $0.1>\mathrm{Kn}>0.001$. For $\mathrm{Kn}<0.001$ the nonslip condition is present and for $\mathrm{Kn}>0.1$ the flow field cannot be assumed to be continuum and Navier–Stokes equations are no longer valid. In our study, the slip and the nonslip regimes that lie in the range $0.1>\mathrm{Kn}>0$ are considered.

For the solution of field equations, the similarity variables introduced by Von Karman are used with coordinate stretching technique to reduce heat and flow field equations to a set of nonlinear ordinary differential equations. The resulting differential equation system is solved as in our previous studies [10,11] by using differential transform method (DTM), on which we have made some theoretical and practical contributions [12,13].

The velocity of the fluid on the surface, where the effect of slip dominates, is related to the slip factor by the boundary conditions (BCs) given in Ref. [14]. The slip dependent velocity means that the reduction in the loss of some part of the mechanical energy into thermal energy, i.e., reducing the entropy generation, results in using the higher portion of the available energy. Also, by relating entropy generation to slip factor on the flow and heat field

---

[1] Corresponding author.

Contributed by the Fluids Engineering Division of ASME for publication in the Journal of Fluids Engineering. Manuscript received November 13, 2007; final manuscript received May 15, 2008; published online September 2, 2008. Assoc. Editor: Phillip M. Ligrani.

solutions gives more accurate results, which help the designer for the correct efficiency calculations and geometrical optimization of such rotating system or systems having rotating parts.

2 Mathematical Modeling of Flow and Thermal Fields

Considering the steady, incompressible flow over a single free disk in a Newtonian fluid, the equations of conservation of momentum and continuity can be given as follows:

$$u\frac{\partial u}{\partial r}+w\frac{\partial u}{\partial z}-\frac{v^2}{r}+\frac{1}{\rho}\frac{\partial p}{\partial r}=\frac{\mu}{\rho}\left(\frac{\partial^2 u}{\partial r^2}+\frac{1}{r}\frac{\partial u}{\partial r}-\frac{u}{r^2}+\frac{\partial^2 u}{\partial z^2}\right) \quad (1)$$

$$u\frac{\partial v}{\partial r}+w\frac{\partial v}{\partial z}+\frac{uv}{r}=\frac{\mu}{\rho}\left(\frac{\partial^2 v}{\partial r^2}+\frac{1}{r}\frac{\partial v}{\partial r}-\frac{v}{r^2}+\frac{\partial^2 v}{\partial z^2}\right) \quad (2)$$

$$u\frac{\partial w}{\partial r}+w\frac{\partial w}{\partial z}+\frac{1}{\rho}\frac{\partial p}{\partial z}=\frac{\mu}{\rho}\left(\frac{\partial^2 w}{\partial r^2}+\frac{1}{r}\frac{\partial w}{\partial r}+\frac{\partial^2 w}{\partial z^2}\right) \quad (3)$$

$$\frac{\partial(ru)}{\partial r}+\frac{\partial(rw)}{\partial z}=0 \quad (4)$$

where u is the radial, v is the circumferential, w is the axial component of the velocity, μ is the dynamic viscosity, and ρ is the density. Slip BCs for the problem considered are introduced as follows [11,14,15].

$$u=\frac{2-\eta}{\eta}\lambda\frac{\partial u}{\partial z}, \quad v=r\Omega+\frac{2-\eta}{\eta}\lambda\frac{\partial v}{\partial z}, \quad w=0 \quad \text{at } z=0 \quad (5)$$

$$u\to 0, \quad v\to 0 \quad \text{as } z\to\infty \quad (6)$$

where η is the tangential momentum accommodation coefficient, λ is the mean free path, and Ω is the angular velocity of the rotating disk. Following Von Karman, a dimensionless axial coordinate $\zeta=z\sqrt{\Omega/\nu}$ is introduced together with the following velocity components and pressure:

$$u=\Omega rF(\zeta), \quad v=\Omega rG(\zeta), \quad w=\sqrt{\Omega\nu}H(\zeta), \quad p=-\rho\Omega\nu P(\zeta) \quad (7)$$

Using the dimensionless axial coordinate, the velocity components, and the pressure, the following system of ordinary differential equations is obtained:

$$F''=HF'+F^2-G^2 \quad (8)$$

$$G''=HG'+2FG \quad (9)$$

$$H'=-2F \quad (10)$$

$$P'=HH'-H'' \quad (11)$$

The BCs in Eqs. (5) and (6) can be written as follows [11]:

$$F(0)=\gamma F'(0), \quad G(0)=1+\gamma G'(0), \quad H(0)=0 \quad (12)$$

$$F(\infty)=0, \quad G(\infty)=0 \quad (13)$$

where $\gamma=[(2-\eta)\lambda\Omega^{1/2}]/\eta\nu^{1/2}$ is defined as the slip factor, which is a measure of the effect of slip.

The energy equation, neglecting dissipation terms and considering that heat transfer is only in the z direction [16], can be written as follows:

$$\rho c_p w\frac{\partial T}{\partial z}-k\frac{\partial^2 T}{\partial z^2}=0 \quad (14)$$

where T is the temperature, c_p is the specific heat, and k is the thermal conductivity. The BCs for temperature are given by

$$T(0)=T_0, \quad T(\infty)=T_\infty \quad (15)$$

Using the dimensionless temperature $\Theta(\zeta)=(T-T_\infty)/(T_0-T_\infty)$, Eq. (14) can be written as follows:

$$\Theta''=\mathrm{Pr}\,H\Theta' \quad (16)$$

where Pr is the Prandtl number. The BCs in Eq. (15) become

$$\Theta(0)=1, \quad \Theta(\infty)=0 \quad (17)$$

By integrating Eq. (16) with the first BC in Eq. (17), dimensionless temperature can be evaluated in terms of the axial part of the velocity field as follows:

$$\Theta(\zeta)=\Theta'(0)\int_0^{\zeta} e^{\mathrm{Pr}\int_0^{\chi}H(\alpha)d\alpha}d\chi+1 \quad (18)$$

and the missing (BC) $\Theta'(0)$ is obtained from Eq. (18) together with the far field BC given in Eq. (17) as follows:

$$\Theta'(0)=-1/\int_0^{\infty} e^{\mathrm{Pr}\int_0^{\chi}H(\alpha)d\alpha}d\chi \quad (19)$$

Once solving the flow field, the thermal field is acquired from Eqs. (18) and (19) by using numerical integration. To solve the problem in a bounded domain, the following dependent and independent variables introduced by Benton are used [17]:

$$\xi=e^{-c\zeta} \quad (20)$$

$$F(\zeta)=c^2f(\xi), \quad G(\zeta)=c^2g(\xi), \quad H(\zeta)=-c[1-h(\xi)] \quad (21)$$

By using the variables in Eqs. (20) and (21), Eqs. (8)–(10) are written as follows:

$$\xi^2f''(\xi)=f^2(\xi)-g^2(\xi)-\xi f'(\xi)h(\xi) \quad (22)$$

$$\xi^2g''(\xi)=2f(\xi)g(\xi)-\xi g'(\xi)h(\xi) \quad (23)$$

$$\xi h'(\xi)=2f(\xi) \quad (24)$$

and by using Eqs. (20) and (21) again, the BCs in Eqs. (12) and (13) can be written as follows:

$$f(1)=\gamma f'(1), \quad g(1)=c^{-2}-\gamma cg'(1), \quad h(1)=1 \quad (25)$$

$$f(0)=0, \quad g(0)=0, \quad h(0)=0 \quad (26)$$

3 Solution Method

To solve the equation system (22)–(24) with the BCs in Eqs. (25) and (26), DTM is applied at $\xi=0$. By using the theorems in Ref. [12], the differential transform of Eqs. (22)–(24) can be evaluated as follows:

$$\tilde{F}(k)=\frac{1}{k(k-1)}\sum_{l=0}^{k}[\tilde{F}(l)\tilde{F}(k-l)-\tilde{G}(l)\tilde{G}(k-l)-l\tilde{F}(l)\tilde{H}(k-l)] \quad (27)$$

$$\tilde{G}(k)=\frac{1}{k(k-1)}\sum_{l=0}^{k}[2\tilde{F}(l)\tilde{G}(k-l)-l\tilde{G}(l)\tilde{H}(k-l)] \quad (28)$$

$$\tilde{H}(k)=\frac{2}{k}\tilde{F}(k) \quad (29)$$

where $k\geqslant 2$ and $\tilde{F}(k)$, $\tilde{G}(k)$, and $\tilde{H}(k)$ denote the differential transforms of $f(\xi)$, $g(\xi)$, and $h(\xi)$, respectively. To evaluate the dependent variables, it is necessary to know the missing BCs $f'(0)$ and $g'(0)$. First, the values of $\tilde{F}(k)$, $\tilde{G}(k)$, and $\tilde{H}(k)$ for $k=2,3,\ldots,N$ in terms of $f'(0)$ and $g'(0)$, which will be called as f_1 and g_1, respectively, are obtained and then by using the BCs given in Eq. (25) for $\xi=1$, f_1, g_1, and c are evaluated numerically. This is much faster and cost efficient than the numerical techniques since it is not iterative. The BCs given in Eq. (26) for $\xi=0$ are transformed as follows:

$$\tilde{F}(0)=0, \quad \tilde{G}(0)=0, \quad \tilde{H}(0)=0, \quad \tilde{F}(1)=f_1 \text{ and } \tilde{G}(1)=g_1 \tag{30}$$

By using the recurrence relations in Eqs. (27)–(29) and the transformed BCs in Eq. (30), $\tilde{F}(k)$, $\tilde{G}(k)$, and $\tilde{H}(k)$ for $k=2,3,\ldots,N$ are evaluated. Then, using the inverse transformation rule in Ref. [12], the series solutions are obtained from

$$f(\xi)=\sum_{k=0}^{N}\tilde{F}(k)\xi^k, \quad g(\xi)=\sum_{k=0}^{N}\tilde{G}(k)\xi^k, \quad h(\xi)=\sum_{k=0}^{N}\tilde{H}(k)\xi^k \tag{31}$$

where N is the number of terms to be calculated. By calculating up to $N=6$, we get

$$\begin{aligned} f(\xi)&=f_1\xi-\tfrac{1}{2}(f_1^2+g_1^2)\xi^2+\tfrac{1}{4}f_1(f_1^2+g_1^2)\xi^3-\tfrac{1}{144}(17f_1^4+18f_1^2g_1^2\\ &\quad+g_1^4)\xi^4+\tfrac{1}{1152}f_1(61f_1^4+74f_1^2g_1^2+13g_1^4)\xi^5-\tfrac{1}{86{,}400}(1971f_1^6\\ &\quad+2825f_1^4g_1^2+889f_1^2g_1^4+35g_1^6)\xi^6+\cdots \end{aligned} \tag{32}$$

$$\begin{aligned} g(\xi)&=g_1\xi-\tfrac{1}{12}g_1(f_1^2+g_1^2)\xi^3+\tfrac{1}{18}f_1g_1(f_1^2+g_1^2)\xi^4-\tfrac{1}{1920}g_1(53f_1^4\\ &\quad+58f_1^2g_1^2+5g_1^4)\xi^5+\tfrac{1}{5400}f_1g_1(65f_1^4+82f_1^2g_1^2+17g_1^4)\xi^6+\cdots \end{aligned} \tag{33}$$

$$\begin{aligned} h(\xi)&=2f_1\xi-\tfrac{1}{2}(f_1^2+g_1^2)\xi^2+\tfrac{1}{6}f_1(f_1^2+g_1^2)\xi^3-\tfrac{1}{288}(17f_1^4+18f_1^2g_1^2\\ &\quad+g_1^4)\xi^4+\tfrac{1}{2880}f_1(61f_1^4+74f_1^2g_1^2+13g_1^4)\xi^5-\tfrac{1}{259{,}200}(1971f_1^6\\ &\quad+2825f_1^4g_1^2+889f_1^2g_1^4+35g_1^6)\xi^6+\cdots \end{aligned} \tag{34}$$

The solutions are given here up to $O(\xi^6)$; however, one can easily obtain higher ordered terms. After evaluating $f(\xi)$, $g(\xi)$, and $h(\xi)$, the original dependent variables $F(\zeta)$, $G(\zeta)$, and $H(\zeta)$ are obtained by using Eqs. (20) and (21). Also, in the case of necessity, one can obtain $P(\zeta)$ from the following equation:

$$P(\zeta)-P_0=H(\zeta)^2/2-H'(\zeta) \tag{35}$$

4 Entropy Generation

Since the temperature is assumed to be a function of z only [16], for the steady and axially symmetrical flow in a Newtonian fluid, the entropy generation rate can be expressed as follows:

$$\begin{aligned} \dot{S}_G'''&=\frac{k}{T_0{}^2}\left(\frac{\partial T}{\partial z}\right)+\frac{\mu}{T_0}\left\{2\left[\left(\frac{\partial u}{\partial r}\right)^2+\frac{1}{r^2}u^2+\left(\frac{\partial w}{\partial z}\right)^2\right]+\left(\frac{\partial v}{\partial z}\right)^2\right.\\ &\quad\left.+\left(\frac{\partial u}{\partial z}\right)^2+\left[r\frac{\partial}{\partial r}\left(\frac{v}{r}\right)^2\right]\right\} \end{aligned} \tag{36}$$

Using the dimensionless variables in Eq. (7) together with the dimensionless temperature, Eq. (36) can be written in the following simple form, which has never been given before in open literature, to the best knowledge of the authors:

$$N_G=\mathrm{Re}\,\Theta'(\zeta)^2+\Psi\{3\,\mathrm{Re}^2\,H'(\zeta)^2+\mathrm{Re}^3\,\bar{r}^2[G'(\zeta)^2+F'(\zeta)^2]\} \tag{37}$$

where $\beta=\Delta T/T_0$ is the dimensionless temperature difference, $\mathrm{Br}=\mu\Omega^2R^2/k\Delta T$ is the rotational Brinkman number, $\mathrm{Re}=\rho\Omega R^2/\mu$ is the rotational Reynolds number, $\bar{r}=r/R$ is the dimensionless radial coordinate, and $N_G=\dot{S}_G'''/(k\beta^2/R^2)$ is the dimensionless entropy generation rate. The ratio $\Psi=\mathrm{Br}/\beta\mathrm{Re}^2$ is called group parameter, which shows the relative importance of viscous effects on heat transfer irreversibility. The effects of Ψ and Re on the entropy generation rate are clearly seen from Eq. (37).

An increase in Ψ is to increase the entropy generation due to viscous effects. The effect of increasing Reynolds number, which is the ratio between inertial and viscous forces, is to increase the effect of viscous dissipation caused by the velocity components in all directions and the heat transfer irreversibilities caused by heat transfer.

The total local entropy generation in Eq. (37) can be written as the summation of entropy generation due to heat transfer irreversibility (N_H), which is the first term, and the entropy generation due to fluid friction irreversibility (N_F), which is the second term on the right-hand side.

$$N_G=N_H+N_F \tag{38}$$

During the calculations it may be possible to evaluate these terms separately then compare them to see the dominance of one term on the other. Entropy generation due to heat transfer (N_H) contains the entropy generation by heat transfer due to axial conduction from the rotating disk. Entropy generation due to fluid friction includes velocity gradients in axial, radial, and circumferential directions.

Irreversibilities of heat transfer and fluid flow processes are analyzed well due to the understanding of entropy generation mechanisms. The irreversibility distribution ratio (Φ) is a dimensionless parameter in the entropy generation analysis of convective heat transfer problem. This ratio represents the proportion between the entropy generation due to fluid friction and heat transfer that can be expressed in the following form for this problem:

$$\Phi=\frac{N_F}{N_H}=\frac{\Psi\{3\,\mathrm{Re}\,H'(\zeta)^2+\mathrm{Re}^2\,\bar{r}^2[G'(\zeta)^2+F'(\zeta)^2]\}}{\Theta'(\zeta)^2} \tag{39}$$

In the range $0<\Phi<1$, heat transfer irreversibility is dominant and when $\Phi>1$, fluid friction dominates on the entropy generation. When $\Phi=1$, the contributions of heat transfer and fluid friction to entropy generation are equal. It must be noted that contribution of heat transfer entropy generation to overall entropy generation rate is needed in many engineering applications [2]. Another alternative irreversibility distribution parameter is the Bejan number (Be), which is the ratio of entropy generation due to heat transfer to the total entropy generation. This number is given in dimensionless form as follows [2]:

$$\begin{aligned} \mathrm{Be}&=\frac{N_H}{N_G}=\frac{1}{1+\Phi}\\ &=\frac{\Theta'(\zeta)^2}{\Theta'(\zeta)^2+\Psi\{3\,\mathrm{Re}\,H'(\zeta)^2+\mathrm{Re}^2\,\bar{r}^2[G'(\zeta)^2+F'(\zeta)^2]\}} \end{aligned} \tag{40}$$

Bejan number has values in the limits $0<Be<1$ and the specific value of $\mathrm{Be}=1$ corresponds to a condition where the heat transfer irreversibility totally dominates and $\mathrm{Be}=0$ corresponds to the case, where fluid friction effects totally dominate on the entropy generation. For $\mathrm{Be}\leq 0.5$, the irreversibility caused by viscous effects dominates and for $\mathrm{Be}\geqslant 0.5$, the irreversibility caused by heat transfer is dominant. When $\mathrm{Be}=0.5$, the heat transfer and the fluid friction entropy generation rates are equal.

The dimensionless volumetric entropy generation rate, which is an important measure of the total global entropy generation, is defined as follows:

$$N_{G,\mathrm{av}}=\frac{1}{\forall}\int_0^m\int_0^1 2\pi\bar{r}N_G\,d\bar{r}\,d\zeta \tag{41}$$

where $\forall$ is the volume considered. Since the gradients in velocity and thermal fields exponentially decay with increasing ζ, consideration of the complete flow domain results in zero volumetric entropy generation. Therefore, the volumetric entropy generation is calculated inside a sufficiently large finite domain, which considers the boundary layer effects of both velocity and thermal fields. Therefore, the integration in Eq. (41) is obtained in the domain $0\leq\bar{r}\leq 1$ and $0\leq\zeta\leq m$, where m is a sufficiently large

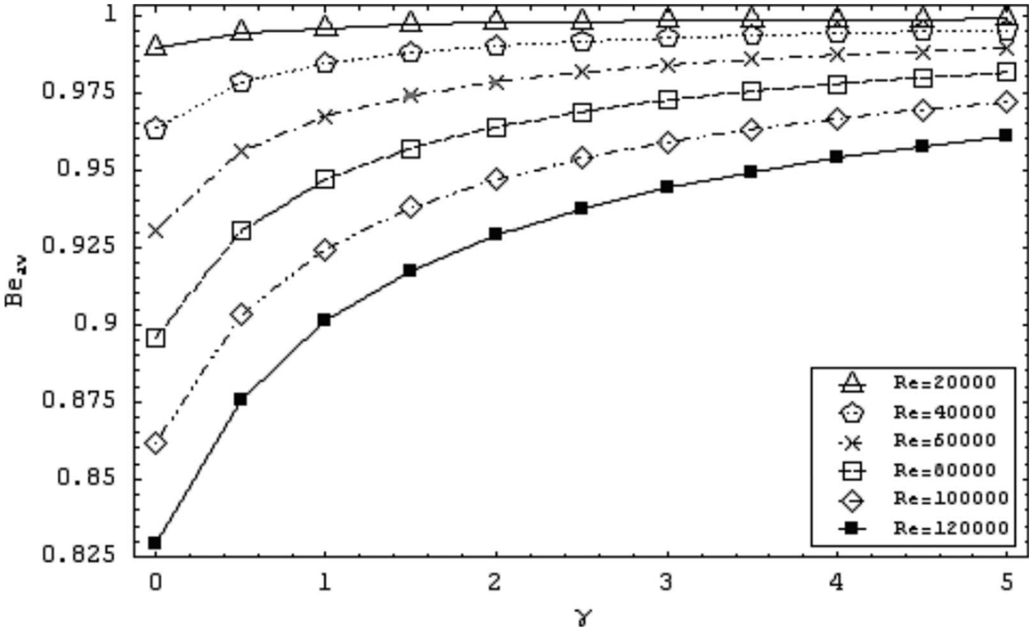

Fig. 1 The change of $\mathrm{Be}_{\mathrm{av}}$ with respect to γ and Re for $\Psi = 10^{-10}$

number. In a similar manner, we introduce the average Bejan number as follows:

$$\mathrm{Be}_{\mathrm{av}} = \frac{1}{\forall}\int_0^m \int_0^1 2\pi\bar{r}\mathrm{Be}\, d\bar{r}\, d\zeta \tag{42}$$

5 Results and Discussion

The change of average entropy generation rate and the average Bejan number with respect to the slip factor, Reynolds number, and group parameter are investigated and depicted in Figs. 1–6.

The average values are considered since they give an idea for the total system performance. Apparently slip factor, e.g., flow over a surface with slip, reduces the loss of mechanical energy. Reducing the entropy generation on the surface leads to the minimization of the entropy generation that maintains the maximum usage of available energy.

Figure 1 shows the effect of the presence of slip on Bejan number for different values of Reynolds number. It is observed that with increasing γ, Be also increases. The axial flow toward the disk that compensates the radial outflow decreases with increasing slip. Therefore the heat transfer with convection decreases and lower temperature gradients are encountered over the disk. As a result, the entropy generation with heat transfer irreversibilities decreases. The effect of slip also reduces the velocities and velocity gradients in all directions, which results in a decrease in viscous contribution to the entropy generation. Since Bejan number increases with increasing slip factor, it is observed

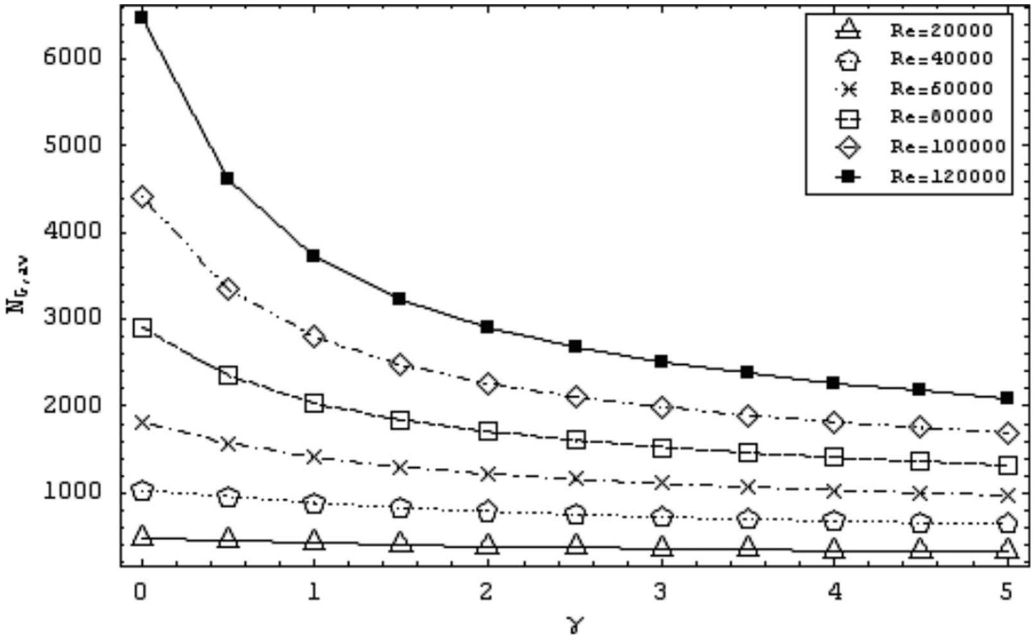

Fig. 2 The change of $N_{G,\mathrm{av}}$ with respect to γ and Re for $\Psi = 10^{-10}$

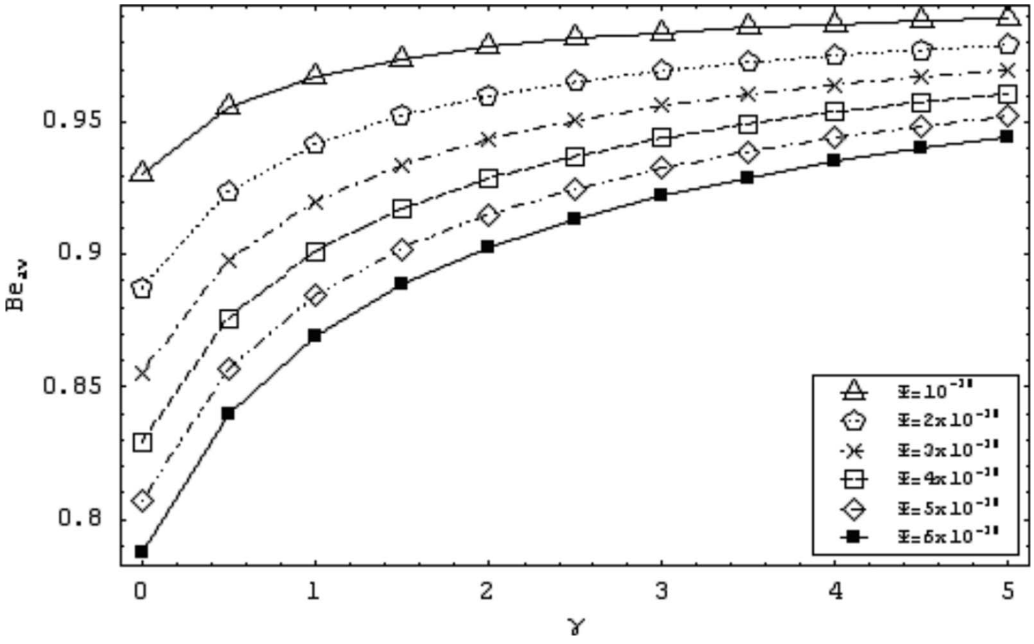

Fig. 3 The change of Be_{av} with respect to γ and Ψ for Re=60,000

that the decrease in heat transfer irreversibility is not as much when compared to the fluid friction irreversibility.

However, the effect of increasing Reynolds number is to decrease the Bejan number. For the constant fluid parameters, Reynolds number increases with increasing radius or the angular velocity of the disk. Any increase in these parameters, i.e., R and Ω, results in higher velocity gradients over the disk surface and the flow field. This increases the viscous contribution to the entropy generation. The irreversibility caused by convective heat transfer mechanism also increases: however, this is not as much as the viscous contribution; therefore the portion of heat transfer irreversibility decreases and, as a result, Bejan number reduces.

Another issue is that Be converges to 1 for increasing γ and decreasing Re. This is quite natural since the effect of fluid friction irreversibility decays and the contribution to the entropy generation from the heat transfer dominates.

One can observe from Fig. 2 that the effect of increasing Re is also to increase the entropy generation due to the intensified fluid friction and heat transfer irreversibilities. The effect of slip factor is to reduce the velocity gradients in radial, circumferential, and axial directions in the entire flow field together with the convective heat transfer. This brings about a reduction in the volumetric entropy generation rate.

The effect of slip on the volumetric Bejan number for different

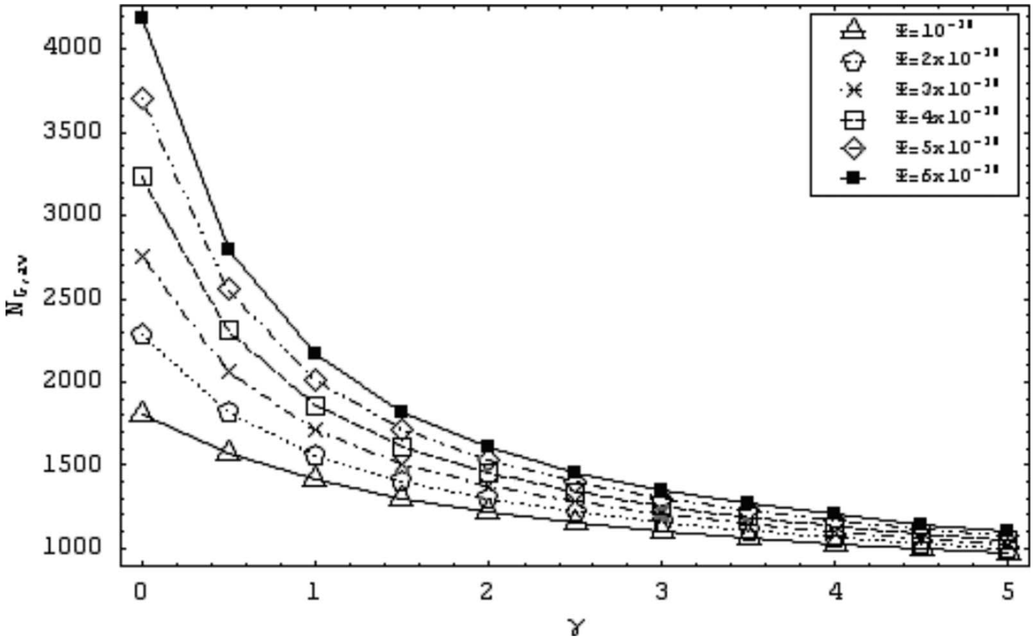

Fig. 4 The change of $N_{G,av}$ with respect to γ and Ψ for Re=60,000

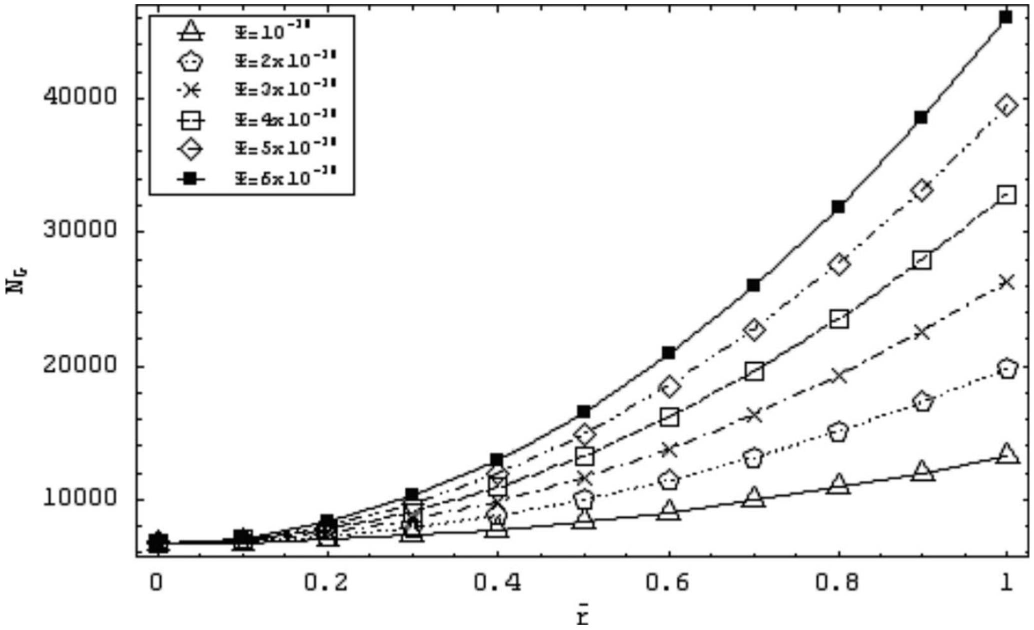

Fig. 5 The change of N_G at $\zeta=0$ with respect to $\bar{r}$ and Ψ for Re=60,000 and $\gamma=0.5$

values of the group parameter (Ψ) is shown in Fig. 3. The effect of increasing Ψ decreases Be due to the increasing viscous effects. Similar to the trend in Fig. 1, as γ approaches to infinity, Be converges to 1 where thermal effects dominate the entropy generation.

Figure 4 summarizes the effect of Ψ on the entropy generation rate. Especially for small values of the slip factor, the increase in Ψ yields a sharp increment on the entropy generation rate. This is a consequence of the fact that the viscous effects are stronger for small values of the slip factor.

Figure 5 shows the variation of total entropy generation with respect to the group parameter at different radial locations on the disk. As a result of higher angular velocities and the velocity gradients, as closer to the outer region of the disk ($\bar{r}=1$), the entropy generation by viscous dissipation increases. Also this effect is intensified for higher values of Ψ. Another issue is that, in the center of the disk ($\bar{r}=0$), the group parameter has no effect on the entropy generation and the effect of Ψ increases with increasing radial coordinate as a result of increasing viscous effects.

From Fig. 6, it can be concluded that the total entropy generation increases with increasing disk radius as an effect of increasing velocity gradients. Also, Re is to increase the entropy generation, especially in the outer region of the disk.

5.1 Performance Parameter. Assuming that there is a temperature difference between the disk and the ambient fluid, the entropy generation is minimum for two cases, which are $\gamma=\infty$ and $\Omega=0$ since the contribution from the viscous dissipation is zero

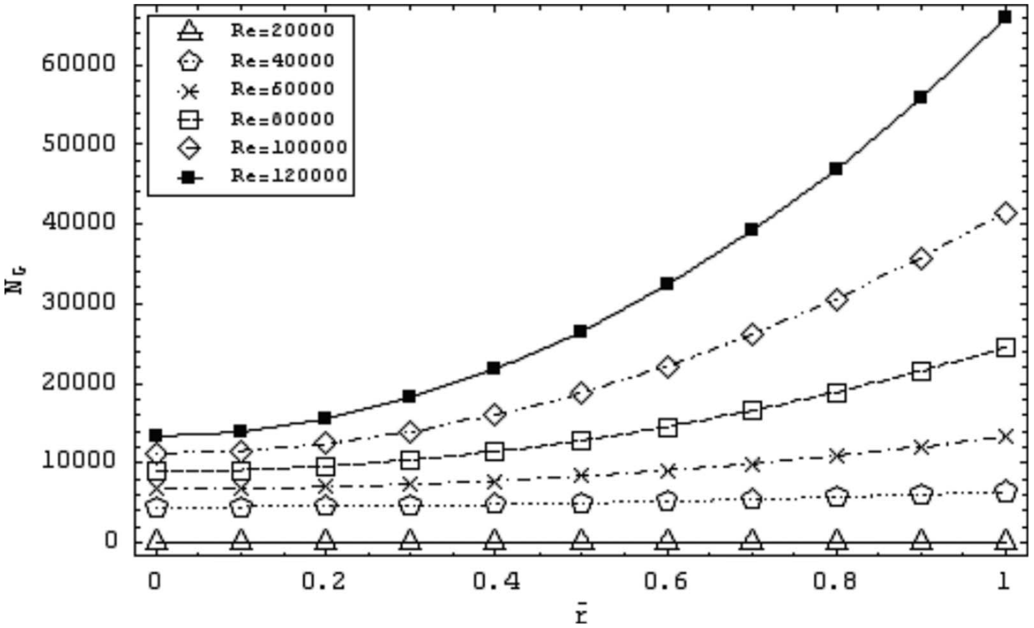

Fig. 6 The change of N_G at $\zeta=0$ with respect to $\bar{r}$ and Re for $\Psi=10^{-10}$ and $\gamma=0.5$

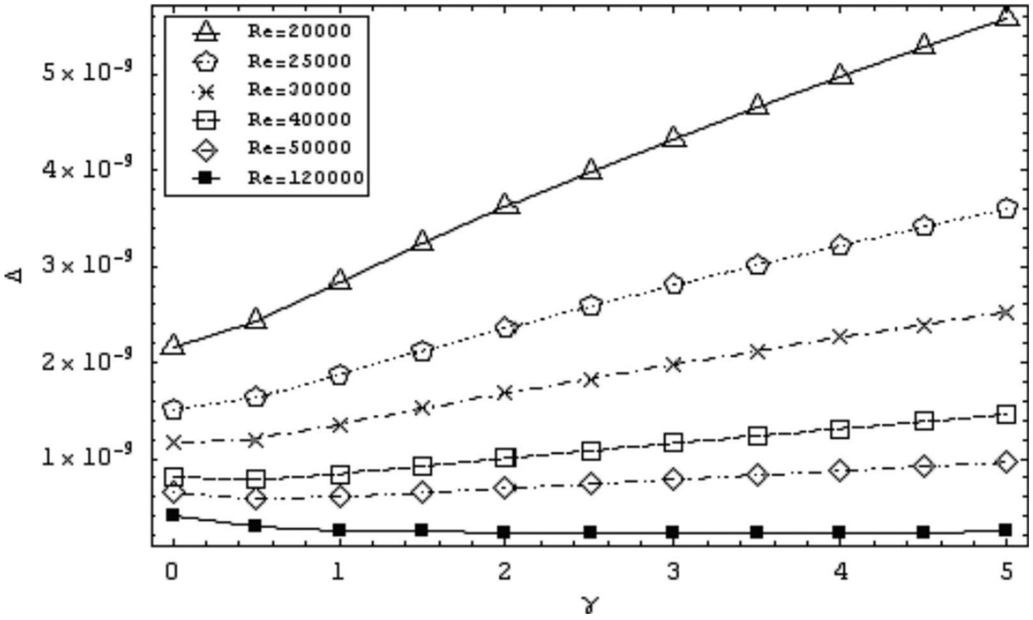

Fig. 7 The change of Δ with respect to γ and Re for $\Psi=5\times10^{-10}$

for these conditions. In both cases, the disk has no capability to rotate the fluid over itself; hence the velocity field and velocity gradients in all directions are zero. Though the disk still produces entropy due to heat conduction, however, no work is done on the fluid. Since there is no work done by the disk, it is not possible to say that the best performance is achieved for $\gamma=\infty$ or $\Omega=0$ even though the minimum entropy is produced at these values.

Therefore a performance parameter (PP) is necessary to be defined in terms of the ratio of entropy generated in the flow domain to the work done on the fluid, namely, the entropy generation per unit work done by the disk. The torque required to maintain steady rotation of the disk is as follows:

$$M=\int_0^R r\tau_{\theta z}2\pi r dr \tag{43}$$

and the power input to the rotating disk can be given by

$$W=\Omega\int_0^R r\tau_{\theta z}2\pi r dr \tag{44}$$

For the present problem, the solution of Eq. (44) with the related parameter gives the following result:

$$W=\frac{\pi}{2}\Omega^2\sqrt{\Omega\rho\mu}R^4G'(0) \tag{45}$$

and by using Eq. (45), the pp can be written in the following form:

$$\Xi=\frac{S_{G,\text{total}}}{W}=\frac{k\beta^2R^2}{\rho G'(0)}\int_0^m\left\{\frac{2}{\text{Re}^2}\Theta'(\zeta)^2+\Psi\left[\frac{6}{\text{Re}}H'(\zeta)^2+F'(\zeta)^2+G'(\zeta)^2\right]\right\}d\zeta \tag{46}$$

The minimum value of this parameter corresponds to the most efficient state of the rotating disk system. The dimensionless pp $\Delta=\Xi/(k\beta^2R^2/\rho)$ can be defined and then Eq. (46) becomes

$$\Delta=\frac{1}{G'(0)}\int_0^m\left\{\frac{2}{\text{Re}^2}\Theta'(\zeta)^2+\Psi\left[\frac{6}{\text{Re}}H'(\zeta)^2+F'(\zeta)^2+G'(\zeta)^2\right]\right\}d\zeta \tag{47}$$

The change of dimensionless pp (Δ) with respect to the slip factor is presented in Figs. 7 and 8 for different values of Reynolds number and different group parameters.

It is observed from Fig. 7 that the dimensionless pp (Δ) decreases with increasing Reynolds number. This means that the rotating disk works with higher performance, i.e., producing less entropy per unit work input, for higher angular velocity or larger radius. The trend with increasing slip factor is that there is a continuous increase for small values of Re, and for the values $\text{Re}\geqslant 40{,}000$ there is a decrease to a global minimum and then a continuous increase is observed.

Figure 8 shows that while the group parameter decreases, the pp also decreases. The change with increasing slip factor for small values of Ψ results in a decrease to a minimum value and then a continuous increase trend is observed. For large values of Ψ, i.e., $\Psi=6\times10^{-10}$, there is a continuous increase. Another issue is that for $\gamma>2$ the change of Δ with increasing slip factor seems to be linear.

6 Conclusion

In this study, the equation of entropy generation for the flow over a rotating free disk for steady and axially symmetrical case in a Newtonian fluid is derived. The already existing semianalytical-numerical solutions for flow and thermal fields, presented in our previous studies [10,11], are utilized. Graphical representations for volumetric values of entropy generation rate and the Bejan number are figured out for different values of the flow parameters. The common fact observed in these figures is that the effects of slip are to reduce the magnitude of entropy generation and to reduce the total energy in the system by reducing velocities and velocity gradients. Some combinations and ranges of Reynolds number, group parameter, and slip factor resulted in a reduction in the relative magnitude of entropy generation, as shown by a smaller magnitude of Δ, while some combinations and ranges of Reynolds number, group parameter, and slip factor resulted in an

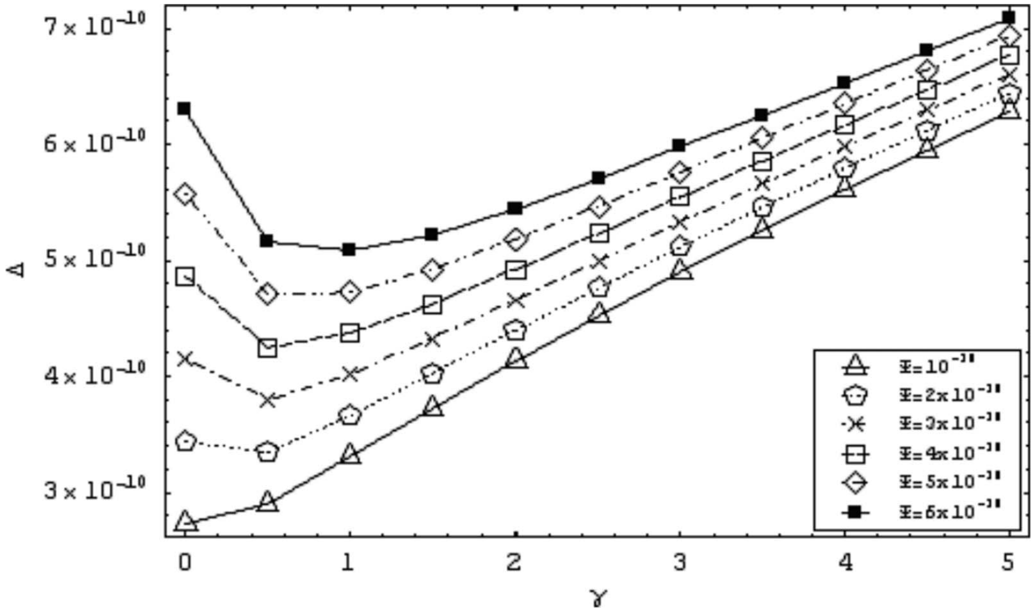

Fig. 8 The change of Δ with respect to γ and Ψ for Re=60,000

increase in the relative magnitude of entropy generation, as shown by a larger magnitude of Δ. Also, for very large values of the slip factor, Bejan number converges to 1.

The essential purpose of this study is to allow the designer to use the second law of thermodynamics in efficiency calculations of rotating fluidic systems, since second law-based calculations for many engineering systems are more reliable than first law-based calculations.

Nomenclature

c = a constant
c_p = specific heat, kJ kg^{-1} K^{-1}
F, f = dimensionless radial velocities
G, g = dimensionless circumferential velocities
H, h = dimensionless axial velocities
$\tilde{F}$ = differential transform of f
$\tilde{G}$ = differential transform of g
$\tilde{H}$ = differential transform of h
k = thermal conductivity, W m^{-1} K^{-1}
M = torque, W s rad^{-1}
N_F = entropy generation due to fluid friction irreversibility
N_G = dimensionless entropy generation rate
N_H = entropy generation due to heat transfer irreversibility
p = pressure, N m^{-2}
P = dimensionless pressure
W = power input, W
Be = Bejan number, N_H/N_G
Kn = Knudsen number, λ/R
Pr = Prandtl number, $\mu c_p/k$
Re = rotational Reynolds number, $\rho\Omega R^2/\mu$
Br = rotational Brinkman number $\mu\Omega^2R^2/k\Delta T$
$\dot{S}'''_G$ = local entropy generation rate, W m^{-3} K^{-1}
R = radius of the disk, m
r = radial coordinate, m
$\bar{r}$ = dimensionless radial coordinate
T = temperature, K
T_0 = temperature on the disk, K
T_∞ = temperature at infinity, K
ΔT = temperature difference, T_0-T_∞
u = radial velocity, m s^{-1}
v = circumferential velocity, m s^{-1}
w = axial velocity, m s^{-1}
z = axial coordinate, m

Greek Symbols

α, χ = dummy variables
β = dimensionless temperature difference, $\Delta T/T_0$
Ξ = performance parameter, K^{-1}
Δ = dimensionless performance parameter
γ = slip factor, $[(2-\eta)\lambda\Omega^{1/2}]/\eta\nu^{1/2}$
ζ = dimensionless axial coordinate, $z\sqrt{\Omega/\nu}$
η = tangential momentum accommodation coefficient
θ = circumferential coordinate, rad
λ = mean free path, m
μ = dynamic viscosity, N m^{-2} s
ξ = stretched dimensionless axial coordinate, $e^{-c\zeta}$
ρ = density, kg m^{-3}
Ω = angular velocity of the rotating disk, rad s^{-1}
Θ = dimensionless temperature
Ψ = group parameter, Br$/\beta$Re^2
$\forall$ = dimensionless volume
Φ = irreversibility distribution ratio, N_F/N_H
τ = shear stress tensor, N m^{-2}

References

[1] Owen, J. M., 1989, *Flow and Heat Transfer in Rotating-Disc Systems*, Research Studies Press, Taunton.
[2] Bejan, A., 1980, "Second Law Analysis in Heat Transfer," Energy, **5**, pp. 721–732.
[3] Ozkol, I., Komurgoz, G., and Arikoglu, A., 2007, "Entropy Generation in the Laminar Natural Convection From a Constant Temperature Vertical Plate in an Infinite Fluid," Proc. Inst. Mech. Eng., Part A, **221**(A5), pp. 609–616.
[4] Baytas, A. C., 1997, "Optimisation in an Inclined Enclosure for Minimum Entropy Generation in Natural Convection," J. Non-Equil. Thermodyn., **22**(2), pp. 145–155.
[5] Ogulata, R. T., Doba, F., and Yilmaz, T., 1997, "Second-Law and Experimental Analysis of a Cross-flow Heat Exchanger," Heat Transfer Eng., **20**(2), pp. 20–27.
[6] Erbay, L. B., Ercan, M. S., Sulus, B., and Yalcin, M. M., 2003, "Entropy Generation During Fluid Flow Between Two Parallel Plates With Moving Bottom Plate," Entropy, **5**(5), pp. 506–518.

[7] Mahmud, S., and Fraser, R. A., 2002, “The Second Law Analysis in Fundamental Convective Heat Transfer Problems,” Int. J. Therm. Sci., **42**(2), pp. 177–186.
[8] Yilbas, B. S., 2001, “Entropy Analysis of Concentric Annuli With Rotating Outer Cylinder,” Exergy Int. J., **1**(1), pp. 60–66.
[9] Abu-Hijleh, B. A. K., and Heilen, W. N., 1999, “Entropy Generation Due to Laminar Natural Convection Over a Heated Rotating Cylinder,” Int. J. Heat Mass Transfer, **42**(22), pp. 4225–4233.
[10] Arikoglu, A., and Ozkol, I., 2005, “Analysis for Slip Flow Over a Single Free Disk With Heat Transfer,” ASME J. Fluids Eng., **127**(3), pp. 624–627.
[11] Arikoglu, A., and Ozkol, I., 2006, “On the MHD and Slip Flow Over a Rotating Disk With Heat Transfer,” Int. J. Numer. Methods Heat Fluid Flow, **16**(2), pp. 172–184.
[12] Arikoglu, A., and Ozkol, I., 2005, “Solution of Boundary Value Problems for Integro-differential Equations by Using Differential Transform Method,” Appl. Math. Comput., **168**(2), pp. 1145–1158.
[13] Arikoglu, A., and Ozkol, I., 2006, “Solution of Difference Equations by Using Differential Transform Method,” Appl. Math. Comput., **174**(2), pp. 1216–1228.
[14] Gad-el-Hak, M., 1999, “The Fluid Mechanics of Microdevices—The Freeman Scholar Lecture,” ASME J. Fluids Eng., **121**(1), pp. 5–33.
[15] Karniadakis, G. E., and Beskok, A., *Micro-Flows: Fundamentals and Simulation*, Springer-Verlag, New York, 2002.
[16] Attia, H. A., 2008, “Rotating Disk Flow and Heat Transfer Through a Porous Medium of a Non-Newtonian Fluid With Suction and Injection,” Commun. Nonlinear Sci. Numer. Simul., **13**(8), pp. 1571–1580.
[17] Benton, E. R., 1966, “On the Flow Due to a Rotating Disc,” J. Fluid Mech., **24** pp. 781–800.

Wall-Modeled Large-Eddy Simulations of Flows With Curvature and Mild Separation

Senthilkumaran Radhakrishnan

Ugo Piomelli[1]

Anthony Keating[2]

University of Maryland,
College Park, MD 20742

The performance of wall-modeled large-eddy simulation (WMLES) based on hybrid models, in which the inner region is modeled by Reynolds-averaged Navier–Stokes (RANS) equation and the outer region is resolved by large-eddy simulation (LES), can make the application of LES attainable at high Reynolds numbers. In previous work by various authors, it was found that in most cases a buffer region exists between the RANS and LES zones, in which the velocity gradient is too high; this leads to an inaccurate prediction of the skin-friction coefficient. Artificially perturbing the RANS/LES interface has been demonstrated to be effective in removing the buffer region. In this work, WMLES has been performed with stochastic forcing at the interface, following the previous work by our group on two nonequilibrium complex flows. From the two flows studied, we conclude that the application of stochastic forcing results in improvements in the prediction of the skin-friction coefficient in the equilibrium regions of these flows, a better agreement with the experiments of the Reynolds stresses in the adverse pressure gradient and the recovery region, and a good agreement of the mean velocity field with experiments in the separation region. Some limitations of this method, especially in terms of CPU requirements, will be discussed. [DOI: 10.1115/1.2969458]

1 Introduction

In large-eddy simulation (LES), the energy carrying large eddies are resolved and the effect of unresolved small scales on the resolved large scales is modeled. This results in considerable savings, in terms of CPU time, compared with direct numerical simulation (DNS). Cost estimates for LES can be found in various references [1–5]. In unbounded flows, the cost of a LES scales with $\mathrm{Re}^{0.6}$ (where the Reynolds number is based on some integral scale of the flow), while the cost of a DNS is proportional to Re^3. In wall-bounded flows, in which the cost of a DNS is proportional to $\mathrm{Re}^{3.6}$, the savings obtained by LES are less significant since its cost scales like $\mathrm{Re}^{2.4}$ if the wall layer is resolved. It is easy to show that this requirement is essentially due to the need to resolve the near-wall eddies since the outer layer has a cost that is only proportional to $\mathrm{Re}^{0.6}$. This high cost requirement makes the application of LES to high Reynolds flows infeasible. The application of LES to wall-bounded flows at high Reynolds numbers is feasible only with the use of wall-layer models, in which the inner layer is not resolved and its effect on the outer layer is modeled. A review of wall-layer models for LES appeared in Refs. [4,5]. Wall-layer models can be broadly divided into three classes. In the first one, the inner layer is bypassed by assuming a velocity profile to relate the outer-layer velocity to the wall stress. Schumann [6], Grötzbach [7], and Piomelli et al. [8] performed simulations using this approach. Recently Templeton et al. [9] and Medic et al. [10] reported improved results with this approach by blending the Reynolds-averaged Navier–Stokes (RANS) eddy viscosity with the subgrid scale (SGS) eddy viscosity in the near wall region. In the second one, the near-wall region is simulated using a simplified set of equations (generally the turbulent boundary layer equations on a finer grid embedded between the first grid point and the wall). In the third, hybrid approaches are used, in which the model changes from a RANS-like model in the inner layer to a SGS one in the outer region. Applications of this methodology are the subject of the present work.

In hybrid RANS/LES models, several strategies can be used to switch between one model and the other, such as changing the length scale in the model from a RANS mixing length to one related to the grid size or using a blending function to merge the SGS and RANS eddy viscosities.

The direct modification of the length scale used the detached eddy simulation (DES) [11] approach and was employed by Nikitin et al. [12] for the simulation of turbulent channel flow at Reynolds numbers (based on the friction velocity $u_\tau=(\tau_w/\rho)^{1/2}$ and the channel half-height) of up to 80,000. The model was able to sustain turbulence, but the logarithmic layer in the LES region was displaced upward, resulting in a 15% underprediction of C_f. Baggett [13] attributed this error (known as "logarithmic law mismatch" (LLM)) to the delayed generation of resolved eddies in the interface region between the RANS and LES zones. Piomelli et al. [14] and Keating and Piomelli [15] found that the addition of stochastic forcing in the interface region accelerated the generation of resolved eddies, leading to more accurate results. Radhakrishnan et al. [16], however, observed that in cases in which mean-flow perturbations (adverse pressure gradients and separation) create more unstable flow conditions, accurate results can be obtained even without stochastic forcing.

Several researchers have used hybrid RANS/LES schemes in which a blending function is used to bridge the RANS and LES zones. Hamba [17,18] performed channel flow simulation using various hybrid RANS/LES models and suggested a method to improve the mean velocity prediction through additional filtering. He observed that the filter width in the RANS region is larger than that in the LES region at the RANS/LES interface. To remove this inconsistency, he defined two wall-normal velocity components at the interface: one based on the LES filter width and the other based on the RANS filter width. The RANS velocity is obtained from the LES one by additional filtering. This method introduces a source term in both continuity and momentum equation and provides forcing at the interface region whose effects are similar to the forcing used in Refs. [14,15].

Temmerman et al. [19] calculated a channel flow and a sepa-

---

[1] Present address: Department of Mechanical and Materials Engineering, Queen's University, Kingston, ON K7L 3N6.

[2] Present address: Exa Corporation, Burlington, MA.

Contributed by the Fluids Engineering Division of ASME for publication in the Journal of Fluids Engineering. Manuscript received January 17, 2008; final manuscript received June 14, 2008; published online September 2, 2008. Assoc. Editor: Paul Durbin.

rated flow in a channel constricted by a curved hill using a hybrid RANS/LES method. In their hybrid method, the eddy viscosity in the RANS region is defined by $C_\mu k_{\text{mod}}^{1/2} l_\mu$, where C_μ is a constant, k_{mod} is the modeled turbulent kinetic energy, and l_μ is the length scale, which is either explicitly prescribed or obtained by solving an additional transport equation. They obtained the constant, C_μ, by equating the RANS eddy viscosity to the LES eddy viscosity at the interface. They were able to remove the shift in the mean velocity when they used the C_μ value obtained instantaneously at every point rather than an averaged value along the homogeneous direction. The use of spatially and temporally varying C_μ also results in the introduction of additional unsteadiness near the RANS/LES interface.

Davidson and Peng [20] calculated channel and separated flows past a hill using a hybrid RANS/LES method based on the k-ω model in the RANS region, and the one-equation subgrid-scale turbulent kinetic energy model of Yoshizawa [21] in the LES region. They also observed the LLM in the channel flow, and obtained better results in the separated flow, which they attributed to the enhanced convective and diffusive transport across the interface in the latter flow. Davidson [22] computed channel flow and flow past an asymmetric plane diffuser using a hybrid RANS/LES method with a one-equation model for turbulent kinetic energy. In their simulation, forcing was provided at the interface by adding a source term to the three momentum equations based on velocity fluctuations taken from a DNS database. With a carefully chosen coefficient for the source term, they were able to remove the LLM in the channel flow. Davidson and Billson [23] explored using forcing from various types of fluctuations: DNS fluctuations, synthetically generated isotropic and nonisotropic fluctuations, and white noise. They conclude that in terms of the complexity and the quality of the flow field predicted, synthetically generated isotropic fluctuations offered the best results.

Travin et al. [24] and Shur et al. [25] followed a different approach: they developed a special blending function for a Spalart–Allmaras (SA)-based wall-modeled LES (WMLES), which decreases the viscosity significantly in the interface region. This makes the flow in the transition region less stable and allows any flow perturbation to be amplified more rapidly. Their calculations show a very good agreement with the data in a variety of flows.

From the works of the authors cited above, it is clear that some sort of forcing is desirable at the RANS/LES interface for an accurate prediction of the mean velocity field in the equilibrium region. In this work, two of the three flows that were studied in Ref. [16] are computed with the addition of the stochastic forcing by Keating and Piomelli [15]. To illustrate the better prediction obtained due to the addition of stochastic forcing, the results from WMLES calculations reported in Ref. [16] are also shown in this paper. In the following section, we will describe the numerical approach and the models used. We will then present the problem formulation and discuss the results for the two flows studied. Finally, we will make some concluding remarks.

2 Methodology

2.1 Mathematical Model and Numerical Techniques for LES. In large-eddy simulations, the velocity field is separated into resolved (large-scale) and subgrid (small-scale) fields, by a spatial filtering operation [26]. The equations of conservation of mass and momentum for the resolved field are

$$\frac{\partial \bar{u}_i}{\partial x_i} = 0 \tag{1}$$

$$\frac{\partial \bar{u}_i}{\partial t} + \frac{\partial(\bar{u}_j \bar{u}_i)}{\partial x_j} = \nu \frac{\partial^2 \bar{u}_i}{\partial x_j \partial x_j} - \frac{\partial \tau_{ij}}{\partial x_j} - \frac{1}{\rho}\frac{\partial \bar{p}}{\partial x_i} + f_i \tag{2}$$

In these equations, $\tau_{ij} = \overline{u_i u_j} - \bar{u}_i \bar{u}_j$ are the SGS stresses and f_i is a stochastic force defined in the next section. The SGS stresses are modeled using an eddy-viscosity approximation,

$$\tau_{ij} - \frac{\delta_{ij}}{3}\tau_{kk} = -2\nu_t \bar{S}_{ij} \tag{3}$$

The governing differential equations (Eqs. (1) and (2)) are discretized on a nonstaggered grid using a curvilinear finite volume code. The method of Rhie and Chow [27] is used to avoid pressure oscillations. Both convective and diffusive fluxes are approximated by second-order central differences. A second-order semi-implicit fractional-step [28] procedure is used for temporal discretization. The Crank–Nicolson scheme is used for the temporal discretization of wall-normal diffusive terms, and the Adams–Bashforth scheme is used for the temporal discretization of all the other terms. Fourier transforms are used to reduce the three-dimensional Poisson equation into a series of two-dimensional Helmholtz equations in wavenumber space, which are then solved iteratively using the biconjugate gradient stabilized (BCGSTAB) method. The code is parallelized using the message-passing interface (MPI) library and the domain-decomposition technique, and it has been extensively tested by Silva Lopes and Palma [29] in isotropic turbulence and by Silva Lopes et al. [30] in an S-shaped duct.

The eddy viscosity, ν_t, is obtained from the SA turbulence model [31]. For the wall-modeled LES equations [12] the length scale in the Spalart–Allmaras model, $\tilde{d}$, is modified so that the model functions in the RANS mode in the near-wall region and in the LES mode in the outer region. The length scale is chosen as the minimum of the RANS and LES length scales,

$$\tilde{d} = \min(y_w, C_{\text{DES}}\Delta) \tag{4}$$

where y_w is the distance from the wall, $C_{\text{DES}}=0.65$, and $\Delta = \max(\Delta x, \Delta y, \Delta z)$. The location where the RANS switches to LES, $y_w = C_{\text{DES}}\Delta$, is denoted here as y_{switch}. More details on the SA model as applied in this problem can be found in Ref. [16].

2.2 Boundary Condition. As boundary conditions, a no-slip condition was enforced at the walls; in the spanwise direction, periodic conditions were applied. At the outlet, the convective condition [32] $\partial \bar{u}_i / \partial t + U_b \partial \bar{u}_i / \partial x = 0$ was used. The above convective boundary condition, which is hyperbolic in nature, is expected to advect all the vortical structures out of the domain without reflecting them. For high Reynolds number flows in complex geometries, disturbance was found to travel upstream from the outlet in previous calculations [30] performed with this code. Following Ref. [30], a buffer layer $10\delta_{\text{ref}}$ long, in which the streamwise grid spacing was slowly stretched, was appended to the physical domain to avoid any upstream propagation of perturbations from the outlet condition into the region of interest. Inlet conditions are the instantaneous flow field taken from a y-z plane of a spatially developing boundary layer simulation in which the Reynolds number is matched to the experimental one. For each of the calculations reported here, an auxiliary spatially developing boundary layer simulation—which had the same domain height, resolution, and turbulence model—was performed. The simulation was performed for ten flow-through times and the statistical sampling was done after six flow-through times so that all the transients can be convected out. The convergence of the results was estimated by comparing the statistics obtained using the two halves of the sample; they did not differ by more than 3%.

2.3 Stochastic Forcing. In hybrid RANS/LES calculations, a region is present in which the flow transitions from a quasisteady RANS near-wall flow to an unsteady LES outer flow. For $y > y_{\text{switch}}$ the eddy viscosity is decreased compared to the RANS value; the resolved stresses are, however, insufficient to maintain the momentum balance since few turbulent eddies exist in the smooth RANS region. Immediately above the nominal interface ($y > y_{\text{switch}}$) then, the modeled stress is larger than the resolved one, despite the fact that the calculation is supposedly in the LES mode (Fig. 1), and most of the stress should be supported by the

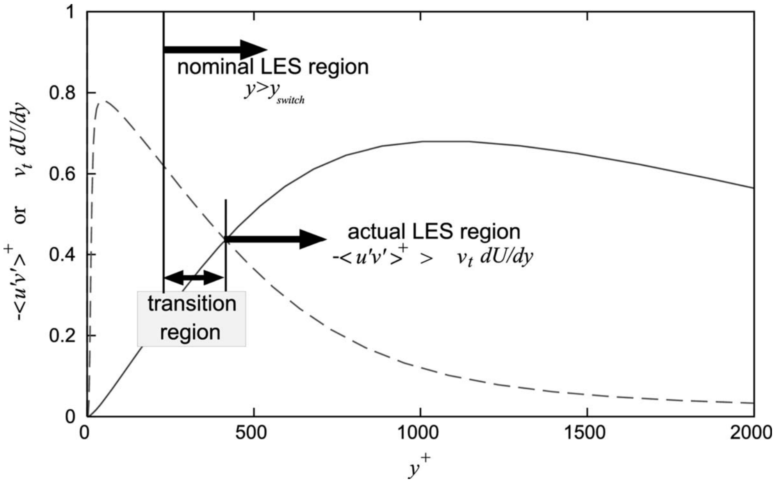

Fig. 1 Resolved (—) and modeled (---) stresses in calculations that use a DES based wall model

resolved eddies.

In this work we use the stochastic forcing method proposed by Keating and Piomelli [15]. This method uses a dynamic control technique, which modulates f_i to amplify the resolved Reynolds shear stress at the nominal interface. The stochastic force f_i is obtained from normally distributed random numbers, whose variance is calculated as explained below (Eq. (6)). Keating and Piomelli [15] defined a transition region (between y_{switch} and the location y_ν of maximum time- and spanwise-averaged ν_t) over which they expect the average resolved and modeled shear stresses to be equal and modulated the stochastic force to achieve this result. The difference between the resolved and modeled Reynolds shear stresses integrated over the transition region is first calculated,

$$\epsilon = \int_{y_{\text{switch}}}^{y_\nu} \left(\nu_t \frac{d\langle \overline{u_s} \rangle}{dy} + \langle u_s' v_n' \rangle \right) dy \tag{5}$$

Here, the angle brackets $\langle \cdot \rangle$ denote time- and spanwise-averaged quantities, while the prime denotes the large-scale part of the fluctuation: $f' = \overline{f} - \langle \overline{f} \rangle$. Also, u_s and v_n denote the streamwise and wall-normal components of the velocity. Then a proportional controller is used to calculate the variance of the force,

$$\sigma_{n+1}(x) = \sigma_n(x) + A\epsilon(x+L) \tag{6}$$

Keating and Piomelli [15] varied the constant, A, in the above controller from 2 to 20 and showed that a higher value of A results in a shorter transient time after which the variance of the force remains almost constant. In this work a value of 10 was chosen for A to reduce the transient time while keeping the calculation stable. Time and spanwise averaging is required in the evaluation of the resolved and modeled shear stress terms in Eq. (5). In spatially developing flows, the stochastic forcing applied at a location affects the error at a downstream location, due to the mean advection. Hence, a streamwise shift L, of the order of the integral length scale, is used in the controller following Ref. [15] (we use $L = \delta_{\text{ref}}$ in this work). The force is enveloped using a top-hat function centered on the location of the maximum turbulent eddy viscosity, whose width is twice the distance between y_ν and y_{switch}. The reader is referred to Ref. [15] for a detailed discussion of the model implementation.

This procedure had to be slightly modified when applied in the complex geometries. In regions of convex curvature, the resolved shear stress decreases, whereas the modeled shear stress increases compared to their equilibrium values. The decrease in the resolved shear stress is consistent with the effects of convex curvature on turbulence. Since the modeled shear stress increases in the convex region, the difference between the two as calculated in Eq. (5) increases, resulting in a need for larger forcing to amplify the resolved shear stress. In the simulations, it was found that the variance of the force (Eq. (6)) increased unboundedly which made the calculation unstable. To make the calculation stable, it was necessary to either restrict the variance of the force to a given value or to turn off the controller and the forcing in this region. As the rms of the force shows a large variation (see Figs. 4 and 10), we chose the second approach to avoid prescribing the maximum value in an ad hoc manner.

3 Flow Past a Contoured Ramp

3.1 Problem Formulation. The performance of the stochastic wall-layer model on flows with separation and recovery is tested on this geometry. Song and Eaton [33] studied this flow experimentally. Figure 2 shows the flow configuration, which consists of a flat-plate followed by a smoothly contoured ramp and another flat-plate region. In the numerical calculations, all the lengths are normalized by the ramp length, $L_R = 70$ mm. The flat-plate section preceding the ramp is $2L_R$ long; the radius of curvature of the ramp is $1.814L_R$ and its height is $0.3L_R$. The computational domain extends $6L_R$ from the trailing edge of the ramp, which is then followed by a buffer zone for the outflow boundary. Similar to the experimental configuration, the computational domain has an upper wall $1.8714L_R$ above the top of the ramp. The boundary layers at the bottom and upper walls do not interact with each other and are separated by a potential core $3\delta_{\text{ref}}$ high at the inlet of the computational domain. The reference location for the simulation is the inlet of the computational domain, the momentum Reynolds number (Re_θ) at the reference location is 13,200, and the boundary layer thickness, δ_{ref}, is 0.38. Velocities are normalized by the freestream velocity at the reference location $x=-2$, $U_{\text{ref}} = 20.3$ m/s. The spanwise width of the computational domain is $3\delta_{\text{ref}}$.

Results from two WMLES calculations with stochastic forcing are reported here. To study the grid independence of the results, simulations were performed with two meshes. The coarse grid had $367 \times 120 \times 36$ nodes in the streamwise, wall-normal, and spanwise directions, respectively. The grid was uniform in the spanwise direction and was stretched in the streamwise and wall-normal directions. In the streamwise direction, the grid was stretched only near the outlet to create a buffer region to avoid upstream propagation of disturbances. There were 12 points per δ_{ref} in the spanwise and streamwise directions (except near the

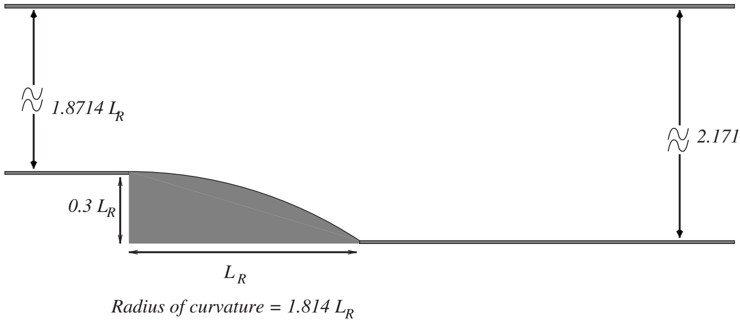

Fig. 2 Flow configuration for the contoured ramp calculation

outflow). In the wall-normal direction, the first point was located at $y^+=1$, and the grid was stretched so that near the boundary layer edge there were 12 points per δ_{ref}, resulting in cubic grid cells in the outer region. The fine mesh calculation had $503 \times 210 \times 54$ nodes in the streamwise, wall-normal, and spanwise directions, respectively, resulting in 18 points per δ_{ref} in the spanwise and streamwise directions.

3.2 Results and Discussion. The flow expansion on the ramp creates an adverse pressure gradient that causes the flow to separate, creating a mild separation region that is then followed by recovery. The accuracy of the predicted flow field in the separation and recovery regions depends critically on the accurate prediction of the separation location. Streamlines in the separation region are shown in Fig. 3 along with the contours of the Reynolds shear stress $\langle u'v' \rangle$. Table 1 shows the predicted separation and reattachment point locations and the error in their prediction. Note that, for consistency with the experiments, the separation and reattachment points were determined from the sign of the velocity at a distance of $(8.6 \times 10^{-4})L_R$ from the wall; in the simulations, this occurs six to seven points away from the wall. Both calculations predict the location of the separation point within 10% of the experimental value and that of the reattachment within 12% of the experimental value (see Table 1).

The amplitude of the stochastic forcing for the fine and coarse mesh calculations is shown in Fig. 4. Note that the oscillations in the forcing amplitude are due to insufficient statistical convergence of the data, which are sampled less frequently than the velocity data. Significant forcing is applied only in the attached boundary layer region ahead of the ramp. Because of the convex curvature of the ramp, forcing is set to zero over the ramp. Although the dynamic controller was active downstream of the ramp, it does not apply stochastic forcing immediately downstream of the ramp as the eddies generated in the separated region resolve most of the Reynolds stress. Only far downstream, where the eddies generated in the separation region have weakened or been dissipated by viscous effects, does forcing become important again.

In Fig. 5 the skin friction and pressure coefficients, defined as

$$C_f = \frac{\tau_w}{\rho U_\infty^2/2}, \quad C_p = \frac{p - p_{\text{ref}}}{\rho U_{\text{ref}}^2/2} \tag{7}$$

where U_∞ is the velocity at the edge of the boundary layer at the current location and p_{ref} is the wall pressure at $x=-1.81$, are shown. The skin-friction coefficient is predicted accurately in both the flat-plate region ahead of the ramp and in the recovery region. Note that the DES based wall model used in Ref. [16] underpredicts the skin-friction coefficient in the flat-plate region ahead of the ramp. The addition of stochastic forcing also results in an improved agreement of the wall-pressure coefficient with the measured one. The fine mesh WMLES calculation with stochastic forcing predicts the height of the bubble particularly accurately.

The mean velocity profile in wall coordinates at the inlet is

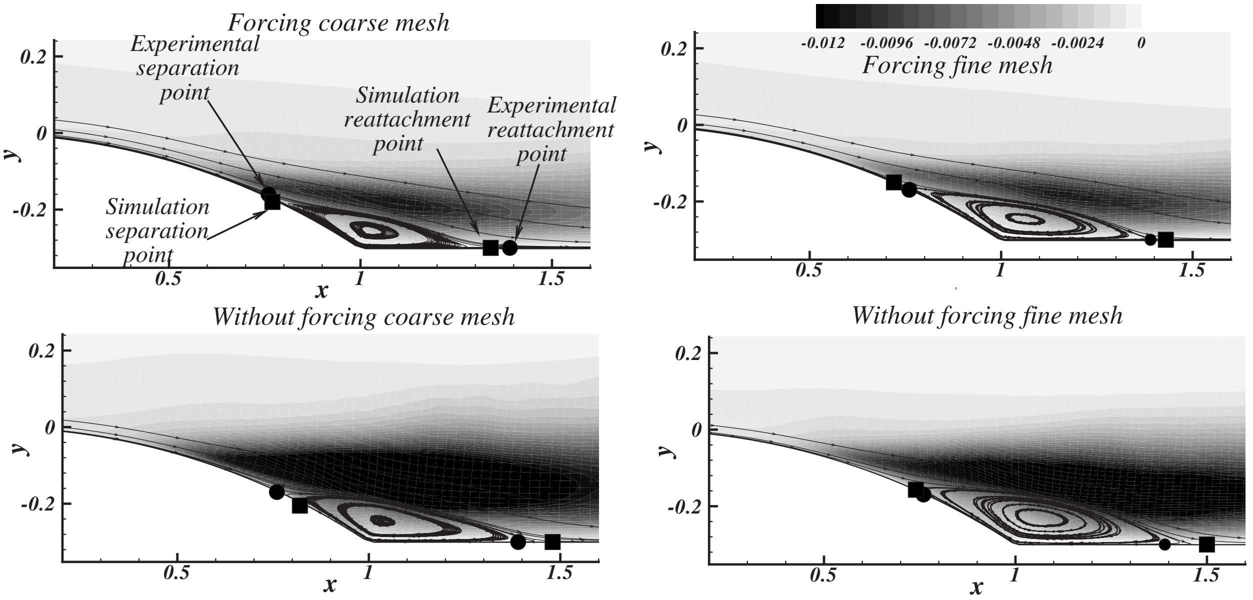

Fig. 3 Mean streamlines and contours of the total Reynolds shear stress ($\langle u'v' \rangle$)

Table 1 Parameters in the simulations of ramp

Case	Resolution	Separation point (% error)	Reattachment point (% error)
Expt.	N/A	0.76	1.39
WMLES with stochastic forcing coarse mesh	$367 \times 120 \times 36$	0.75 (−1.6%)	1.32 (−11.1%)
WMLES with stochastic forcing fine mesh	$503 \times 210 \times 54$	0.7 (−9.5%)	1.41 (3.2%)
WMLES without stochastic forcing coarse mesh	$367 \times 120 \times 36$	0.80 (6.3%)	1.46 (11.1%)
WMLES without stochastic forcing fine mesh	$503 \times 210 \times 54$	0.72 (−6.3%)	1.48 (14.2%)

shown in Fig. 6. The addition of the stochastic forcing has removed the shift observed in the DES based wall model. Figure 7 compares numerical and experimental data at five locations: in the equilibrium region, near separation, in the middle of the separation region, near reattachment, and in the recovery region. The application of the stochastic force improves the prediction of Reynolds shear stress compared to WMLES in Ref. [16], which overpredicts it by as much as 100% in the separation region. The improved prediction is the result of stochastic force breaking up the artificially strong streamwise coherent structures that cause the overprediction of the Reynolds stresses in the separation region.

Two-point correlations for the two calculations that used forcing and also for the two DES based WMLES calculations reported in Ref. [16] are compared to the experimental values. The streamwise two-point correlation is defined as

$$R_{uu,x} = \frac{\overline{u'(x)u'(x_0)}}{\sqrt{\overline{u'^2(x)}}\sqrt{\overline{u'^2(x_0)}}}, \quad R_{vv,x} = \frac{\overline{v'(x)v'(x_0)}}{\sqrt{\overline{v'^2(x)}}\sqrt{\overline{v'^2(x_0)}}} \tag{8}$$

where u' and v' denote the fluctuating velocities and x_0 is the two-point correlation origin. Streamwise two-point correlations at three locations $x_0=1, 1.39$, and 4 are shown in Fig. 8. Correlations at $x_0=4$ are evaluated at a fixed height of 0.5δ, whereas those at $x_0=1$ and 1.39 are evaluated along the mean streamline passing through the respective two-point correlation origin, which is at a height of 0.5δ.

In Fig. 8, one can see that the calculations with the fine mesh predict a smaller length scale than the calculations with the coarse mesh, and the addition of stochastic forcing further reduces the length scale. The length scale of the u' fluctuations are predicted better than the length scale of the v' fluctuations, which is generally overpredicted. Note that in the separation region at $x=1$, a much larger length scale is predicted by the calculation without forcing, which results in stronger eddies and overprediction of the Reynolds stresses.

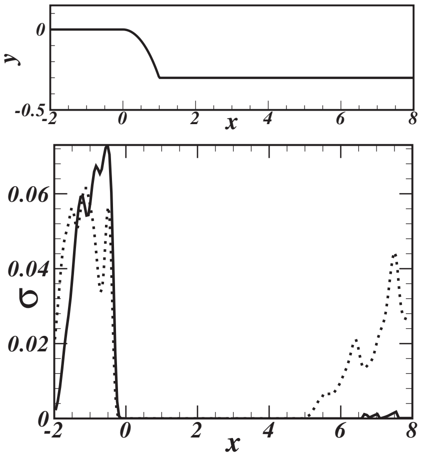

Fig. 4 rms of the stochastic forcing: —, coarse mesh; ------, fine mesh

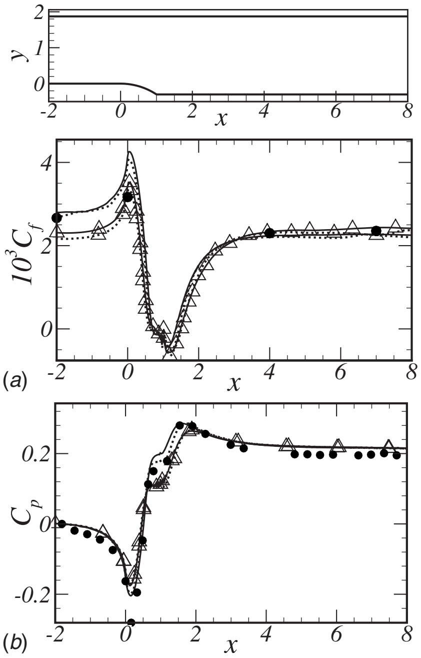

Fig. 5 Profiles of the (*a*) skin-friction coefficient and (*b*) pressure coefficient —. WMLES with stochastic forcing, coarse mesh; ------, WMLES with stochastic forcing, fine mesh; –△–, WMLES without stochastic forcing, coarse mesh; ---△---, WMLES without stochastic forcing, fine mesh; ●, experiments.

4 Flow Past a Two-Dimensional Bump

4.1 Problem Formulation. The performance of the WMLES with stochastic forcing in the presence of curvature and pressure gradient effects is tested on the flow past a two-dimensional bump. The bump geometry (shown in Fig. 9) is formed by tangentially connecting two short concave arcs to a longer convex arc. Simulation results are compared to the experimental results of

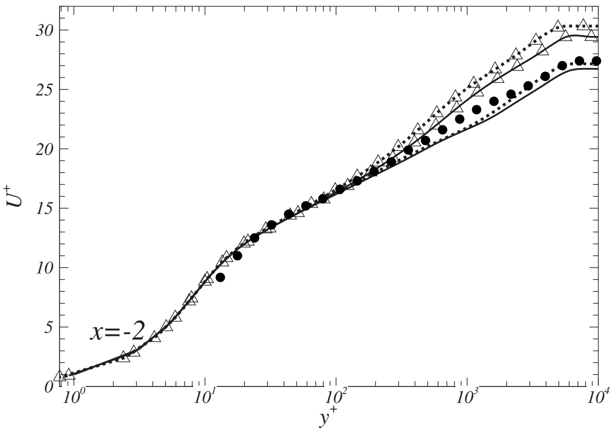

Fig. 6 Mean velocity profile in wall coordinates. —, WMLES with stochastic forcing, coarse mesh; ------, WMLES with stochastic forcing, fine mesh; –△–, WMLES without stochastic forcing, coarse mesh; ---△---, WMLES without stochastic forcing, fine mesh; ●, experiments.

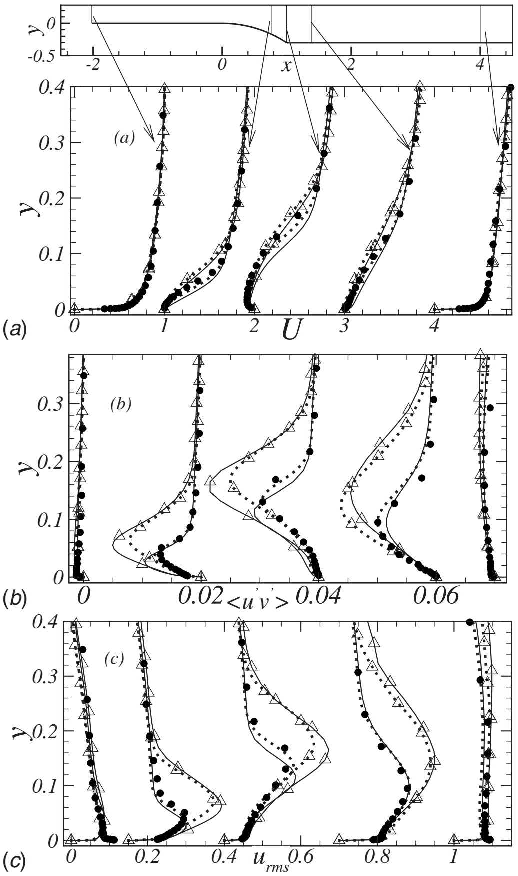

Fig. 7 Profiles of the (*a*) mean horizontal velocity, (*b*) total (resolved + modeled) Reynolds shear stress, and (*c*) rms of horizontal velocity fluctuations. —, WMLES with stochastic forcing, coarse mesh; ------, WMLES with stochastic forcing, fine mesh; –△–, WMLES without stochastic forcing, coarse mesh; ---△---, WMLES without stochastic forcing, fine mesh; ●, experiments.

DeGraaff [34]. Webster et al. [35] also studied this flow experimentally at a lower Reynolds number than the one studied here, and Wu and Squires [36] performed LES of this flow at the same low Reynolds number. The inlet of the simulation domain, which is also the reference location, is located one-half chord length upstream of the leading edge of the bump. The momentum Reynolds number Re_θ at the inlet is 12,170. In the simulation, all lengths are nondimensionalized by the chord length ($L_c = 305$ mm) of the bump. At the inlet, the boundary layer thickness is $\delta_{\mathrm{ref}}=0.09718L_c$, and the top wall is located $0.498L_c$ above the bottom wall. The two boundary layers at the top and bottom walls are separated by a potential core whose height is $2\delta_{\mathrm{ref}}$. The maximum height of the bump is $0.0659L_c$, and the boundary layer thickness at the inlet is 1.5 times larger than the maximum height of the bump. The simulation domain is $3\delta_{\mathrm{ref}}$ wide in the spanwise direction, and it extends two chord lengths downstream of the trailing edge and then by a buffer region for the outflow. The grid used in the simulation has $538\times150\times36$ nodes in the streamwise, wall-normal, and spanwise directions, respectively. In the spanwise direction, the grid spacing was uniform and it was stretched in the streamwise and wall-normal directions. There were approximately 12 points per δ_{ref} in the spanwise and streamwise directions (except near the outflow). In the wall-normal direction, the first point was located at $y^+=1$, and the grid was stretched so that near the boundary layer edge there were 12 points per δ_{ref}, resulting in cubic grid cells in the outer region. These resolutions are comparable to the coarse grid discussed in the previous section, which gave acceptable results.

4.2 Results and Discussion. The amplitude of the stochastic forcing used in the WMLES calculation is shown in Fig. 10. Note that forcing is set to zero in the convex region of the bump. In the first concave region, forcing becomes inactive naturally due to the resolved stresses being larger than the modeled stress in the interface region. Similar to the ramp problem, the adverse pressure gradient in the second half of the bump causes the resolved eddies to become energetic, so that the forcing becomes inactive for a short distance downstream of the trailing edge.

Figure 11 shows the skin-friction and pressure coefficients, which are defined in Eq. (7). In this case, U_∞ is the velocity at the edge of the boundary layer at the current location, p_{ref} is the wall pressure at $x=1.667$, and U_{ref} is the velocity at the edge of the boundary layer at $x=1.667$. In the experiments, both the wall-pressure and the skin-friction coefficients were measured in a lower Reynolds number case, with $\mathrm{Re}_\theta=3120$ at the reference section. DeGraaff [34] estimated the wall shear-stress for a high Reynolds number case by assuming that the ratio of skin friction at any position to the skin friction at the reference position is independent of the Reynolds number, and at the reference location, he estimated the skin friction by a logarithmic law fit.

The WMLES underpredicts the skin friction in the upstream flat-plate region but shows a reasonable agreement everywhere. With the addition of stochastic forcing, the prediction of the skin

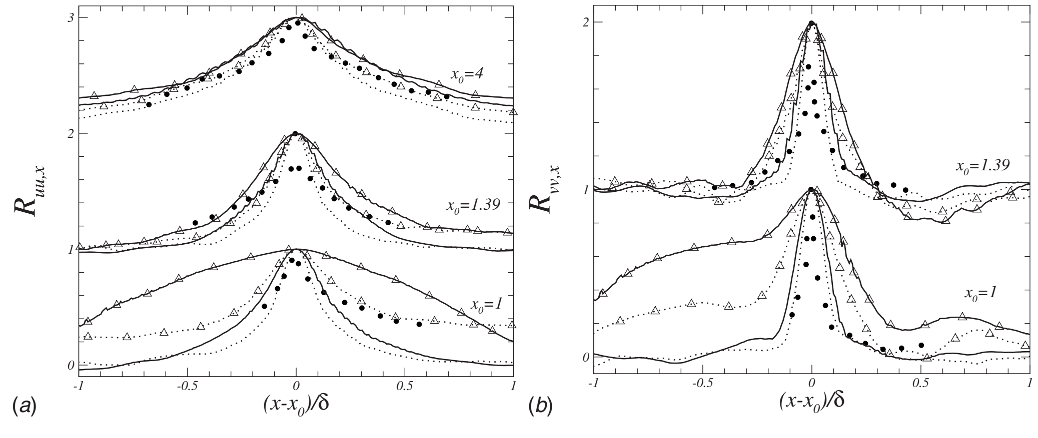

Fig. 8 Profiles of the (*a*) streamwise two-point correlation of *u*′ fluctuations and (*b*) streamwise two-point correlation of *v*′ fluctuations. —, WMLES with stochastic forcing, coarse mesh; ------, WMLES with stochastic forcing, fine mesh; –△–, WMLES without stochastic forcing, coarse mesh; ---△--- WMLES without stochastic forcing, fine mesh; ●, experiments.

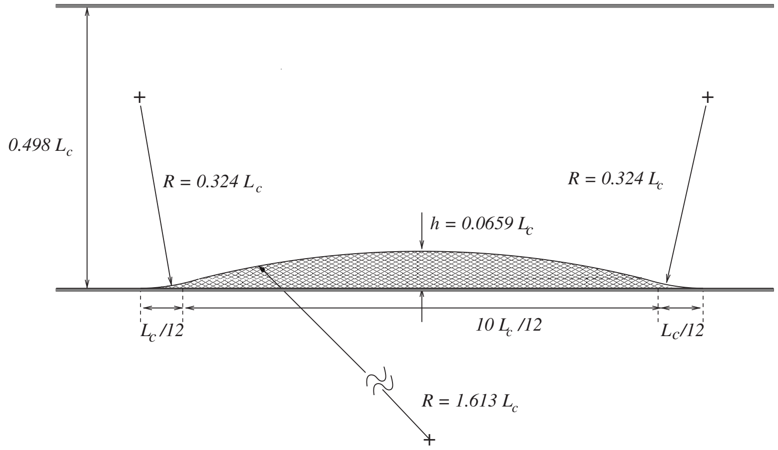

Fig. 9 Flow configuration for the two-dimensional bump calculation

friction is improved in the upstream flat-plate region. In the downstream region, which is dominated by nonequilibrium effects, we see a good agreement with the experimental values for both cases.

Figure 12 shows the mean horizontal velocity normalized by the local freestream velocity at select locations. The flow decelerates near the leading edge due to the concave streamline curvature effect and then accelerates until it reaches the summit of the bump due to constriction in the geometry. Beyond the summit of the bump, the flow decelerates due to the adverse pressure gradient caused by expansion. Near the trailing edge, the flow experiences a favorable pressure gradient due to the concave curvature, and downstream of the trailing edge, it returns to equilibrium. The predicted mean velocity shows a good agreement with the experimental values at all locations.

Figure 13 shows the rms of the fluctuations of the x-component of the velocity at select locations, which decreases in the first half of the bump due to the favorable pressure gradient and also due to the convex curvature. Beyond the summit of the bump, it increases due to the adverse pressure gradient. After the trailing edge, it decays to the zero-pressure gradient value. The WMLES with no forcing overpredicts the rms of the fluctuations by as much as 40% in the recovery region; the addition of stochastic forcing results in a better agreement with the experimental values.

5 Conclusions

WMLES with stochastic forcing have been performed on two flows. Significant computational savings have been achieved by modeling the inner layer compared to cases in which the wall layer is resolved. For the contoured ramp problem, a wall-resolved LES calculation (with $\Delta x^+ = 50$, $\Delta z^+ = 25$, and $y = \delta_{\text{ref}}/18$ at the boundary layer edge) would have required $3676 \times 210 \times 696$ points. With the DES based wall model, this calculation has been carried out with 1% of the grid nodes. Similar savings were achieved for the two-dimensional bump problem.

In the two flows studied, the addition of stochastic forcing results in the removal of the shift in the log law and the accurate prediction of the skin-friction coefficient in the equilibrium region. For the contoured ramp flow, the overprediction of the Reynolds stresses in the separation and recovery regions in WMLES with no forcing is caused by the artificially strong streamwise coherent motion in the attached boundary layer region. The addi-

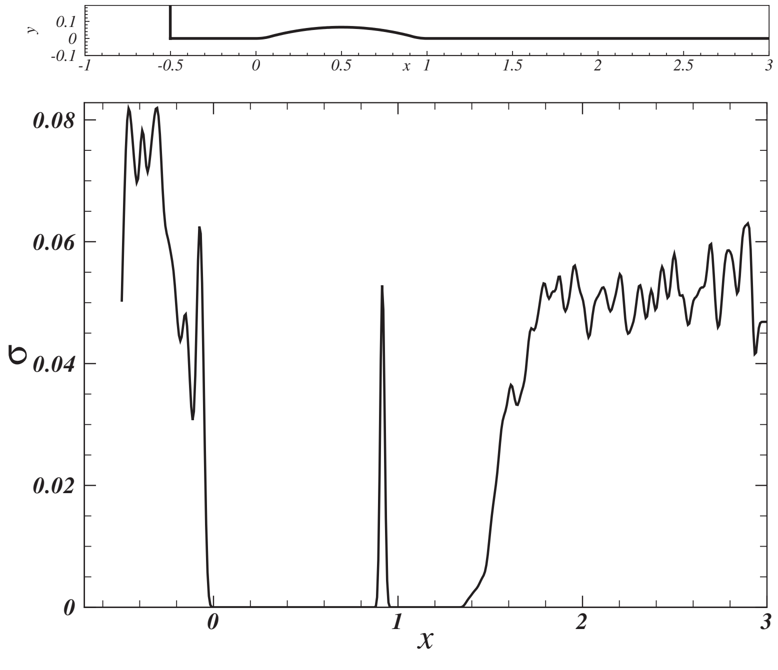

Fig. 10 rms of the stochastic forcing

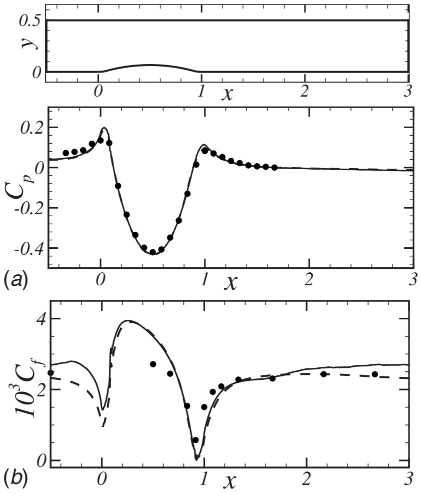

Fig. 11 Profiles of the (*a*) pressure coefficient and (*b*) skin-friction coefficient. —, WMLES with stochastic forcing; ---, WMLES without stochastic forcing; ●, experiments.

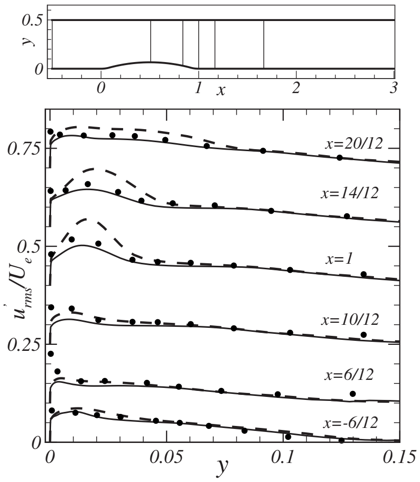

Fig. 13 Streamwise velocity rms fluctuations. —, WMLES with stochastic forcing; ---, WMLES without stochastic forcing; ●, experiments.

tion of stochastic forcing breaks up this coherent structures and results in a better agreement of the predicted Reynolds stresses. The predicted mean velocity in the separation region is also in good agreement with experimental values. For the two-dimensional bump problem, the errors in the prediction of the Reynolds stress with WMLES have been removed with the addition of stochastic forcing.

The WMLES with stochastic forcing has been applied to two flows that exhibit a mix of complex physics, typically encountered in engineering flows, such as concave and convex curvature effects and favorable and adverse pressure gradients. In both the flows, the addition of stochastic forcing has improved the prediction of the flow field, which implies that the application of some sort of stochastic forcing may be beneficial for an accurate prediction. Overall, it has shown a good prediction of the skin-friction coefficient, mean velocity, and Reynolds stresses on these complex flows. With the cost savings achieved in this methodology, WMLES with stochastic forcing can be a viable tool for studying engineering flows and a better alternative to RANS whose accuracy depends on the flow configuration.

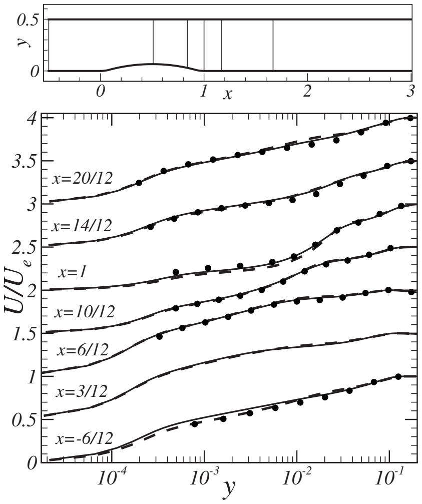

Fig. 12 Mean horizontal velocity profile. —, WMLES with stochastic forcing; ---, WMLES without stochastic forcing; ●, experiments.

Despite the positive results obtained with this method, two issues limit its general application and require further study. The first issue is related to higher CPU time needed compared to calculations in which no forcing is applied. The controller needs the values of the modeled and resolved Reynolds shear stresses (see Eq. (5)), and a reasonably converged value of these quantities can be obtained only after temporal averaging for at least one quarter of a large-eddy turnover time. The amplitude of the forcing is set to zero initially and the controller takes about 35–40 updates (using Eq. (6)) before the forcing value stabilizes. This requires running the code for ten large-eddy turnover times just to get the forcing value, and it doubles the CPU time needed for the calculation with forcing compared to the calculation without forcing. In problems with mean-flow unsteadiness (oscillating or pulsating flows, for instance) in which the time averages are replaced by phase averages, the increase in computational time may make this method impractical. Another issue that requires further study is the application of stochastic forcing to cases with a strong favorable pressure gradient or a strong convex curvature. In these cases, the flow tends to relaminarize, and the application of forcing may become unstable. In the present study, we forced the forcing magnitude to be zero where it was unstable. However, a more general methodology is required to make this method more robust, and efforts in this direction are underway.

Acknowledgment

Support for this work was provided by the Office of Naval Research under Grant No. N00014-03-1-0491 monitored by Dr. R. D. Joslin. The authors are grateful to Dr. Alexandre Silva Lopes for providing the finite volume code used in this work.

References

[1] Chapman, D. R., 1979, “Computational Aerodynamics Development and Outlook,” AIAA J., **17**, pp. 1293–1313.
[2] Reynolds, W. C., 1990, “The Potential and Limitations of Direct and Large Eddy Simulations,” *Whither Turbulence? Turbulence at the Crossroads*, Lecture Notes in Physics Vol. 357, J. L. Lumley, ed., Springer-Verlag, Berlin, pp. 313–343.
[3] Spalart, P. R., 2000, “Strategies for Turbulence Modelling and Simulations,” Int. J. Heat Fluid Flow, **21**, pp. 252–263.
[4] Piomelli, U., and Balaras, E., 2002, “Wall-Layer Models for Large-Eddy Simulations,” Annu. Rev. Fluid Mech., **34**, pp. 349–374.
[5] Piomelli, U., 2008, “Wall-Layer Models for LES,” AIAA Paper No. 2008-0603.
[6] Schumann, U., 1975, “Subgrid-Scale Model for Finite Difference Simulation of Turbulent Flows in Plane Channels and Annuli,” J. Comput. Phys., **18**, pp. 376–404.
[7] Grötzbach, G., 1987, “Direct Numerical and Large Eddy Simulations of Tur-

bulent Channel Flows," *Encyclopedia of Fluid Mechanics*, Vol. 6, N. P. Chereminisoff, ed., Gulf, West Orange, NJ, pp. 1337–1391.

[8] Piomelli, U., Ferziger, J. H., Moin, P., and Kim, J., 1989, "New Approximate Boundary Conditions for Large Eddy Simulations of Wall-Bounded Flows," Phys. Fluids A, **1**, pp. 1061–1068.

[9] Templeton, J. A., Medic, G., and Kalitzin, G., 2005, "An Eddy-Viscosity Based Near-Wall Treatment for Coarse Grid Large-Eddy Simulation," Phys. Fluids, **17**(10), p. 105101.

[10] Medic, G., Templeton, J., and Kalitzin, G., 2006, "A Formulation for Near-Wall RANS/LES Coupling," Int. J. Eng. Sci., **44**(17), pp. 1099–1112.

[11] Spalart, P. R., Jou, W. H., Strelets, M. K., and Allmaras, S. R., 1997, "Comments on the Feasibility of LES for Wings, and on a Hybrid RANS/LES Approach," *Advances in DNS/LES*, C. Liu and Z. Liu, eds., Greyden, Columbus, OH, pp. 137–148.

[12] Nikitin, N. V., Nicoud, F., Wasistho, B., Squires, K. D., and Spalart, P. R., 2000, "An Approach to Wall Modeling in Large-Eddy Simulations," Phys. Fluids, **12**, pp. 1629–1632.

[13] Baggett, J. S., 1998, "On the Feasibility of Merging, LES With RANS in the Near-Wall Region of Attached Turbulent Flows," *Annual Research Briefs-1998*, Center for Turbulence Research, Stanford University, Stanford, CA, pp. 267–277.

[14] Piomelli, U., Balaras, E., Pasinato, H., Squires, K. D., and Spalart, P. R., 2003, "The Inner-Outer Layer Interface in Large-Eddy Simulations With Wall-Layer Models," Int. J. Heat Fluid Flow, **24**, pp. 538–550.

[15] Keating, A., and Piomelli, U., 2006, "A Dynamic Stochastic Forcing Method as a Wall-Layer Model for Large-Eddy Simulation," J. Turbul., **7**(12), pp. 1–24.

[16] Radhakrishnan, S., Piomelli, U., Keating, A., and Silva Lopes, A., 2006, "Reynolds-Averaged and Large-Eddy Simulations of Turbulent Non-Equilibrium Flows," J. Turbul., **7**(63), pp. 1–30.

[17] Hamba, F., 2003, "A Hybrid RANS/LES Simulation of Turbulent Channel Flow," Theor. Comput. Fluid Dyn., **16**, pp. 387–403.

[18] Hamba, F., 2006, "A Hybrid RANS/LES Simulation of High-Reynolds-Number Channel Flow Using Additional Filtering at the Interface," Theor. Comput. Fluid Dyn., **20**, pp. 89–101.

[19] Temmerman, L., Hadziabdic, M., Leschziner, M. A., and Hanjalic, K., 2005, "A Hybrid Two-Layer URANS-LES Approach for Large Eddy Simulation at High Reynolds Numbers," Int. J. Heat Fluid Flow, **26**, pp. 173–190.

[20] Davidson, L., and Peng, S., 2003, "Hybrid LES-RANS Modelling: A One Equation SGS Model Combined With a k-ω Model for Predicting Recirculating Flows," Int. J. Numer. Methods Fluids, **43**, pp. 1003–1018.

[21] Yoshizawa, A., 1993, "Bridging Between Eddy-Viscosity-Type and Second-Order Turbulence Models Through a Two-Scale Turbulence Theory," Phys. Rev. E, **48**(1), pp. 273–281.

[22] Davidson, L., 2005, "Hybrid LES-RANS: Inlet Boundary Conditions," *Third National Conference on Computational Mechanics—MekIT'05*, B. Skallerud and H. Andersson, eds., Trondheim, Norway, May 11–12, pp. 7–22.

[23] Davidson, L., and Billson, M., 2006, "Hybrid LES-RANS Using Synthesized Turbulent Fluctuations for Forcing in the Interface Region," Int. J. Heat Fluid Flow, **27**(6), pp. 1028–1042.

[24] Travin, A. K., Shur, M., Spalart, P., and Strelets, M. K., 2006, "Improvement of Delayed Detached-Eddy Simulation for LES With Wall Modelling," *European Conference on Computational Fluid Dynamics ECCOMAS CFD 2006*, TU Delft, P. Wesseling, E. Oñate, and J. Pèriaux, eds., Egmond aan Zee, The Netherlands, pp. 410–432.

[25] Shur, M. L., Spalart, P. R., Strelets, M. K., and Travin, A. K., 2008, "A Hybrid RANS/LES Model With Delayed DES and Wall-Modeled LES Capabilities," Int. J. Heat Fluid Flow, accepted for publication.

[26] Leonard, A., 1974, "Energy Cascade in Large-Eddy Simulations of Turbulent Fluid Flows," Adv. Geophys., **18A**, pp. 237–248.

[27] Rhie, C., and Chow, W., 1983, "Numerical Study of the Turbulent Flow Past an Airfoil With Trailing Edge Separation," AIAA J., **21**, pp. 1525–1532.

[28] Kim, J., and Moin, P., 1985, "Application of a Fractional Step Method to Incompressible Navier-Stokes Equations," J. Comput. Phys., **59**, pp. 308–323.

[29] Silva Lopes, A., and Palma, J. M. L. M., 2002, "Simulations of Isotropic Turbulence Using a Non-Orthogonal Grid System," J. Comput. Phys., **175**(2), pp. 713–738.

[30] Silva Lopes, A., Piomelli, U., and Palma, J. M. L. M., 2006, "Large-Eddy Simulation of the Flow in an S-Duct," J. Turbul., **7**(11), pp. 1–24.

[31] Spalart, P., and Allmaras, S., 1994, "A One-Equation Turbulence Model for Aerodynamic Flows," Rech. Aerosp., **1**, pp. 5–21.

[32] Orlanski, I., 1976, "A Simple Boundary Condition for Unbounded Hyperbolic Flows," J. Comput. Phys., **21**, pp. 251–269.

[33] Song, S., and Eaton, J. K., 2004, "Reynolds Number Effects on a Turbulent Boundary Layer With Separation, Reattachment, and Recovery," Exp. Fluids, **36**, pp. 246–258.

[34] DeGraaff, D. B., 1999, "Reynolds Number Scaling of the Turbulent Boundary Layer on a Flat Plate and on a Swept and Unswept Bumps," Ph.D. thesis, Stanford University.

[35] Webster, D., DeGraaff, D. B., and Eaton, J. K., 1996, "Turbulence Characteristics of a Boundary Layer Over a Two-Dimensional Bump," J. Fluid Mech., **320**, pp. 53–69.

[36] Wu, X., and Squires, K. D., 1998, "Prediction of the Three-Dimensional Turbulent Boundary Layer Over a Swept Bump," AIAA J., **36**(4), pp. 505–514.

W. Sheng
Research Assistant
e-mail: wsheng@aero.gla.ac.uk

R. A. McD. Galbraith
Professor
e-mail: r.a.m.galbraith@aero.gla.ac.uk

F. N. Coton
Professor
e-mail: f.coton@aero.gla.ac.uk

Department of Aerospace Engineering,
University of Glasgow,
Glasgow G12 8QQ, UK

Prediction of Dynamic Stall Onset for Oscillatory Low-Speed Airfoils

This research presents some common features of oscillatory airfoils, and the method for indicating dynamic stall onset for the unsteady process. Under deep stall conditions, the stall-onset angle in oscillation is independent of the mean angle of the oscillatory motion, and by combining the reduced frequency and the amplitude of the oscillatory motion, the equivalent reduced pitch rate is an analog of this motion to the constant reduced pitch rate of the ramp-up motion. By correlating with the measured data, and with the ramp-up results, the equivalent reduced pitch rate can be defined as a representation for the oscillatory motion. Accordingly, the triple-parameter problem of an oscillation (mean angle, reduced frequency, and amplitude) degrades into the single-parameter problem (equivalent reduced pitch rate). Based on these foundations, an extension of the stall-onset criterion is then made for oscillatory airfoils: a method of extracting the stall-onset parameters directly from oscillatory test data, and an indication of stall onset for the oscillatory airfoils. The results from the new proposed method have shown the consistency with the data of Glasgow University and the public data.

[DOI: 10.1115/1.2969450]

1 Introduction

Dynamic stall usually occurs on an airfoil or on a lifting surface when it is subjected to pitching, plunging, or vertical motion, or other type of unsteady motion inducing a time-dependent angle of attack (AOA)/equivalent AOA. The discussion and reviews on this phenomenon have been well documented [1–6]. Traditionally, different approaches, such as experimentations [7–15], numerical simulations [16,17], and semi-empirical methods [18–27], have been widely employed to investigate this complicated phenomenon. Regardless of the complicated process, experimental and numerical results have shown that the pronounced features in the dynamic-stall process are the delay of stalling and a subsequently concentrated vortex shedding over an airfoil chord. The former is caused by the dynamically induced camber effect and thus delays the trailing-edge separation under the dynamic condition. The latter induces a pressure wave over the airfoil upper surface. As a result, a much larger normal force and a large nose-down pitching moment may be produced. Figure 1 shows the typical measured unsteady normal force and pitching moment including dynamic stall in low Mach numbers. For comparison, the measured normal force and pitching moment in the static case are also plotted. In detail, the unsteady aerodynamic process including dynamic stall comprises the following important events in a closed hysteresis loop (see Fig. 1).

(1) When an airfoil is pitched up from a small angle of attack, the flow remains fully attached to the upper surface of the airfoil until the static stall angle, α_{ss}, is exceeded, sometimes significantly. Accordingly, a pronounced larger normal force (overshoot) may be attained.
(2) Further pitching-up the airfoil, a concentrated vortex is initiated at the leading-edge region. The vortex then separates from the leading-edge region and convects downstream over the airfoil chord. This process results in a further increase in normal force (an additional overshoot) as well as a large nose-down pitching moment.
(3) After the vortex sheds into the wake, a fully separated flow is attained on the upper surface and the normal force collapses.
(4) After the angle of attack reaches its maximum value, the airfoil is then pitched down. The separated flow remains on the upper surface of the airfoil ("bluff body effect," Niven et al. [13]) until the onset of flow reattachment process. The reattachment starts from the leading-edge region and moves toward the trailing edge until $\alpha_{\min}$ is reached (see Fig. 1). This phenomenon is also identified as "undershoot" by Ericsson [28], analogous to "overshoot" during the upstroke motion of airfoils. The separated flow over the upper surface is gradually convected into the wake. Dependent on the pitch-down speed, the re-establishment of a fully attached boundary layer may begin, but is more likely to follow this process.
(5) After this the re-attachment process develops quickly and flow finally returns to the fully attached state.

The dynamic-stall phenomenon, however, could be considered a "problem" or a "solution," depending on the circumstances under which it appears. It could be a problem because the large nose-down pitching moment excursions after stall onset that limit the flight envelope. It could be a solution because the dynamically induced larger lift may be used for improvement and enhancement of aircraft maneuverability [4] or because the dynamically induced large drag regulates the maximum power output at high winds for stall regulated wind turbines. Regardless of the circumstances, for a better utilization and understanding of this dynamic phenomenon, a reliable prediction method is demanded. For a successful prediction, stall onset must be indicated reliably.

Traditionally, semi-empirical dynamic-stall models have been an unsurpassed tool in the development of helicopter aerodynamics and will be the tool in the near future. Among the semi-empirical models, the Leishman–Beddoes (LB) dynamic-stall (DS) model is one of the most popular, probably due to its physical representation of the overall unsteady aerodynamic problem. The recent versions of the LB DS model [21,22] consist of the indicial functions for assessment of attached flow, the Kirchhoff equation for assessment of trailing-edge separation, the Evans–Mort correlation/shock reversal condition [18] for stall-onset indication, and the process for modeling vortex formation and convection. Among them, the stall-onset indication is a vital factor for a successful assessment of the unsteady airloads.

Contributed by the Fluids Engineering Division of ASME for publication in the Journal of Fluids Engineering. Manuscript received October 5, 2007; final manuscript received July 1, 2008; published online September 4, 2008. Assoc. Editor: Chunill Hah.

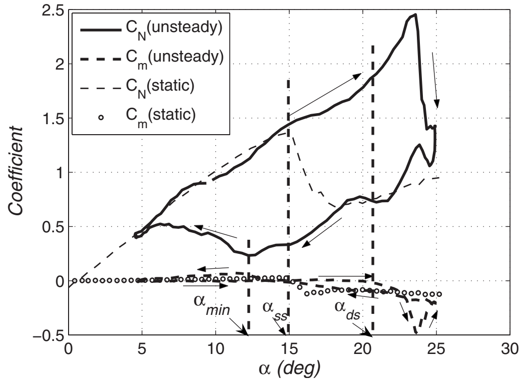

Fig. 1 Comparison of static and unsteady forces including dynamic stall

In order to investigate the unsteady phenomenon, the University of Glasgow has developed a device for airfoil dynamic-stall experiment [12]. The device has a capability of producing oscillatory, ramp-type (constant pitch-rate motion), and triangular wave motion for airfoils. With this device, the University of Glasgow could amass a large amount of unsteady airfoil data for its database. Presently, the database contains the data of 15 airfoils [23].

Investigation carried out at Glasgow University has illustrated that the applicability of the L-dynamic-stall model is reduced when used to reconstruct the unsteady airloads at low Mach numbers of about 0.12, and especially poorly predicts the stall-onset incidence (see Ref. [24]).

In analyzing the unsteady airfoil data, ramp-type data (positive and negative uniform pitch rates) are most interesting and useful because they have isolated the unfavorable dynamic effects. Thus, the analysis of the complicated phenomenon can be simplified. The usefulness of the ramp-type measured data was recently demonstrated in the development of a new stall-onset criterion for low-speed dynamic stall [24,25] and in modeling the return from the stalled state [23]. In the development of the stall-onset criterion, a mathematical deduction has been employed to fit the correlation of the measured data. As a result, a reliable and accurate stall-onset prediction model for low-speed airfoils has been obtained. This new stall-onset criterion requires two stall-onset parameters, which were only derived from the ramp-up data. It is understood, therefore, that there may be a limit for the application of the new criterion in the circumstances where there may be no ramp-up data and hence a lack of the stall-onset parameters. This is particularly so for the early unsteady airfoil tests where there were only oscillatory tests, while the ramp-type tests have been only conducted much later. That is because the value of the ramp-type data for simplifying the analyzis of the problem had not been recognized then and also the ramp-type motion was more difficult to generate.

For a wider use of the stall-onset criterion of Sheng et al. [25] to predicting the stall-onset angle for the oscillatory airfoils, in this paper, a procedure is proposed for extracting the onset parameters directly from oscillatory data and thus extends the application of the criterion to oscillatory cases.

2 Stall-Onset Criterion From Ramp-Up Tests

As illustrated by Sheng et al. [24], there are several stall-onset indications, such as C_N deviation, C_m break ($\Delta C_m=0.05$), C_c maximum, and C_d deviation (identified as α_{ds} in Fig. 2). Some others may be defined via individual pressure signals, such as C_p collapse at the leading edge, C_p deviation at about a quarter chord, or via flow visualization techniques. For some airfoils, all these definitions may give much close results (Fig. 2 gives an example) and some others may not. Individually, any of these indications could be applied, largely depending on the importance of the factor, which is concerned for the problem. For example, the large nose-down pitching moment is a restriction of the helicopter flight profile and of the structural responses; hence, the pitching moment break can be often taken as the criterion. For a continuity of the new criterion development in this research, as done in Refs. [24,25] C_c maximum is taken as the dynamic stall-onset criterion, because it is relatively easy to indicate and removes the local abnormalities. In principle, the new stall-onset indication could be feasible for all stall-onset criteria; only the values of the stall-onset parameters can be different.

Figure 2 gives the loops of forces during an oscillatory motion for a NACA 0012 airfoil. The stall-onset angle has been indicated via different criteria. For this particular airfoil, different criteria

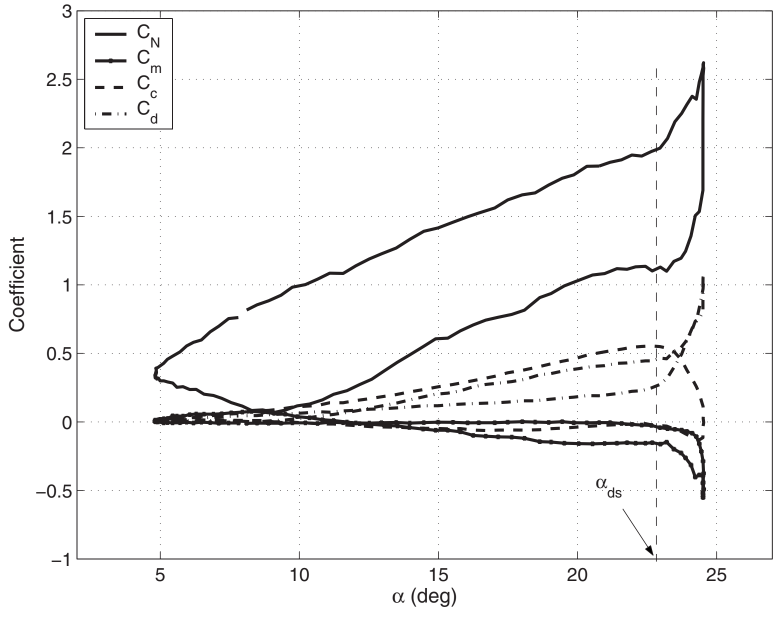

Fig. 2 Stall-onset incidences, α_{ds}, for the NACA 0012 oscillatory test (data taken from Galbraith et al. [29])

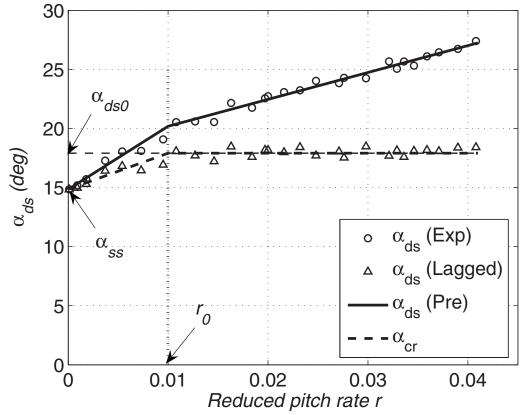

Fig. 3 A schematic for the stall-onset criterion (NACA 23012 ramp-up tests)

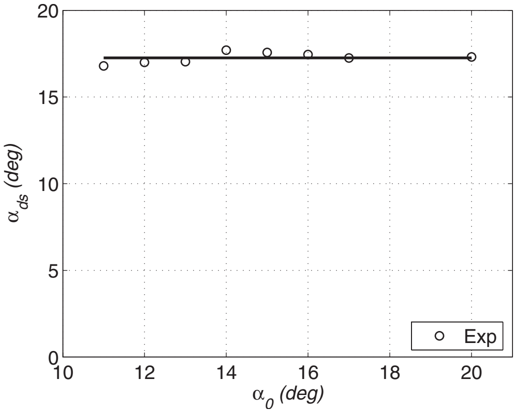

Fig. 4 Stall-onset angles against mean angles of attack (NACA 0012, κ=0.025)

give much similar results. Similarly, the same conclusion can be found for some other NACA airfoils. As an example, Fig. 1 gives the measured stall-onset angles of ramp-up test against the reduced pitch rate for the NACA 23012 airfoil (circles). Obviously, a linear dependency can be easily obtained when the reduced pitch rate is larger than r_0 (0.01 for many NACA series airfoils; a reduced pitch rate delimits the dynamic and quasisteady effects). To correlate to the measured data, Sheng et al. [24,25] have developed a criterion for the cases, and the method is outlined as follows.

First, a linear function is used to fit the measured stall-onset angles (circles in Fig. 3) for the reduced pitch rate larger than r_0,

$$\alpha_{\text{ds}} = \alpha_{\text{ds0}} + \lambda_1 r \tag{1}$$

A least square method is used to obtain two constants, α_{ds0} and λ_1. The first derived parameter is the constant critical onset angle, and from the latter, a time constant T_α is defined as

$$T_\alpha = \lambda_1 \tag{2}$$

Further, a critical onset angle, α_{cr}, is finally defined as

$$\begin{aligned} \alpha_{\text{cr}} &= \alpha_{\text{ds0}} \quad (r \ge r_0) \\ \alpha_{\text{cr}} &= \alpha_{\text{ss}} + (\alpha_{\text{ds0}} - \alpha_{\text{ss}})\frac{r}{r_0} \quad (r < r_0) \end{aligned} \tag{3}$$

An effective angle of attack can be calculated by lagging the angle of attack performed by

$$\Delta\alpha'(s) = \Delta\alpha(s)(1 - e^{-s/T_\alpha}) \tag{4}$$

with

$$\begin{aligned} \Delta\alpha(s) &= \alpha(s) - \alpha(s - \Delta s) \\ \Delta\alpha'(s) &= \alpha'(s) - \alpha'(s - \Delta s) \end{aligned} \tag{5}$$

then the stall is said to occur when

$$\alpha' \ge \alpha_{\text{cr}} \tag{6}$$

An advantage of the stall-onset indication above is that the stall-onset parameters, T_α and α_{ds0}, are all well defined and derived directly from ramp-up experimental data. Thus it is a more accurate and deterministic stall-onset criterion for low-speed airfoils. This has been confirmed by the applications of the stall-onset criterion [26,27].

3 Dynamic Stall Onset for Oscillatory Airfoils

In this section, the dynamic stall onset for oscillatory airfoils is investigated. For the cases of ramp-up tests at Glasgow University, the airfoil sweeps an arc from −2 deg to 40 deg. Virtually, the dynamic stall-onset angle is both well larger than the ramp-up starting angle and well smaller than the maximum angle. The start angle of ramp-up is so small that the stall-onset angle is actually independent of the starting angle, and the ending angle is so large that the stall-onset angle is usually independent of the maximum angle of attack under experimental condition. This motion ensures that the stall-onset angle is only dependent on the reduced pitch rate. While in an oscillatory motion, all three parameters, namely, the mean angle (α_0), amplitude (θ_0), and reduced frequency (κ), may affect the stall-onset angle. No doubt, it is more difficult to indicate the stall-onset angle than that of the ramp-up case, and this makes the oscillation problem much more complicated. However, under some conditions, as shown later in this paper, the triple-parameter problem of oscillation can be degraded into a single-parameter problem. This is the basis of a new method for extracting stall-onset parameters from the oscillatory experimental data.

3.1 Equivalent Reduced Pitch Rate. For an oscillatory motion, a sinusoidal function can be used to represent the angle of attack of airfoil as follows:

$$\alpha = \alpha_0 + \theta_0 \sin \omega t \tag{7}$$

Its corresponding time-dependent pitch rate is

$$\dot{\alpha} = \theta_0 \omega \cos \omega t \tag{8}$$

thus the corresponding reduced pitch rate is also time dependent,

$$r = \frac{\dot{\alpha} c}{2V} = \kappa \theta_0 \cos \omega t \tag{9}$$

An equivalent reduced pitch rate is then defined as the maximum reduced pitch rate in Eq. (9), so

$$r_{\text{eq}} = \kappa \theta_0 \tag{10}$$

This equivalent reduced pitch rate effectively combines two parameters (κ and θ_0) of oscillatory motion into one parameter. This particular parameter is an analog to the constant reduced pitch rate in ramp-up motion.

3.2 Stall-Onset Angle Via Mean Angle. Figure 4 shows the results of the stall-onset angles under different mean angles under deep stalled condition (amplitude and reduced frequency are kept the same, 8 deg and 0.025, respectively). It has been found that the onset angles are actually independent of the mean angles α_0 if the stall-onset angles are well below the maximum angles in the oscillatory motion (the cases shown in Fig. 4). Under these conditions, after dynamic stall onset, the dynamic vortex has enough time to travel over the chord, and then the airfoil is well penetrated into the deep stall region.

Additional confirmation of this is given in Fig. 5, where the

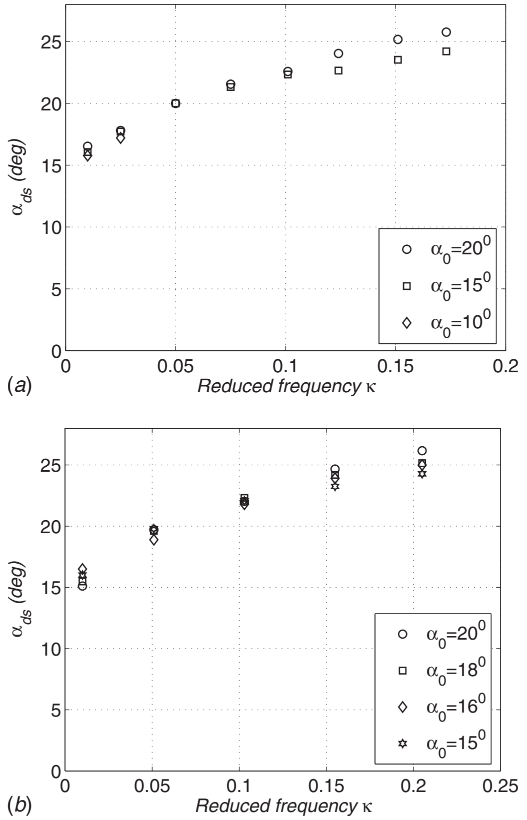

Fig. 5 Stall-onset angles against the reduced frequency, κ. (*a*) $\alpha=\alpha_0+10$ deg $\sin\omega t$ (NACA 0012), (*b*) $\alpha=\alpha_0+10$ deg $\sin\omega t$ (NACA 23012).

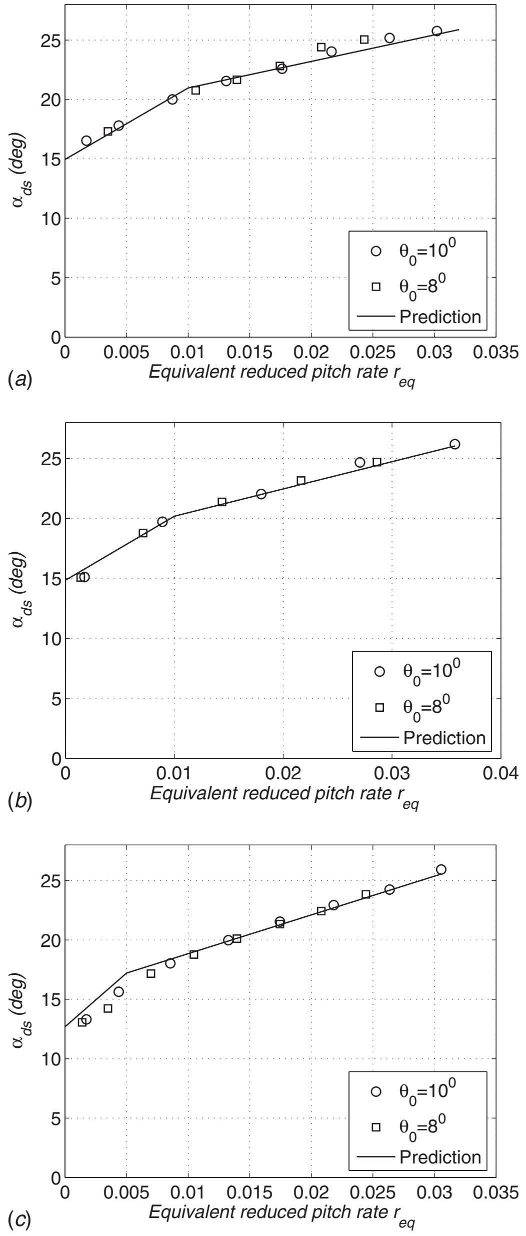

Fig. 6 Stall-onset angle dependence on the equivalent reduced pitch rate, r_{eq}. (*a*) NACA 0012, (*b*) NACA 23012, (*c*) GUVA 10.

onset angles of dynamic stall, though strongly dependent on the reduced frequency, may be seen to be independent of mean angles, α_0. It may also be observed that, for low reduced frequencies, the dynamic stall-onset angles are much smaller than the maximum angles that the airfoil attained and independent of mean angle, α_0. At high reduced frequencies, however, the stall-onset angles tend to be close to the maximum angles of the airfoil. Therefore, at these high reduced pitch rates, the data may not coincide. However, for those with lower mean angles, the stall-onset angle is still much smaller than the maximum angle, thus independent of the reduced pitch rate.

To remove the effects of mean angle, the condition that the maximum angle is much larger than the stall-onset angle must be met. Under this condition, the stall is occurring in the region of maximum pitch rate. It is for this reason that the equivalent reduced pitch rate is proposed.

3.3 Stall-Onset Angle Via Equivalent Reduced Pitch Rate. Figures 6(*a*)–6(*c*) plot the comparisons of the experimental stall-onset angles (symbols) and the predictions (solid lines) by the stall-onset criterion of Sheng et al. [25]. For the predictions, the stall-onset parameters, which have been derived from the ramp-up data, are used.

The experimental data in Fig. 6 are all taken from the oscillatory tests under deep stall conditions. From Figs. 6(*a*)–6(*c*), the stall-onset angles for oscillatory cases are very close to the prediction via ramp-up stall-onset parameters. In these figures, the equivalent reduced pitch rates represent the oscillatory motions and perform an identical role as the constant reduced pitch rate in ramp-ups, regardless of their different amplitudes and reduced frequencies. In this way, the equivalent reduced pitch rate can be considered a very good representative of reduced pitch rates for oscillatory motions. Hence, the triple-parameter problem can be finally reduced into the single-parameter problem, and the single parameter is the equivalent reduced pitch rate, r_{eq}.

Based on the analysis above, and a similarity to the stall-onset indication in Ref. [25], a new method of extracting stall-onset parameters is proposed, as well as a stall-onset criterion for oscillatory motion of airfoil.

From the appearance of the stall-onset angles against r_{eq} (see Fig. 6), a linear function can be used to fit the stall-onset angles of oscillatory airfoils when the equivalent reduced pitch rate is larger than r_0,

$$\alpha_{\text{ds}} = \alpha_{\text{ds0}} + \lambda_2 r_{\text{eq}} \tag{11}$$

A least square method, fitting Eq. (11) to the measured stall-onset angles of oscillatory motions, yields the constant critical stall-onset angle, α_{ds0} and a constant, λ_2. A nondimensional time constant is then simply obtained as follows:

Table 1 Values of α_{ds0} and T_α

	α_{ds0} (deg)		T_α	
Airfoil	Oscillatory	Ramp-up	Oscillatory	Ramp-up
NACA 0012	18.84	18.73	4.08	3.90
NACA 0015	17.15	17.81	5.82	5.78
NACA 0018	17.34	17.46	6.20	6.22
NACA 0021	17.40	17.91	6.30	6.30
NACA 23012	18.42	17.91	3.87	3.97
NACA 23012A	16.86	17.19	5.33	5.11
NACA 23012B	18.12	18.07	5.72	6.14
NACA 23012C	18.13	18.06	5.33	5.59
AHAVAW	15.11	14.88	5.98	6.27
GUVA 10	15.58	15.82	5.86	5.70

$$T_\alpha = \lambda_2 \tag{12}$$

Obtaining the stall-onset parameters, the indication of stall onset is the same as that of the ramp-up cases (Eqs. (3)–(6)).

Table 1 lists the values of the stall-onset parameters α_{ds0} and T_α, which are extracted from oscillatory airfoil data via Eqs. (11) and (12). For a comparison, the stall-onset parameters derived from ramp-up data are also included. It is surprising to notice that the onset parameters derived from both motion types are very close to each other (see Table 1).

4 Result Analysis and Discussion

In this section, the comparisons of stall-onset angle prediction with experimental results for oscillatory airfoils are made for three airfoils, namely, the NACA 0012, the NACA 23012, and the GUVA 10. These airfoils are chosen because they represent three different airfoil types (the profiles shown in Fig. 7). It must be emphasized that the same principle can be applicable to other airfoils.

4.1 Oscillatory Cases: Deep Stall Conditions. The comparisons have been made for stall-onset angle predictions and the experimental data from deep stall conditions. In Fig. 8, the predictions of stall-onset angles have been made by two different sets of stall-onset parameters, α_{ds0} and T_α, which are extracted from oscillatory test data (identified as "os paras" in Fig. 8) and from ramp-up data (identified as "rup paras"), respectively. The values of α_{ss} and r_0 are taken from Ref. [25].

From Fig. 8, it can be seen that the predictions, via different onset parameter sets, are both very close to the test data. The differences may come from the different test conditions of ramp-up and oscillatory tests, but both stall-onset parameter sets are acceptable. It can be concluded that the method developed for extracting stall-onset parameters from oscillatory experimental data is feasible.

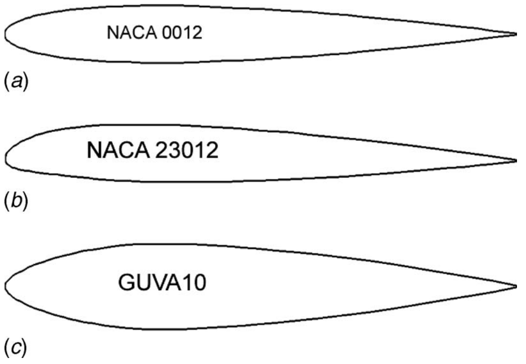

Fig. 7 Airfoil profiles studied in this research

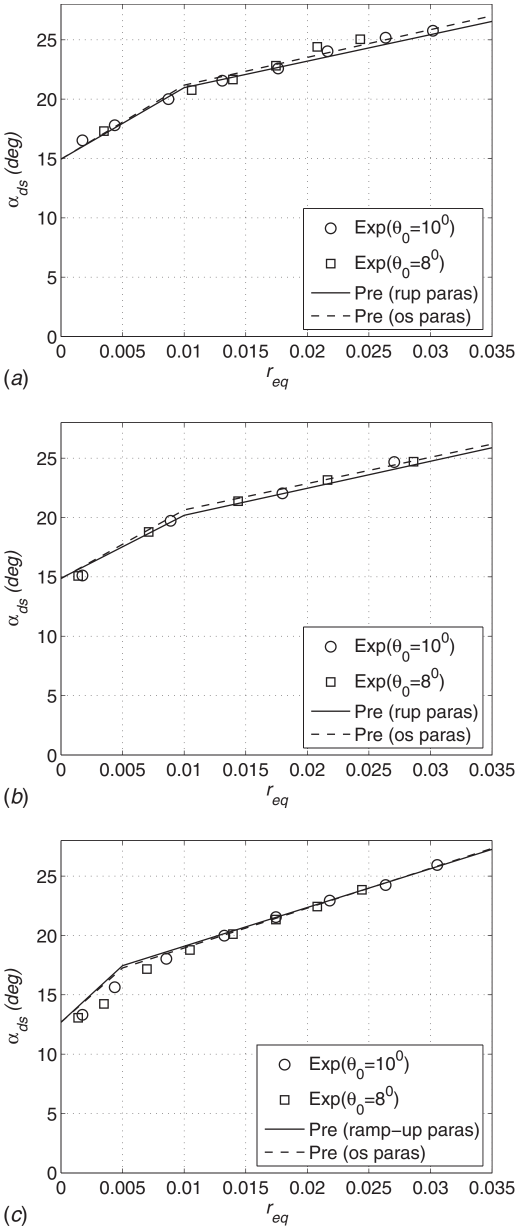

Fig. 8 Comparisons of dynamic stall-onset predictions. (*a*) NACA 0012, (*b*) NACA 23012, (*c*) GUVA 10.

4.2 Oscillatory Cases: All Cases. The method for extracting stall-onset parameters from oscillatory test data has been carried out only under deep stall conditions. From the discussion above, it can be seen that the parameters derived from oscillatory test data are much close to those from ramp-up tests. They can, thus, be used to predict the stall-onset angles for the deep stall conditions (see Fig. 8). This, however, is certainly not enough. The method must be applicable for all oscillatory cases, regardless of the stall conditions. The following examples are the comparisons of predictions and experimental results for those cases where light and deep stall conditions are both included.

Figures 9–11 are the comparisons of normal force predictions with the experimental data for three airfoils. The predictions of normal force (identified as "new method") are made via the modified dynamic-stall model of Sheng et al. [26] and with the stall-onset parameters obtained from oscillatory test data (see Table 1). For each airfoil, two cases of both deep stall condition (at low

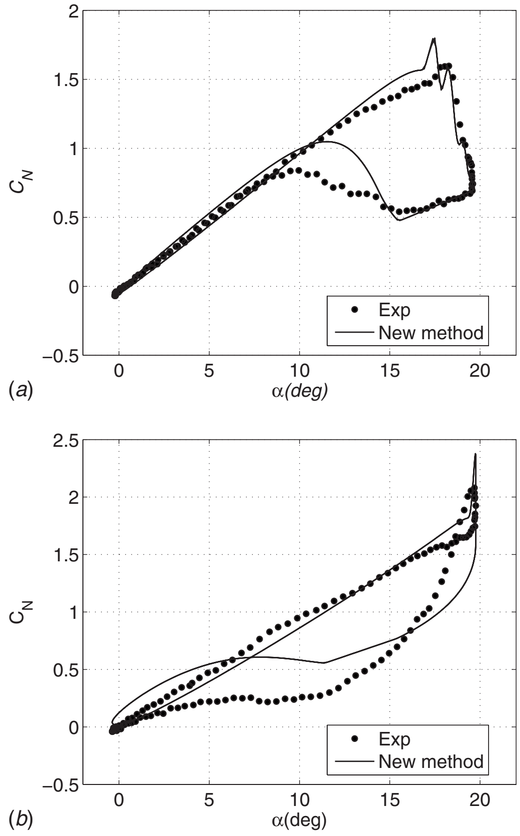

Fig. 9 Comparisons of predictions and experimental results for NACA 0012. (*a*) α=10 deg+10 deg sin ωt, κ=0.025, (*b*) α =10 deg+10 deg sin ωt, κ=0.099.

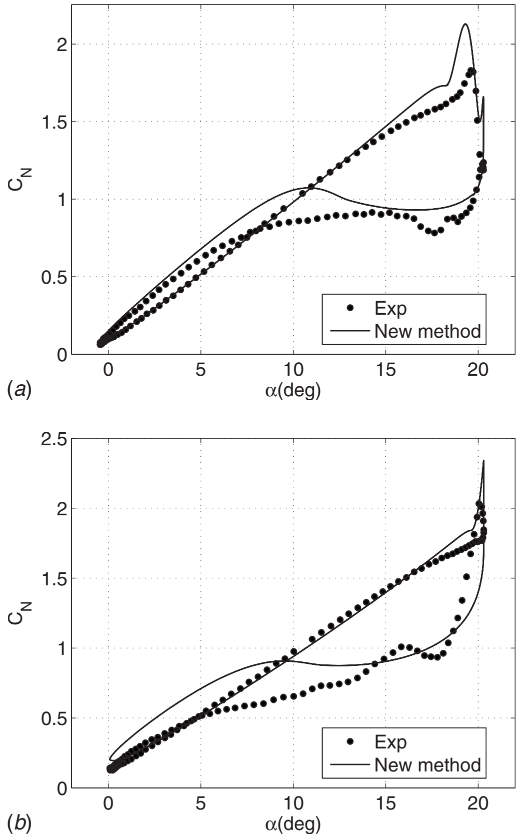

Fig. 10 Comparisons of predictions and experimental results for NACA 23012. (*a*) α=10 deg+10 deg sin ωt, κ=0.051, (*b*) α =10 deg10+ deg sin ωt, κ=0.102.

reduced frequency) and light stall condition (at high reduced frequency) are given. From these figures, it may be seen that the stall-onset angles are all well captured, regardless of stall conditions.

It is interesting to notice that under deep stall conditions, the predictions are good, even for the return from the stalled state. However, in the light stall conditions, the return from stall is not so good.

4.3 More Validations. The values of onset parameters included in Table 1 are all obtained from the data of one wind tunnel, the Glasgow University's "Handley-Page" wind tunnel, which has an octagonal working section with a height of 1.61 m and a width of 2.14 m. The airfoils have normally been tested at Reynolds number of 1.5×10^6 and Mach number of 0.12 (chord length is 0.55 m), so their universality has yet not been validated. Hence some doubt may arise as to the universality of the model. Fortunately, some alternative independent data are available to the public [9]. The data were taken for a NACA 0012 airfoil at a mean angle of 15 deg and an amplitude of 10 deg. The Mach number and Reynolds number are broadly similar to those of the Glasgow experiments.

These data are used to derive the values of α_{ds0} and T_α by the procedure for oscillatory motions proposed in this paper and quoted in Eqs. (11) and (12). The derived onset parameters are α_{ds0}=18.6 deg and T_α=3.79. It must be pointed out that the limited data are available to extracting the onset parameters, i.e., the reduced frequencies of κ=0.05, 0.10, and 0.15, corresponding to the equivalent reduced pitch rates of r_{eq}=0.0087, 0.0175, and 0.026, respectively. The unsuitable onset angles are those at a very low reduced frequency/low equivalent reduced pitch rate (κ =0.025/r_{eq}=0.0035) or at a very high reduced frequency (κ =0.20) in which the deep stall condition is not met. The onset angle is much close to the maximum angle of attack of the airfoil. Even with such a small data set to work with, the derived onset parameters are very close to the results from the Glasgow database, α_{ds0}=18.84 deg and T_α=4.08 for oscillatory and α_{ds0} =18.73 deg and T_α=3.90 for ramp-up. Figure 12 shows the comparison of the predictions by the stall-onset parameters from Glasgow University ("GU paras") and by the stall-onset parameters derived from the data in Ref. [9] ("New paras"). Clearly, these two parameter sets are all acceptable. From this figure, it can be seen that the new developed stall-onset indication performs well for the whole range of reduced frequencies. This once again confirmed similar result and the explanations of Sheng et al. [24,25].

5 Conclusions

A new method for extracting the onset parameters from oscillatory test data and a stall-onset indication with these parameters are presented in this paper. The method yields good reconstructions for the data of the Glasgow database, and consistent predictions for the public data. Recently, the method has been successfully used for extracting the stall-onset parameters for the NREL airfoils, which have been tested at Ohio State University [30]. From the discussion and analyses above, the following conclusions can be made.

- Stall-onset angle, α_{ds}, is independent of the mean angles of oscillatory motion under deep stall conditions.
- For deep dynamic-stall condition, the equivalent reduced pitch rate is a good representation of reduced pitch rate for extracting the stall-onset parameters.
- The method for extracting the onset parameters of α_{ds0} and T_α from oscillatory tests provides much close results to those from the ramp-up tests.

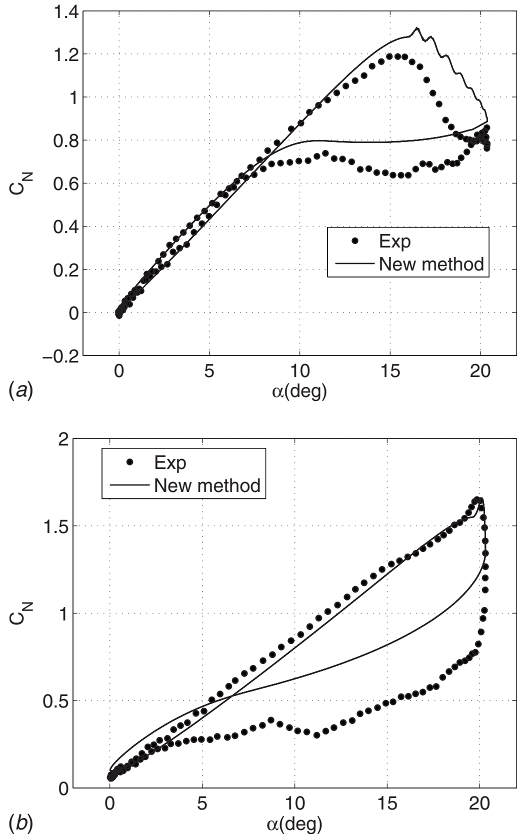

Fig. 11 Comparisons of predictions and experimental results for GUVA 10. (*a*) α=100 deg+10 deg sin ωt, κ=0.025, (*b*) α =10 deg+10 deg sin ωt, κ=0.100.

- The proposed method predicts the stall-onset angles for oscillatory motions of airfoils, regardless of stall conditions.
- The method has been further validated by limited public data.

Acknowledgment

This research work was sponsored by Engineering and Physical Sciences Research Council (EPSRC, UK), Research Grant No. GR/S42446/01, in collaboration with Garrad Hassan Ltd. and the National Renewable Energy Laboratory's, National Wind Turbine Center, CO.

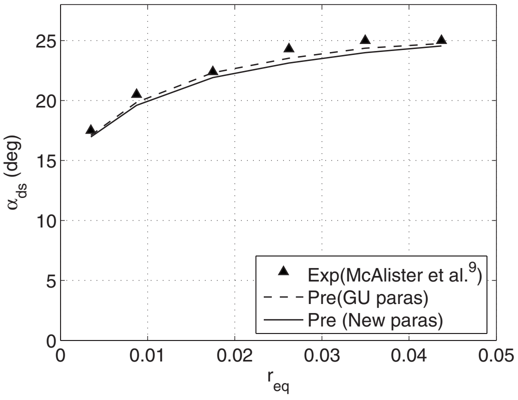

Fig. 12 A validation for the public data

Nomenclature

c = chord length, m
C_c = chordwise force coefficient
C_d = drag coefficient
C_m = pitching moment coefficient about $\frac{1}{4}$-chord axis
C_N = normal force coefficient
C_p = pressure coefficient
r = reduced pitch rate ($r=\dot{\alpha}c/2V$)
r_0 = reduced pitch rate, which delimits dynamic stall and quasisteady stall
r_{eq} = equivalent reduced pitch rate of oscillating test
s = nondimensional time ($s=2Vt/c$)
T_α = nondimensional time delay constant for angle of attack during upstroke (onset parameter)
T_b = modification time constant of Niven et al.
T_p = Beddoes's time lagging constant for normal force
V = freestream velocity, m/s
α = angle of attack or incidence
α_0 = mean angle of oscillatory motion
α_{cr} = critical stall-onset angle (reduced pitch rate dependent)
α_{ds} = dynamic stall-onset angle
α_{ds0} = constant critical stall-onset angle
$\alpha_{\min}$ = angle of local minimum normal force during downstroke
α_{ss} = static stall angle
θ_0 = amplitude of angle of attack of airfoil oscillating motion
κ = reduced frequency ($\kappa=\omega c/2V$)
λ_1, λ_2 = linear fitting coefficients
ω = circular frequency of oscillatory motions
Δ = a step change in a sampled system

References

[1] Harris, F. D., and Pruyn, R. R., 1968, "Blade Stall—Half Fact, Half Fiction," J. Am. Helicopter Soc., **13**, pp. 27–48.
[2] Ham, N. D., and Garelick, M. S., 1968, "Dynamic Stall Considerations in Helicopter Rotors," J. Am. Helicopter Soc., **13**, pp. 49–55.
[3] Carr, L. W., 1988, "Progress in Analysis and Prediction of Dynamic Stall," J. Aircr., **25**, pp. 6–17.
[4] Carr, L. W., and Chandrasekhara, M. S., 1996, "Compressibility Effects on Dynamic Stall," Prog. Aerosp. Sci., **32**, pp. 523–573.
[5] Ekaterinaris, J. A., and Platzer, M. F., 1997, "Computational Prediction of Airfoil Dynamic Stall," Prog. Aerosp. Sci., **33**, pp. 759–846.
[6] McCroskey, W. J., McAlister, K. W., Carr, L. W., Pucci, S. L., Lambert, O., and Indergrand, R. F., 1981, "Dynamic Stall on Advanced Airfoil Sections," J. Am. Helicopter Soc., **26**, pp. 40–50.
[7] Bousman, W. G., 1998, "A Qualitative Examination of Dynamic Stall From Flight Test Data," J. Am. Helicopter Soc., **43**, pp. 279–295.
[8] Bousman, W. G., 2000, "Evaluation of Airfoil Dynamic Stall Characteristics for Maneuverability," *26th European Rotorcraft Forum*, The Hague, Netherlands, Sep. 26–29.
[9] McAlister, K. W., Carr, L. W., and McCroskey, W. J., 1978, "Dynamic Stall Experiments on the NACA 0012 Airfoil," NASA, Technical Paper No. 1100.
[10] McCroskey, W. J., 1976, "Dynamic Stall Experiments on Oscillating Airfoils," AIAA J., **14**, pp. 57–63.
[11] Wilby, P. G., 1980, "The Aerodynamic Characteristics of Some New RAE Blade Sections, and Their Potential Influence on Rotor Performance," Vertica, **4**, pp. 121–133.
[12] Galbraith, R. A. McD., and Leishman, J. G., 1983, "A Micro-Computer Based Test Facility for the Investigation of Dynamic Stall," *International Conference on the Use of Micros in Fluid Engineering*, London, UK, June, British Hydromechanics Research Association, Paper No. E3.
[13] Niven, A. J., Galbraith, R. A. McD., and Herring, D. G. F., 1989, "Analysis of Reattachment During Ramp Down Tests," Vertica, **13**, pp. 187–196.
[14] Wilby, P. G., 2001, "The Development of Rotor Airfoil Testing in the UK," J. Am. Helicopter Soc., **46**, pp. 210–220.
[15] Lee, T., and Gerontakos, P., 2004, "Investigation of Flow Over an Oscillating Airfoil," J. Fluid Mech., **512**, pp. 313–341.
[16] Guilmineau, E., and Queutey, P., 1999, "Numerical Study of Dynamic Stall on Several Airfoil Sections," AIAA J., **37**, pp. 128–130.
[17] Spentzos, A., Barakos, G. N., Badcock, K. J., Richards, B. E., Wernert, P., Schreck, S., and Raffel, M., 2005, "Investigation of Three-Dimensional Dynamic Stall Using Computational Fluid Dynamics," AIAA J., **43**, 1023–1033.
[18] Beddoes, T. S., 1978, "Onset of Leading Edge Separation Effects Under Dy-

namic Conditions and Low Mach Number," *34th Annual National Forum of the American Helicopter Society*, Washington DC, May.

[19] Beddoes, T. S., 1983, "Representation of Airfoil Behaviour," Vertica, **7**, pp. 183–197.

[20] Beddoes, T. S., 1984, "Practical Computational of Unsteady Lift," Vertica, **8**, pp. 55–71.

[21] Leishman, J. G., and Beddoes, T. S., 1989, "A Semi-Empirical Model for Dynamic Stall," J. Am. Helicopter Soc., **34**, pp. 3–17.

[22] Beddoes, T. S., 1993, "A Third Generation Model for Unsteady Aerodynamics and Dynamic Stall," Westland Helicopter Limited, Report No. RP-908.

[23] Sheng, W., Galbraith, R. A. McD., and Coton, F. N., 2007, "Return From Airfoil Stall During Ramp-Down Pitching Motions," J. Aircr., **44**(6), pp. 1856–1864.

[24] Sheng, W., Galbraith, R. A. McD., Coton, F. N., 2006, "A New Stall-Onset Criterion for Low Speed Dynamic-Stall," ASME J. Sol. Energy Eng., **128**, pp. 461–471.

[25] Sheng, W., Galbraith, R. A. McD., and Coton, F. N., 2007, "Improved Dynamic Stall Onset Criterion at Low Mach Numbers," J. Aircr., **44**, pp. 1049–1052.

[26] Sheng, W., Galbraith, R. A. McD., and Coton, F. N., 2008, "A Modified Dynamic Stall Model for Low Mach Numbers," ASME J. Sol. Energy Eng., **130**, p. 031013.

[27] Sheng, W., Galbraith, R. A. McD., and Coton, F. N., "A Refined Dynamic Stall Model for the NREL Airfoils," Wind Energy, to be published.

[28] Ericsson, L. E., 1995, "Dynamic Airfoil Flow Separation and Reattachment," J. Aircr., **32**, pp. 1191–1197.

[29] Galbraith, R. A. McD., Gracey, M. W., and Leitch, E., 1992, "Summary of Pressure Data for Thirteen Airfoils on the University of Glasgow Airfoil Database," University of Glasgow, GU Aero Report No. 9221.

[30] Sheng, W., Galbraith, R. A. McD., and Coton, F. N., 2008, "Applications of Low Speed Dynamic Stall Model to the NREL Airfoils," presented at the 46th AIAA Aerospace Sciences Meeting and Exhibit, Reno, Jan., AIAA-2008-1329.

A General Macroscopic Turbulence Model for Flows in Packed Beds, Channels, Pipes, and Rod Bundles

A. Nakayama
Professor

F. Kuwahara
Associate Professor

Department of Mechanical Engineering,
Shizuoka University,
3-5-1 Johoku,
Hamamatsu 432-8561, Japan

This study focuses on Nakayama and Kuwahara's two-equation turbulence model and its modifications, previously proposed for flows in porous media, on the basis of the volume averaging theory. Nakayama and Kuwahara's model is generalized so that it can be applied to most complex turbulent flows such as cross flows in banks of cylinders and packed beds, and longitudinal flows in channels, pipes, and rod bundles. For generalization, we shall reexamine the extra production terms due to the presence of the porous media, appearing in the transport equations of turbulence kinetic energy and its dissipation rate. In particular, we shall consider the mean flow kinetic energy balance within a pore, so as to seek general expressions for these additional production terms, which are valid for most kinds of porous media morphology. Thus, we establish the macroscopic turbulence model, which does not require any prior microscopic numerical experiments for the structure. Hence, for the given permeability and Forchheimer coefficient, the model can be used for analyzing most complex turbulent flow situations in homogeneous porous media without a detailed morphological information. Preliminary examination of the model made for the cases of packed bed flows and longitudinal flows through pipes and channels reveals its high versatility and performance.

[DOI: 10.1115/1.2969461]

Keywords: turbulence model, packed bed, porous media, channel, pipes, volume averaging

Introduction

Turbulent flows take place in complex geometrical configurations such as in the core of nuclear reactor and in the engine compartments of ground vehicles or aircrafts. However, even with the most powerful computer available today, it is still impractical to perform direct numerical simulation of the turbulent flows within such complex geometrical configurations. An alternative and practical approach may be to appeal to a macroscopic mathematical description designed for turbulent flows in porous media.

There are two different paths in the literature to derive macroscopic equations for turbulent flows in porous media. Antohe and Lage [1] obtained a two-equation turbulence model applying the Reynolds averaging operator to the volume-averaged macroscopic equations, namely, Vafai and Tien's equations [2], whereas Nakayama and Kuwahara [3] chose to obtain a two-equation turbulence model by spatially averaging the turbulence transport equations associated with the turbulence kinetic energy, following the procedure taken by Masuoka and Takatsu [4] for their zero-equation model. Pedras and de Lemos [5] showed that the two approaches lead to two different definitions of macroscopic turbulence kinetic energy. In particular, they presented that the definition of the macroscopic turbulence kinetic energy in the latter approach, namely, applying the spatial averaging operator to the Reynolds averaged equations, allows one to take account of the turbulence within a pore, while that in the former approach does not. Extensive discussions on this controversial issue on the two different approaches are available in the literature [6,7].

Within recent years, Nakayama and Kuwahara's model [3] and its modifications have been extensively used to investigate a variety of turbulent flows, such as flows in a packed bed [8,9], suppressant flows in engine naccelle clutter [10], longitudinal flows in channels, pipes, and rod bundles [11], flows through vegetable stacks [12], flows through densely vegetated channels [13], and flows through a stratified porous medium [14]. This recent record shows that the approach based on the spatial average of the Reynolds average is preferred in most engineering applications.

These macroscopic turbulence transport equations involve additional source terms, which quantify the extra production terms for the turbulence kinetic energy and its dissipation rate due to the presence of the porous media. The source terms vary in formulation, as studied by Guo et al. [8]. They examined three different expressions for the terms, namely, Nakayama and Kuwahara [3], Pedras and de Lemos [5], and Takeda [15], to study the gas flow through a randomly packed bed and found that three models perform rather differently with Nakayama and Kuwahara's model giving the most reasonable eddy viscosity. In these models, however, the extra source terms are commonly formulated based on numerical experiment results from two-dimensional periodic structures. Even though reasonable success has been made for the flows in a randomly packed bed with Nakayama and Kuwahara's model, a more general model, which does not require such a detailed morphology, is in need for practical engineering applications.

In this paper, we shall focus on Nakayama and Kuwahara's two-equation turbulence model and its modifications and try to generalize them for a universal use in most complex flows in homogeneous porous media. For generalization, we shall reexamine these extra production terms due to the presence of the porous media, appearing in the transport equations of turbulence kinetic energy and its dissipation rate, and seek general expressions for these additional production and dissipation terms, valid

---

Contributed by the Fluids Engineering Division of ASME for publication in the Journal of Fluids Engineering. Manuscript received October 24, 2007; final manuscript received June 15, 2008. published online September 4, 2008. Assoc. Editor: Ugo Piomelli.

for most kinds of porous media morphology. In particular, we shall investigate the mean flow kinetic energy balance and model these extra terms accordingly to establish the macroscopic turbulence model, which does not require any prior numerical experiments for the structure, and can be used for most kinds of porous media morphology without detailed morphological information.

Volume-Averaged Equations

Along the lines of the approach proposed by Nakayama [16] and Nakayama and Kuwahara [3], we integrate the set of Reynolds averaged equations, namely, the continuity and the Navier–Stokes equations, along with the standard two-equation model of turbulence, namely, the transport equations of turbulence kinetic energy and its dissipation rate, over an elementary control volume V, which is much larger than a microscopic (pore structure) characteristic size but much smaller than a macroscopic characteristic size. The resulting transport equations for macroscopic momentum, turbulence kinetic energy, and its dissipation rate run as

$$\begin{aligned}\frac{\partial\langle\overline{u}_i\rangle^f}{\partial t}&+\frac{\partial}{\partial x_j}\langle\overline{u}_j\rangle^f\langle\overline{u}_i\rangle^f\\ &=-\frac{1}{\rho}\frac{\partial}{\partial x_i}\left(\langle\overline{p}\rangle^f+\frac{2}{3}\rho_f\langle k\rangle^f\right)+\frac{\partial}{\partial x_j}[2(\nu+\nu_t)\langle s_{ij}\rangle^f]\\ &\quad\underline{+\frac{1}{V_f}\int_{A_{\mathrm{int}}}\left[2(\nu+\nu_t)s_{ij}-\frac{\overline{p}}{\rho}\delta_{ij}\right]n_j dA-\frac{\partial}{\partial x_j}\langle\overline{u}_j''\overline{u}_i''\rangle^f}\end{aligned}\tag{1}$$

$$\begin{aligned}\frac{\partial\langle k\rangle^f}{\partial t}+\frac{\partial}{\partial x_j}\langle\overline{u}_j\rangle^f\langle k\rangle^f&=\frac{\partial}{\partial x_j}\left[\left(\nu+\frac{\nu_t}{\sigma_k}\right)\frac{\partial\langle k\rangle^f}{\partial x_j}-\underline{\langle\overline{u}_j''k''\rangle^f}\right]\\ &\quad+2\nu_t\langle s_{ij}\rangle^f\langle s_{ij}\rangle^f-\langle\varepsilon\rangle^f+\underline{2\nu_t\langle s_{ij}''s_{ij}''\rangle^f}\end{aligned}\tag{2}$$

$$\begin{aligned}\frac{\partial\langle\varepsilon\rangle^f}{\partial t}+\frac{\partial}{\partial x_j}\langle\overline{u}_j\rangle^f\langle\varepsilon\rangle^f&=\frac{\partial}{\partial x_j}\left[\left(\nu+\frac{\nu_t}{\sigma_\varepsilon}\right)\frac{\partial\langle\varepsilon\rangle^f}{\partial x_j}-\langle\overline{u}_j''\varepsilon''\rangle^f\right]\\ &\quad+(2c_1\nu_t\langle s_{ij}\rangle^f\langle s_{ij}\rangle^f-c_2\langle\varepsilon\rangle^f)\frac{\langle\varepsilon\rangle^f}{\langle k\rangle^f}\\ &\quad\underline{+2c_1\nu_t\langle s_{ij}''s_{ij}''\rangle^f\frac{\langle\varepsilon\rangle^f}{\langle k\rangle^f}+\frac{\nu}{V_f}\int_{A_{\mathrm{int}}}\frac{\partial\varepsilon}{\partial x_j}n_j dA}\end{aligned}\tag{3}$$

where the underlined terms need to be expressed in terms of determinable variables. The mean strain tensor is given by

$$s_{ij}=\frac{1}{2}\left(\frac{\partial\overline{u}_i}{\partial x_j}+\frac{\partial\overline{u}_j}{\partial x_i}\right)\tag{4}$$

where the Reynolds stress $-\rho\overline{u_i'u'_j}$ is modeled according to the effective viscosity formula. Moreover, the symbol

$$\langle a\rangle^f=\frac{1}{V_f}\int_{V_f}a dV\tag{5}$$

denotes the intrinsic average of a. For integrations, the spatial averaging rules are exploited as follows:

$$\langle a_1a_2\rangle^f=\langle a_1\rangle^f\langle a_2\rangle^f+\langle a_1''a_2''\rangle^f\tag{6}$$

$$\left\langle\frac{\partial a}{\partial x_j}\right\rangle^f=\frac{\partial\langle a\rangle^f}{\partial x_j}+\frac{1}{V_f}\int_{A_{\mathrm{int}}}a n_j dA\tag{7}$$

where A_{int} is the total interface between the fluid and solid phases while n_j is the unit vector pointing normally outward from the fluid to the solid side. In this section, the single prime is reserved for the turbulence fluctuating quantities, whereas the double prime is used to indicate the deviation from the intrinsic average, such that

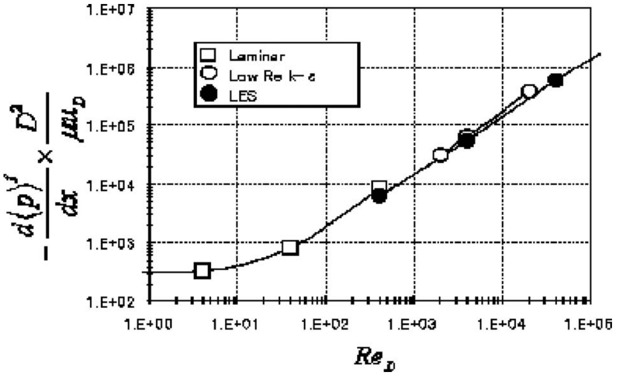

Fig. 1 Effect of Reynolds number on macroscopic pressure gradient

$$a''\equiv a-\langle a\rangle^f\tag{8}$$

The eddy diffusivity ν_t is expressed in terms of the intrinsically averaged turbulence kinetic energy $\langle k\rangle^f$ and its dissipation rate $\langle\varepsilon\rangle^f$ as

$$\nu_t=c_{\mathrm{D}}\frac{(\langle k\rangle^f)^2}{\langle\varepsilon\rangle^f}\tag{9}$$

where $c_{\mathrm{D}}=0.09$ is the empirical constant.

Comparison of Turbulence Models

In the numerical study of turbulent flow through a periodic array, Kuwahara et al. [17] concluded that Forchheimer-extended Darcy's law holds even in the turbulent flow regime in porous media. The experimental data, provided by Fand et al. [18] and the recent large eddy simulation (LES) study on a periodic porous structure by Kuwahara et al. [19], also support the validity of Forchheimer-extended Darcy's law. In Fig. 1, such LES results obtained for cross flows through an array of rods are presented in a dimensionless fashion against the Reynolds number Re_{D} based on Darcian velocity u_{D} for the case of $\phi=0.84$, where the previous microscopic numerical results [17] based on the low Reynolds number version of the $k-\varepsilon$ model are also plotted for comparison.

Thus, Nakayama and Kuwahara [3] introduced Forchheimer's modification for the last two terms on the right-hand side of Eq. (1), representing the intrinsic volume average of the total surface force (acting onto the fluid inside the pore) and the inertial dispersion, respectively.

$$\begin{aligned}\frac{\partial\langle\overline{u}_i\rangle^f}{\partial t}+\frac{\partial}{\partial x_j}\langle\overline{u}_j\rangle^f\langle\overline{u}_i\rangle^f&=-\frac{1}{\rho}\frac{\partial}{\partial x_i}\left(\langle\overline{p}\rangle^f+\frac{2}{3}\rho_f\langle k\rangle^f\right)\\ &\quad+\frac{\partial}{\partial x_j}[2(\nu+\nu_t)\langle s_{ij}\rangle^f]\\ &\quad-\phi\left(\frac{\nu}{K}+\phi b(\langle\overline{u}_j\rangle^f\langle\overline{u}_j\rangle^f)^{1/2}\right)\langle\overline{u}_i\rangle^f\end{aligned}\tag{10}$$

where ϕ, K, and b are the porosity, the permeability, and the Forchheimer constant, respectively. The same modeling in the momentum equation was adopted by Pedras and de Lemos [5]. The dispersion terms such as $-\langle\overline{u}_j''k''\rangle^f$ in Eq. (2) and $-\langle\overline{u}_j''\varepsilon''\rangle^f$ in Eq. (3) may be modeled according to the gradient hypothesis, as done in Nakayama and Kuwahara [3]. Therefore, in order to close the set of macroscopic equations, we only need to express the extra production terms due to the presence of the porous media, appearing in Eqs. (2) and (3), namely,

$$S_k\equiv 2\nu_t\langle s_{ij}''s_{ij}''\rangle^f\tag{11}$$

and

Table 1 Expressions for extra production terms

	S_k	S_ε
Nakayama and Kuwahara (1999)	$S_k=39\phi^2(1-\phi)^{5/2}\frac{(\langle\bar{u}_j\rangle^f\langle\bar{u}_j\rangle^f)^{3/2}}{d}$ where d is the particle diameter	$S_\varepsilon=c_2\frac{{S_k}^2}{3.7\phi^{3/2}(1-\phi)(\langle\bar{u}_j\rangle^f\langle\bar{u}_j\rangle^f)}$ $=411c_2\phi^{5/2}(1-\phi)^4\frac{(\langle\bar{u}_j\rangle^f\langle\bar{u}_j\rangle^f)^2}{d^2}$
Pedras and de Lemos (2001)	$S_k=0.28\phi\frac{\langle k\rangle^f(\langle\bar{u}_j\rangle^f\langle\bar{u}_j\rangle^f)^{1/2}}{\sqrt{K}}$ where K is the permeability	$S_\varepsilon=0.28c_2\phi\frac{\langle\varepsilon\rangle^f(\langle\bar{u}_j\rangle^f\langle\bar{u}_j\rangle^f)^{1/2}}{\sqrt{K}}$
Takeda (1994)	$S_k=0.0413\frac{R_0}{\rho}(\langle\bar{u}_j\rangle^f\langle\bar{u}_j\rangle^f)^2$ where R_0 is the resistance coefficient	$S_\varepsilon=0.0413c_2\frac{R_0}{\rho}\frac{\langle\varepsilon\rangle^f\langle\bar{u}_j\rangle^f\langle\bar{u}_j\rangle^f}{\langle k\rangle^f}$
	$c_D=0.09$, $c_1=1.44$, $c_2=1.92$, $\sigma_k=1.00$, $\sigma_\varepsilon=1.30$	

$$S_\varepsilon \equiv 2c_1\nu_t\langle s_{ij}''s_{ij}''\rangle^f\frac{\langle\varepsilon\rangle^f}{\langle k\rangle^f}+\frac{\nu}{V_f}\int_{A_{\mathrm{int}}}\frac{\partial\varepsilon}{\partial x_j}n_j dA \tag{12}$$

in terms of the determinable volume-averaged variables.

The expressions proposed for these extra terms by Nakayama and Kuwahara [3], Pedras and de Lemos [5], and Takeda [15] are listed in Table 1. Both Nakayama and Kuwahara [3] and Pedras and de Lemos [5] appealed to microscopic numerical calculations within a unit structure of rod bundles to determine the constants associated with these extra terms. The resulting expressions, however, are claimed to be valid for packed bed flows as well.

Guo et al. [8] chose a flow through a packed bed and carried out numerical simulations using the three turbulence models to compare the effective eddy diffusivity ν_t average over the cross section of the packed bed. They found that the models of Takeda [15] and Pedras and de Lemos [5] generate an eddy diffusivity one to two orders of mangitude higher than the model of Nakayama and Kuwahara [3], which gives a reasonable order of magnitude as compared with the empirical correlation established by Bey and Eigenberger [20]. Guo et al. pointed out that the models of Takeda [15] and Pedras and de Lemos [5] suffer from a deficiency in the source terms, such that the two equations for the transport of turbulence kinetic energy and its dissipation rate reduce to a single equation far downstream. They also noted that with a fixed pore Reynolds number, the effective eddy diffusivity based on Ref. [3] is insensitive to the change in particle size, whereas the other two models show strong dependency on it, namely, a lower eddy diffusivity corresponding to a larger particle size. The dependency on the particle size for a fixed pore Reynolds number contradicts the fact that the ratio of the effective diffusivity to the molecular diffusivity is only a function of porosity and pore Reynolds number, when the turbulence is controlled mainly by a local equilibrium between its production and dissipation within the voids, as in the case of fully developed turbulent flow in homogeneous porous media. The foregoing comparison suggests that a model capable of predicting a reasonable eddy diffusivity must be compatible with the energy budget prevailing within the voids. Thus, we shall consider the mean flow kinetic energy balance within a pore, to seek simple and yet general expressions for the extra source terms for production and dissipation associated with the presence of porous media.

General Expressions Based on Mean Flow Kinetic Energy Balance

Appropriate characteristic time scales for the extra source terms have been discussed extensively in recent publications. Pinson et al. [14] modified the time scale based on their friction factor model so as to modify Nakayama and Kuwahara's model [3] for the study of turbulent flow in a stratified medium. Their model is capable of capturing the dynamic behavior of turbulence kinetic energy. However, it requires a priori microscopic simulation to determine the volume average wake dissipation in advance; hence, its use may not be straightforward. On the other hand, in order to avoid an overestimation of the dissipation of turbulence kinetic energy, Chandesris et al. [11] chose the production time scale proposed by Chen and Kim [21] and Guo et al. [9], which Nakayama and Kuwahara [3] also have indirectly chosen. We shall follow them and adopt their production time scale.

The mean flow kinetic energy transport eqation [22] for clear fluid flow through a pore may be given by

$$\frac{\partial}{\partial t}\left(\frac{1}{2}\overline{u_iu_i}\right)+\frac{\partial}{\partial x_j}\left(\overline{u_j}\left(\frac{1}{2}\overline{u_iu_i}+\frac{2}{3}k\right)-2(\nu+\nu_t)\overline{u_i}s_{ij}\right)$$
$$=-\frac{1}{\rho}\overline{u_j}\frac{\partial\bar{p}}{\partial x_j}-2(\nu+\nu_t)s_{ij}s_{ij} \tag{13}$$

The terms on the left-hand side of the foregoing equation represent spatial transport of mean flow kinetic energy $\overline{u_iu_i}/2$, as the divergence theorem implies. Therefore, they cannot influence the overall aspect of the mean flow kinetic energy balance. (Note that they integrate to zero if the boundary is subject to the no-slip condition, and also that they are negligibly small anyway for homogeneous porous media.) Hence, we have

$$\left\langle -\frac{1}{\rho}\overline{u_j}\frac{\partial\bar{p}}{\partial x_j}-2(\nu+\nu_t)s_{ij}s_{ij}\right\rangle^f \approx 0 \tag{14}$$

This practice, namely, forcing the transport terms to be zero, is often introduced in algebraic models of turbulence, so as to remove the need for empirical results for tuning unknown model constants. Expanding the pressure work term and noting the no-slip condition as

$$\left\langle -\frac{1}{\rho}\overline{u_j}\frac{\partial\bar{p}}{\partial x_j}\right\rangle^f=\left\langle -\frac{1}{\rho}\frac{\partial\overline{u_j}\bar{p}}{\partial x_j}\right\rangle^f=-\frac{1}{\rho}\frac{\partial\langle\overline{u_j}\bar{p}\rangle^f}{\partial x_j}+\frac{1}{V_f}\int_{A_{\mathrm{int}}}\overline{u_j}\bar{p}dA$$
$$=-\frac{1}{\rho}\frac{\partial\langle\overline{u_j}\rangle^f\langle\bar{p}\rangle^f}{\partial x_j}-\frac{1}{\rho}\frac{\partial\langle\overline{u_j}''\bar{p}''\rangle^f}{\partial x_j}\approx-\frac{1}{\rho}\langle\overline{u_j}\rangle^f\frac{\partial\langle\bar{p}\rangle^f}{\partial x_j} \tag{15}$$

and

$$\langle 2(\nu+\nu_t)s_{ij}s_{ij}\rangle^f=2(\nu+\nu_t)\langle s_{ij}\rangle^f\langle s_{ij}\rangle^f+2(\nu+\nu_t)\langle s_{ij}''s_{ij}''\rangle^f$$
$$\approx 2\nu_t\langle s_{ij}''s_{ij}''\rangle^f \tag{16}$$

Note that $\partial\langle\overline{u_j}''\bar{p}''\rangle^f/\partial x_j=0$ for homogenous porous media and

$\langle s_{ij}\rangle^f \langle s_{ij}\rangle^f \ll \langle s''_{ij} s''_{ij}\rangle^f$ for macroscopically fully developed flows in homogeneous porous media. Hence, we may estimate the extra source terms for production and dissipation due to the presence of porous media, using Forchheimer-extended Darcy's law as

$$S_k \equiv 2\nu_t \langle s''_{ij} s''_{ij}\rangle^f \approx -\frac{1}{\rho}\langle \bar{u}_j\rangle^f \frac{\partial \langle \bar{p}\rangle^f}{\partial x_j}$$

$$\approx \phi\left(\frac{\nu}{K} + \phi b (\langle \overline{u_i}\rangle^f \langle \overline{u_i}\rangle^f)^{1/2}\right)\langle \bar{u}_j\rangle^f \langle \bar{u}_j\rangle^f \approx \phi^2 b (\langle \overline{u_j}\rangle^f \langle \overline{u_j}\rangle^f)^{3/2} \tag{17}$$

and

$$S_\varepsilon \equiv c_1 2\nu_t \langle s_{ij}'' s_{ij}''\rangle^f \frac{\langle \varepsilon\rangle^f}{\langle k\rangle^f} + \frac{\nu}{V_f}\int_{A_{\text{int}}} \frac{\partial \varepsilon}{\partial x_j} n_j dA \approx c_2 \frac{(2\nu_t \langle s_{ij}'' s_{ij}''\rangle^f)^2}{\langle k\rangle^f}$$

$$\approx c_2 \phi^2 b \sqrt{\frac{c_D \phi}{2K}} (\langle \overline{u_j}\rangle^f \langle \overline{u_j}\rangle^f)^2 \tag{18}$$

where we exploited the relation

$$-\frac{1}{\rho}\frac{\partial \langle \bar{p}\rangle^f}{\partial x_j} \approx \phi^2 b \langle \bar{u}_j\rangle^f \langle \bar{u}_j\rangle^f \approx 4\frac{\langle \tau\rangle^f}{\rho d_h} \approx 4\frac{{c_D}^{1/2}\langle k\rangle^f}{\sqrt{32K/\phi}} \tag{19}$$

noting $K = 32\phi/d_h$, as will be presented by Eq. (29) for channel and pipe flows and the Townsend approximation [23] $\tau/\rho = {c_D}^{1/2} k$. Note that we have chosen the production time scale $\langle k\rangle^f / S_k$ rather than the decay time scale $\langle k\rangle^f / \langle \varepsilon\rangle^f$ for the foregoing extra source terms.

Thus, the final set of the turbulence transport equations runs as

$$\frac{\partial \langle k\rangle^f}{\partial t} + \frac{\partial}{\partial x_j}\langle \overline{u_j}\rangle^f \langle k\rangle^f = \frac{\partial}{\partial x_j}\left(\left(\nu + \frac{\nu_t}{\sigma_k}\right)\delta_{ij} + \frac{(k_{\text{dis}})_{ij}}{Le_k \phi \rho c_p}\right)\frac{\partial \langle k\rangle^f}{\partial x_j}$$

$$+ 2\nu_t \langle s_{ij}\rangle^f \langle s_{ij}\rangle^f - \langle \varepsilon\rangle^f + \phi^2 b (\langle \overline{u_j}\rangle^f \langle \overline{u_j}\rangle^f)^{3/2} \tag{20}$$

and

$$\frac{\partial \langle \varepsilon\rangle^f}{\partial t} + \frac{\partial}{\partial x_j}\langle \bar{u}_j\rangle^f \langle \varepsilon\rangle^f = \frac{\partial}{\partial x_j}\left(\left(\nu + \frac{\nu_t}{\sigma_\varepsilon}\right)\delta_{ij} + \frac{(k_{\text{dis}})_{ij}}{Le_\varepsilon \phi \rho c_p}\right)\frac{\partial \langle \varepsilon\rangle^f}{\partial x_j}$$

$$+ (2c_1 \nu_t \langle s_{ij}\rangle^f \langle s_{ij}\rangle^f - c_2 \langle \varepsilon\rangle^f)\frac{\langle \varepsilon\rangle^f}{\langle k\rangle^f}$$

$$+ c_2 \phi^2 b \sqrt{\frac{c_D \phi}{2K}} (\langle \overline{u_j}\rangle^f \langle \overline{u_j}\rangle^f)^2 \tag{21}$$

where Le_k and Le_ε are the Lewis numbers for mechanical dispersion, which are believed to be close to unity. The empirical and theoretical expressions for thermal dispersion tensor $(k_{\text{dis}})_{tj}$ may be found elsewhere [24,25]. The resulting turbulence model is so general that it can be used for most kinds of porous media morphology, since it only requires the permeability K and the Forcheimer constant b, which can easily be determined from the pressure drop measurements.

Turbulent Flow in a Packed Bed

For the case of packed bed, the permeability K and the Forchheimer constant b may be given by the empirical Ergun equation [26]:

$$K = \frac{\phi^3}{150(1-\phi)^2} d^2 \tag{22}$$

and

$$b = \frac{1.75(1-\phi)}{\phi^3 d} \tag{23}$$

Substituting the foregoing expressions in the extra production terms, we have

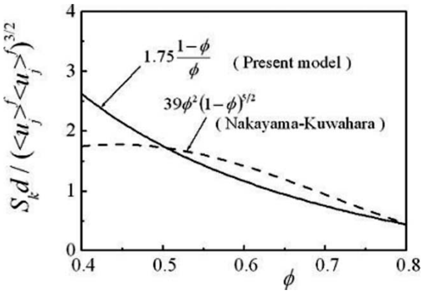

Fig. 2 Comparison of the model coefficients associated with S_k

$$S_k = \phi^2 b (\langle \overline{u_j}\rangle^f \langle \overline{u_j}\rangle^f)^{3/2} = \frac{1.75(1-\phi)}{\phi}\frac{(\langle \overline{u_j}\rangle^f \langle \overline{u_j}\rangle^f)^{3/2}}{d} \tag{24}$$

and

$$S_\varepsilon = c_2 \phi^2 b \sqrt{\frac{c_D \phi}{2K}} (\langle \overline{u_j}\rangle^f \langle \overline{u_j}\rangle^f)^2 = 4.55 c_2 \left(\frac{1-\phi}{\phi}\right)^2 \frac{(\langle \overline{u_j}\rangle^f \langle \overline{u_j}\rangle^f)^2}{d^2} \tag{25}$$

The resulting Eqs. (20) and (21) are consistent with Nakayama and Kuwahara's expressions [3], as listed in Table 1. In particular, the source terms S_k and S_ε given by Eqs. (24) and (25) conform to those of Nakayama and Kuwahara [3] with the coefficients $\phi^2 b = 1.75(1-\phi)/\phi d$ and $c_2 \phi^2 b \sqrt{c_D \phi / 2K} = 4.55 c_2 (1-\phi)^2/\phi^2 d^2$ corresponding to $39\phi^2(1-\phi)^{5/2}/d$ and $411 c_2 \phi^{5/2}(1-\phi)^4/d^2$, respectively, in their expressions. This could be partly the reason why their model gave the most reasonable eddy diffusivity for packed bed flows.

The present expressions for $S_k d / (\langle \overline{u_j}\rangle^f \langle \overline{u_j}\rangle^f)^{3/2} = 1.75(1-\phi)/\phi$ and $S_\varepsilon d^2 / c_2 (\langle \overline{u_j}\rangle^f \langle \overline{u_j}\rangle^f)^2 = 4.55(1-\phi)^2/\phi^2$ are compared in Figs. 2 and 3, respectively, against Nakayama and Kuwahara's expressions [3] based on microscopic numerical results from periodic structures for a wide porosity range $0.4 \le \phi \le 0.8$. Despite the difference in functional appearances, the two sets of the expressions give values close to one another particularly in the range $0.5 \le \phi \le 0.8$.

For the case of unidirectional flow without macroscopic mean shear, Eqs. (20) and (21) far downstream readily give

$$\langle \varepsilon\rangle^f = \phi^2 b (\langle \bar{u}\rangle^f)^3 = \frac{1.75(1-\phi)}{\phi}\frac{(\langle \bar{u}\rangle^f)^3}{d} \tag{26}$$

and

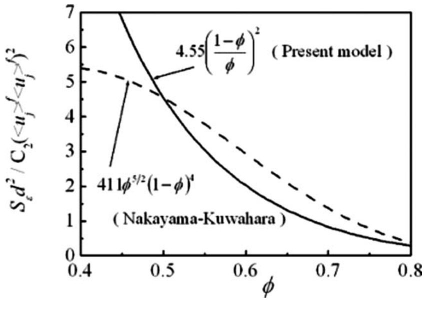

Fig. 3 Comparison of the model coefficients associated with S_ε

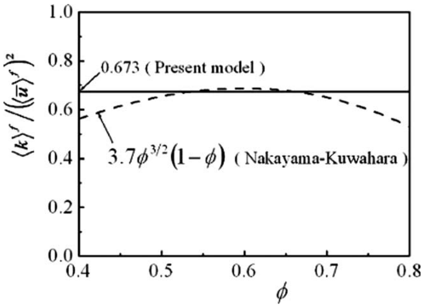

Fig. 4 Turbulence kinetic energy in a packed bed

$$\langle k\rangle^f = \phi^2 b\sqrt{\frac{2K}{c_D\phi}}(\langle\bar{u}\rangle^f)^2 = 1.75\sqrt{\frac{2}{150c_D}}(\langle\bar{u}\rangle^f)^2 = 0.673(\langle\bar{u}\rangle^f)^2 \tag{27}$$

Hence,

$$\frac{\nu_t}{\nu} = c_D\frac{\langle k\rangle^2}{\nu\langle\varepsilon\rangle} = 0.0233\frac{\phi}{1-\phi}\left(\frac{\langle\bar{u}\rangle^f d}{\nu}\right) \tag{28}$$

It is interesting to note that, for homogeneous porous media, the ratio of the limiting value of the volume-averaged kinetic energy to the square of the intrinsically volume-averaged velocity is constant irrespective of the porosity. This constancy is confirmed in Fig. 4 in which the numerical results obtained by Nakayama and Kuwahara [3] for two-dimensional periodical structures appear to stay nearly at the level indicated by Eq. (27) over a wide range of porosity.

In Fig. 5, the effective eddy kinematic viscosity, as given by Eq. (28), is compared against the empirical correlation established by Bey and Eigenberger [20] and also the results obtained by Guo et al. [8] using the Nakayama and Kuwahara model in which the porosity for the packed bed is assumed to be ϕ=0.4. Guo et al. [8] carried out the computations using Pedras and de Lemos [5] and Takeda [15] and found that their effective viscosities are one to two orders of mangitude higher than the model of the empirical correlation and concluded that Nakayama and Kuwahara's model gives most reasonable effective viscosity. Although the present model and the Nakayama and Kuwahara model perform better than the other two models, a substantial difference still exists between the present prediction and the empirical correlation proposed by Bey and Eigenberger. Guo et al. [9] listed several reasons associated with experimental uncertainties. Even though experimental error may not be negligible, there is certainly a further need for experimetal and theoretical work to improve the macroscopic models.

Nakayama and Kuwahara [3] carried out microscopic computations using the standard two-equation turbulence model for the case of turbulent flow through an array of rods with the Reynolds number based on the Darcian velocity the and length of structural unit u_DH/ν=10^5, the porosity ϕ=0.75, and the inlet values of turbulence quantities $\langle k\rangle^f/u_D{}^2$=10 and $\langle\varepsilon\rangle^f$=$30u_D{}^3/H$. The microscopic results were integrated over a unit to obtain the volume-averaged turbulence quantities, which were then compared with those based on their macroscopic model. In Figs. 6(*a*) and 6(*b*), these two sets of the results for turbulence kinetic energy and its dissipation rate are compared against the macroscopic results obtained using the present macroscopic model, namely, Eqs. (20) and (21). Excellent agreement is seen among the three sets of the results.

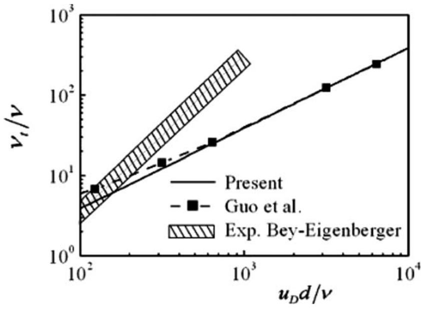

Fig. 5 Effective viscosity in a packed bed

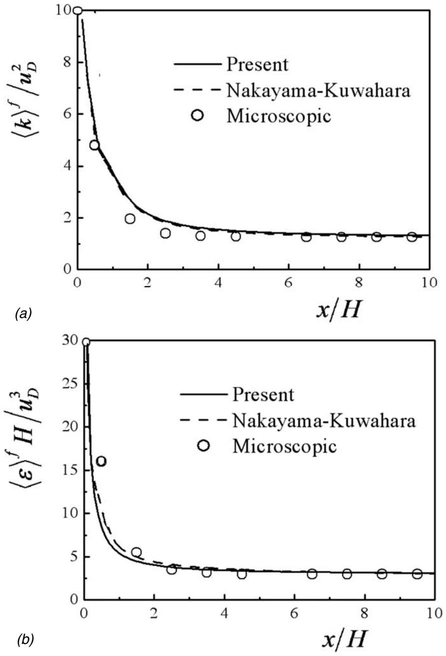

Fig. 6 Decay of turbulence in flow through an array of rods: (*a*) turbulence kinetic energy and (*b*) dissipation rate of turbulence kinetic energy

Turbulent Flow in Channels and Pipes

We shall adapt this general model to longitudinal turbulent flows in channels, pipes, and rod bundles such as found in nuclear power circuits and core. For the case of longitudinal flows in channels, pipes, and rod bundles, the permeability K and the Forchheimer constant b may be set according to the Hargen–Poiseuille flow solution and the Blasius friction law, namely,

$$K = \frac{\phi}{32}d_h{}^2 \tag{29}$$

such that

$$-\frac{1}{\rho}\frac{\partial\langle\bar{p}\rangle^f}{\partial x_j} \approx \phi\frac{\nu}{K}\langle u\rangle^f = \nu\frac{32}{d_h}\langle u\rangle^f \tag{30}$$

and

$$b = \frac{\lambda_f}{2d_h\phi^2} = \frac{0.3164}{2d_h\left(\frac{\langle\bar{u}\rangle^f d_h}{\nu}\right)^{1/4}\phi^2} \tag{31}$$

such that

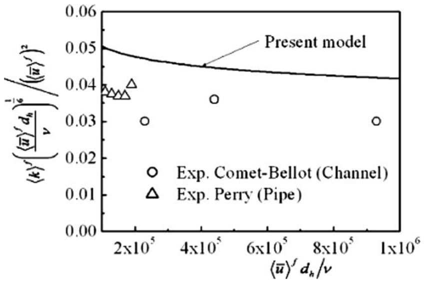

Fig. 7 Effect of Reynolds number on turbulence kinetic energy in channel and pipe flows

$$-\frac{1}{\rho}\frac{\partial\langle\overline{p}\rangle^f}{\partial x_j}\approx\phi^2 b(\langle u\rangle^f)^2=\frac{\lambda_f}{2d_h}(\langle u\rangle^f)^2 \tag{32}$$

where d_h is the hydraulic diameter of the passage under consideration and $\lambda_f\equiv-(2d_h/\rho(\langle\overline{u}\rangle^f)^2)(d\langle\overline{p}\rangle^f/dx)$ is the Moody friction factor.

For the case of longitudinal flow without macroscopic mean shear such as found in the case of channel, pipe, and rod bundle flows, Eqs. (20) and (21) far downstream readily give

$$\langle\varepsilon\rangle^f=\phi^2 b(\langle\overline{u}\rangle^f)^3=\frac{\lambda_f}{2d_h}(\langle\overline{u}\rangle^f)^3=\frac{0.158}{\left(\frac{\langle\overline{u}\rangle^f d_h}{\nu}\right)^{1/4}}\frac{(\langle\overline{u}\rangle^f)^3}{d_h} \tag{33}$$

and

$$\langle k\rangle^f=\phi^2 b\sqrt{\frac{2K}{c_{\mathrm{D}}\phi}}(\langle\overline{u}\rangle^f)^2=\frac{\lambda_f}{8\sqrt{c_{\mathrm{D}}}}(\langle\overline{u}\rangle^f)^2=\frac{0.132}{\left(\frac{\langle\overline{u}\rangle^f d_h}{\nu}\right)^{1/4}}(\langle\overline{u}\rangle^f)^2 \tag{34}$$

Hence,

$$\frac{\nu_t}{\nu}=c_D\frac{\langle k\rangle^2}{\nu\langle\varepsilon\rangle}=\frac{\lambda_f}{32}\left(\frac{\langle\overline{u}\rangle^f d_h}{\nu}\right)=0.00990\left(\frac{\langle\overline{u}\rangle^f d_h}{\nu}\right)^{3/4} \tag{35}$$

The limiting values of the turbulence kinetic energy obtained for the fully developed channel and pipe flows are plotted in Fig. 7 in terms of the dimensionless form $\langle k\rangle^f(\langle\overline{u}\rangle^f d_h/\nu)^{1/6}/(\langle\overline{u}\rangle^f)^2$ along with the experimental data of Comte-Bellot [27] and Perry et al. [28]. A reasonably good agreement is seen among the values in the figure. Furthermore, it is interesting to note that the present model estimates the value $c_k=(\langle\varepsilon\rangle^f d_h)/(4\langle k\rangle^f\langle\overline{u}\rangle^f)$ (focused by Chandesris et al. [11]) to be $c_k=\sqrt{c_{\mathrm{D}}}=0.3$ irrespective of the Reynolds number. The constancy of c_k is clearly confirmed in Fig. 8, which presents the numerical results for channels and pipe flows, obtained by Chandesris et al. [11] using a modified version of Nakayama and Kuwahara's turbulence model.

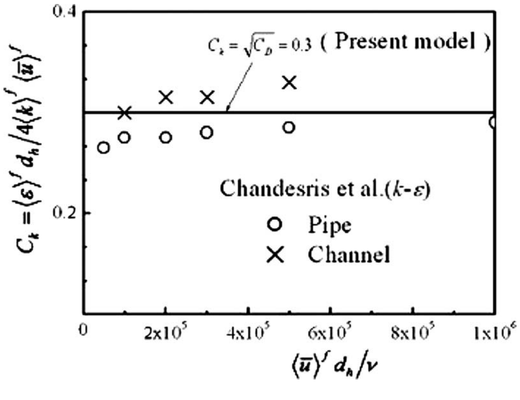

Fig. 8 Effect of Reynolds number on $c_k=(\langle\varepsilon\rangle^f d_h)/(4\langle k\rangle^f\langle\overline{u}\rangle^f)$ in channel and pipe flows

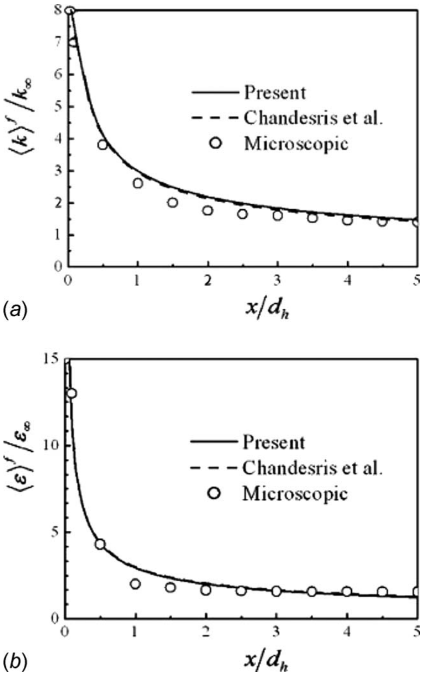

Fig. 9 Decay of turbulence in flow through a stratified medium made by channels; (*a*) turbulence kinetic energy and (*b*) dissipation rate of turbulence kinetic energy

Chandesris et al. [11] studied the decay of turbulence inside a stratified medium made by plane channels from both microscopic and macroscopic views. Their macroscopic turbulence model uses the kinetic energy balance, an estimation of the direct viscous dissipation and an ad hoc length scale. The volume-averaged turbulence quantities such as turbulence kinetic energy and its dissipation rate obtained by them for the case of $\langle\overline{u}\rangle^f d_h/\nu=10^5$ are plotted in Figs. 9(*a*) and 9(*b*) along with the macroscopic results obtained by solving Eqs. (20) and (21) and for a uniform unidirectional flow without mean shear with $\langle k\rangle^f=10\langle k\rangle^f_\infty$ and $\langle\varepsilon\rangle^f=15\langle\varepsilon\rangle^f_\infty$, where $\langle k\rangle^f_\infty$ and $\langle\varepsilon\rangle_{f\infty}$ are the fully developed values of turbulence kinetic energy and its dissipation rate. A good agreement among the three sets of the results gives strong support to the present general turbulence model.

Conclusions

Nakayama and Kuwahara's two-equation turbulence model previously introduced for turbulent flows in porous media has been generalized to treat most kinds of complex turbulent flows in homogeneous porous media. In order to generalize the model, the extra production terms due to the presence of the porous media, appearing in the transport equations of turbulence kinetic energy and its dissipation rate, were re-examined in consideration of the mean flow kinetic energy balance. The resulting turbulence model is so versatile that it can be used to attack cross flows in banks of cylinders and packed beds, and longitudinal flows in channels, pipes, and rod bundles. The model does not require any prior numerical experiments for the structure. Preliminary examination of the model made for the cases of packed bed flows and longitudinal flows through pipes and channels reveals that, for a given permeability and Forchheimer coefficient, it can be used for most kinds of porous media morphology without detailed morphological information.

Nomenclature

A = surface area
A_{int} = total interface between the fluid and solid
b = Forchheimer constant
c_1, c_2, c_D = turbulence model constants
d = particle diameter
d_h = hydraulic diameter
k = turbulence kinetic energy
K = permeability
Le = Lewis number
p = pressure
Re = Reynolds number
u_i = velocity vector
x_i = Cartesian coordinates
ε = dispassion rate of turbulence kinetic energy
λ_f = friction factor
ν = kinematic viscosity
ν_t = eddy diffusivity
$\sigma_k, \sigma_\varepsilon$ = effective Prandtl number
τ = shear stress
ρ = density
ϕ = porosity

Special Symbols

$\bar{a}$ = ensemble mean
a' = turbulent fluctuation
a'' = deviation from intrinsic average
$\langle a \rangle^f$ = intrinsic average

Subscripts and Superscripts

dis = dispersion
f = fluid
tor = tortuosity

References

[1] Antohe, B. V., and Lage, J. L., 1997, "A General Two-Equation Macroscopic Turbulence Model for Incompressible Flow in Porous Media," Int. J. Heat Mass Transfer, **13**, pp. 3013–3024.

[2] Vafai, K., and Tien, C. L., 1981, "Boundary and Inertia Effects on Flow and Heat Transfer in Porous Media," Int. J. Heat Mass Transfer, **24**, pp. 195–203.

[3] Nakayama, A., and Kuwahara, F., 1999, "A Macroscopic Turbulence Model for Flow in a Porous Medium," ASME J. Fluids Eng., **121**, pp. 427–433.

[4] Masuoka, T., and Takatsu, Y., 1996, "Turbulence Model for Flow Through Porous Media," Int. J. Heat Mass Transfer, **39**, pp. 2803–2809.

[5] Pedras, M. H. J., and de Lemos, M. S. J., 2001, "Macroscopic Turbulence Modeling for Incompressible Flow Through Undeformable Porous Media," Int. J. Heat Mass Transfer, **44**, pp. 1081–1093.

[6] Nield, D. A., 2001, "Alternative Models of Turbulence in Porous Media and Related Matters," ASME J. Fluids Eng., **123**, pp. 928–931.

[7] de Lemos, M. S. J., 2006, *Turbulence in Porous Media*, Elsevier, Amsterdam.

[8] Guo, B., Yu, A., Wright, B., and Zulli, P., 2003, "Comparison of Several Turbulence Models Applied to the Simulation of Gas Flow in a Packed Bed," *Proceedings of the Third International Conference on CFD in the Minerals and Process Industries*, CSIRO, Melbourne, Australia, Dec. 10–12, pp. 509–514.

[9] Guo, B., Yu, A., Wright, B., and Zulli, P., 2006, "Simulation of Turbulent Flow in a Packed Bed," Chem. Eng. Technol., **29**, pp. 596–603.

[10] DesJardin, P. E., Nelsen, J. M., Gritzo, L. A., Keyser, D. R., Ghee, T. A., Disimile, P. J., and Tucker, J. R., 2001, "Towards Subgrid Scale Modeling of Suppressant Flow in Engine Nacelle Clutter," *Halon Options Technical Working Conference*, Albuquerque, NM, Apr. 24–26, pp. 99–110.

[11] Chandesris, M., Serre, G., and Sagaut, P., 2006, "A Macroscopic Turbulence Model for Flow in Porous Media Suited for Channel, Pipe, and Rod Bundle Flows," Int. J. Heat Mass Transfer, **49**, pp. 2739–2750.

[12] Alvarez, G., and Flick, D., 2007, "Modelling Turbulent Flow and Heat Transfer Using Macro-Porous Media Approach Used to Predict Cooling Kinetics of Stack of Food Products," J. Food. Eng., **80**, pp. 391–401.

[13] Hoffmann, M. R., 2004, "Application of a Simple Space-Time Averaged Porous Media Model to Flow in Densely Vegetated Channels," J. Porous Media, **7**, pp. 183–191.

[14] Pinson, F., Gregoire, O., and Simonin, O., 2006, "Macro-Scale Modeling of Turbulence Based on a Two Scale Analysis in Porous Media," Int. J. Heat Fluid Flow, **27**, pp. 955–966.

[15] Takeda, K., 1994, "Mathematical Modeling of Pulverized Coal Combustion in a Blast Furnace," Ph.D. thesis, Imperial College, London.

[16] Nakayama, A., 1995, *PC-Aided Numerical Heat Transfer and Convective Flow*, CRC, Boca Raton, FL.

[17] Kuwahara, F., Kameyama, Y., Yamashita, S., and Nakayama, A., 1998, "Numerical Modeling of Turbulent Flow in Porous Media Using a Spatially Periodic Array," J. Porous Media, **1**, pp. 47–55.

[18] Fand, R. M., Kim, B. Y. K., Lam, A. C. C., and Phan, R. T., 1987, "Resistance to Flow of Fluids Through Simpae and Complex Porous Media Whose Matrices are Composed of Randomly Packed Spheres," ASME Trans. J. Fluids Eng., **109**, pp. 268–274.

[19] Kuwahara, F., Yamane, T., and Nakayama, A., 2006, "Large Eddy Simulation of Turbulent Flow in Porous Media," Int. Commun. Heat Mass Transfer, **33**, pp. 411–418.

[20] Bey, O., and Eigenberger, G., 1997, "Fluid Flow Through Catalyst Filled Tubes," Chem. Eng. Sci., **52**, pp. 1365–1376.

[21] Chen, Y. S., and Kim, S. W., 1987, "Computation of Turbulent Flows, Using an Extended k-ε Turbulence Closure Model," NASA CR-179204.

[22] Tennekes, H., and Lumley, J. L., 1972, *A First Course in Turbulence*, MIT, Cambridge, pp. 62–63.

[23] Townsend, A. A., 1961, "Equilibrium Layers and Wall Turbulence," J. Fluid Mech., **11**, pp. 97–120.

[24] Kuwahara, F., Nakayama, A., and Koyama, H., 1996, "A Numerical Study of Thermal Dispersion in Porous Media," ASME J. Heat Transfer, **118**, pp. 756–761.

[25] Kaviany, M., 1991, *Principles of Heat Transfer in Porous Media*, Springer-Verlag, New York, pp. 42–49.

[26] Ergun, S., 1952, "Fluid Flow Through Packed Columns," Chem. Eng. Prog., **48**, pp. 89–94.

[27] Comte-Bellot, G., 1965, "Ecoulement Turbulent Entre Deux Parois Paralleles," Publications Scientifiques et Techniques du Ministere de l'Air, No. 419.

[28] Perry, A. E., Henbest, S. M., and Chong, M. S., 1986, "A Theoretical and Experimental Study of Wall Turbulence," J. Fluid Mech., **165**, pp. 163–199.

Performance Characteristics of a Microscale Ranque–Hilsch Vortex Tube

A. F. Hamoudi
Hatch Energy,
1235 North Service Road West,
Oakville, ON, L6M 2W2, Canada

A. Fartaj

G. W. Rankin[1]
e-mail: rankin@uwindsor.ca

Department of Mechanical, Automotive
and Materials,
University of Windsor,
Windsor, ON, N9B 3P4, Canada

The results of an experimental investigation of the energy separation performance of a microscale Ranque–Hilsch vortex tube are presented. The supply channel Reynolds number of a microscale Ranque–Hilsch vortex tube is varied over a considerable range, which extends into the laminar flow regime in order to determine the minimum conditions for cooling. Experiments are conducted for a fixed geometry and control valve setting. At low Reynolds numbers based on the inlet tube hydraulic diameter and average velocity, the results exhibit an increase in dimensionless temperature in both the hot and cold outlets as the Reynolds number is increased from zero, reaching maximum values below 500 and 1000, respectively. The hot outlet dimensionless temperature decreases after reaching its maximum and achieves a minimum value at a Reynolds number below 1500. It then increases steadily with further increases in Reynolds number. The cold outlet dimensionless temperature decreases steadily after the maximum to become negative at a Reynolds number of approximately 1800. This implies that the cooling effect occurs at Reynolds numbers consistent with turbulent flow. The performance characteristics of the microscale vortex tube operating at higher inlet pressures of 200 kPa, 300 kPa, and 400 kPa with an average inlet temperature of 293.6 K are also presented for cold air mass ratio values over the range of 0.05–0.95. An increase in the inlet pressure causes the values of the dimensionless cold temperature difference to increase over the whole range of the cold air mass fraction. An unstable operation is observed at a length to diameter ratio of approximately 10, causing radial mixing between the cold and hot flow streams and a dramatic change in the cold mass flow fraction plot.

[DOI: 10.1115/1.2969442]

Keywords: Ranque–Hilsch effect, microfluidics, vortex cooling, energy separation

1 Introduction

The development of new microfabrication techniques has led to a resurgence of research in microfluidic devices. The devices that have received much attention in the literature include pumps, valves, flow sensors, and heat exchangers [1]. The performance of microscale Ranque–Hilsch tubes, nonmoving part pneumatic devices that separate cold fluid from hot fluid for the purpose of cooling, has not received much attention. Traditionally, the vortex tube has been used in many low temperature applications where efficiency is not the most important factor. For example, the vortex tube has been used to cool parts of machines, dehumidify gas samples, cool electronic control enclosures, chill environmental chambers, and test temperature sensors. A microscale Ranque–Hilsch tube in combination with a microfluidic pump has potential application in the cooling of electronic chips.

The phenomenon of temperature separation occurring inside a cylindrical tube was reported for the first time by a French physicist by the name of Ranque [2], who applied for a U.S. patent and subsequently presented a paper to the French Society of Physics [3]. The discovery was further advanced by Hilsch in 1947 [4], who published some constructional details of the vortex tube along with the performance curves of the device for different tube diameters at various operating conditions. The vortex tube is a very simple device without moving parts (i.e., diaphragm, pistons, shafts, etc.), as shown in Fig. 1. In this arrangement a stream of a compressed gas (usually air) is injected tangentially into the vortex tube, which has a diameter D, using one or more nozzles symmetrically located around the tube. The injected flow accelerates at the entrance, establishing a strong swirl flow, which causes a region of increased pressure near the wall and a region of decreased pressure near the axis.

The presence of an end wall alongside the inlet nozzles forces some of the injected gas to flow axially in a helical motion toward the far end of the tube (the hot end) where a control valve is located. In the usual operation of this device, the flow through the hot end is restricted by partially closing the control valve. This causes even the low pressure at the center of the tube to be higher than atmospheric, and hence flow exits the central orifice in the end wall. This also causes some of the flow that had been directed to the far end of the tube to reverse direction along the center of the tube and also to leave the tube through the central orifice. The gas escaping near the tube wall at the far end of the inlet nozzles has a higher stagnation temperature than the incoming gas, and the gas exiting through the central orifice has a lower stagnation temperature than the inlet gas.

A very low temperature can be obtained from the cold end by operating the device at a supply pressure of a few atmospheres. For example, Hilsch [4] operated a 9.6 mm diameter tube using compressed air at an inlet pressure of approximately 600 kPa and an inlet temperature of 293 K to produce a cold temperature, T_c, of 245 K. The temperatures of the hot and the cold stream are varied by properly changing the cold mass ratio, $\dot{m}_c/\dot{m}_o$, which can be entirely regulated through the control valve located at the hot exit.

---

[1] Corresponding author.

Contributed by the Fluids Engineering Division of ASME for publication in the JOURNAL OF FLUIDS ENGINEERING. Manuscript received June 28, 2007; final manuscript received May 18, 2008; published online September 8, 2008. Assoc. Editor: Steven Ceccio. Paper presented at the 2006 ASME International Mechanical Engineering Congress (IMECE2006), Chicago, IL, November 5–10, 2006.

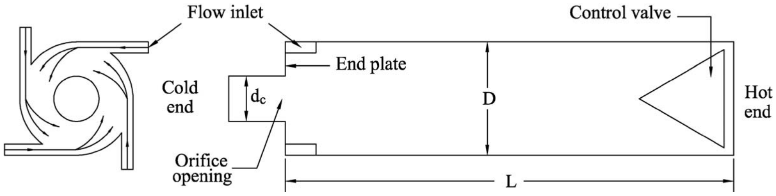

Fig. 1 Vortex tube schematic drawing

2 Literature Review

The most recent review of the literature related to the Ranque–Hilsch tube is given in the thesis of Gao [5]. Previous reviews [6–8] reveal hundreds of papers dealing with this topic. Only those papers pertinent to this study will be mentioned in the following. In spite of the large volume of research that has been devoted to this subject over the years, there is still a disagreement regarding the mechanism that accounts for the operation of this device. Although it has been shown that energy separation can theoretically occur in laminar flow [9,10], most explanations involve turbulent fluctuations [11]. Bruun [12] and Hinze [13] explained the mechanism of the energy separation as mainly being caused by the adiabatic contraction and expansion of turbulent eddies in a centrifugal pressure field. The turbulent fluid parcels achieve temperatures different from that of their new surrounding, hence transferring heat from the low temperature regions to the high temperature regions. Kurosaka [14] gave an acoustic streaming explanation, while others claimed that the operation is based on secondary flows and a thermodynamic refrigeration cycle [15].

The only study that was specifically directed toward microscale vortex tube devices was that of Dyskin and Kramarenko [16]. They reported experimentally determined performance characteristics (adiabatic efficiency) for vortex tubes operating with a pressure ratio of 6 with diameters of 1 mm, 2 mm, and 3 mm. The corresponding mass flow rates were 14.3×10^{-5} kg/s, 40.0×10^{-5} kg/s, and 94.0×10^{-5} kg/s, respectively. Although details of the geometry are not given, an estimate of the inlet Reynolds numbers used for these cases yields values greater than 6000. It was, however, noted that the cooling effect decreased with decreasing flow rate. This is consistent with the speculation of Negm et al. [17] that the cooling effect should decrease with decreasing Reynolds number.

The objective of the current work is to experimentally investigate the characteristics of a vortex tube at supply channel Reynolds numbers that extend from the laminar into the turbulent flow regime in order to determine the minimum operating conditions of these devices for cooling applications. The performance of the microscale vortex tube over a wide range of possible cold air mass ratios for higher inlet pressure values of 200 kPa, 300 kPa, and 400 kPa is also determined. In addition, the effect of tube length and cold outlet orifice size on the performance characteristic of microscale vortex tubes is determined.

3 Experimental Facility

A 2 mm diameter vortex tube was manufactured at the University of Windsor from pieces of Plexiglas and aluminum using a multiple layered fabrication technique. This allowed accurate machining of the inlet slots, the cold outlet orifice, and the hot flow control valve. The Plexiglas layers were sandwiched between two aluminum end pieces, which represent the hot and the cold end of the vortex tube, as shown in Fig. 2. Four bolts and nuts were used to tighten the different pieces of the vortex tube running through longitudinal holes at the corners of each piece. Two stainless steel guide pins were used to align the multiple layers forming the vortex tube.

Different tube lengths are achieved by using extension pieces of different thicknesses. The thicknesses of the extension pieces are 5 mm, 10 mm, and 20 mm and allow variation in the tube length in the range of 20–100 mm, which gives L/D values in the range of 10–50. Three different sizes of the cold orifice diameter are used in this research to investigate its effect on the vortex tube performance. These sizes are 0.5 mm, 0.8 mm, and 1.1 mm and give d_c/D ratios of 0.25, 0.40, and 0.55, respectively. The cold orifice piece forms one end of the vortex tube, while the control valve forms the other end of the vortex tube.

Since the scope of this research is to investigate the vortex effect at supply channel Reynolds numbers that extend from the laminar into the turbulent flow regime, the supply air slots are designed to be very small to ensure a laminar flow in that region at low values of supply pressure. The hydraulic diameter of the supply channel is 229 μm. This gives a ratio of the nozzle area, A_n, to the tube area, A_d, of 0.15. This ratio is more than 25% larger than that suggested by Soni and Thompson [18] to obtain a maximum cold temperature drop, ΔT_c. The main inlet nozzle section is machined from one piece of Plexiglas material having a square cross-sectional area of 30×30 mm with a 20 mm thickness. As depicted in Fig. 3, the inlet connection for the compressed air line (1) is attached to the body of this section of the vortex tube. A 4×3 mm channel (3) is connected to the inlet nozzle (1) through a longitudinal hole (2). The channel (3) is provided to act as a pressurized manifold so that the flow enters the inlet slots (4) at a pressure and a temperature very close to those measured at the inlet nozzle (1). The vortex is formed by four inlet slots (4) that are symmetrically located around the 2 mm tube diameter (5). The inlet slots (4) are 382 μm in width and 164 μm in height each.

As indicated in Fig. 4, filtered and dehumidified compressed air passes through a control valve (1), a 5 μm air filter (2), and a pressure-regulating valve (3) before entering the vortex tube. A manometer (4) is used to measure the low supply pressures, which range from 2 kPa to 17.5 kPa with an uncertainty of ±0.01 kPa. For the supply pressures within the range of 18–82 kPa, a Bourdon pressure gage with an uncertainty of ±1.7 kPa is used, and for pressures of 200 kPa, 300 kPa, and 400 kPa, a higher range Bourdon pressure gage having an uncertainty of ±3.4 kPa is used. The temperatures of the inlet, cold, and hot air are measured using type T thermocouple probes located at (5), (8), and (11) respec-

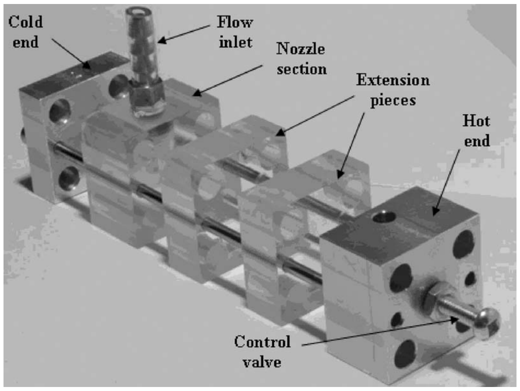

Fig. 2 Expanded view of the microscale vortex tube

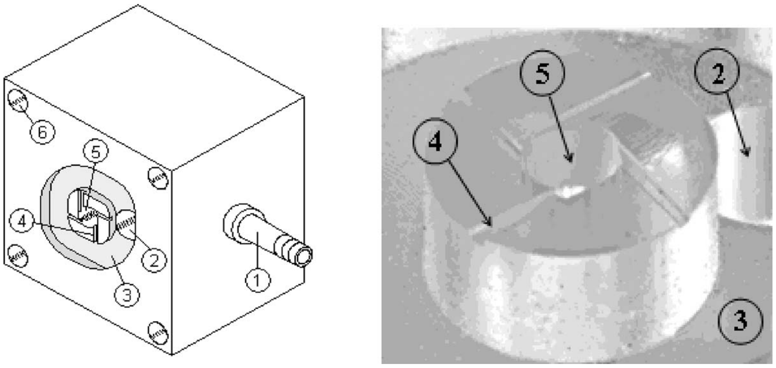

Fig. 3 Nozzle section of the vortex tube. (Left) Front view of the inlet nozzle section. (Right) Perspective view showing the details of the inlet nozzles.

tively. The compressed air is injected into the vortex tube through the manifold (6) and the inlet slot (7). The cold outlet exit pressure, P_c, and hot outlet exit pressure, P_h, are measured using digital manometers (9) and (12) with an uncertainty of 0.01 kPa. The volumetric flow rate of air, $\dot{Q}$, exiting the cold and hot openings is measured using separate rotameters, (10) and (13). The rotameters are calibrated while connected to the apparatus, as shown in the experimental setup presented in Fig. 4, so that both are subjected to the same working pressures as encountered in the experiment to avoid the need for corrections.

Atmospheric pressure and temperature are measured to an uncertainty of ±0.7 kPa and ±0.5 K respectively. Assuming an ideal gas, the densities of the hot and cold gases are calculated using the equation of state. Using the uncertainty values mentioned above gives an uncertainty in air density of $\pm 2.3 \times 10^{-3}\ \mathrm{kg/m^3}$.

The individual mass flow rates leaving the cold and hot ends are determined, knowing the measured values of the volume flow rate and the associated densities calculated using the perfect gas law and the measured temperature and pressure. The total flow rate entering the apparatus is obtained by the summation of the cold flow with the hot mass flow rate values to determine the cold air mass ratio, y_c, which is defined as

$$y_c = \frac{\textit{cold gas mass flow rate}}{\textit{total inlet gas mass flow rate}} \tag{1}$$

The uncertainty in the cold air mass ratio depends on the values of the mass flow rate. However, they are all within the range of ±0.018 to ±0.13. The inlet Reynolds number is also calculated using

$$\mathrm{Re} = \frac{\dot{m} d_n}{4A\mu} \tag{2}$$

where $\dot{m}$ is the mass flow entering the vortex tube through one slot, d_n is the equivalent diameter of that inlet slot, equal to 229 μm, and A is the cross-sectional area of one of the inlet slots, found to be $6.25 \times 10^{-8}\ \mathrm{m}^2$. The viscosity of the inlet air, μ, is taken to be 1.82×10^{-5} kg/m s. This results in an uncertainty in Re that is within the range of ±73 to ±196.

At the low values of operating pressure used in the experiments, the adjustment of the cold air mass ratio using the control valve placed at the hot end significantly altered the exit pressures of the cold and hot exit tubes due to the resistance of the rotameters. Each is altered by a different amount, which effectively created a different exit pressure in each case. To avoid this problem, the flow of the cold or the hot air stream is restricted with a flow

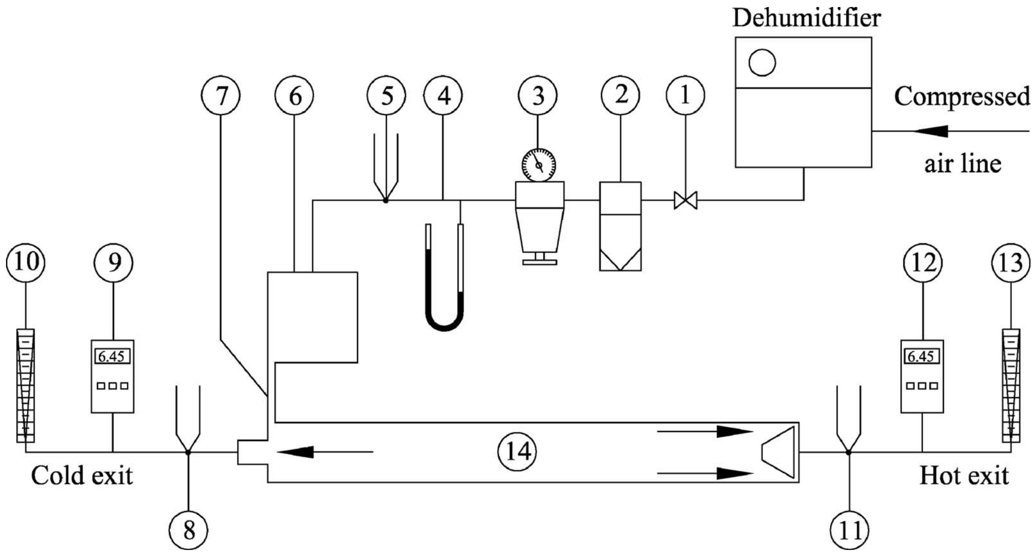

Fig. 4 Experimental test facility

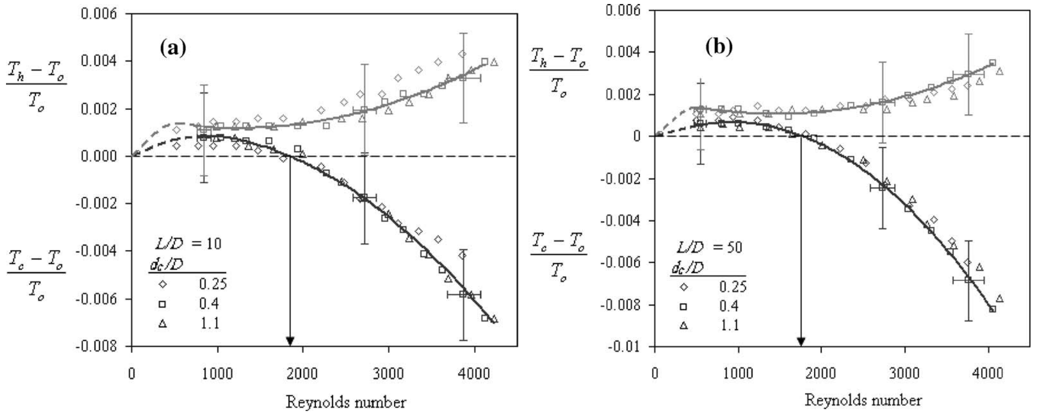

Fig. 5 Temperature separation at low Reynolds numbers for $L/D=10$ and 50

restriction device in such a manner that the pressures of the cold and hot air exit flows are approximately kept equal. The method of Kline and McClintock [19] is used to determine the propagation of uncertainties in the above calculations. Further details of the test facility may be found in the thesis of Hamoudi [20].

4 Experimental Methodology

Two types of experimental tests are conducted in this study to investigate the characteristics of the microscale vortex tube. These are referred to as the low pressure tests and the high pressure tests. Each test is conducted at a different tube length, L, orifice diameter, d_c and inlet pressure, P_o. A set of nine combinations of vortex tube geometrical parameters consisting of three different L/D ratios (10, 30, and 50) with three different d_c/D ratios (0.25, 0.4, and 0.55) forms the geometry of the devices under investigation.

In the low pressure tests, the performance characteristics of the microscale vortex tubes are determined at low supply pressure and fixed geometry. This means that the control valve is arbitrarily opened to a certain setting and is kept constant throughout the entire set of tests as the supply pressure and, hence, the Reynolds number is varied. The supply pressures range from approximately 2.5 kPa to 82 kPa, giving a Reynolds number range of 500–4500. The measured cold and hot air dimensionless temperatures of the air leaving the vortex tube are determined using the expressions $(T_c-T_o)/T_o$ and $(T_h-T_o)/T_o$, where T_c, T_h, and T_o are the cold outlet, hot outlet, and inlet temperatures, respectively. These parameters are chosen to eliminate the effect of the inlet air temperature. The uncertainty in both the dimensionless cold and hot temperatures is found to be approximately ± 0.0019.

The high pressure tests are conducted using the same tube geometrical combinations as in the low pressure tests. In this case, however, the performance characteristics of the microscale vortex tube at higher inlet pressures and at different cold air mass ratios are determined. The supply pressure values are 200 kPa, 300 kPa, and 400 kPa, and the value of y_c is varied from approximately 0.05 to 0.95 by adjusting the control valve at the hot end.

5 Results

The results are best discussed under the headings of low pressure performance tests, high pressure performance tests, and the effect of geometry. Each of these are considered separately in the following paragraphs.

5.1 Results of Low Pressure Performance Tests. For the working pressures used in this experiment, the cold and hot exit air velocities are found to be in the ranges of 0.15–1.84 m/s and 0.14–1.08 m/s respectively. The maximum dynamic temperatures calculated for both cold and hot temperatures are found to be 1.7×10^{-3} K and 5.8×10^{-4} K, respectively and are hence negligible. The total and static temperatures are therefore essentially equal.

The plots of dimensionless cold and hot air temperatures as a function of the inlet Reynolds number for $L/D=10$ and 50 are presented in Figs. 5(*a*) and 5(*b*), respectively. The uncertainties in these figures and the remaining figures are indicated by the error bars unless they are within the size of the symbol. The minimum total flow rate has a value of 9.72×10^{-6} kg/s, which results in a Reynolds number of approximately 500. It can be seen that at this low Reynolds number, both hot and cold exit temperatures are higher than the inlet temperature. The trend of the curves at Reynolds numbers below 500 is estimated, as shown in the dashed line, as it is known that all temperatures must be equal for the case of no flow. At these low Reynolds numbers, the vortex motion is not likely well established and the effect of the viscous term is the dominating factor. Viscous dissipation, hence, causes the increase in the temperatures of both outlet streams. In the case of the hot outlet, the dimensionless temperature decreases after reaching its maximum at a Reynolds number of about 500 after which it achieves a minimum value at a Reynolds number of approximately 1500. The curve then increases steadily with a further increase in Reynolds number. The cold outlet dimensionless temperature decreases steadily after reaching the maximum at a Reynolds number of about 800 to become negative at Reynolds numbers over 1800. In the cases of both hot and cold flows, the trend of increasing temperatures with Reynolds number is reversed at a Reynolds number of approximately 500 for the hot flow and 800 for the cold flow. These are roughly consistent with the critical Reynolds number estimated for tubes with a length shorter than that required for fully developed flow, which is common in micro-fluidic devices [1]. It is speculated that the reversal of temperature increase is due to the initiation of turbulence either in the supply nozzle or in the jet that forms in the vortex chamber just downstream of the supply nozzle and to the mechanisms of energy transfer that are associated with the turbulence that have been reported in the literature [12,13].

The crossover Reynolds number and the curve trends are approximately the same for $L/D=10$ and 50, and the values are within the data uncertainty. Similar results (not shown) were found for $L/D=30$. It can be concluded that the inlet nozzle geometry is the most important factor as it affects the Reynolds number. It should be recalled that this part of the test is conducted at an arbitrary fixed hot control valve opening.

One might expect that the cold air mass fraction for such a case would remain the same if the resistance to flow out of the cold and hot ends is constant. As indicated in Fig. 6, for Reynolds numbers below approximately 2000, the value of the cold air mass fraction decreases with an increase in the Reynolds number due to flow resistance changes. It remains almost constant for Reynolds num-

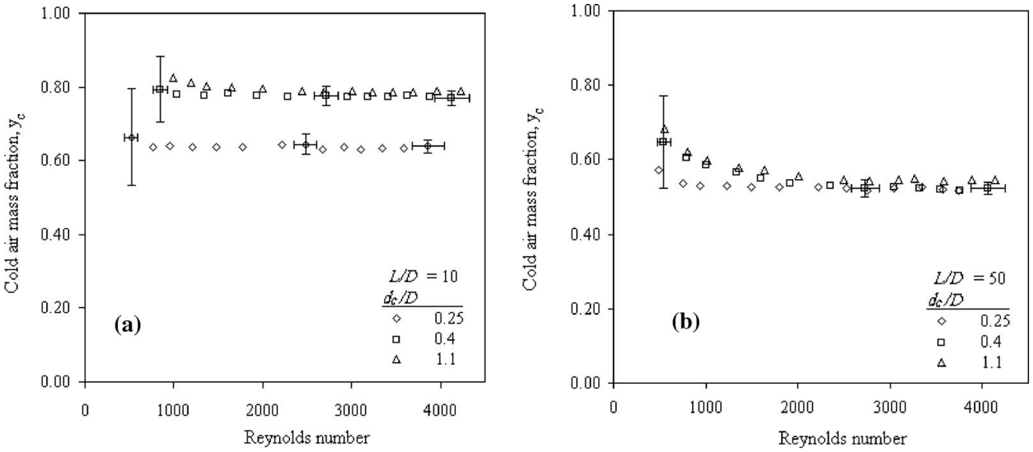

Fig. 6 Variation in the cold air mass ratio with Reynolds number for $L/D=10$ and 50

ber values above 2000. This general trend is similar to that of other fluid mechanic quantities such as drag coefficient and friction factor.

For smaller orifice diameter and hence smaller d_c/D ratio, the cold air mass fraction is decreased. This is likely due to the increase in the resistance in the cold flow. The cold air mass fraction is also reduced with higher values of the L/D ratio. This variation is not as obvious as in the case of d_c/D. An increase in the L/D value changes the internal flow pattern, allowing the cold air to travel toward the hot end before reversing direction and passing through the cold exit. This increased cold flow path causes larger resistance. The change in the inlet Reynolds number with increasing supply pressure is shown in Fig. 7. This reflects the total resistance of the flow through both hot and cold air outlets. In general, for the same inlet pressure, there was a slight shift to the right of the curve in the Reynolds number as the d_c/D increases. This is as expected since decreasing *dc* has the effect of increasing the total resistance. It would be expected that increasing the L/D ratio would also increase the pressure required for any Reynolds number. For the shortest L/D ratio, a higher pressure is, however, required to achieve the same Reynolds number value obtained for the longer L/D ratio. This anomaly may be due to the pressure fluctuation observed for this case and mentioned later.

5.2 Results of High Pressure Performance Tests. The dimensionless hot and cold temperatures are plotted as functions of the cold air mass ratio, with the inlet pressure as a parameter in Figs. 8(*a*) and 8(*b*) for the smallest L/D ratio of 10. The cold flow dimensionless temperature is represented by the lower curves, while the upper curves are for the hot flow dimensionless temperature. The symbols in these particular curves represent data points collected at different cold air mass ratios and different inlet pressures, and the lines are interpolating splines.

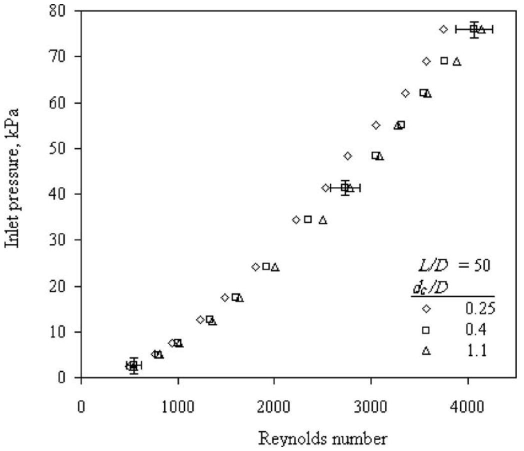

Fig. 7 Inlet pressure as a function of Reynolds number

In Fig. 8(*a*), for an inlet pressure of 400 kPa, when the value of y_c is increased, the temperature of the cold flow drops until it reaches its lowest value at $y_c=0.22$. With a slight increase in y_c, a rather sharp increase in the cold flow temperature is observed. The increase is less obvious for the 300 kpa and 200 kPa inlet pressure cases. It is noticed that the hot flow temperature experiences an abrupt drop at approximately the same value of y_c. The drastic changes are also associated with a noticeable increase in fluctuations in the measured pressures and flow rates of the cold and hot streams under these conditions. It is believed that a flow instability phenomenon is responsible for this occurrence, which causes radial mixing between the cold and hot temperature flows. The instability needs further investigation for a proper explanation. This phenomenon is only observed with the shortest tube length, which has a L/D equal to 10. By further increasing the value of y_c, the cold flow dimensionless temperature increases and approaches zero as y_c approaches 1. For the same $L/D=10$ but with a larger d_c/D ratio, the instability phenomenon and hence the radial mixing between the hot and cold flows still exist for higher inlet pressures as shown in Fig. 8(*b*).

The results obtained for larger L/D ratios as indicated in Figs. 8(*c*)–8(*f*) show a smooth variation in the cold and hot flow temperatures for different inlet pressures and different values of y_c. No sharp increases in the cold flow temperature are observed. As a general observation, an increase in the inlet pressure is seen to cause the values of the dimensionless cold temperature difference to increase over the whole range of the cold air mass fraction. Furthermore, it is found that the cold air mass ratio corresponding to the lowest cold air stream temperature decreases with the increasing supply of pressure for a similar tube geometry.

For $d_c/D=0.25$, the y_c value for the minimum cold flow temperature is found to be in the range of 0.2–0.4. This value of y_c is different from the values for conventional devices (approximately 0.3) and appears to be related to the relative size of the inlet nozzle hydraulic diameter to the size of the orifice diameter used. Similarly, the maximum hot air temperatures are seen to have cold mass ratio values different from those of the conventional devices.

5.3 Effect of Tube Geometry. In this section only the temperature drop is considered as these devices have their primary application in cooling. Two aspects of the geometry are considered: the cold orifice diameter and the tube length.

Figure 9 shows the optimum dimensionless cold temperature

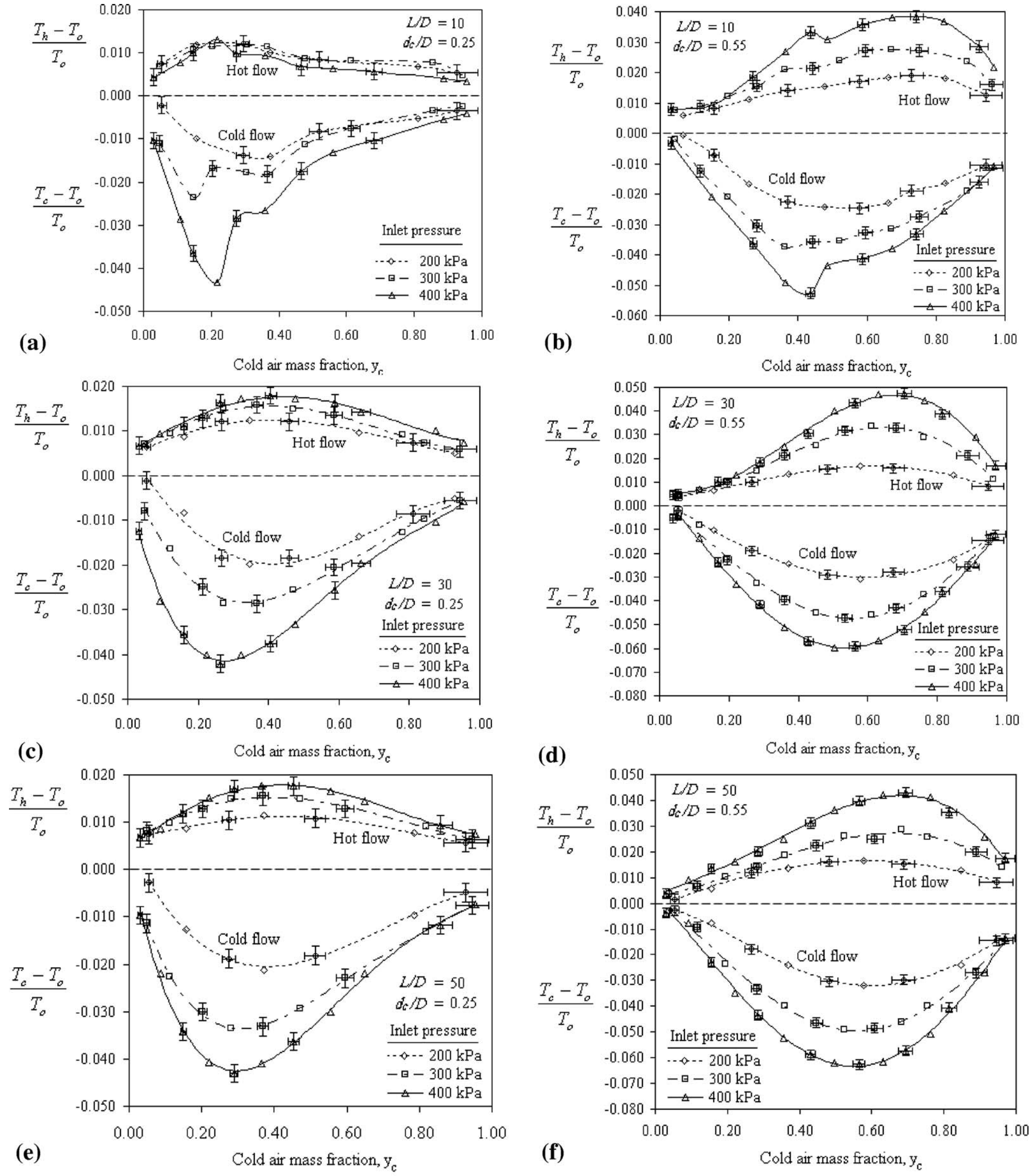

dc/D = 0.25

dc/D = 0.55

Fig. 8 Vortex tube performance for $L/D=10$, 30, and 50; $d_c/D=0.25$ and 0.55 for different inlet pressures

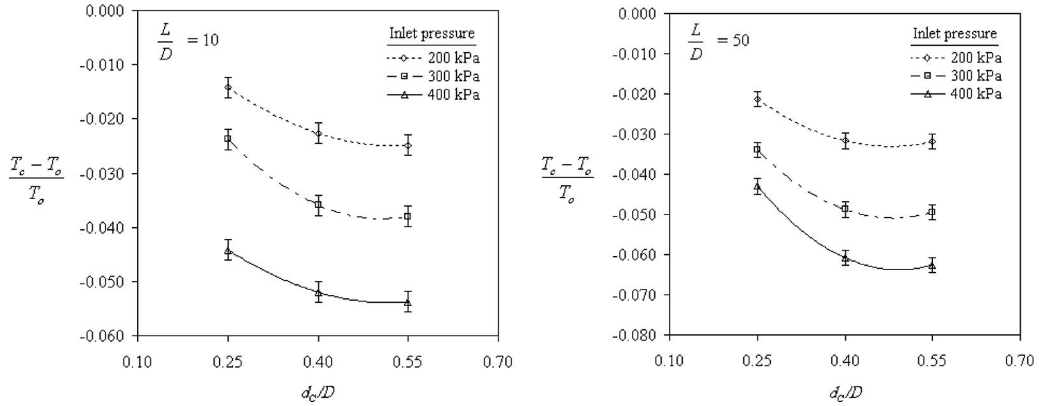

Fig. 9 Optimum conditions versus the dimensionless orifice diameter for $L/D=10$ and 50

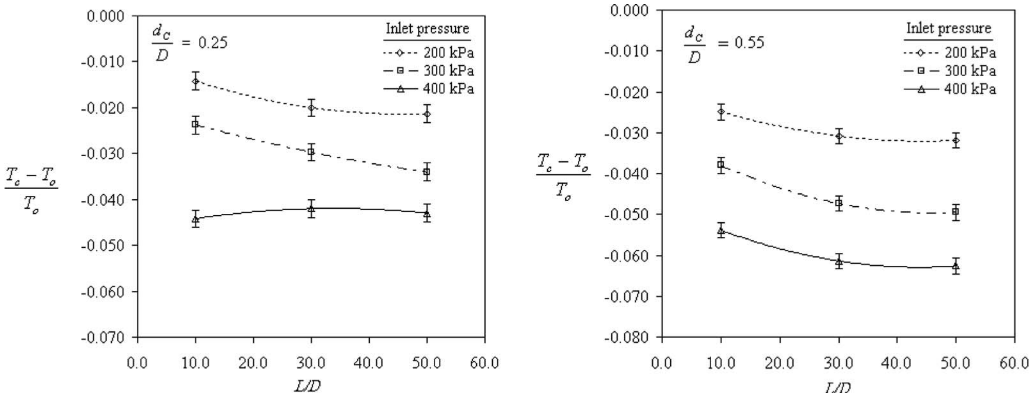

Fig. 10 Optimum conditions versus the dimensionless tube length for $d_c/D=0.25$ and 0.55

performance of the microscale vortex tube for different sizes of the orifice diameter for $L/D=10$ and 50. In all cases, the dimensionless cold temperature decreases with increasing d_c/D ratio reaching constant values at d_c/D in the range of 0.5–0.55. All the results regarding the orifice diameter are in good agreement with the conventional vortex tube [6,21].

The effects of the L/D ratios on the optimum dimensionless cold temperature are shown in Fig. 10. It can be generally observed that the maximum L/D ratio of 50 gives the maximum cold temperature drop. Although the curves do not indicate a mathematical optimum tube length, by looking at the trend of the curves, it can be inferred that increasing the L/D ratio beyond 50 will not be of great advantage. The results of the L/D value obtained are in close agreement with those reported by Dyskin and Kramarenko [16], who also conducted their experiment on a microscale vortex tube.

6 Conclusions

The performance characteristics of a microscale vortex tube are presented over a wide range of working pressures, different cold air mass ratios, different vortex tube lengths, and orifice diameters. Experiments conducted on the microscale vortex tube with a fixed geometry at low Reynolds numbers show the following:

(a) Dimensionless temperature increases in both the cold and hot air flows as the Reynolds number increases from zero and reaches maximum values below approximately 500 and 800 for the hot and cold flows, respectively.
(b) The cold outlet dimensionless temperature decreases steadily after reaching the maximum to become negative at a Reynolds number in the order of 2000. This implies that the cooling effect occurs at inlet Reynolds numbers consistent with the turbulent flow. A determination of the precise mechanism associated with turbulence that causes the cooling effect cannot be made from this study and is a consideration for future work.
(c) Except for low Reynolds numbers (i.e., less than 2000), the cold mass fraction is approximately constant as the Reynolds number increases.

Experiments conducted to determine the performance curves of the microscale vortex tube at high inlet pressures indicate that

(a) the optimum cold air mass fraction, y_c, is not constant and can be higher than the conventional vortex tube
(b) the effects of L/D and d_c/D ratios are similar to those in the conventional devices
(c) an unstable operation can occur at small L/D and high inlet pressures

Acknowledgment

This project was mainly funded and supported through Discovery Grants from the Natural Sciences and Engineering Research Council of Canada (Grant Nos. OGP0001403 and OGP0105727).

Nomenclature

A = cross-sectional area of the inlet slot
c_p = specific heat at constant pressure
D = vortex tube inner diameter
d_c = cold exit (orifice) diameter
d_n = equivalent diameter of the inlet slot
L = vortex tube length
$\dot{m}$ = mass flow rate
P = pressure
R = gas constant
T = temperature
u = axial velocity
y_c = cold gas mass flow ratio

Greek Symbols

ρ = density
μ = dynamic viscosity
η = efficiency
ν = kinematics viscosity

Subscripts

s = static
t = total
c = cold
h = hot
o = inlet

References

[1] Gravesen, P., Branebjerg, J., and Jensen, O. S., 1993, "Microfluidics: A Review," J. Micromech. Microeng., **3**(4), pp. 168–182.
[2] Ranque, G., 1932, "Method and Apparatus for Obtaining From a Fluid Under Pressure Two Currents of Fluids at Different Temperatures," U.S. Patent No. 1.952,281.
[3] Ranque, G., 1933, "Expériences Sur La Détente Giratoire Avec Productions Simultanées D'un Enchappement D'air Chaud Et D'un Enchappement D'air Froid," J. Phys. Radium, **4**, pp. 1125–1155.
[4] Hilsch, R., 1947, "The Use of the Expansion of Gases in a Centrifugal Field as Cooling Process," Rev. Sci. Instrum., **18**(2), pp. 108–113.
[5] Gao, C., 2005, "Experimental Study on the Ranque-Hilsch Vortex Tube," Ph.D. thesis, Department of Applied Physics, Eindhoven University of Technology, The Netherlands.
[6] Cockerill, T. T., 1998, "Thermodynamics and Fluid Mechanics of a Ranque-Hilsch Vortex Tube," MS thesis, Department of Engineering, University of Cambridge, England.
[7] Westley, R., 1954, *A Bibliography and Survey of the Vortex Tube*, College of Aeronautics, Cranfield, England, Cranfield College Note 9.

[8] Soni, Y., 1973, "A Parameteric Study of the Ranque-Hilsch Tube," Ph.D. thesis, University of Idaho Graduate School, ID.
[9] Kassner, R., and Knoernschild, E., 1948, "Friction Laws and Energy Transfer in Circular Flow," Wright-Patterson Air Force Base, Technical Report No. F-TR-2198-ND.
[10] Deissler, R. G., and Perlmutter, M., 1958, *An Analysis of the Energy Separation in Laminar and Turbulent Compressible Vortex Flows*, Heat Transfer and Fluid Mechanics Institute, Stanford University Press, Palo Alto, CA, pp. 40–53.
[11] Deissler, R. G., and Perlmutter, M., 1960, "Analysis of the Flow and Energy Separation in a Turbulent Vortex," Int. J. Heat Mass Transfer, **1**, pp. 173–191.
[12] Bruun, H., 1969, "Experimental Investigation of the Energy Separation in Vortex Tube," J. Mech. Eng. Sci., **11**(6), pp. 567–582.
[13] Hinze, O., 1975, *Turbulence*, McGraw-Hill Series in Mechanical Engineering, 2nd ed., McGraw-Hill, New York.
[14] Kurosaka, M., 1982, "Acoustic Streaming in Swirling Flow and the Ranque-Hilsch (Vortex-Tube) Effect," J. Fluid Mech., **124**, pp. 139–172.
[15] Ahlborn, B., Keller, J. U., and Rebhan, E., 1998, "The Heat Pump in a Vortex Tube," J. Non-Equilib. Thermodyn., **23**(2), pp. 159–165.
[16] Dyskin, M., and Kramarenko, P., 1984, "Energy Characteristics of Vortex Microtube," J. Eng. Phys., **47**(6), pp. 1394–1395.
[17] Negm, M. I. M., Serag, A. Z., and Ghany, S. M. Abdel, 1988, "Generalized Correlations for the Process of Energy Separation in Vortex Tube," Modelling, Simulation & Control B: Mechanical & Thermal Engineering, Materials & Resources, Chemistry, **14**(4), pp. 47–64.
[18] Soni, Y., and Thompson, W. J., 1975, "Optimal Design of the Ranque-Hilsch Vortex Tube," ASME Trans. J. Heat Transfer, **94**(2), pp. 316–317.
[19] Kline, S. J., and McClintock, F. A., 1953, "Describing Uncertainties in Single-Sample Experiments," Mech. Eng. (Am. Soc. Mech. Eng.), **75**, pp. 3–8.
[20] Hamoudi, A., 2006, "An Investigation of Micro-Scale Ranque-Hilsch Vortex Tube," MS thesis, Mechanical, Automotive and Materials Engineering Department, University of Windsor, Windsor, ON, Canada.
[21] Saidi, M. H., and Valipour, M. S., 2003, "Experimental Modeling of Vortex Tube Refrigerator," Appl. Therm. Eng., **23**, pp. 1971–1980.

Microscale Flow Through Channels With a Right-Angled Bend: Effect of Fillet Radius

V. Raghavan[1]
Assistant Professor
Thermodynamics and Combustion Laboratory,
Department of Mechanical Engineering,
Indian Institute of Technology Madras,
Tamilnadu, Chennai 600 036, India

B. Premachandran
Engineer
AECI Pvt. Limited,
Old Madras Road,
Karnataka, Bangalore 560 016, India

Microscale gas flow through channels with a right-angled bend has been numerically analyzed to study the effect of the fillet radius on flow characteristics. The flow is assumed to be incompressible, laminar, and hydrodynamically developing. The fillet radius has been varied from zero, representing a sharp corner, to 0.6 times the height of the channel. The Knudsen number has been varied from zero, representing no-slip at the boundary, to 0.1, which is the limiting case for the slip-flow regime. A low Reynolds number of value 1 has been considered in the present study, which makes the flow to be within the incompressible slip-flow regime. The flow characteristics in terms of velocity profiles, velocity vectors, and the pressure ratio between the inlet and outlet of the channel have been presented for several cases. Results show that for the case of the fillet radius equal to zero, the flow separation occurs after the bend and due to this, the exit velocity profile changes significantly. The highest pressure ratio between the inlet and the outlet is required to maintain a specific mass flow rate for this case. The cases with a nonzero fillet radius exhibit exit velocity profiles identical to that of a straight channel. The pressure ratio decreases when the fillet radius and the Knudsen number are increased. [DOI: 10.1115/1.2969455]

Keywords: *microchannel, microflows, slips flows, fillet effect, pressure drop*

Introduction

Micron-sized devices are fabricated using micro-electronic fabrication processes and are extensively used in micro-electro-mechanical systems (MEMSs). Microfabricated devices are used in electronics cooling, sensor applications, and fluidic control systems. In order to design such devices, a thorough knowledge of the flow field and the pressure drop in similar-sized geometries is necessary. Several experimental and theoretical studies on microflows through various microdevices are reported in literature [1–10]. The measured friction factors in the above studies suggested that there is less momentum exchange between the fluid and the solid surface for the microflow process. It was also observed that the pressure drop along the microchannel was lower than that of the no-slip-flow regime. Simulations of gas flows in microgeometries have been carried out by Quarmby [11], Beskok and Karniadakis [12], Chen et al. [13], Barber and Emerson [14], and Raju and Roy [15]. Papautsky et al. [16] and Rostami et al. [17] recently reviewed the flow through microchannels. In the above studies, numerical analysis was carried out in the range of continuum and slip-flow regimes. The ratio of the mean free path λ and the characteristic length of the geometry H, termed as the Knudsen number (Kn), ranges between 0 and 0.1 to cover the continuum to slip-flow range. In the slip-flow regime ($0.001 < \mathrm{Kn} < 0.1$), the governing equations are solved in conjunction with slip-boundary conditions [2,8,10,14,15,18].

Bends or curves in microchannels are present either due to design concepts or due to constraints. Lee et al. [19] investigated the gas flow in microchannels with bends, where they measured the mass flow rates and the pressure distributions. They showed that an additional pressure drop is produced due to the presence of a bend. Raju and Roy [15] also showed similar results with their numerical simulations in their investigation of slip flows through microchannels with two 90 deg bends. They considered the 2D flow in their study because of the very low ratio of the channel height to its width. They reported that for a given inlet to outlet pressure ratio, the mass flow rate for the geometry considered is reduced by around 160% than that obtained for a straight microchannel, which means that to maintain a particular mass flow rate, a higher pressure drop is required when a bend is present. Typically, various devices, such as one for the passive mixing of liquids, require microchannels with more number of bends [20].

Investigation of the pressure distribution along the microchannels with bends is therefore necessary in order to arrive at an optimum size and shape of the device. It is obvious that a sharp corner present in a bend would induce a flow separation after the bend. This flow separation causes an additional pressure drop and an increase in the pumping power required to maintain a particular mass flow rate. A sharp corner can be avoided by adding a fillet radius (radius of curvature) to the bend, without changing the angle of the bend. In doing so, it is expected that the flow would be streamlined and the pressure drop due to flow separation would be minimized. Even though investigations of the flow field in microchannels with bends have been reported, the effect of the fillet radius has not been reported. Hence, in this paper, a numerical study of the microscale gas flow through channels with a right-angled bend having various fillet radii is presented. The effects of the fillet radius and the Knudsen number on the flow pattern and the pressure drop are presented. A low Reynolds number of value 1 has been employed so as to maintain the flow within the incompressible slip-flow regime. Also, the width of the channel is such that the height to width ratio is very small (the height is around 1 μm and the width is around 20 μm) and due to this the flow is predominantly two dimensional. To study the validity of this statement, a 3D model for simulating the flow through a channel in which width was five times its height was created and solved in FLUENT, a commercial computational fluid dynamics (CFD) software for Kn=0. The exit velocity profiles obtained from the 3D model and the present 2D model are shown in Fig. 1. With this exercise, it can be concluded that employing a 2D solver for the

---

[1] Corresponding author.

Contributed by the Fluids Engineering Division of ASME for publication in the JOURNAL OF FLUIDS ENGINEERING. Manuscript received December 2, 2007; final manuscript received June 4, 2008; published online September 12, 2008. Assoc. Editor: Ali Beskok.

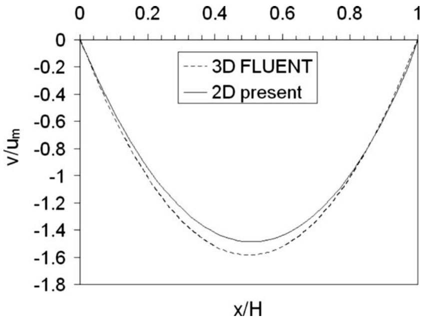

Fig. 1 Flow through a microchannel with a right-angled bend: effect of the 3D flow

case where the height of the channel is around 1 μm and its width is around 20 μm is justified.

Mathematical Model and Method of Solution

The geometry under consideration is shown in Fig. 2. The total length of the right-angled bend is $2L$ and the bend is present at half of its length. The height of the channel is H, which is the characteristic length. The flow is assumed to be laminar, incompressible, and hydrodynamically developing. A pseudotransient approach is used to obtain steady-state solutions. In view of this, the governing equations are given in the time dependent form. The dimensional form of governing equations is as follows.

Continuity equation:

$$\frac{\partial u}{\partial x}+\frac{\partial v}{\partial y}=0 \tag{1}$$

Momentum equations:

$$\frac{\partial u}{\partial t}+u\frac{\partial u}{\partial x}+v\frac{\partial u}{\partial y}=-\frac{1}{\rho}\frac{\partial p}{\partial x}+\nu\left(\frac{\partial^2 u}{\partial x^2}+\frac{\partial^2 u}{\partial y^2}\right) \tag{2}$$

$$\frac{\partial v}{\partial t}+u\frac{\partial v}{\partial x}+v\frac{\partial v}{\partial y}=-\frac{1}{\rho}\frac{\partial p}{\partial y}+\nu\left(\frac{\partial^2 v}{\partial x^2}+\frac{\partial^2 v}{\partial y^2}\right) \tag{3}$$

Boundary conditions:

At the inlet of the computational domain, a uniform velocity profile is assumed.

$$u=u_m=1.0 \tag{4}$$

$$v=0 \tag{5}$$

At the outlet of the channel, the normal derivative to the exit plane is expected to tend to zero and therefore, the following boundary conditions are used:

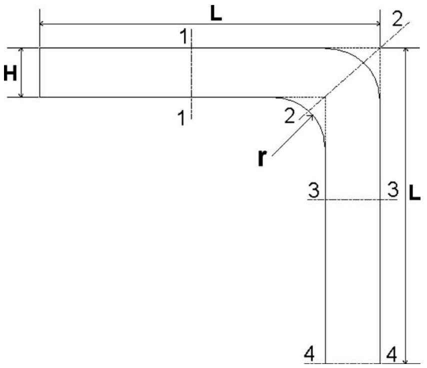

Fig. 2 Computational domain for the microbend; *r* varies from 0 to 0.6*H*, sections where profiles are plotted are shown by 1-1, 2-2, 3-3, and 4-4

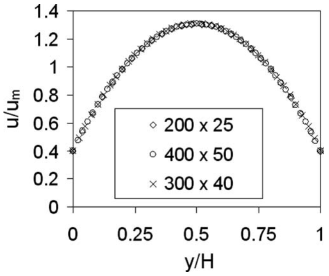

Fig. 3 Validation of the numerical model results with the analytical solution with different grids; Re=1, Kn=0.10

$$\frac{\partial u}{\partial n}=0 \tag{6}$$

$$\frac{\partial v}{\partial n}=0 \tag{7}$$

A first order slip velocity has been employed along the walls [2,8,10,14,15,18], which is valid for $0.001<\mathrm{Kn}<0.1$.

$$u_f-u_w=\frac{2-\sigma}{\sigma}\mathrm{Kn}\frac{\partial u_t}{\partial n} \tag{8}$$

where u_f is the velocity of the fluid, u_w is the velocity of the wall (in this case it is zero), σ is the tangential accommodation coefficient, which has been assigned a value of 0.95 for all the slip-flow cases, and $\partial u_t/\partial n$ is the derivative of the tangential velocity normal to the wall.

Solution Procedure

Complete transient Navier–Stokes equations have been solved by employing a nonorthogonal control/finite volume method. A finite volume method with semicollocated nonorthogonal quadrilateral grids has been used. The semi-implicit method for pressure-linked equations (SIMPLE) algorithm has been employed to correct the pressure field. All the governing equations are solved using a point-by-point Gauss–Seidel iteration method. A convergence criterion defined using the δ relation (refer to Nomenclature) has been imposed for all the variables.

Validation

The numerical model has been validated against analytical results as reported in Ref. [9] for the Poiseuille flow with slip-boundary conditions. A straight channel of height H and a length equal to 40 times the height has been considered. The Reynolds number is defined based on the channel height H and the mean

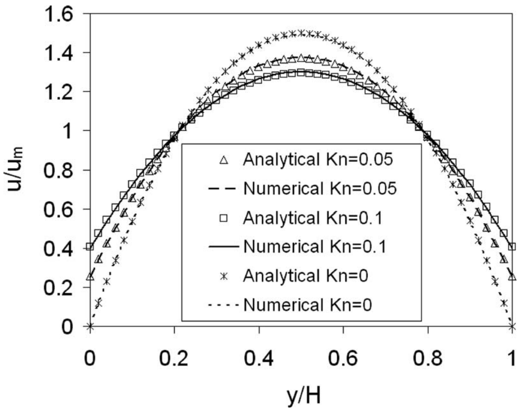

Fig. 4 Validation of the numerical results with the analytical solution [9]; Re=1, various Kn

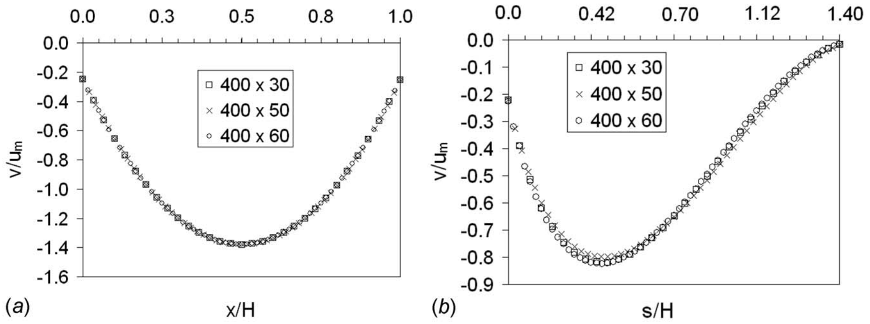

Fig. 5 **(*a*) Profile of the velocity *v* at Section 4 and (*b*) profile of the nondimensional velocity *v* at Section 2 for Re=1, Kn=0.05, and *r*=0.4*H* using different transverse direction grids**

(uniform) inlet velocity u_m and has a value of 1. A grid independence study has been systematically conducted. Figure 3 shows the velocity profiles at the channel outlet for Re=1 and Kn=0.1 for various grid densities. In the limit of the slip-flow regime, the Knudsen number has been varied from 0 to 0.1, implying no-slip (Kn=0) and slip-flow (Kn>0) boundary conditions at the walls. The numerical model has been able to accurately predict the velocity profiles (Fig. 4) for all the values of Knudsen numbers considered.

After validating the model, the incompressible slip-flow regime gas-flow through a microchannel with a 90 deg bend has been analyzed. As mentioned earlier, the fillet radius at the bend has been varied from 0 to 0.6 times the channel height and Kn has been varied from 0.0 to 0.10. A low Reynolds number of value 1 has been employed. The flow characteristics in terms of velocity profiles, velocity vectors, and the inlet to outlet pressure ratio have been presented for several cases.

Results and Discussion

The computational domain for the cases considered in the present study has been illustrated in Fig. 2. The height of the channel, H, has been used as the length scale and the value of L has been fixed as 20 times the height. Figure 2 also shows Sections 1, 2, 3, and 4, where velocity profiles have been plotted (presented later). The effect of parameters on the flow field has been presented in detail subsequently.

To ensure that the results obtained from the numerical study are independent of the computational grid, a grid independence study has been carried out. For example, Fig. 5 shows velocity profiles at Section 4 (Fig. 5(*a*)) and Section 2 (Fig. 5(*b*)) in the domain using different grid densities in the y-direction for Re=1, Kn =0.05, and $R=0.4$. At Section 2, a local coordinate s has been defined to represent the direction vector and the profile is drawn with respect to it. Similarly, the number of grids in x or the axial direction has also been examined thoroughly. After investigating the results obtained by various number of grids in x and y directions, it was found that the optimum grid size for the present study would be 400×50.

Effect of Fillet Radius on Flow Pattern

The effect of the fillet radius of the bend is presented below. Figure 6 illustrates various nondimensional velocity profiles at Sections 1-1 and 2-2 for Re=1 and Kn=0.05. Obviously, the effect of the bend radius is not observed at Section 1-1 (Fig. 6(*a*)).

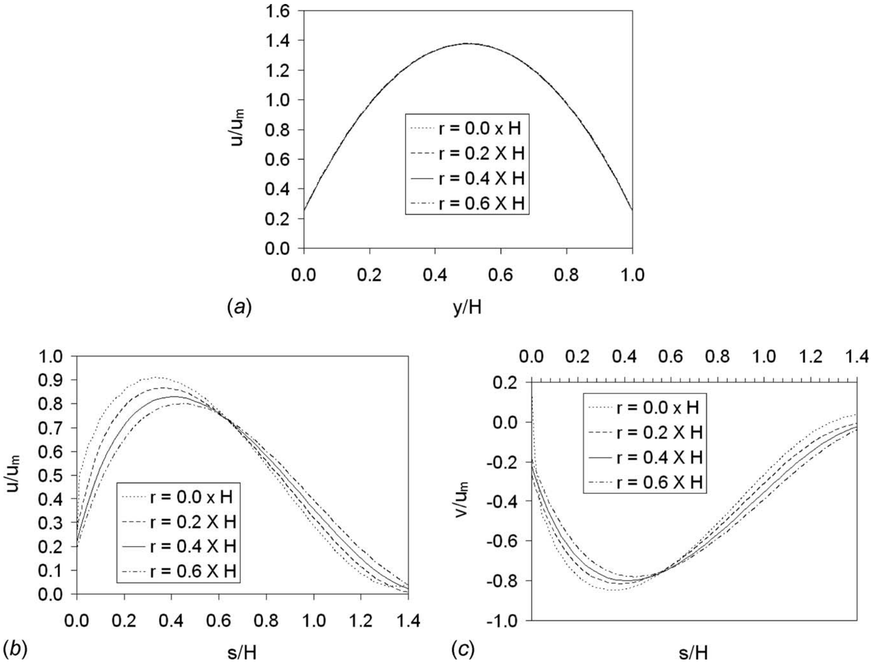

Fig. 6 **Profiles of velocities at (*a*) Section 1 and (*b*) and (*c*) Section 2 for Re=1, Kn =0.05 and different bend radii**

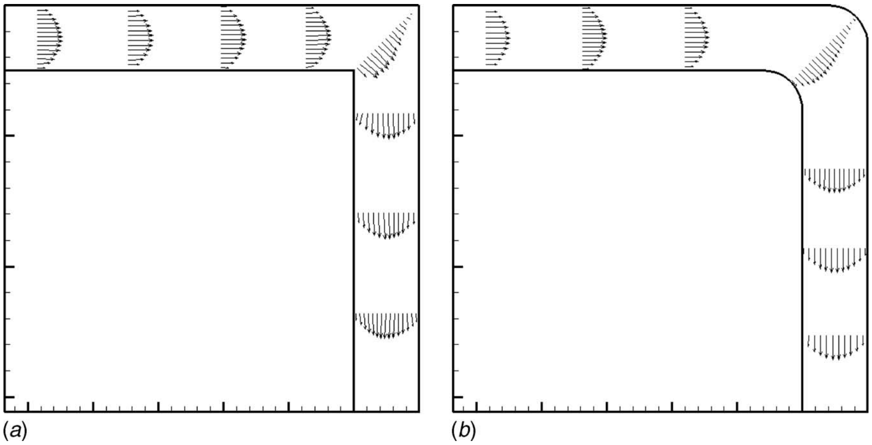

Fig. 7 Velocity vectors at various sections (*a*) $r=0.0$ and (*b*) $r=0.6H$ for Re=1 and Kn=0.05

The axial velocity (u) is almost the same for all the cases at this section. The nonzero velocities at the walls (which are the same at the top and bottom walls) are due to slip-flow conditions at Kn $=0.05$. At the bend (Section 2-2, Figs. 6(*b*) and 6(*c*)), considerable variations in the profile shapes are observed between the cases. The sharp cornered bend ($R=0$) presents the maximum value for the x-component velocity and the maximum (negative) value for the y-component velocity. Also in this case, the slip-flow condition has a negligible effect at the outer corner, where the velocity tends to a zero value. Velocity vectors shown in Fig. 7 help in clearly visualizing the flow pattern near the bend region for the cases of $R=0$ and 0.6 and Kn=0.05.

The case of the sharp corner ($R=0$) presents slightly different velocity profiles at Section 3-3 (Figs. 8(*a*) and 8(*b*)). Due to the combined effects of the bend and expansion of the flow in the bend region, there is an inception of a small axial velocity fluctuation at Section 3-3 (Fig. 8(*a*)) near the left and right walls for $R=0$. At the exit plane (Section 4-4), the fluctuation in the axial velocity (u/u_m) component has grown further (Fig. 8(*c*)). However, for the cases where $R>0$, the axial velocity has been close to zero (Fig. 8(*c*)). Even though the magnitude of the axial velocity is negligible when compared to the normal component, the very small fluctuations in the axial velocity component have been able to produce a slightly asymmetric normal velocity (v/u_m) profile for this case ($R=0$, Fig. 8(*d*)). For $R>0$ cases, the normal velocity profiles are no different, irrespective of the radius (Fig. 8(*d*)). The exit velocity profile obtained for the case of a straight channel with the same Re and Kn values is identical to the velocity profiles obtained from $R>0$ cases. This means that for this configuration, when the bend radius is at least 20% of the channel height, the effect of the bend is not seen and the flow at the exit is similar to the exit flow from a straight channel.

Effect of Fillet Radius on Pressure Variation

The ratio of pressure at any location along the central line of the channel to the exit pressure is plotted along the central line of the

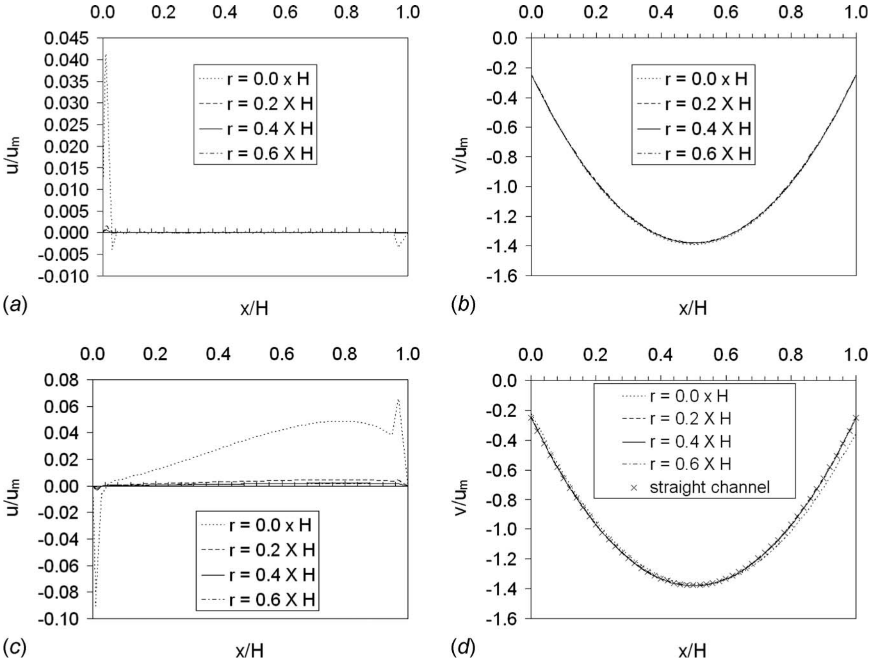

Fig. 8 Profiles of *u* and *v*-velocities at (*a*) and (*b*) Section 3 and (*c*) and (*d*) Section 4 for Re=1, Kn=0.05, and different bend radii ($r=0-0.6H$)

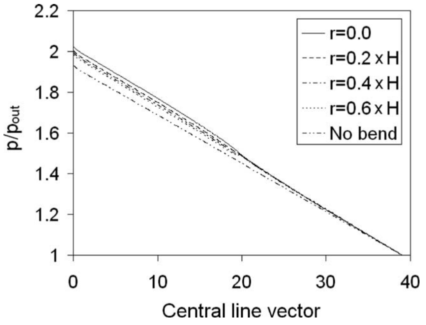

Fig. 9 Variation of p/p_{out} along the channel center line for various bend radii; Re=1, Kn=0.05

channel in Fig. 9, for Re=1, Kn=0.05,… and various bend radii. The pressure ratio decreases from the inlet to the outlet as expected. The variation is not perfectly linear and is consistent with literature [1,3–7,9,10]. The bend produces a change of slope for the variation of the pressure ratio. Also, it can be seen in Fig. 8 that after the bend, the variation of the ratio of pressure is the same for all the cases. Typical variation of the ratio of pressure for a straight channel of the same height and length is also shown as a "no bend" case. It can be seen that due to the presence of the bend, for the same flow rate (Re=1), a higher inlet to outlet pressure ratio is required. This is consistent with literature [15,19]. This inlet to outlet pressure ratio decreases as R increases and approaches the pressure ratio for a straight channel (see Table 1).

Table 1 p_{in}/p_{out} for all Knudsen numbers and bend radii along with that for a straight channel

	p_{in}/p_{out} for various Kn		
r/H	0	0.05	0.1
0	2.338	2.024	1.834
0.2	2.321	2.002	1.813
0.4	2.311	1.993	1.805
0.6	2.303	1.985	1.798
no bend	2.246	1.929	1.742

Effect of Knudsen Number, Kn

The validation case presented in Fig. 4 presents the effect of Kn for a straight channel. The slip velocity at the wall increases as Kn increases and the maximum velocity value decreases. For a bend, the nondimensional velocity profiles at Section 2-2 have been plotted for the cases of $R=0$, Re=1, and Kn=0, 0.05, and 0.1 in Fig. 10. A similar plot for $R=0.6$ is shown in Fig. 11. The plots with other nonzero radii are also similar to that of $R=0.6$.

It can be observed that the cases with a nonzero bend radius produce velocity profiles, which vary in slope and maximum values (Fig. 11), as Kn is varied. Also, this clearly illustrates the effect of the Knudsen number. On the other hand, for $R=0$, the velocity profiles for various Kn values do not produce a clear-cut variation as in $R>0$ cases (see Fig. 10).

Figure 12 shows the distribution of the pressure ratio along the centerline of the channel for Re=1 and $R=0.0, 0.6$ cases. Table 1 supports these results. As Kn increases (read horizontally in Table 1), the ratio of p_{in} to p_{out} decreases. This proves that slip flows need a smaller pressure difference as the shear stress that has to be overcome by the flow decreases as Kn increases and is consistent with earlier observations [1–10]. Also from Fig. 12, it can be observed that the variation of the pressure ratio changes its slope near the bend region. The change pattern in the slope of the pressure ratio is different for the $R=0$ and $R=0.6$ cases. The slope change is significant for Kn>0 for the $R=0$ case, but it is significant at the Kn=0 for the $R=0.6$ case.

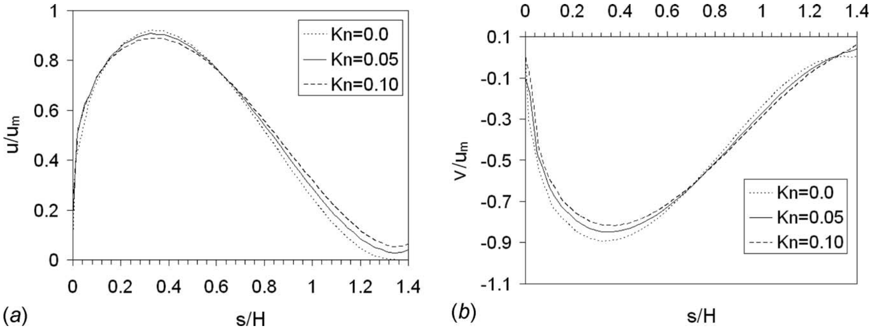

Fig. 10 Profiles of velocities at Section 2: (*a*) *u* and (*b*) *v* for Re=1, *r*=0.0, and different Kn

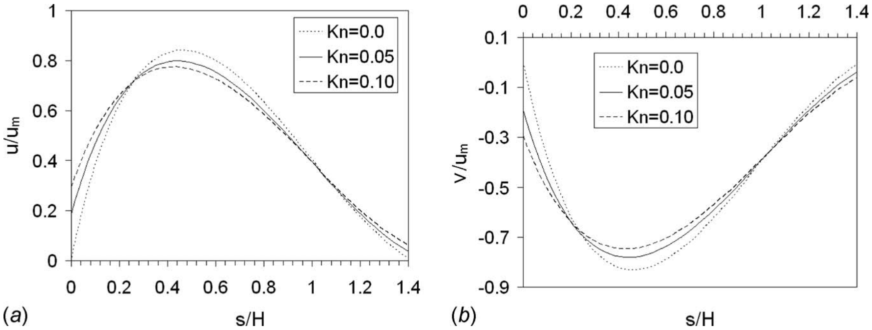

Fig. 11 Profiles of velocities at Section 2: (*a*) *u* and (*b*) *v* for Re=1, *r*=0.6*H*, and different Kn

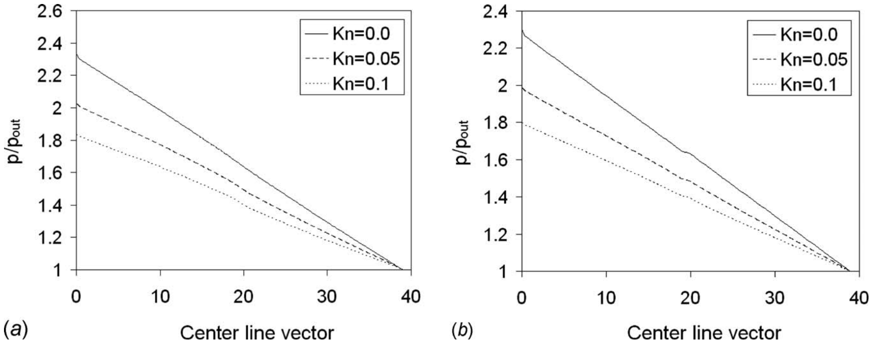

Fig. 12 Variation of p/p_{out} along the channel center line for various Kn values; Re =1 and (*a*) $r=0.0$ and (*b*) $r=0.6H$

Conclusion

Microscale gas flow through channels with a right-angled bend has been numerically analyzed. Complete transient Navier–Stokes equations have been solved by employing a nonorthogonal control volume method. First order slip velocity has been employed along the walls for $\mathrm{Kn}>0$. The numerical method has been validated with the analytical solutions for flow through a straight channel. The fillet radius has been varied from zero, representing a sharp corner, to 0.6 times the height of the channel. The Knudsen number has been varied from zero, representing no-slip at the boundary, to 0.1, which is the limiting case for the slip-flow regime. The flow characteristics in terms of velocity profiles, velocity vectors, and the pressure ratio variation along the centerline of the channel have been presented for several cases.

Based on the parametric study, following conclusions are arrived at.

1. Results show that for the case of the fillet radius equal to zero, flow separation occurs after the bend and due to this, the exit velocity profile changes significantly. The highest pressure ratio between the inlet and the outlet is required to maintain a specific mass flow rate for this case.
2. The cases with a nonzero fillet radius exhibit identical exit velocity profiles, which is also the same as that of a straight channel. The inlet to outlet pressure ratio decreases as the fillet radius increases.
3. As the Knudsen number increases, the pressure ratio required to maintain a specific mass flow rate decreases.

Nomenclature

H = channel height, m
Kn = Knudsen number, λ/H
n = normal direction
p = pressure, $\mathrm{N/m^2}$
r = radius of fillet, m
R = nondimensional radius of fillet, r/H
Re = Reynolds number
t = time, s
x, y = nondimensional Cartesian coordinates
u_m = inlet velocity
u = horizontal velocity, m/s
v = vertical velocity, m/s

Greek Symbols

δ = convergence criterion, in fractional form, $|(\phi_{\mathrm{new}}-\phi_{\mathrm{old}})/\phi_{\mathrm{new}}|$
ϕ = variable u or v over which the convergence is being tested for
λ = molecular mean free path of fluid
ν = kinematic viscosity, $\mathrm{m^2/s}$
σ = slip velocity accommodation coefficient (=0.95)

Subscripts

f = fluid
t = tangential component
w = wall

References

[1] Keenan, J. H., and Neumann, E. P., 1946, “Measurements of Friction in a Pipe for Subsonic and Supersonic Flow of Air,” ASME J. Appl. Mech., **13**(2), pp. 91–100.
[2] Schaaf, S. A., and Chambre, P. L., 1961, *Flow of Rarefied Gases*, Princeton University Press, Princeton, NJ.
[3] Ebert, W. A., and Sparrow, E. M., 1965, “Slip Flow in Rectangular and Annular Ducts,” ASME J. Basic Eng., **87**, pp. 1018–1024.
[4] Sreekanth, A. K., 1968, “Slip Flow Through Long Circular Tubes,” *Rarefied Gas Dynamics*, L. Trilling and H. Y. Wachman, eds., Academic, New York.
[5] Prudhomme, R. K., Chapman, T. W., and Bowen, J. R., 1986, “Laminar Compressible Flow in a Tube,” Appl. Sci. Res., **43**, pp. 67–74.
[6] Pfahler, J., Harley, J. C., Huang, Y., Bau, H. H., and Zemel, J. N., 1991, “Gas and Liquid Flow in Small Channels,” *Symposium on Micro-Mechanical Sensors, Actuators and Systems*, New York, ASME DSC 32, pp. 49–60.
[7] Choi, S. B., Barron, R. F., and Warrington, R. O., 1991, “Fluid Flow and Heat Transfer in Micro-Tubes,” *Symposium on Micro-Mechanical Sensors, Actuators and Systems*, New York, ASME DSC 32, pp. 123–134.
[8] Bird, G. A., 1994, *Molecular Gas Dynamics and the Direct Simulation of Gas Flows*, Clarendon, Oxford.
[9] Harley, J. C., Huang, Y., Bau, H. H., and Zemel, J. N., 1995, “Gas Flow in Micro-Channels,” J. Fluid Mech., **284**, pp. 257–274.
[10] Arkilic, E. B., Schmidt, M. A., and Breuer, K. S., 1997, “Gaseous Slip Flows in Long Micro-Channels,” J. Microelectromech. Syst., **6**(2), pp. 167–178.
[11] Quarmby, A., 1968, “A Finite-Difference Analysis of Developing Slip Flow,” Appl. Sci. Res., **19**, pp. 18–33.
[12] Beskok, A., and Karniadakis, G. E., 1995, “Simulation of Heat and Momentum Transfer in Complex Micro-Geometries,” J. Thermophys. Heat Transfer, **8**(4), pp. 647–655.
[13] Chen, C. S., Lee, S. M., and Sheu, J. D., 1998, “Numerical Analysis of Gas Flow in Micro-Channels,” Numer. Heat Transfer, Part A, **33**(7), pp. 749–762.
[14] Barber, R. W., and Emerson, D. R., 2001, “A Numerical Investigation of Low Reynolds Number Gaseous Slip Flow at the Entrance of Circular and Parallel Plate Micro-Channels,” *ECCOMAS Computational Fluid Dynamics Conference*, University of Swansea, Swansea, Wales, UK, September 4–7.
[15] Raju, R., and Roy, S., 2004, “Hydrodynamic Model for Micro-Scale Flows in a Channel With Two 90 Deg Bends,” ASME J. Fluids Eng., **126**, pp. 489–492.
[16] Papautsky, I., Ameel, T., and Frazier, A. B., 2001, “A Review of Laminar Single-Phase Flow in Micro-Channels,” *ASME IMECE Conference*, New York, November.
[17] Rostami, A. A., Mujumdar, A. S., and Saniei, N., 2002, “Flow and Heat Transfer for Gas Flowing in Micro-Channels: A Review,” Heat Mass Transfer, **38**, pp. 359–367.
[18] Gad-el-hak, M., 1999, “The Fluid Mechanics of Micro-Devices—The Freeman Scholar Lecture,” ASME J. Fluids Eng., **121**, pp. 5–33.
[19] Lee, S. Y. K., Wong, M., and Zohar, Y., 2001, “Gas Flow in Micro-Channels With Bends,” J. Micromech. Microeng., **11**, pp. 635–644.
[20] Robin, H. L., Mark, A. S., Dendra, V. S., Michael, G. O., Juan, G. S., Ronald, J. A., Hassan, A., and David, J. B., 2000, “Passive Mixing in a Three-Dimensional Serpentine Microchannel,” J. Microelectromech. Syst., **9**(2), pp. 190–197.

The Influence of Viscous Effects and Physical Scale on Cavitation Tunnel Contraction Performance

P. A. Brandner
Australian Maritime Hydrodynamics Research Centre,
Australian Maritime College,
University of Tasmania,
Locked Bag 1395,
Launceston,
Tasmania 7250, Australia

J. L. Roberts
Tasmanian Partnership for Advanced Computing,
University of Tasmania,
Private Bag 37,
Hobart,
Tasmania 7001, Australia

G. J. Walker
School of Engineering,
University of Tasmania,
Private Bag 65,
Hobart,
Tasmania 7001, Australia

The general performance of an asymmetric cavitation tunnel contraction is investigated using computational fluid dynamics (CFD) including the effects of fluid viscosity and physical scale. The horizontal and vertical profiles of the contraction geometry were chosen from a family of four-term sixth-order polynomials based on results from a CFD analysis and a consideration of the wall curvature distribution and its anticipated influence on boundary layer behavior. Inviscid and viscous CFD analyses were performed. The viscous predictions were validated against boundary layer measurements on existing full-scale cavitation tunnel test section ceiling and floor and for the chosen contraction geometry against model-scale wind tunnel tests. The viscous analysis showed the displacement effect of boundary layers to have a fairing effect on the contraction profile that reduced the magnitude of local pressure extrema at the entrance and exit. The maximum pressure gradients and minimum achievable test section cavitation numbers predicted by the viscous analysis are correspondingly less than those predicted by the inviscid analysis. The prediction of cavitation onset is discussed in detail. The minimum cavitation number is shown to be a function of the Froude number based on the test section velocity and height that incorporate the effects of physical scale on cavitation tunnel performance. [DOI: 10.1115/1.2969274]

1 Introduction

The Tom Fink cavitation tunnel at the Australian Maritime College is currently being upgraded (Brandner et al. [1,2]) as part of a facility development for the Australian Maritime Hydrodynamics Research Centre (AMHRC).[1] These tunnel improvements necessitate redesign and/or replacement of most sections of the existing tunnel circuit including the contraction. To optimize the performance of the new contraction, it was decided that flow analysis would be performed using computational fluid dynamics (CFD), and the results were validated by comparison with measurements made in the existing contraction and test section.

The function and fundamental importance of the contraction in a wind or water tunnel in creating a high quality test section flow for experimentation and in influencing other tunnel parameters have been well reported in literature (see, e.g., Barlow et al. [3] and Wetzel and Arndt [4]). Many tunnels use axisymmetric or two-dimensional (2D) contractions designed by using inviscid or coupled inviscid/viscous flow analyses (see, e.g., Chmielewski [5], Morel [6], and Mikhail [7]). In these analyses the pressure distributions derived from potential flow solutions of the contraction flow were used to predict turbulent separation due to the adverse pressure gradients at the entrance and exit using Stratford's criterion and relaminarization using a flow acceleration parameter. The application of Stratford's criterion requires the estimation of a virtual origin for the turbulent boundary layer corresponding to the length of zero pressure gradient flow needed to produce the same local boundary layer thickness. Chmielewski [5] and Mikhail [7] noted the most critical factor to be the separation at the inlet, although they found that relaminarization and its effect on the boundary layer at the exit also needed to be considered. Formulations for the contraction profile have varied significantly. For axisymmetric contractions, Morel [6] used two cubics matched at the inflection point. Chmielewski [5] described the contraction profile indirectly in terms of the longitudinal variation of average streamwise acceleration; this was specified by a family of contours based on a continuous cosine function and two arbitrary exponents. Mikhail [7] specified the second derivative of the contraction radius in terms of a sine function raised to an arbitrary power; as with Morel [6], separate functions for the inlet and outlet regions were matched at the inflection point.

More recently, attention has been given to three-dimensional (3D) symmetric and asymmetric contractions with square or rectangular cross sections intended for low speed wind tunnels. Downie et al. [8] used an iterative finite volume method to satisfy Laplace's equation for the analysis of an asymmetric rectangular cross section contraction. In this case the contraction profiles were generated from two matched elliptic arcs. The 3D nature of the velocity and pressure extrema (occurring at the corners of the entrance and exit) was noted, but no analysis of the boundary layers was made. Su [9] used a similar numerical method involving a difference equation to satisfy Laplace's equation for symmetric square and rectangular cross section contractions. Contractions where the cross-sectional aspect ratios varied between the entrance and exit were also investigated. By considering planes of symmetry, these results may also be applied to asymmetric contractions with one side flat, which are frequently used for cavitation tunnels for reasons described below. Fang [10] used a finite volume Euler solver for the analysis of symmetric contractions of square cross sections. Results presented include the location and magnitude of corner pressure extrema and pressure gradients.

In addition to the flow quality parameters suggested by Morel [6], Su [9] introduced a quantitative cross-flow parameter based on the transverse gradients imposed by pressure extrema in the corners of rectangular section contractions and showed how these increase with the change in cross-sectional aspect ratio from unity. The resulting three-dimensional boundary layer flows were briefly discussed, but no viscous flow analyses were conducted. Differing locations of the inflection points on the sides and the ceiling/floor were not recommended as these were found to further exacerbate the transverse pressure gradients. Su [9] mostly used two matched

---

[1] The AMHRC is a collaborative venture involving the Australian Maritime College (AMC), the Australian Defence Science and Technology Organisation (DSTO), and the University of Tasmania (UTAS).

Contributed by the Fluids Engineering Division of ASME for publication in the Journal of Fluids Engineering. Manuscript received May 15, 2007; final manuscript received July 3, 2008; published online September 4, 2008. Assoc. Editor: Steven Ceccio.

cubics for generating the contraction profiles. Some results were also presented for higher-order profiles; the use of a cubic entrance profile and a higher-order exit profile was deemed beneficial.

Significant investigations of cavitation tunnel contractions were made with the development of the world's largest cavitation tunnels during the 1980s, including Le Grand Tunnel Hydrodynamique (GTH) for the Bassin d'Essais des Carènes, France, the Large Cavitation Channel (LCC) for the U.S. Navy, and the Hydrodynamics and Cavitation Tunnel (HYKAT) for the Hamburg Ship Model Basin, Germany. All these studies involved the design of asymmetric contractions with little or no contraction on the ceiling to minimize the volume of water to be displaced for test section access and to minimize the test section static pressure (or cavitation number). Lecoffre et al. [11] reported on the design of contractions for both the large and small test sections of the GTH using a 3D flow solver with consideration given to maximizing cavitation performance; the boundary layer behavior was analysed using integral techniques. The profiles for these contractions were generated using a fifth-order polynomial; although asymmetric, some contraction was retained on the ceiling. For the LCC and the HYKAT, Wetzel and Arndt [4] also used a 3D Euler solver for the contraction analysis. The contraction profiles were generated using a three-term fifth-order polynomial, for which the inflection point could be adjusted simultaneously with the second derivative at the entrance. The location of the inflection point and, hence, the entrance second derivative were chosen as a trade-off between the minimum pressure coefficient at the exit and the likelihood of upstream turbulent separation assessed by using Stratford's criterion. However it was concluded that the minimum pressure coefficient at the exit and, hence, cavitation inception were the controlling factor. Investigations into the effect of entrance velocity nonuniformity and varying degrees of asymmetry were also conducted. In this case, profiles with no contraction on the ceiling were chosen.

While the above-mentioned techniques provide significant guidance in the analysis and design of contractions, the subsequent development of CFD capability since these earlier design studies means that greater insight into the viscous aspects of contraction flow can now be gained. In particular, the three-dimensional nature of the boundary layers and their effect on various flow quality parameters can be better accounted for by fully viscous Reynolds averaged Navier–Stokes (RANS) computations. The inception cavitation number is shown in the present study to depend on both Reynolds number and Froude number effects. The viscosity influences only the Reynolds number, while the physical scale influences both Reynolds and Froude numbers. A comparison of results from fully viscous (RANS) and inviscid solutions indicates that changes in surface pressure distribution due to boundary layer development may significantly influence both flow separation and cavitation inception.

2 Geometry and Parametrization

As discussed in the Introduction, the formulation of contraction profiles has varied significantly in past designs. In many cases two curves matched at the inflection point have been used, although continuous polynomials have also been popular. Wetzel and Arndt [4] discussed the use of a two-term sixth-order polynomial, although a three-term fifth-order was finally chosen for the LCC and HYKAT. Lecoffre et al. [11] also reported on using a fifth-order polynomial for the GTH contractions. Keith et al. [12] used a four-term ninth-order polynomial for the modification of a hydroacoustic test facility. For the present modification to the AMC cavitation tunnel, a sixth-order polynomial was adopted to enable an independent choice or variation of the inflection point location and the first and second derivatives of the wall profiles at the entrance and exit.

The major geometric parameters of the current contraction, which were to be retained, include an entrance cross section of 1.6 m^2, an exit cross section of 0.6 m^2, and a length of 2.5 m, giving a length to entrance dimension ratio of 1.56 and a contraction ratio of 7.11. For reasons mentioned above, there is no contraction on the ceiling, a feature that is also to be retained. In accordance with the recommendations of Su [9], it was decided that the location of the inflection point on the sides would be the same as that on the floor. As the contraction of each sidewall is only half that of the floor, the entrance second derivative on the sides was chosen to be half that on the floor. The current test section, which is to be retained, has a sloping floor to compensate for the boundary layer growth and to improve the longitudinal velocity uniformity. This slight slope, 1/130, was considered small enough that the first as well as the second derivative at the contraction exit would be set to zero on the floor as well as the sides. With these choices, and the first derivative at the entrance chosen to be zero, the remaining parameters are the entrance second derivative and the location of the inflection point.

A coordinate system is defined with the origin located on the test section centerline at the exit of the contraction, with the x coordinate directed positive downstream and the z coordinate directed positive upward. The floor and wall contour profiles are generated by sixth-order polynomials satisfying the above constraints,

$$z - z_0 = ax^6 + bx^5 + cx^4 + dx^3 \tag{1}$$

where z, z_0, and x are nondimensionalized by the contraction length L.

The coefficients in Eq. (1) may be easily derived from the boundary conditions using computational symbolic manipulation, details of which are given in the Appendix. The resulting family of profiles may be investigated to examine the influence of changing the entrance second derivative and the location of the inflection point. Equation (1) gives profiles monotonic in z for locations of the inflection point in the range $-0.6 \leqslant x(z''=0) \leqslant -0.4$ and values of the entrance second derivative on the floor in the range $0 \leqslant z''_{-1} \leqslant 6$. Figure 1 shows example profiles of $z(x)$, $z'(x)$, and $z''(x)$ from Eq. (1) for varying inflection location, $x(z''=0)$, with the entrance second derivative, $z''_{-1}=3$; Fig. 2 shows similar profiles with the entrance second derivative, $z''_{-1}=0$. Figure 1 shows that for $z''_{-1}=3$ two of the profiles initially decrease monotonically and pass through a minimum before increasing to zero at the exit. The value of the curvature near the exit and its location may influence the minimum pressure, which affects the minimum cavitation number achievable, the potential for separation, and the test section flow quality. For small values of the entrance second derivative, or zero as shown in Fig. 2, the profiles must have two turning points—a maximum near the entrance as well as a minimum near the exit. For small values of the entrance second derivative, the turning point near the entrance may result in larger curvature values or at least a greater curvature extending downstream. The curvature at the entrance may adversely influence the boundary layer behavior, including the potential for separation.

The wall curvature K exhibits a similar behavior to the second derivative, and values of its minimum near the exit and their location have been plotted across the above-mentioned parameter range, as shown in Fig. 3. The maximum curvature near the exit is a minimum when the inflection point is located at $x=-0.6$ and is mildly dependent on the entrance second derivative. The location of the the maximum curvature is, however, strongly dependent on the entrance second derivative. The point of the maximum curvature (minimum z'') near the exit may be moved upstream by reducing the entrance second derivative, although this may have the effect of increasing the curvature at the entrance as mentioned above. There is therefore a trade-off between the location of the maximum curvature near the exit and the entrance second derivative. To minimize the velocity overshoot near the contraction exit and hence the minimum operable cavitation number, it would appear desirable to reduce the minimum curvature near the exit and

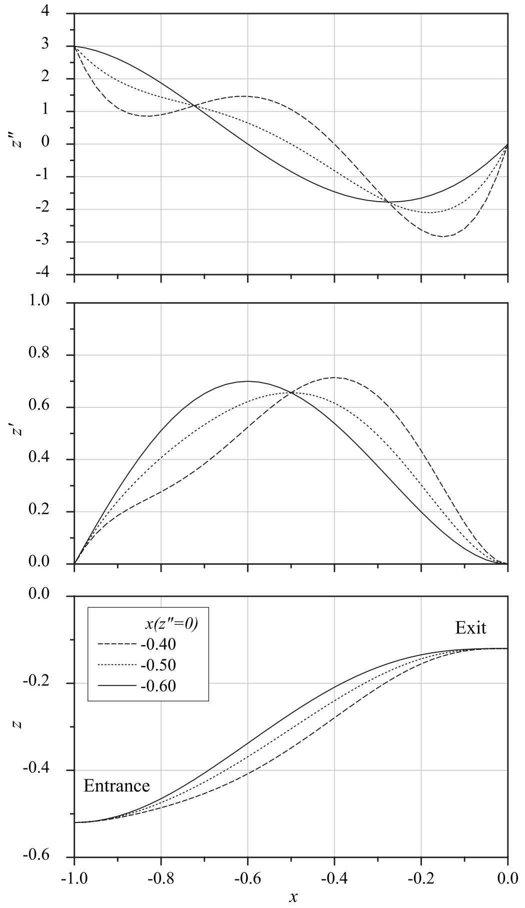

Fig. 1 Floor profiles $z(x)$, $z'(x)$, and $z''(x)$ from Eq. (1) with varying inflection location, $x(z''=0)$, and entrance second derivative, $z''_{-1}=3$

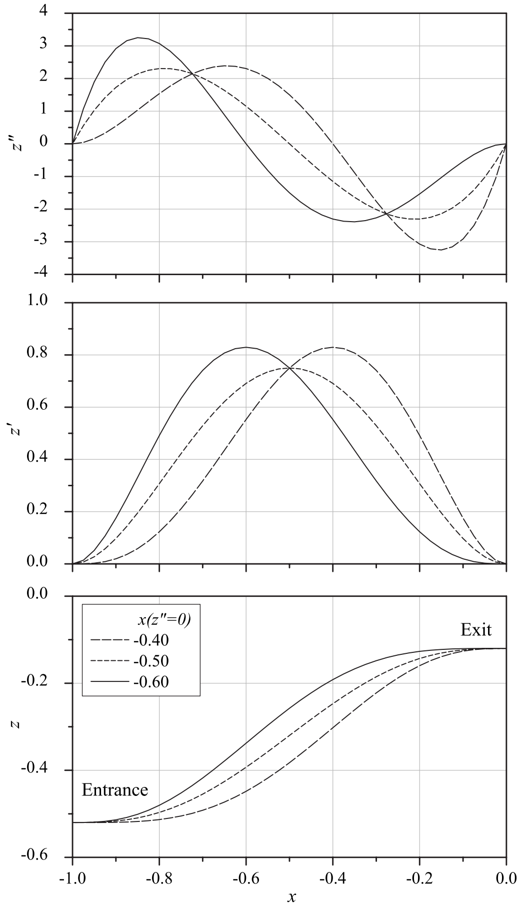

Fig. 2 Floor profiles $z(x)$, $z'(x)$, and $z''(x)$ from Eq. (1) with varying inflection location, $x(z''=0)$, and entrance second derivative, $z''_{-1}=0$

to move its location upstream. However, the magnitude of the entrance second derivative may also influence the likelihood of separation at the inlet. These aspects are discussed in detail below as part of the CFD analysis, along with qualitative considerations of the inlet boundary layer behavior.

3 CFD Analysis

3.1 Viscous Analysis. The commercial CFD code CFX 5.5 was used for the viscous flow analysis. It is a finite volume *Reynolds Averaged Navier* RANS solver, details of which are given in AEA Technology Engineering Software [13]. Computations were performed on the SGI Origin 3400 high-performance computer of the Tasmanian Partnership for Advanced Computing (TPAC) at UTAS. A hybrid mesh is used with a Delaunay surface algorithm whereby a prismatic mesh may be attached to any surface. For this problem, a prismatic mesh five element thick was attached to the walls with a geometric growth factor of 1.3 and a typical inflated boundary thickness (IBT) of 50 mm. Figure 4 shows a typical surface mesh for a maximum edge length (MEL) of 100 mm.

The computational domain extends from $x=-2.08$ to $x=1.04$. It commences with a parallel duct 1.6 m^2 and 2.7 m long at the inlet, followed by the contraction length of 2.5 m and the test section 2.6 m long. The inlet boundary conditions were specified as uniform velocity and isotropic turbulence with kinetic energy corresponding to a 2% streamwise turbulence component. To test the sensitivity of the results to inlet turbulence intensity, a second solution for the final chosen geometry was run with a 4% streamwise turbulence component. The results showed no significant difference.

A free outflow condition was specified at the exit from the computational domain, corresponding to the downstream end of the test section. The honeycomb at the upstream end of the contraction was not modeled. The parallel duct is long enough to ensure that upstream flow perturbations caused by the contraction are negligible at the inlet plane. This length, together with the moderately high initial turbulence level, also ensured a well-established turbulent boundary layer at the entry to the contraction.

The actual conditions at the entry to the cavitation tunnel contraction are unknown due to the lack of measurement access. As with other contraction flow analyses reported in the literature, the inlet flow assumptions are somewhat arbitrary. Many such studies have ignored viscous effects entirely and assumed totally inviscid flow. Typical approaches for previous studies, including a boundary layer analysis, have been to assume the boundary layer to originate at the exit from the most downstream flow manipulating device (usually a honeycomb for cavitation tunnels), i.e., at the inlet to the settling chamber. For studies of axisymmetric contractions, Chmielewski [5] and Mikhail [7] used settling chamber lengths around one contraction inlet radius, that is, about one-third the length adopted in the present work. The present study is therefore more conservative as regards avoiding separation at the entry to the contraction.

The global minimum pressure and the resultant viscous force acting on the contraction floor were chosen as suitable parameters to investigate the grid independence of the numerical solution. The grid density is principally controlled by the IBT and MEL.

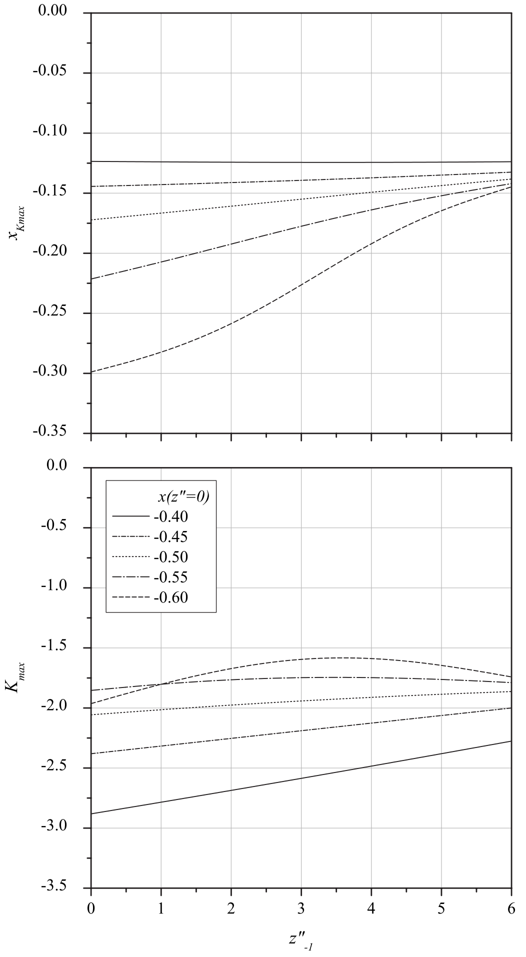

Fig. 3 Variation of location and magnitude of maximum curvature near the contraction exit for practical values of inflection point location and inlet curvature

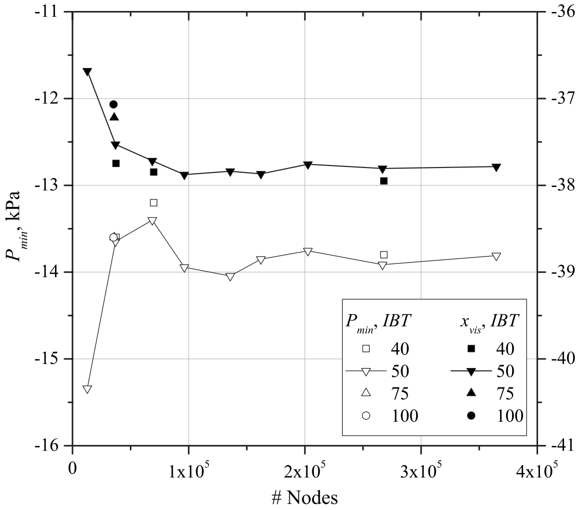

Fig. 5 Viscous CFD grid independence test for various values of IBT

The MEL has a significant influence on the total number of nodes, whereas the IBT has little. A standard k-ε turbulence model was chosen for the grid independence test, the results of which are shown in Fig. 5. The effect of grid refinement on the global minimum pressure can be clearly seen, as well as the relative insensitivity to the IBT. The solution was deemed grid independent at approximately 200,000 nodes, with an IBT of 50 mm. This mesh was used for all further analyses.

Test section boundary layer measurements in the existing AMC cavitation tunnel were the only practicable means of comparing the CFD predictions with experiment due to the lack of access to the contraction and settling chamber. The profile of the existing contraction floor is closely approximated using Eq. (1) with the inflection at $x=-0.55$ and the entrance second derivative z''_{-1} equal to 3. Measured test section floor and ceiling centerline boundary layers were used for the validation of the CFD model and the choice of the optimum turbulence model. A comparison of measured integral boundary layer properties with predictions of a standard k-ε model and the SSG Reynolds stress model (RSM) of

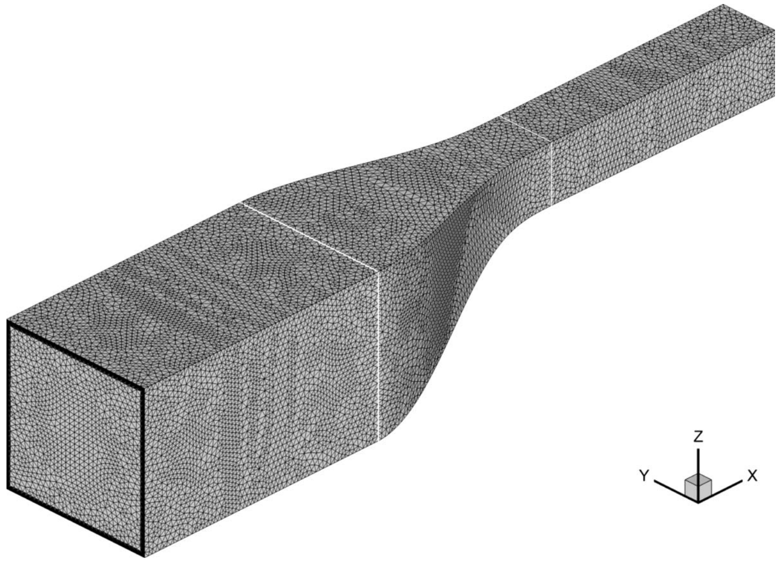

Fig. 4 Typical surface mesh for viscous CFD analysis for a maximum edge length (MEL) of 100 mm and an inflated boundary thickness (IBT) of 50 mm

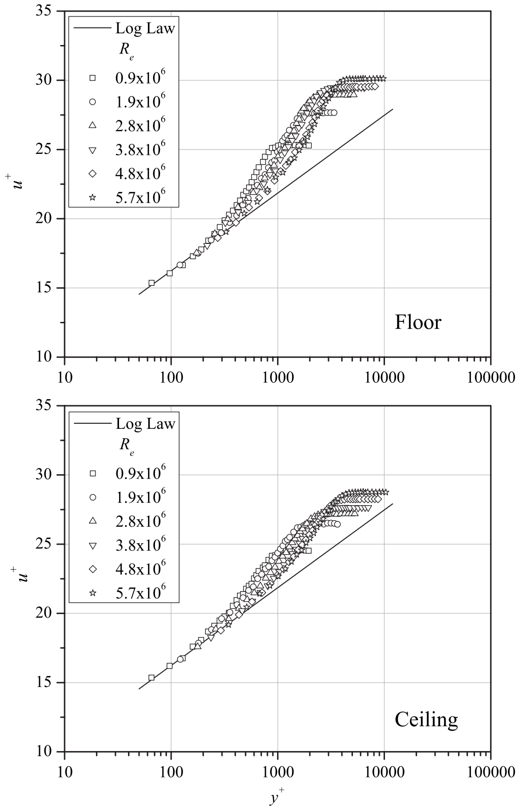

Fig. 6 Measured test section floor/ceiling boundary layer profiles at $x=0.12$

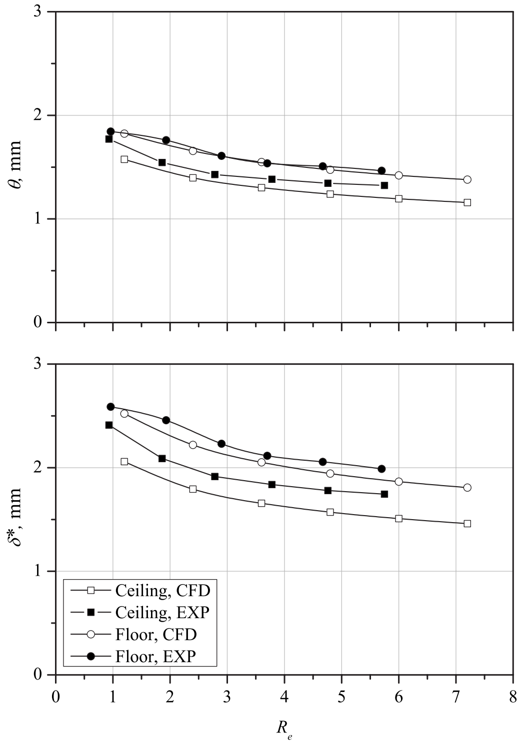

Fig. 7 Comparison of measured and predicted test section ceiling/floor centerline boundary layer displacement and momentum thicknesses at $x=0.12$

Speziale et al. [14] showed the former to be inadequate. The latter model gave reasonable predictions and was therefore chosen for all further analyses.

The AMC cavitation tunnel has been designed to operate with the nominal test section velocity varying between 2 m/s and 12 m/s. CFD predictions and boundary layer measurements were performed over a corresponding Reynolds number range. Boundary layers on the test section floor and ceiling were measured at $x=0.12$ on the test section vertical centerline using a 1.2 mm diameter Pitot tube and wall static tapping in the plane of the Pitot head. The Pitot tube was positioned with a computer controlled automated traverse. Pressures were measured sequentially using a *Validyne* Model DP15TL differential pressure transducer via a *Scanivalve* Model 48J7-1 pressure multiplexer. Pressure transducer zero errors were minimized by observing the zero readings on each pressure scan. The tunnel contraction differential was also monitored on each scan and was used to nondimensionalize measured pressures to eliminate pressure transducer span error. Acquired data were corrected for small temporal changes using the tunnel contraction differential during postprocessing. Further details of the experimental setup and procedures used and measurement accuracy are given in Brandner et al. [15].

Figure 6 shows semilogarithmic plots of the measured floor and ceiling profiles with the Reynolds number as a parameter. These profiles are in good agreement with the standard law of the wall for turbulent flow, with the expected reduction in the magnitude of the wake component as the Reynolds number increases. The floor boundary layers exhibit slightly greater wake components than those on the ceiling due to the adverse pressure gradient on the floor at the contraction exit. Figure 7 shows measured integral properties for the floor and ceiling boundary layers, together with those from CFD prediction, as a function of Reynolds number. The favorable agreement between measured and predicted values with Reynolds number gives confidence in the accuracy of predicting viscous effects on the pressure minima near the contraction exit.

3.2 Inviscid Analysis. Given the history of contraction analysis using inviscid methods, it is of particular interest to compare inviscid predictions with those of viscous RANS-based computations. An inviscid analysis was carried out using a boundary element method as implemented in the NASA AMES PMARC code, Ashby et al. [16]. The PMARC code uses combined source/doublet elements with constant strength singularity distributions and may be used for both internal and external potential flow analyses.

The extents of the computational domain were set the same as those for the viscous computation. The inlet and outlet conditions were specified with uniform velocity. The boundary element gridding was arranged with rectangular arrays of equal dimensions on all four sides. Five grid densities were chosen to test the convergence, ranging from 3,888 to 30,976 elements on half the geometry. Symmetry about the vertical center plane was used to halve the size of the matrix to be solved. In each case the number of longitudinal elements was set to achieve a square grid at the test section inlet and a continuous variation of element length thereafter. The computational domain and an example of the boundary element gridding are shown in Fig. 8. The magnitude of the minimum pressure near the contraction exit, $(C_{p_o})_{\min}$, was chosen to test convergence with the number of elements. Figure 9 shows the convergence with an increase in the number of elements. The solution was deemed converged at 30,976 elements.

4 Experimental Investigation

To validate the CFD predictions and provide a final check on the chosen geometry, a 1/4 scale wind tunnel model of the contraction and test section was built. Details of the model are shown in Fig. 10. Measurements made include the static pressure distribution on the centerline and the side of the contraction floor, test section vertical and horizontal velocity distributions, and floor

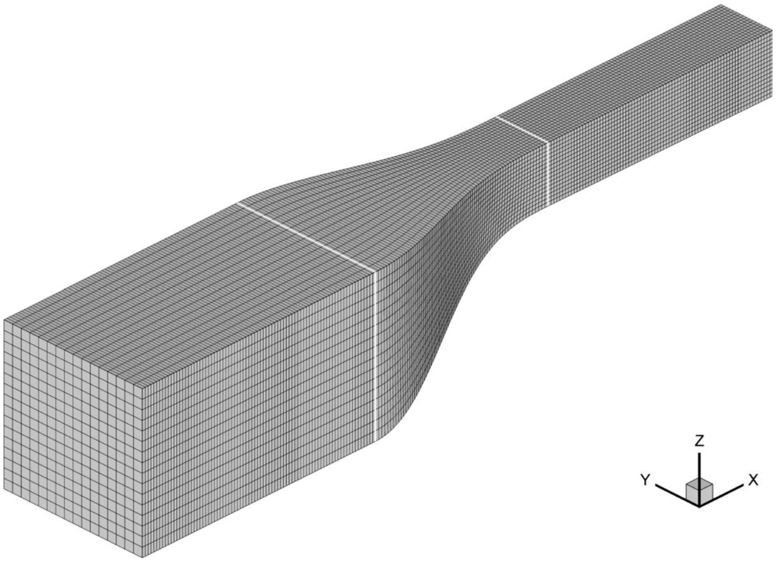

Fig. 8 Boundary element mesh for inviscid CFD analysis with 7744 elements

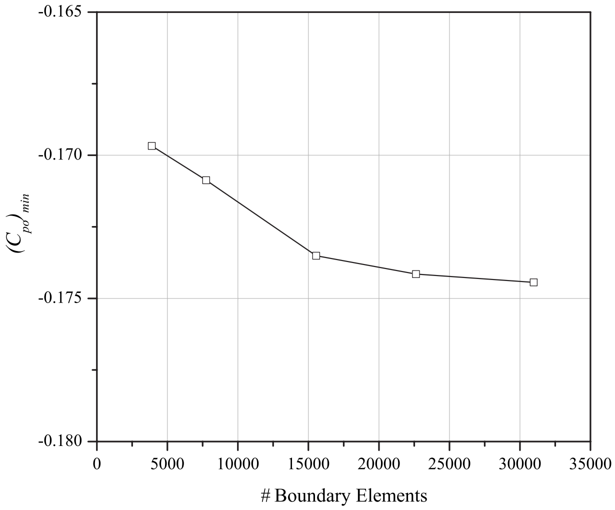

Fig. 9 Inviscid CFD grid convergence test with number of boundary elements

boundary layer thicknesses at the contraction inlet and outlet. Tests were carried out at Reynolds numbers—based on the test section height and core velocity at the test section entrance—varying between 2×10^5 and 5.5×10^5 compared with full-scale Reynolds numbers for the existing tunnel varying from 1.2×10^6 to 7.2×10^6.

Probe traverses were carried out using a computer controlled automated traverse. All pressures were measured sequentially using a Validyne Model DP105 differential pressure transducer via a Scanivalve Model 48J7-1 pressure multiplexer. Pressure transducer zero errors were minimized by observing the zero readings on each pressure scan. The tunnel contraction differential was also monitored on each scan and was used to nondimensionalize measured pressures to eliminate pressure transducer span error. Acquired data were corrected for small temporal changes using the tunnel contraction differential during postprocessing.

5 Discussion

5.1 Choice of Contraction Geometry. The viscous CFD model described above was solved for 35 combinations of the entrance second derivative and inflection location values that re-

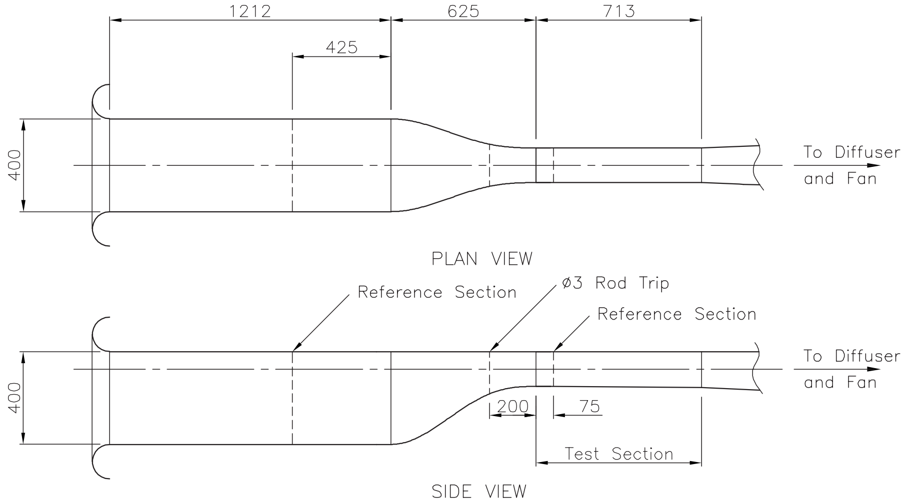

Fig. 10 Model-scale wind tunnel test setup (dimensions in mm)

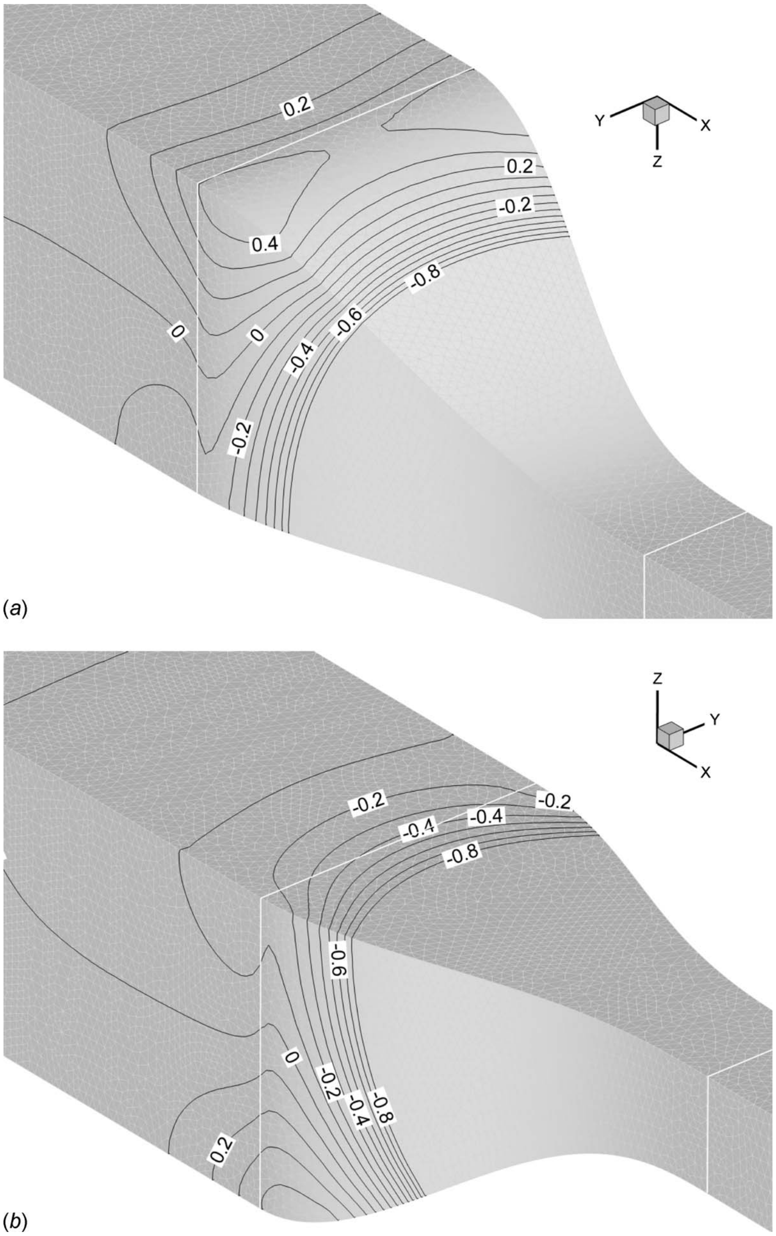

Fig. 11 C_{p_i} **distribution at the contraction inlet from viscous (RANS) CFD prediction,** R_e**=7.2×10**^{6} **(*a*) Floor and sides (*b*) Ceiling and sides**

sult in monotonic profiles from Eq. (1). Two reference sections were defined to analyze the CFD results for values of pressure coefficients and for a consideration of flow properties at the contraction entrance and exit. These were defined at $x=-1.68$ and $x=0.12$, where the effects of residual flow curvature were deemed negligible. At these sections the centerline streamwise velocity and pressure were used to derive pressure coefficients and the cavitation number.

Key aspects of contraction design include the avoidance of flow separation, minimum achievable cavitation number, and test section flow quality. Measures of the test section flow quality include the thickness of boundary layers, core flow streamwise velocity uniformity, and magnitude of spanwise flow components. Flow separations near the entrance and exit are possible due to adverse pressure gradients from the undershoot of velocity at the entrance and the overshoot at the exit. The pressure minima that occur at the exit corners also control the test section flow uniformity and the minimum operable cavitation number at high Froude numbers. It is the latter factor that makes cavitation tunnel contraction design more complex than that of low speed aeronautical facilities.

In choosing an "optimum" contraction geometry, the longitudinal pressure distribution is initially of most interest, as this affects the potential for separation and the minimum achievable cavitation number. Wall pressure distributions from viscous CFD predictions for the chosen AMC tunnel geometry at the greatest Reynolds number ($R_e=7.2\times10^6$) are shown in Figs. 11 and 12. While the results shown in Figs. 11 and 12 are for the chosen geometry, the overall pressure distribution is typical of those for all the parameter space. The results are presented as distributions of pressure coefficients based on centerline pressure and velocity at the entrance and exit reference sections, respectively. The overall pressure distribution for the inviscid case is generally similar to that for the viscous case and is not shown.

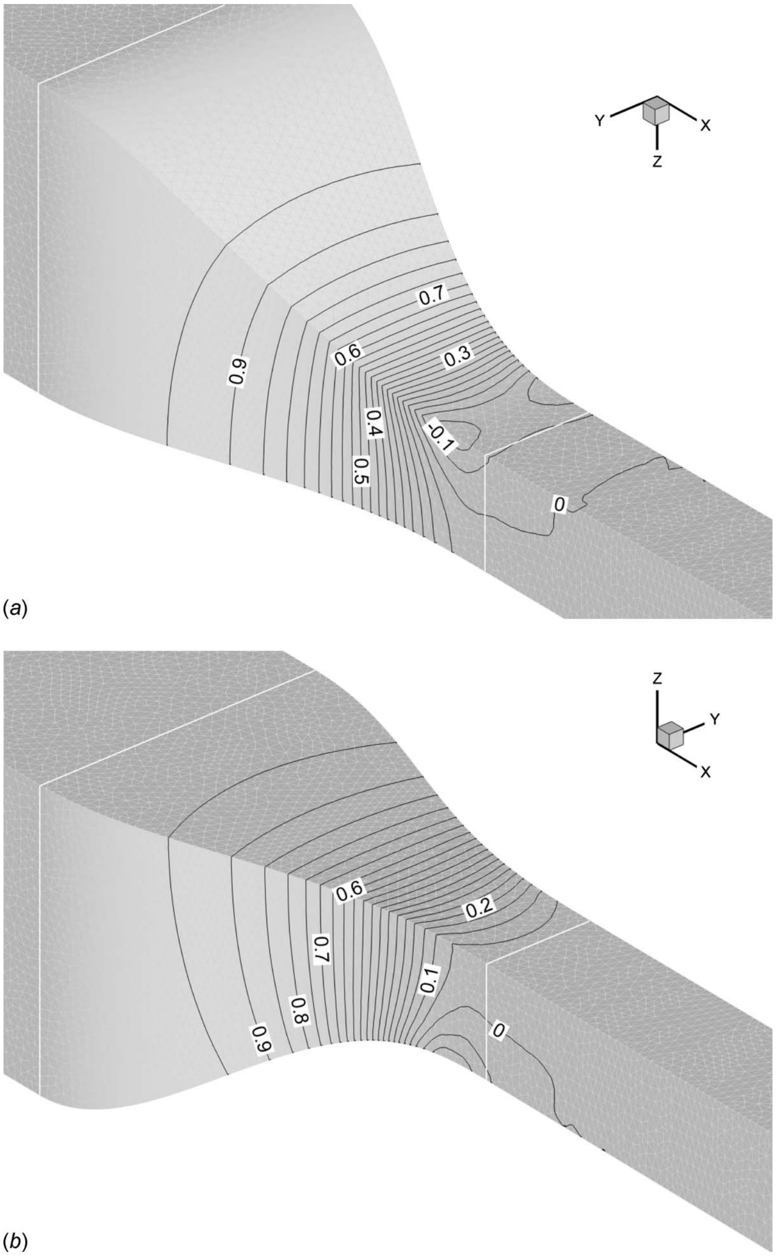

Fig. 12 C_{p_o} **Distribution at the contraction exit from viscous (RANS) CFD prediction,** $R_e=7.2\times10^6$ **(*a*) Floor and sides (*b*) Ceiling and sides**

For the contraction inlet, Fig. 11(*a*) shows the favorable pressure gradient on the ceiling and Fig. 11(*b*) shows the adverse gradient on the floor and sidewall, with the maximum value of $C_{p_i}(>0)$ occurring in the corner between these two surfaces downstream of the inlet. Similarly for the contraction exit, Fig. 12(*a*) shows the favorable gradient on the ceiling and Fig. 12(*b*) shows the adverse gradient on the floor and sidewall, with the minimum value of $C_{p_o}(<0)$ occurring in the corner upstream of the exit. The rationale for choosing this geometry is discussed below through the consideration of the CFD results across the parameter space investigated.

Figures 13(*a*) and 13(*b*) show the variation of minimum pressure coefficient near the contraction exit with the inlet second derivative and inflection location for the minimum and maximum Reynolds numbers, $R_e=1.2\times10^6$ and 7.2×10^6, respectively. The minimum pressure coefficient always occurs at the corners of the contraction floor and sidewalls near the exit. Figure 13 shows the minimum pressure coefficient at the outlet to be weakly dependent on the entrance second derivative and strongly dependent on the inflection location for both Reynolds numbers. The least negative minimum pressure coefficient occurs at an entrance second derivative, $z''_{-1}=0$, and inflection location, $x(z''=0)=-0.6$, supporting the qualitative discussion above based on the curvature distribution: that is, for these parameter values the curvature near the outlet is minimized and moved further upstream by moving the inflection point closer to the contraction outlet; but in so doing the curvature near the entrance is increased and reaches a maximum for the parameter space.

Figures 14(*a*) and 14(*b*) show the variation of the global minimum of the wall friction coefficient with the inlet second derivative and inflection location for the minimum and maximum Reynolds numbers, respectively. The results for the global minimum friction coefficient, which occurs near the contraction inlet, are also consistent with earlier considerations on the curvature distri-

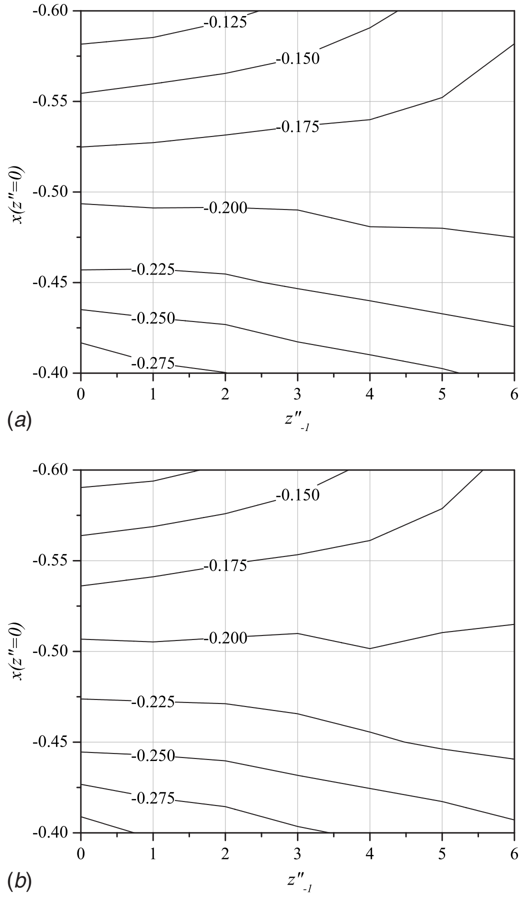

Fig. 13 Variation of minimum pressure coefficient, C_{p_o}, near contraction outlet with the inlet second derivative and inflection point location from CFD prediction (*a*) $R_e=1.2\times10^6$ (minimum for existing tunnel) (*b*) $R_e=7.2\times10^6$ (maximum for existing tunnel)

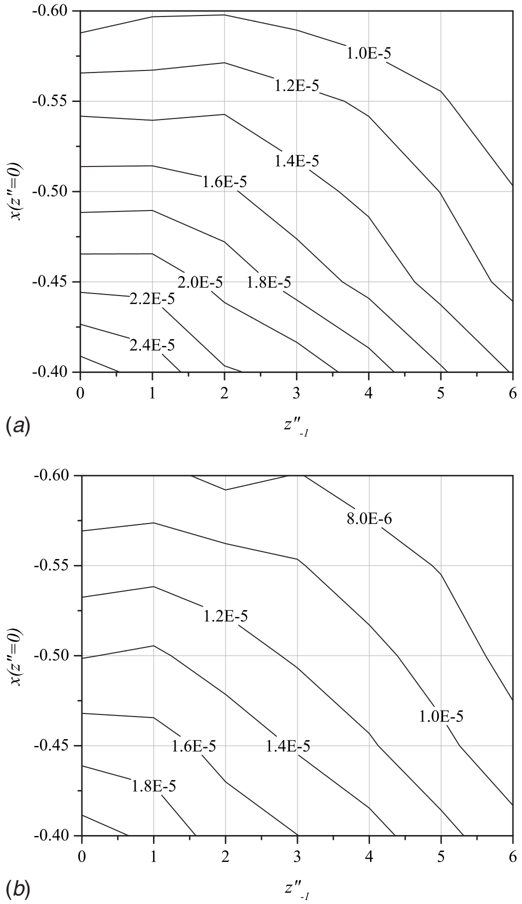

Fig. 14 Variation of global minimum friction coefficient, C_f, near the contraction inlet with the inlet second derivative and inflection point location from CFD prediction (*a*) $R_e=1.2\times10^6$ (minimum for existing tunnel) (*b*) $R_e=7.2\times10^6$ (maximum for existing tunnel)

bution. Minimum wall shear always occurs at the corners on the entrance floor, showing this location to be the most critical for separation. The friction coefficient here is a maximum for an entrance second derivative $z''_{-1}=0$, and inflection location $x(z''=0)=-0.4$; it decreases as the inflection point moves upstream and the entrance second derivative increases, but for $x(z''=0)-0.6$ the changes are minimal for $z''_{-1}<3$. The parameters for the maximum global friction coefficient also give the most negative pressure coefficient at the outlet, demonstrating the trade-off of biasing the inflection point toward the entrance or exit in terms of entrance separation and minimum pressure at the outlet.

While the friction coefficient reduces to a minimum for the parameters that correspond to the maximum of the outlet minimum pressure coefficient, it does not reduce to zero, implying that this geometry is still satisfactory for avoiding flow separation. The present computational results are conservative in that the origin of the turbulent boundary is some distance upstream of the likely virtual origin of the contraction inlet boundary in the real tunnel; hence the simulated boundary layer thickness at the contraction inlet should exceed the actual thickness.

The prediction of separation at the inlet is difficult due to unknown upstream flow conditions and complicated by the effects of upstream turning vanes, the settling chamber, and turbulence management devices. For the AMC facility the turbulence management device consists of a honeycomb located only a short distance upstream of the contraction entrance. The honeycomb affects the entrance flow due to its straightening effect by influencing the bulk flow and by modifying both the mean velocity and turbulence distributions of the upstream boundary layer. The turbulence introduced by the honeycomb will promote boundary layer transition and help to avoid laminar separation at very low Reynolds numbers. The honeycomb will also assist in avoiding turbulent separation at high Reynolds numbers by suppressing the large mixing eddies of the upstream flow generating a new, more energetic turbulent boundary layer with a virtual origin slightly upstream of the honeycomb exit.

In the absence of further considerations, the CFD results imply the best geometry to be that with entrance second derivative $z''_{-1}=0$ and inflection location $x(z''=0)=-0.6$, i.e., that giving the least negative pressure coefficient (or the lowest cavitation number) at the exit. In Fig. 2, however, it can be seen that for this geometry the curvature must necessarily pass through a maximum just downstream of the entrance, which as mentioned above is a maximum value for the parameter space. Figure 1 shows that for a choice of an entrance second derivative $z''_{-1}=3$ and inflection location $x(z''=0)=-0.6$, the curvature at the entrance will be monotonically decreasing. These later parameters were chosen over those that gave the absolute maximum of the pressure coefficient at the exit on the basis of a fairer geometry and decreasing curvature at the entrance. This change has relatively little effect on either the friction coefficient at the entrance or the minimum pressure coefficient at the exit and is more favorable for avoiding the Görtler instability of the contraction inlet boundary layer. The centrifugal instability of boundary layers on concave surfaces (or Görtler instability) leads to the formation of alternately rotating streamwise vortices, as reviewed by Schlichting and Gersten [17].

The associated transverse flows produce periodic spanwise concentrations of low energy fluid that make the boundary layer locally more susceptible to separation in the adverse pressure gradient region approaching the location of the maximum curvature. The detachment of counter-rotating streamwise vortex pairs in this region was observed by Lanspeary and Bull [18] at very low Reynolds numbers (maximum of about 1×10^5) to cause strong disturbances at the exit of an octagonal to a square wind tunnel contraction. They ascribed this phenomenon to the combined effects of lateral and streamwise pressure gradients and the amplification of inflow nonuniformities by the Görtler instability.

The criterion for the Görtler instability involves the product of the boundary layer thickness and wall curvature. For the contraction floor profile with $z''_{-1}=0$ (shown in Fig. 1), this product will be initially zero; however z'' increases rapidly with distance downstream to reach a maximum at around 3.2 at $x=-0.85$. Here the local value of the Görtler number will exceed that at $x=-1.0$ for the floor profile with $z''_{-1}=3$ shown in Fig. 2. This crude qualitative analysis indicates that the profile with $z''_{-1}=0$ is not necessarily preferable from the viewpoint of avoiding the Görtler instability. In any case, the inlet boundary layers of the full-scale water tunnel are likely to be turbulent, and their large scale mixing eddies should reduce the coherence of any Görtler vortices and mitigate their undesirable effects.

The CFD predictions for the entire parameter space investigated show relatively small variations of test section boundary layer thickness, streamwise velocity uniformity, and spanwise velocity components of the core flow at the contraction exit reference section. As shown by Morel [6], for axisymmetric contractions, streamwise velocity uniformity is essentially related to the minimum pressure at the exit. For the chosen geometry, the streamwise velocity uniformity and spanwise velocity components of the core flow at the exit reference section were within ±0.5% of the reference velocity.

In summary, the contraction geometry was chosen on the basis of geometrical considerations supported by the CFD analysis and the qualitative assessment of the effects of entrance geometry and turbulence management devices on the inlet boundary layer. To more fully investigate the performance of this geometry, the effects of the Reynolds number on the surface pressure distribution and the Froude number on cavitation inception are discussed below.

5.2 Surface Pressure Distribution.

As shown in Figs. 11 and 12, pressure extrema occur at the corners on the floor of the contraction near the inlet and outlet. The peak at the inlet leads to adverse gradients upstream of the contraction entrance that may lead to separation, while that at the outlet controls the minimum achievable test section cavitation number and test section flow uniformity. Figures 15 and 16 show local plots of corner pressure against longitudinal position, x, at the inlet and outlet, respectively, from the various investigations performed. These include inviscid and viscous (RANS) CFD computations for the existing full-scale water tunnel and model-scale wind tunnel tests for the chosen new geometry.

The inviscid flow computations provide results at effectively infinite Reynolds numbers, whereas the viscous CFD results shown in Fig. 15 are for the maximum and minimum Reynolds numbers corresponding to a full-scale tunnel operation. The model test results were obtained at a Reynolds number one order of magnitude less than the maximum full-scale value. Both the inviscid and viscous CFD methods predict the adverse gradient upstream of the contraction entrance, but the inviscid method predicts a far greater adverse gradient and peak entrance pressure. A difference in the peak pressure coefficient between the maximum and minimum Reynolds numbers is also evident from the viscous CFD. The experimental results show both reduced pressures upstream of the entrance and a significantly reduced peak pressure. These variations with Reynolds number in the peak pressure and adverse gradient show the displacement effect of the boundary layer in fairing the contraction profile. They also show the classical inviscid theory to be quite conservative as regards the prediction of entrance separation.

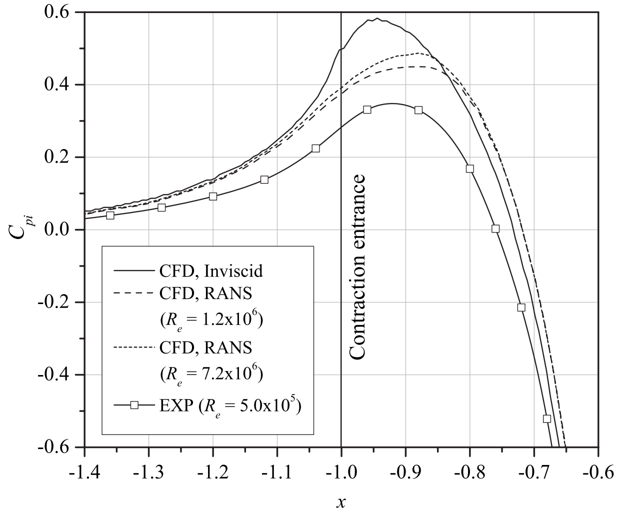

Fig. 15 Comparison of floor corner pressure distributions near the contraction inlet from viscous (RANS) and inviscid CFD predictions and experiment

Similar effects are also evident at the outlet, as shown in Fig. 16. The lowest minimum pressure is predicted by the inviscid CFD, with progressively less negative values predicted by the viscous CFD for the largest and smallest Reynolds numbers and the lower Reynolds number model tests. The viscous predictions and model tests show that the minimum achievable cavitation number should be slightly, but significantly, lower than that predicted from the inviscid analysis. The experimental results exhibit a marked discontinuity in pressure gradient along the floor corner at $x=0$, which is suggestive of turbulent reattachment behind a laminar separation bubble. This feature is not evident in pressure distributions measured along the centerline of the contraction floor at the outlet.

Both the CFD and experimental results indicate that entrance separation should not occur for the chosen geometry. As discussed previously, this conclusion is considered conservative in view of

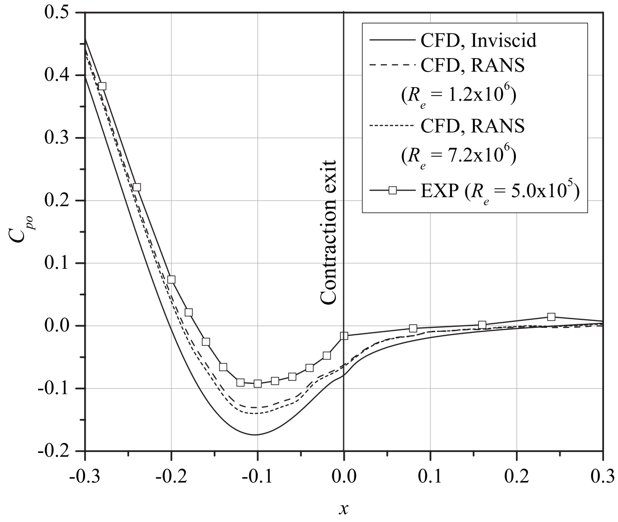

Fig. 16 Comparison of floor corner pressure distributions near the contraction outlet from viscous (RANS) and inviscid CFD predictions and experiment

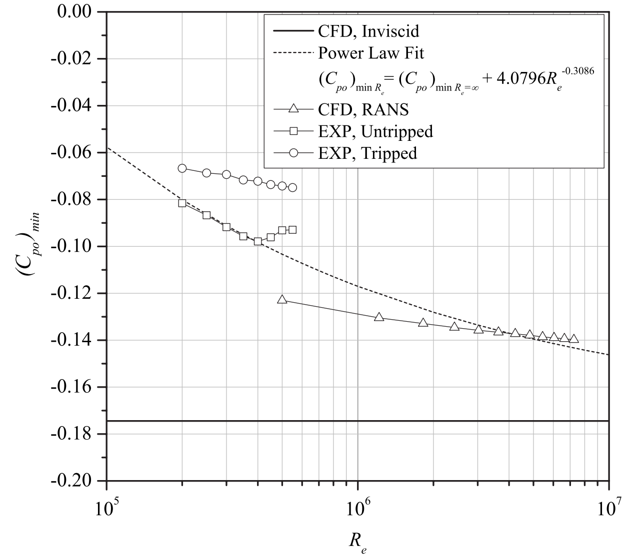

Fig. 17 Comparison of predicted minimum pressure near the contraction outlet from viscous (RANS) and inviscid CFD predictions and experiment

the associated inlet boundary layer thicknesses exceeding the likely values for the full-scale tunnel. This makes the outlet minimum pressure the major design consideration in controlling the minimum operable cavitation number.

Figure 17 summarizes the influence of the Reynolds number on the outlet minimum corner pressure coefficient as obtained from all CFD predictions and experimental results. The inviscid CFD predictions indicate the limiting value of minimum pressure expected at infinite Reynolds number, $(C_{po})_{\min R_e=\infty}=-0.174$. The viscous CFD results from RANS calculations, for which the boundary layer is turbulent within the contraction, show a monotonic decrease in the outlet minimum pressure with increasing Reynolds number. This is to be expected, as the magnitude of surface curvature relief around the minimum pressure location should decrease as the incident boundary layer becomes thinner.

The experimental results from low speed wind tunnel tests, however, show a nonmonotonic variation of the minimum pressure with Reynolds number. This is probably due to the movement of a laminar-turbulent transition region past the minimum pressure location in the upper Reynolds number range of the model tests. At low Reynolds number a turbulent boundary layer may relaminarize due to the high acceleration of flow in a contraction inlet and, subsequently, retransition near the outlet as observed by Nishizawa et al. [19]; at high Reynolds number the relaminarization disappears and the boundary layer within the contraction becomes fully turbulent. The above hypothesis for the nonmonotonic effect of the Reynolds number on the minimum pressure in the model tests was confirmed by inserting a 3 mm diameter trip wire on all sides of the contraction at $x=-0.32$ to force the exit boundary layer to be fully turbulent. As seen in Fig. 17, this produced a monotonic variation of minimum pressure with Reynolds number in the model tests; the minimum pressure was also increased due to the boundary layer thickening effect of the trip wire. The minimum outlet pressure decreases at a slower rate in this case, as the boundary layer thickness near the outlet is dominated by the momentum deficit introduced by the trip wire.

The experimental pressure measurements with the trip wire indicate that artificial thickening of the boundary layer within the contraction might be used to decrease the minimum achievable cavitation number of a water tunnel. This would depend on the thickening device being installed far enough upstream to prevent it from promoting cavitation. A further benefit would be the improvement of flow uniformity in the test section; the associated costs would be increases in the contraction loss and test section boundary layer thickness.

To provide a final comparison between the experiment and the numerical methods, a further solution of the viscous CFD was obtained for a Reynolds number of 500,000, which was near the upper limit of the model tests. The result presented in Fig. 17 shows the inviscid CFD to be conservative, although a smaller minimum pressure coefficient than that measured in the experiment is predicted. The tripped experimental results and the viscous CFD overall show a similar sensitivity to Reynolds number variations but are offset by about 0.05 in $(C_{p_o})_{\min}$. The latter shift is attributable to differences in entrance boundary layer development and the much thicker boundary layer at the exit due to the trip.

Due to the complexity of flow phenomena within the contraction, there can be no unique relation between the outlet pressure minimum and the Reynolds number. However, as shown by the example in Fig. 17, the data can be broadly correlated by a power law of the form

$$(C_{p_o})_{\min R_e} = (C_{p_o})_{\min R_e=\infty} + AR_e^{-B} \tag{2}$$

where A and B are constants. This relation may be useful for preliminary design purposes.

5.3 Cavitation Onset Prediction. Cavitation performance may be characterized by the minimum achievable cavitation number at the exit reference position defined above. The pressure extrema at the corners near the exit control the minimum cavitation number only at higher Froude numbers. Here the reduction in static pressure associated with the higher dynamic pressure exceeds the hydrostatic pressure imposed by the liquid column extending to the ceiling of the test section. At lower Froude numbers, cavitation will occur first on the ceiling, where the lower static pressures will then dominate. The test section or reference cavitation number σ_o may be found as a function of the dimensionless test section velocity (i.e., Froude number, F_n) by calculating the local cavitation number from the contraction surface pressure distribution. Assuming that the critical pressure is the vapor pressure, the minimum reference cavitation number and inception location may be found from equating the global minimum of the local cavitation number, σ_l, to zero as follows:

$$\sigma_l = \frac{p - p_v}{\frac{1}{2}\rho U_o^2} = C_{p_o} + (\sigma_o)_{\min} + \frac{2gz}{U_o^2} = 0 \tag{3}$$

The pressure coefficient C_{p_o} in Eq. (3) is evaluated with gravity forces neglected, as these are explicitly given by the term $2gz/U_o^2$, and is thus a direct function of the flow pattern.

Figure 18 shows the reference cavitation number, σ_o, at inception as a function of the Froude number for four cases. These include the inviscid prediction and viscous predictions at the maximum and minimum Reynolds numbers analyzed; the case of the Reynolds number varying with the Froude number corresponding to a full-scale operation is also shown. At low Froude numbers, where cavitation occurs on the ceiling, the incipient reference cavitation number is insensitive to viscous effects and is closely proportional to the inverse of the dynamic pressure increase or the inverse square of the test section Froude number; i.e., the inception value of σ_o decreases as F_n increases.

Due to the uniform pressure distribution on the ceiling, the local cavitation number is essentially zero everywhere on that surface. This is confirmed by experimental observations, indicating that cavitation occurs uniformly on the test section ceiling as a bubbly mixture. At higher Froude numbers the local cavitation number minimum occurs only locally at the pressure minima in the duct corners near the contraction exit, and the inception value of σ_o increases with F_n.

Experimental observations show the floor cavitation to com-

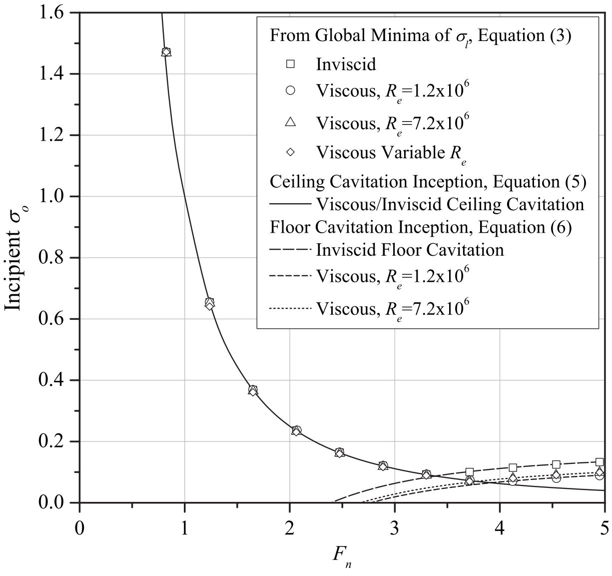

Fig. 18 Comparison of predicted contraction cavitation inception from viscous (RANS) and inviscid computations

mence in the corners and then spread over the whole floor width as the Froude number is further increased. It occurs as transient bubble and sheet cavitation, which is undesirable in that it can affect pressure tappings connected to instrumentation in addition to having adverse effects on testing. The opposing trends of the inception cavitation number at the high and low Froude numbers imply that there is a minimum attainable value of σ_o for inception at an intermediate value of F_n for which the effects of dynamic and hydrostatic pressure are balanced, as can be seen in Fig. 18. At this Froude number the local cavitation number is zero over a large area including the sidewalls.

As the global minimum of the local cavitation number at higher Froude numbers occurs close to the test section entrance, it can be assumed to be located at the test section floor level. For cavitation inception to occur either on the ceiling or floor of the test section, Eq. (3) then reduces to

$$\sigma_o = -(C_{p_o})_{\min} \pm \frac{1}{F_n^2} \tag{4}$$

where the + and − signs refer to the ceiling and floor, respectively.

Therefore, for test section ceiling cavitation inception

$$\sigma_o = \frac{1}{F_n^2} \tag{5}$$

and for test section floor cavitation inception

$$\sigma_o = -(C_{p_o})_{\min} - \frac{1}{F_n^2} \tag{6}$$

as $(C_{p_o})_{\min}$ on the test section ceiling is globally zero for both inviscid and viscous cases.

Equation (5) describing ceiling cavitation inception is plotted in Fig. 18 and shows the expected close agreement with points derived from Eq. (3). Equation (6) for floor inception is also plotted using constant values of $(C_{p_o})_{\min}$ obtained for the cases of inviscid prediction and viscous prediction at the maximum and minimum Reynolds numbers for the AMC cavitation tunnel; the corresponding $(C_{p_o})_{\min}$ values are −0.174, −0.14, and −0.13, respectively. The compound curve constructed from the greater of the values given by Eqs. (5) and (6) agrees closely with the points derived from Eq. (3). There is very little difference between the incipient reference cavitation number for the maximum and minimum Reynolds number cases, but these both differ significantly from the inviscid case.

It should be noted that the minimum achievable cavitation number at low speeds will also depend on the absolute minimum static pressure achievable in the test section. This, in turn, will depend on the circuit characteristics between the test section and the location of the free surface to which vacuum is applied and on the tunnel vacuum system. The minimum cavitation number at high Froude numbers, however, will normally be controlled by the pressure minima occurring near the contraction exit.

At low Froude numbers, where cavitation is initiated on the ceiling, there is virtually no difference between the inviscid and viscous predictions of the incipient cavitation number for reasons mentioned above. In the high Froude number regime, where cavitation is initiated on the floor, the critical cavitation number is noticeably lower for the viscous cases due to boundary layer displacement effects on the pressure minima arising the from relaxation of the local freestream curvature. This also has the effect of moving incipient cavitation to a higher Froude number, as shown in Fig. 18. The presence of a minimum reference cavitation number at a particular Froude number makes it logical to design a contraction with this value of F_n corresponding to a maximum speed or Reynolds number. Equating Eqs. (5) and (6) gives the following relations for the minimum σ_o and the corresponding F_n value in terms of $(C_{p_o})_{\min}$,

$$(\sigma_o)_{\min} = \frac{-(C_{p_o})_{\min}}{2} \tag{7}$$

$$(F_n)_{\min\,\sigma_O} = \sqrt{\frac{2}{-(C_{p_o})_{\min}}} \tag{8}$$

Table 1 compares the characteristics of several modern large and medium scale cavitation tunnel facilities using asymmetric contractions with data for the contraction analyzed in this study. Assuming at least a similar contraction performance to that of the present study, it can be seen for the larger facilities that their maximum speeds correspond closely to the minimum inception

Table 1 Comparison of basic parameters for several medium to large cavitation tunnels

Facility	max U_o (m/s)	h (m)	max F_n	$1/F_n^2$ (at max F_n)	min σ_o	F_n (at min σ_o)	CR	L/h
LCC[a]	18	3.05	3.32	0.091	0.13	2.82	6	3.93
HYKAT[a]	12.6	1.60	3.18	0.099	0.16	3.18	4	4.81
GTH, large TS[b]	12	1.35	3.30	0.092	0.25	3.30	4.8	7.41
GTH, small TS[b]	20	1.14	5.98	0.028	0.065	5.98	10	5.26
AMC	12	0.60	4.95	0.069	0.041	3.80	7.11	4.17

[a] ITTC Catalogue of Facilities [20].
[b] Lecoffre et al. [11].

value of σ_o found in this study. Presumably this is for the reasons discussed, although higher speeds can be achieved with a relatively small increase in the minimum achievable cavitation number. This is especially the case for smaller facilities where the relatively thicker boundary layer will have a greater fairing effect on the contraction profile.

6 Conclusions

A four-term sixth-order polynomial has been used to parametrize wall profiles for an asymmetric square section contraction. It allows an independent choice of the inflection point location and the value of the entrance second derivative.

A RANS-based CFD model for contraction design and optimization has been validated against observations of test section boundary layer properties in the exisiting AMC cavitation tunnel. This model has been applied to specify an improved contraction geometry for the tunnel redevelopment.

Viscous CFD predictions showed that boundary layer displacement effects may alter the effective curvature of the contraction profile and reduce the magnitudes of local pressure extrema at the contraction entrance and exit below the values predicted by inviscid CFD. The maximum pressure gradients and minimum achievable test section cavitation numbers predicted by the viscous CFD are correspondingly less than those predicted by inviscid CFD.

The prediction of cavitation onset has been discussed in detail. The minimum cavitation number has been shown to be a function of Froude number based on the test section velocity and height that incorporate the effects of physical scale on cavitation tunnel performance.

At low Froude numbers, cavitation will be initiated on the test section ceiling for tunnels having an asymmetric contraction with a horizontal roof. In this case, the minimum achievable cavitation number is a function of the Froude number only.

At high Froude numbers, cavitation inception in this type of tunnel will occur at the point of minimum pressure at the corner of the floor near the contraction exit. The minimum cavitation number is then controlled by both the Froude number and the minimum pressure coefficient experienced in the contraction.

Artificial thickening of the contraction exit boundary layer may be used to decrease the minimum achievable cavitation number at high Froude numbers and to improve test section flow uniformity at the expense of increased contraction loss and higher test section boundary layer thickness.

Acknowledgment

The authors gratefully acknowledge the support from the Australian Research Council, the Australian Commonwealth Government through the AusIndustry–Major National Research Facilities Program, the Australian Maritime College, the Tasmanian Partnership for Advanced Computing and the University of Tasmania. The authors are also grateful for the provision of an academic licence for the CFX software package.

Nomenclature

g = gravitational acceleration
h = contraction outlet height
p = static pressure
p_i = reference pressure at the contraction inlet (defined at the duct center, $x=-1.68$, $y=0$, $z=-0.2$)
$p_{\min}$ = global minimum static pressure
p_o = reference pressure at the contraction exit (defined at the duct center, $x=0.12$, $y=0$, $z=0$)
p_v = vapor pressure
u = velocity parallel to the wall
u^+, y^+ = boundary layer inner variables: $u^+=u/u^*$; $y^+=yu^*/\nu$
u^* = wall friction velocity $=\sqrt{\tau_w/\rho}$
y = wall normal coordinate for the boundary layer
x,y,z = coordinate directions nondimensionalized by the contraction length: x longitudinal, y transverse (horizontal), z transverse (vertical) (origin on the test section centerline at the contraction exit)
x_{vis} = x-component of viscous force acting on the floor of contraction
C_{p_i} = inlet static pressure coefficient $=(p-p_i)/\frac{1}{2}\rho U_i^2$
C_{p_o} = outlet static pressure coefficient $=(p-p_o)/\frac{1}{2}\rho U_o^2$
CR = contraction ratio (inlet area/outlet area)
F_n = Froude number $=U_o/\sqrt{gh}$
K = curvature
L = contraction length
R_e = Reynolds number $=hU_o/\nu$
U_i = reference velocity at the contraction inlet (defined at the duct center, $x=-1.68$, $y=0$, $z=-0.2$)
U_o = reference velocity at the contraction exit (defined at the duct center, $x=0.12$, $y=0$, $z=0$)
δ^* = boundary layer diplacement thickness
θ = boundary layer momentum thickness
σ_o = cavitation number at the contraction exit reference position $=(p_o-p_v)/\frac{1}{2}\rho U_o^2$
σ_l = local cavitation number $=(p-p_v)/\frac{1}{2}\rho U_o^2$
ρ = fluid density
ν = kinematic viscosity
τ_w = wall shear stress

Subscripts

min = minimum

Appendix

A sixth-order polynomial was adopted to generate the contraction profiles as this enables an independent choice or variation of the inflection point location and the first and second derivative values at the entrance and exit. The coordinate system is defined with the origin located at the exit of the contraction, with the x coordinate directed positive downstream and the z coordinate directed positive upward. If the first and second derivatives at the exit are chosen to be zero, then only a four-term polynomial is required,

$$z - z_0 = ax^6 + bx^5 + cx^4 + dx^3 \quad (-1 \leqslant x \leqslant 0) \tag{A1}$$

where z and x are nondimensionalized by the contraction length L. Using the entrance ordinate, z_{-1}, the entrance first and second derivatives, $z'_{-1}=0$ and z''_{-1}, and the location of the inflection point, x_i, the following equation may be solved for the coefficients a, b, c, and d:

$$\begin{bmatrix} 1 & -1 & 1 & -1 \\ -6 & 5 & -4 & 3 \\ 30 & -20 & 12 & -6 \\ 30x_i^4 & 20x_i^4 & 12x_i^4 & 6x_i^4 \end{bmatrix} \begin{Bmatrix} a \\ b \\ c \\ d \end{Bmatrix} = \begin{Bmatrix} z_{-1} \\ 0 \\ z''_{-1} \\ 0 \end{Bmatrix} \tag{A2}$$

The solution to Eq. (A2), found from a computational symbolic manipulation using the program MAPLE, is given by

$$\begin{Bmatrix} a \\ b \\ c \\ d \end{Bmatrix} = \left\{ \begin{array}{c} \dfrac{60z_{-1} + 3z''_{-1} - 180x_i z_{-1} + 10x_i^2 z''_{-1} - 12x_i z''_{-1} + 120x_i^2 z_{-1}}{6(5x_i^3 + 6x_i + 1 + 10x_i^2)} \\ \dfrac{48z_{-1} + 2z''_{-1} - 108x_i z_{-1} + 6x_i z''_{-1} - 5x_i^3 z''_{-1} - 60x_i^3 z_{-1}}{6(5x_i^3 + 6x_i + 1 + 10x_i^2)} \\ \dfrac{30z_{-1} + z''_{-1} - 180x_i^2 z_{-1} - 10x_i^2 z''_{-1} - 10x_i^3 z''_{-1} - 150x_i^3 z_{-1}}{6(5x_i^3 + 6x_i + 1 + 10x_i^2)} \\ -\dfrac{x_i(180z_{-1} + 6z''_{-1} + 20x_i z''_{-1} + 480x_i^2 z_{-1} + 300x_i^2 z_{-1} + 15x_i^2 z''_{-1})}{6(5x_i^3 + 6x_i + 1 + 10x_i^2)} \end{array} \right\} \tag{A3}$$

References

[1] Brandner, P. A., Lecoffre, Y., and Walker, G. J., 2006, "Development of an Australian National Facility for Cavitation Research," *Proceedings of the Sixth International Symposium on Cavitation—CAV2006*, Wageningen, The Netherlands, Sep. 11–15, pp. 1–9 (on CD).

[2] Brandner, P. A., Lecoffre, Y., and Walker, G. J., 2007, "Design Considerations in the Development of a Modern Cavitation Tunnel," *Proceedings of the 16th Australasian Fluid Mechanics Conference*, P. Jacobs, T. McIntyre, M. Cleary, D. Buttsworth, D. Mee, R. Clements, R. Morgan, and C. Lemckert, eds., Gold Coast, Australia, Dec. 3–8, pp. 630–637 (on CD).

[3] Barlow, J. B., Rae, W. H., and Pope, A., 1999, *Low Speed Wind Tunnel Testing*, 3rd ed., Wiley, New York, Chap. 3, pp. 62–123.

[4] Wetzel, J. M., and Arndt, R. E. A., 1994, "Hydrodynamic Design Considerations for Hydroacoustic Facilities: Part I—Flow Quality," ASME J. Fluids Eng., **116**(2), pp. 324–331.

[5] Chmielewski, G. E., 1974, "Boundary-Layer Considerations in the Design of Aerodynamic Contractions," J. Aircr., **11**(8), pp. 435–438.

[6] Morel, T., 1975, "Comprehensive Design of Axisymmetric Wind Tunnel Contractions," ASME J. Fluids Eng., **97**(2), pp. 225–233.

[7] Mikhail, M. N., 1979, "Optimum Design of Wind Tunnel Contractions," AIAA J., **17**(5), pp. 471–477.

[8] Downie, J. H., Jordinson, R., and Barnes, F. H., 1984, "On the Design of Three-Dimensional Tunnel Contractions," Aeronaut. J., **87**, pp. 287–297.

[9] Su, Y.-x., 1991, "Flow Analysis and Design of Three-Dimensional Wind Tunnel Contractions," AIAA J., **29**(11), pp. 1912–1919.

[10] Fang, F.-M., 1997, "A Design Method for Contractions With Square End Sections," ASME J. Fluids Eng., **119**(2), pp. 454–458.

[11] Lecoffre, Y., Chantrel, P., and Teiller, J., 1987, "Le Grand Tunnel Hydrodynamique (GTH): France's New Large Cavitation Tunnel for Hydrodynamics Research," *International Symposium on Cavitation Research Facilities and Techniques*, Boston, MA, Dec. 13–18, ASME FED-Vol. 54, pp. 1–10.

[12] Keith, W., Bennett, J., and Barclay, J., 1991, "Hydroacoustic Research at the Quiet Water Tunnel Facility of the Naval Underwater Systems Division," *Hydro-Acoustic Facilities, Instrumentation and Experimental Facilities*, Atlanta, GA, Dec. 1–6, ASME, NCA-Vol. 10, pp. 43–54.

[13] AEA Technology Engineering Software, 2002, CFX-5 Solver, pp. 208–546.

[14] Speziale, J. G., Sarker, S., and Gatski, T. B., 1991, "Modelling the Pressure Strain of Turbulence: An Invariant Dynamical Systems Approach," J. Fluid Mech., **277**, pp. 245–272.

[15] Brandner, P. A., Clarke, D. B., and Walker, G. J., 2004, "Development of a Fast Response Pressure Probe for Use in a Cavitation Tunnel," *Proceedings of the 15th Australasian Fluid Mechanics Conference*, Sydney, Australia, Dec. 13–17, M. Behnia, W. Lin, and G. D. McBain, eds., 4 pages (on CD).

[16] Ashby, D., Dudley, M., Iguchi, S., Browne, L., and Katz, J., 1990, "Potential Flow Theory and Operation Guide for the Panel Code PMARC," NASA, Report No. TM 102851.

[17] Schlichting, H., and Gersten, K., 1960, *Boundary Layer Theory*, 8th ed., Springer-Verlag, Berlin, Chap. 15, pp. 480–483.

[18] Lanspeary, P. V., and Bull, M. K., 1998, "A Mechanism for Three-dimensional Separation in Duct Contractions," *Proceedings of the 13th Australasian Fluid Mechanics Conference*, Melbourne, Australia, Dec. 13–18, M. C. Thompson and K. Hourigan, eds., Vol. 2, pp. 687–690.

[19] Nishizawa, A., Takagi, S., Togugawa, N., and Sobagaki, T., 2001, "Rebirth of Turbulence in Laminarized Boundary Layers Along the Wind Tunnel Contraction," *39th Aerospace Sciences Meeting and Exhibit*, Reno, NV, Jan. 8–11, AIAA Paper No. 2001-0277.

[20] 1992, International Towing Tank Conference Catalogue of Facilities.

Raúl Sánchez
e-mail: raul.sanchez@upm.es

Luis Juana
e-mail: luis.juana@upm.es

Departamento de Ingeniería Rural,
Technical University of Madrid (UPM),
ETSI Agrónomos,
Ciudad Universitaria s/n,
Madrid 28040, Spain

Francisco V. Laguna
Departamento de Ingeniería Civil: Hidráulica y Energética,
Technical University of Madrid (UPM),
ETSI Caminos,
Canales y Puertos,
C/Profesor Aranguren s/n,
Madrid 28040, Spain
e-mail: he15@caminos.upm.es

Leonor Rodríguez-Sinobas
Departamento de Ingeniería Rural,
Technical University of Madrid (UPM),
ETSI Agrónomos,
Ciudad Universitaria s/n,
Madrid 28040, Spain
e-mail: leonor.rodriguez.sinobas@upm.es

Estimation of Cavitation Limits From Local Head Loss Coefficient

Cavitation effects in valves and other sudden transitions in water distribution systems are studied as their better understanding and quantification is needed for design and analysis purposes and for predicting and controlling their operation. Two dimensionless coefficients are used to characterize and verify local effects under cavitating flow conditions: the coefficient of local head losses and the minimum value of the cavitation number. In principle, both coefficients must be determined experimentally, but a semianalytical relationship between them is here proposed so that if one of them is known, its value can be used to estimate the corresponding value of the other one. This relationship is experimentally contrasted by measuring head losses and flow rates. It is also shown that cavitation number values, called cavitation limits, such as the critical cavitation limit, can be related in a simple but practical way with the mentioned minimum cavitation number and with a given pressure fluctuation level. Head losses under conditions of cavitation in sharp-edged orifices and valves are predicted for changes in upstream and downstream boundary conditions. An experimental determination of the coefficient of local head losses and the minimum value of the cavitation number is not dependent on the boundary conditions even if vapor cavity extends far enough to reach a downstream pressure tap. Also, the effects of cavitation and displacement of moving parts of valves on head losses can be split. A relatively simple formulation for local head losses including cavitation influence is presented. It can be incorporated to water distribution analysis models to improve their results when cavitation occurs. Likewise, it can also be used to elaborate information about validity limits of head losses in valves and other sudden transitions and to interpret the results of head loss tests. [DOI: 10.1115/1.2969453]

Keywords: local head losses, cavitation, valve, orifice, pipeline design

Introduction

As dictated by Bernoulli's equation, there is a drop in the pressure of the permanent regime flow in a constriction, such as a valve, due to increased velocity. The phenomenon of cavitation can materialize if the pressure drop is big enough. It is also known that local head losses take place primarily in the expansion, characterized by the presence of vortices, which exist in the turbulent wake, downstream of the point of flow separation. In addition vortices contain regions of high velocity and hence low pressure. These areas of low pressure are potential sites for vapor formation.

Cavitation reduces a device's flow capacity, or, concurrently, head losses are greater as the more intense cavitation is. Tullis [1] set out several definitions of cavitation limits according to observable effects on flow. These limits include the choking cavitation limit, from which cavitation affects the flow capacity of a device. Unless this limit is reached, even if cavitation takes place, the effects of this phenomenon on head losses are practically negligible and scale effect is appreciated (Ball and Tullis [2]; Tullis [3]). Similarly, Testud et al. [4] studied experimentally the noise generated by a single hole and a multihole sharp-edged orifice, both with the same cross-sectional opening, in a water pipe. They concluded that below the choking cavitation limit the multihole is more silent than the single hole orifice. Also, it can be observed in the experimental results that the head loss coefficient and the choking cavitation limit are equivalent in both, indicating that the distribution of cross-sectional opening should not have any effect on these two coefficients.

Zhang and Cai [5] studied experimentally the geometric shape of orifices that produce the same head loss with the aim of reducing the pressure drop associated with the cavitation risk. Similarly, Zhang and Chai [6] indicated the importance of quantifying cavitation in energy dissipation hydraulic works and, particularly, when examining a serial arrangement of orifices to achieve this goal. In this respect, there is a complementary wide technical literature, such as ANSI/ISA [7] and Idel'cik [8], which compiled many particular empirical studies about head losses and cavitation, in general without relation to each other.

From experimental determinations, the choking cavitation limit for sharp-edged orifices is a function of geometric parameters only, and the effect of the scale is negligible (Tullis [9]; Tullis and Govindarajan [10]). Mishra and Peles [11] also reached the same conclusion again for orifices. In this last paper, they examined the size-dependent similarities and differences in cavitation, for which purpose they use orifices measuring from just a few micrometers to several centimeters. Additionally, as head losses are also dependent on the geometric shape, it is possible to get an analytical relationship between the head loss coefficient and the choking cavitation limit in relatively simple sudden transitions, as shown by Sarpkaya [12] and Nurick [13]. In the last two papers, the flow has been characterized by means of the contraction coefficient.

One of the objectives of this paper was to predict the head losses in a sudden transition for any boundary condition imposed by the distribution system and especially in cases with uncertainty about the cavitation impact on such head losses. In principle, two independent coefficients, one for head losses and another for cavitation, should suffice to characterize a particular transition and

---

Contributed by the Fluids Engineering Division of ASME for publication in the JOURNAL OF FLUIDS ENGINEERING. Manuscript received October 11, 2007; final manuscript received May 19, 2008; published online September 4, 2008. Assoc. Editor: Theodore Heindel.

achieve the objective. On the other hand, information about head losses in valves and other singular elements is relatively extensive. However the one concerned on cavitation is scarce. Thus, it is worthwhile to estimate the cavitation-related coefficient from the head loss coefficient.

Additionally, the elements of valves are subject to drag force. On top of the possible variability of head losses due to the displacement of their closing elements are losses induced by the potential impact of cavitation. By predicting head losses under circumstances in which they are significantly affected by cavitation, it will be possible to separate cavitation effect and, consequently, to specify what effects the above displacement has on head losses and draw conclusions about the behavior of such control devices.

Finally, the presence of cavitation does not imply a significant effect on head losses, but other unwanted effects, such as noise, vibration, and erosion damage, can be found. Therefore, another objective of this paper is to develop a procedure for estimating a value of the cavitation number for use as a reference against which to compare and to determine other cavitation limits.

Materials and Methods

The hydraulics general equation for the study of local head losses h_f in transitions can be expressed as

$$h_f = K\left(\frac{l}{l'}, \frac{l}{l''}, \ldots, \mathrm{Re}, \ldots\right)\frac{U^2}{2g} \tag{1}$$

As the length of a transition is relatively short, friction-induced head losses are negligible as compared with separation-induced losses. Additionally, rapidly varied flow in a transition between straight cross-sections with uniform movement is often considered in practice to be given in terms of fully developed turbulence. Then, the Reynolds number Re is not part of the local head loss coefficient K, and this only depends on the relations between the geometric dimensions l, l', l''. This way, local head losses in any given geometric shape are characterized by a constant coefficient K.

In a transition with identical sections at each end and disregarding the differences of elevation between their centroids, the coefficient is determined by

$$K = \frac{p_1 - p_2}{\rho\dfrac{U^2}{2}} \tag{2}$$

Subindex 1 refers to section 1 immediately upstream of the transition, and 2 refers to the downstream section 2. ρ is the water density, U is the mean flow velocity determined from the reference section, generally the nominal section, and $(p_1 - p_2)$ is the pressure difference between the section immediately upstream of the transition and the downstream section in which the regime returns to uniform.

Because of the fact that for constant flow rate, head losses are greater the more intense cavitation is, the minimum value K_m of the dimensionless local head loss coefficient has been used when cavitation has no influence on head losses.

Besides, the dimensionless cavitation number σ is used to characterize the phenomenon of cavitation. Batchelor [14] showed this parameter, in its general form, as the pressure over vapor pressure/velocity head. In particular, for either the upstream or the downstream sections, this parameter is expressed as

$$\sigma_1 = \frac{p_1 - p_v}{\rho\dfrac{U^2}{2}} = \frac{p_1 - p_2 + p_2 - p_v}{\rho\dfrac{U^2}{2}} = K + \frac{p_2 - p_v}{\rho\dfrac{U^2}{2}} = K + \sigma_2 \tag{3}$$

Another way of expressing the parameter σ, often used in research looking at cavitation in internal flows, is to divide by the likewise dimensionless parameter K. This gives

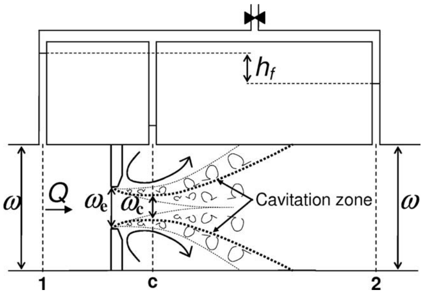

Fig. 1 Cavitating region downstream a sharp-edged orifice and piezometric levels indicated by a differential air manometer

$$\sigma_{p1} = \frac{\sigma_1}{K} = \frac{p_1 - p_v}{p_1 - p_2} = \frac{p_1 - p_2 + p_2 - p_v}{p_1 - p_2} = 1 + \frac{p_2 - p_v}{p_1 - p_2}$$
$$= 1 + \sigma_{p2} = 1 + \frac{\sigma_2}{K} \tag{4}$$

σ is a parameter that characterizes the system-imposed pressure boundary conditions. If the pressure in section 2 were equal to the vapor pressure, there would be a vapor filled cavity stretching at least as far as that section. In this case, σ_{p2} would be equal to zero, or the equivalent σ_{p1} would be equal to 1.

In short, K characterizes head losses as σ does for system-imposed boundary conditions. When cavitation has influence on head losses, they are related. Thus, we have proposed a relationship between them, at first for sharp-edged orifices, in which upstream head losses can be neglected in comparison with downstream ones. Secondly, the relationship for transitions such as sharp-edged orifices have been modified to extend it to general transitions, such as valves.

Sharp-Edged Orifices. Flow expressions for sharp-edged orifices were obtained by considering friction head losses negligible, so they are due exclusively to separation effects and, therefore, are concentrated where the streamlines are divergent (see the diagram in Fig. 1). Thus, the losses between sections 1 and c were neglected, as the streamlines in this region are convergent, and only the losses that take place in the flow expansion between c and 2 were considered.

On the other hand, the continuity equation was expressed as

$$Q = U \cdot \omega = U_c \cdot \omega_c = U_c \cdot C_c \cdot \omega_e \tag{5}$$

where U is the mean water velocity in section ω and U_c is the mean water velocity in the contracted jet section ω_c. This latter section is usually expressed as the product of the orifice section ω_e multiplied by the contraction coefficient C_c. This latter is a classic coefficient in hydraulics, which is dimensionless and is related to the ratio between the section immediately upstream of the orifice and the orifice section.

Bearing in mind that the head losses between sections 1 and c are negligible, the difference between the respective pressure heads is exclusively a function of the difference between the velocity heads. Therefore, taking into account Eq. (5), flow discharge expressed as a function of the pressure difference is

$$Q = \omega\sqrt{\frac{p_1 - p_c}{\dfrac{\rho}{2}\left[\left(\dfrac{\omega}{C_c \cdot \omega_e}\right)^2 - 1\right]}} \tag{6}$$

From the comparison between Eqs. (6) and (3) and Eq. (3), it can be found that when cavitation occurs in section c with intensity enough for p_c to lessen and approximately reach p_v, the value of σ_1 is minimum (σ_{1m}), and this latter is a function of geometric parameters only. It can be equated to the choking cavitation limit. For the sharp-edged orifice in question, this limit is

$$\sigma_{1m} = \left(\frac{\omega}{C_c \cdot \omega_e}\right)^2 - 1 \tag{7}$$

Due to the nature of C_c mentioned above, the coefficient σ_{1m} characterizes the flow pattern upstream of the contracted section c.

To study the cavitation influence on head losses, the flow rate Q has been expressed as a function of these, which are related to the pressure head difference between the two end sections of the transition. Thus, head losses need to be included. Belanger–Borda's expression, in which head losses are related to the square of the difference between velocities, is useful when considering that head losses occur exclusively at the flow expansion between sections c and 2. Moreover, together with the continuity (Eq. (5)), they can be expressed as

$$h_f = H_1 - H_2 = \frac{p_1 - p_2}{\gamma} \approx H_c - H_2 = \frac{(U_c - U)^2}{2g} = \left(\frac{\omega}{C_c \cdot \omega_e} - 1\right)^2 \frac{U^2}{2g} = K_m \frac{U^2}{2g} \tag{8}$$

Note that K_m depends only on just the geometric parameters, as was the case for σ_{1m}. Moreover, under the assumption of friction-induced head losses being negligible, it characterizes the flow pattern downstream of section c, unlike σ_{1m}, which characterized the flow pattern upstream. Our proposal is that these two parameters, K_m and σ_{1m}, should characterize a transition to simulate and predict head losses under cavitation conditions.

From Eqs. (5) and (8), flow can be expressed as

$$Q = \omega \sqrt{\frac{p_1 - p_2}{\frac{\rho}{2}\left(\frac{\omega}{C_c \cdot \omega_e} - 1\right)^2}} = \omega \sqrt{\frac{p_1 - p_2}{\frac{\rho}{2}K}} \tag{9}$$

From the elimination of Q from Eqs. (6) and (9), it is inferred that $p_2 > p_c$ because $C_c \cdot \omega_e < \omega$. Additionally, due to the constraint that within tap water (with nuclei), the pressure cannot fall below its vapor pressure p_v, the flow (Eq. (9)) will be valid only if $p_c > p_v$. When this limit materializes in section c, flow will be conditioned by cavitation. This latter is denoted by Q_v, which is obtained by substituting p_c by p_v in Eq. (6), giving

$$Q_v = \omega \sqrt{\frac{p_1 - p_v}{\frac{\rho}{2}\left[\left(\frac{\omega}{C_c \cdot \omega_e}\right)^2 - 1\right]}} = \omega \sqrt{\frac{p_1 - p_v}{\frac{\rho}{2}\sigma_{1m}}} \tag{10}$$

Notice that under the above stated conditions flow depends on p_1 only.

In conclusion, in cases with the head losses upstream of section ω_c being negligible and with the downstream flow pattern following a sudden expansion from the contracted section $\omega_c = C_c\ \omega_e$, the coefficients K_m and σ_{1m} are related. The relationship in question can be obtained by eliminating the ratio between ω_c and $C_c\ \omega_e$ from expressions of σ_{1m} and K in Eqs. (7) and (8), respectively, as follows:

$$\sigma_{1m} = K_m + 2\sqrt{K_m} \tag{11}$$

Valves. Valves are geometric transitions more complex than sharp-edged orifices. In the case of a nonaxisymmetric flow pattern, a conclusion in Rouse and Jezdinsky's [15] paper is that measurements of cavitation and pressure fluctuation made under conditions of axial symmetry should not be applied quantitatively. Besides, some particularities of flow inside valves must be borne in mind. First, it could be possible that downstream of the closing element of a valve, a cross jet section with uniform flow would not occur. So then, an energy conservation equation could not be applied between sections with nonuniform flow. Second, head losses could not adapt precisely to a sudden expansion. Even so, and being less precise than for circular orifices, it is worthwhile to formulate an approximate expression for studying in a general way a great number of possible specific cases. Thus, the relation between the coefficients K_m and σ_{1m} can also be approximated as follows. In essence, a part of the head losses will also take place in the expansion downstream of the regions in which the flow is contracted, where the streamlines are divergent, and ω_c has been used for the equivalent contracted section that would produce such losses in a sudden expansion, such a what occurs downstream a sharp-edged orifice. In a manner akin to the way in which K_m was represented in Eq. (8), the corresponding head loss coefficient is now expressed as

$$K_m = \left(\frac{\omega}{\omega_c} - 1\right)^2 \tag{12}$$

In contrast, with respect to cavitation, because flow in the region where the streamlines are convergent will not be axisymmetric either, velocity distribution in the contracted jet section will be more dispersed than in the axisymmetric flow, and cavitation could now appear at particular locations under less severe conditions. Therefore, bearing in mind the above mentioned particularities, the equivalent contracted section ω_c has been corrected with coefficient r, which is positive and less than 1 and is characteristic of every geometric shape. This coefficient attempts to take into account the mentioned particularities. As shown in Eq. (7) for sharp-edged orifices, σ_{1m} is a function of the geometric parameters and is now expressed as

$$\sigma_{1m} = \left(\frac{\omega}{r \cdot \omega_c}\right)^2 - 1 \tag{13}$$

Eliminating the ratio between the nominal and the equivalent contracted section from Eqs. (12) and (13), a relationship between K_m and σ_{1m} can be obtained. Furthermore, on top of the head losses in the expansion from the contracted region induced by the closing element of valves, there are losses caused by separation effects inside the body of such valves. Denoting the coefficient that quantifies the closing element-independent upstream losses as K_0, already included in K_m, the relation between K_m and σ_{1m} is now expressed as

$$\sigma_{1m} = \frac{1}{r^2}(\sqrt{K_m - K_0} + 1)^2 - 1 \tag{14}$$

The coefficient K_0 will be small or even zero in valves in which head losses are relatively low when they are fully open, as can be the case with butterfly valves. For other valve types, in the absence of specific studies, the value of the coefficient K_m for a valve that is in a completely open position could be considered to approximate K_0 (more details about K_0 and head losses for seat valves can be found in Sánchez [16]). The value of r is harder to approximate than K_0 and is therefore only studied experimentally in this paper.

Application. If the parameters K_m and σ_{1m} are known, either the head losses or the flow can be obtained from the system-imposed boundary conditions. These conditions are characterized by the cavitation number σ in its forms σ_2 and σ_{p2} shown in Eqs. (3) and (4).

Thus, Eqs. (9) and (10) for flow rate Q can be generally expressed, under both cavitating and noncavitating conditions, as a function of the pressure difference between the sections upstream and downstream of the singularity, $p_1 - p_2$, or the head losses h_f, with

$$Q = \omega \sqrt{\frac{p_1 - p_2}{\frac{\rho}{2}K}} = \omega \sqrt{\frac{2 \cdot g \cdot h_f}{K}} \tag{15}$$

where K is the only coefficient that has to be evaluated. This can be achieved with the function detailed below.

The value of K can be obtained from the value of the cavitation number in its forms σ_2 (if p_2 and U—or Q—are known) and σ_{p2} (if p_2 and p_1 are known). In the first case, if $0 \leqslant \sigma_2 \leqslant \sigma_{2v}$, this last being equal to $\sigma_{1m}-K_m$, there would be cavitation and it would affect the head losses. If $\sigma_2 > \sigma_{2v}$, either there would be no cavitation or there would be but it would not affect the head losses. In either case, coefficient K would be given by

$$K\begin{cases} 0 \leqslant \sigma_2 \leqslant \sigma_{2v} \rightarrow\ K = \dfrac{p_1 - p_2}{\rho\dfrac{U^2}{2}} = \dfrac{p_1 - p_v - (p_2 - p_v)}{\rho\dfrac{U^2}{2}} = \sigma_{1m} - \sigma_2 \geqslant K_m \\ \sigma_2 > \sigma_{2v} \rightarrow\ K = K_m \end{cases} \tag{16}$$

If the network is analyzed using the termed node head correction method, in which head pressures at nodes are corrected to fulfil continuity equations, then the following formulation solves the analysis:

$$K\begin{cases} 0 \leqslant \sigma_{p2} \leqslant \sigma_{p2v} = \dfrac{\sigma_{1m}}{K_m} - 1 \rightarrow\ K = \dfrac{p_1 - p_2}{\rho\dfrac{U^2}{2}} = \dfrac{p_1 - p_2}{p_1 - p_v}\cdot \sigma_{1m} = \dfrac{\sigma_{1m}}{1 + \sigma_{p2}} \geqslant K_m \\ \sigma_{p2} > \sigma_{p2v} \rightarrow\ K = K_m \end{cases} \tag{17}$$

On the other hand, if the loop flow correction method of network analysis is used, in which flow rates are corrected to fulfil energy equations, then Eq. (16) solves the problem. However, the value of p_2 is necessary and can be obtained from the previous iteration.

In spite of the fact that σ_1 can be used instead of σ_2, it is useful to determine the latter to quantify the head losses increased by cavitation and to compare qualitatively the possible lengthening of the vapor cavity. While σ_{1m} is the minimum value of σ_1, which is reached when the pressure in the contracted section is equal to p_v, the minimum value of σ_2 is zero (when $p_2 = p_v$), and cavitation materializes its effects on head losses when $\sigma_2 \leqslant \sigma_{2v}$. So, σ_2 gives more information than σ_1.

To illustrate the utility of Eqs. (15) and (16), a system such as that shown in Fig. 2(*a*) has been considered. The system boundary conditions are imposed by the tank levels. Additionally, if the head losses in the pipes upstream and downstream of the valve V are considered negligible, the pressures resulting from the above boundary conditions can also be considered in the sections immediately upstream and downstream of that valve. The coefficient K has been calculated using Eq. (17) for each situation imposed on the system, which is characterized by the parameter σ_{p2}.

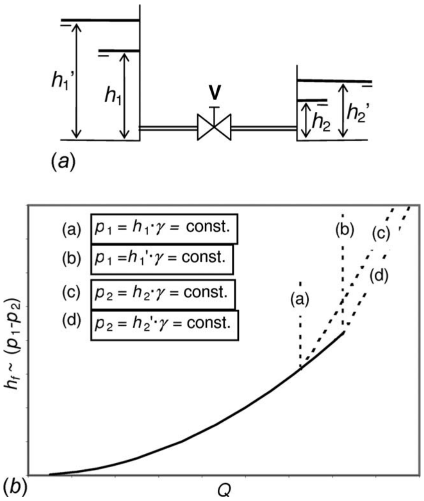

Fig. 2 (*a*) Valve between two tanks. (*b*) Head losses as a function of flow under different system-imposed boundary conditions.

Figure 2(*b*) shows the possible shapes of the curves plotting the head losses in the valve V, or other transition, as a function of flow rate for different boundary conditions indicated in Fig. 2(*a*). Curves (a) and (b) match permanent flow regime situations where the water level in the upstream tank is constant, whereas the downstream pressure changes. The opposite applies to curves (c) and (d), and the water level in the downstream tank is constant, whereas the upstream pressure changes. All four curves have a common section, depicted as a solid line, in which the cavitation effects do not affect head losses. This is compatible with situations in which $K = K_m$.

Additionally, where $\sigma_{p1} \leqslant \sigma_{1m}/K_m$ or $\sigma_{p2} \leqslant \sigma_{1m}/K_m - 1$, cavitation effects affect head losses, the value of K depends on the value of σ_{p1}, and, therefore, the relations between head losses and the flow rate differ depending on the boundary condition, which is changed. It can be seen that if p_1 is constant, then Q is too, irrespective of the value of p_2, which conforms to Eq. (10). This also applies when p_2 is constant and p_1 changes. Under these conditions, Q is a function of p_1.

In a real system, because head losses in upstream and downstream pipes cannot be considered negligible, the hypothetically observed lines would be positioned in-between the dashed plotted curves. Therefore, the representation of $h_f(Q)$ is inadequate for determining the parameters that quantify cavitation effects on head losses. However, the one of $K(\sigma_1)$ represents the head losses irrespective of the operation of the rest of the system components, and it should then be an effective tool for determining such parameters.

Experimental Verification. The above mentioned developments have been verified experimentally. We tested the following devices: three 7.56 mm, 8.93 mm, and 11.59 mm circular sharp-edged orifices, a butterfly valve with a nominal diameter of 75 mm and a symmetric closing disk, and a hydraulically operated seat globe valve with a nominal diameter of 50 mm. The orifices were positioned in transparent methacrylate (see Fig. 3) and opaque polyvinyl chloride (PVC) pipes with internal diameters of 16 mm and 16.2 mm, respectively. The two valves were positioned in their respective PVC pipes with the same nominal diameters.

All the listed devices were arranged in a test rig. Figure 4 is a

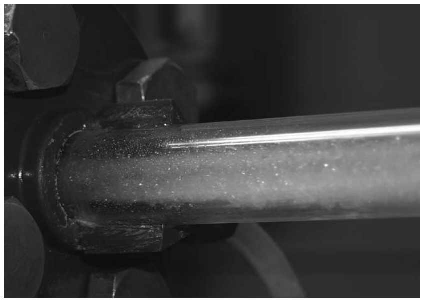

Fig. 3 View of cavitating flow downstream of one of the tested sharp-edged orifices

simplified diagram of the test rig. The diagram represents a closed circuit whose storage element is tank T and the energy comes from pump P, driven by a frequency converter-controlled electric motor.

The measurement equipment was composed of the next elements. The electromagnetic flowmeter F was used to measure flow, a digital differential manometer M_2 was used to measure the head losses in the tested elements V, and the digital manometer M_1 was used to measure the upstream pressure. Pressure h_2 was calculated as the difference between h_1 and h_f, measured by M_1 and M_2, respectively.

The distances between the element under testing and the measurement and control elements L_1, L_2, L_3, and L_4 in Fig. 4 conformed to ISA [17] and ASAE [18] instructions. In particular, L_2 and L_3 were equal to one and five times internal pipe diameters, respectively, while L_1 and L_4 were greater than ten and two times this diameter.

The control of the boundary conditions during the tests was achieved as follows. The upstream boundary condition was controlled by valves V_r and V_1, the above frequency converter, and a combination of any of these elements. Because valves affect the uniformity of flow downstream of them, it was done almost exclusively using the frequency converter. The only way to control the downstream boundary condition was to actuate on valve V_2.

The upstream and downstream boundary conditions of the element under testing, V, were relations between the pressure heads h_1 and h_2, respectively, and flow Q. For predicting head losses in the tested element under the particular conditions imposed in the test rig, these last ones in a permanent regime have been modeled by the following two equations:

$$h_1 = a_0 \cdot N^2 + a_1 \cdot N \cdot Q + a_2 \cdot Q^2 \tag{18}$$

$$Q = C_D \sqrt{h_2 - \Delta z} \tag{19}$$

Equation (18) is a standard expression for pumping head characteristic curves and is applicable in this case if V_r is closed. N represents the relation between the real frequency provided by the converter and the nominal frequency of the motor that drives the pump. The coefficients a_0, a_1, and a_2 were obtained by fitting. The last two coefficients appear to account for the head losses in the pipes making up the upstream section, whereas the first coefficient gives the pressure head with zero flow.

As regards the downstream section, the coefficients C_D and Δz of Eq. (19) were also obtained by fitting. In physical terms, the second coefficient means the height difference between the free water level in tank T and the section at which h_2 is measured. C_D covers the head losses in both V_2 and the downstream pipes, assuming a full turbulence regime. Additionally, if the vapor cavity extends to the downstream manometer tap, the approximate boundary value of the measure here would be p_v, and then this boundary condition would be $p_2 \approx p_v$.

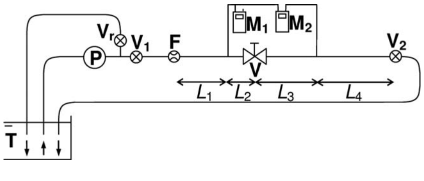

Fig. 4 Hydraulic schematic diagram of the test rig

As far as the test procedure is concerned, the above devices were tested under constant downstream and upstream discharge conditions. In the first case, valve V_2 was fixed in a fully open position. This way we were able to model this condition using Eq. (19), unless the vapor cavity had, due to its extension, affected the measurements of p_2. In the case of the fixed upstream condition, the tests were run with valve V_r at a closed position, V_1 at a fully open position, and pump P at a constant rotation regime. All the tests were run with tap water contained in tank T at a temperature of approximately 20°C, and the absolute vapor pressure at the saturation point considered was 2.4 kPa. As observed experimentally by Tullis and Skinner [19], air injection downstream the valves reduces the critical cavitation index and the magnitude of the low frequency pressure fluctuations but not the local head loss coefficient, so the presence of small quantities of dissolved or undissolved air in water should not affect the determinations of either the last mentioned coefficient or the choking cavitation index.

Also, the closing elements of valves were subject to the force generated by the fluid. As Sarpkaya [12] had observed and analyzed, the drag force on the round disk of an axisymmetric butterfly valve generates a torque that tends to close the valve.

Even though the tested butterfly valve has a latching device designed to fix the position of the handle and, therefore, the round disk, the tests were achieved with strictly increasing flows up to the maximum test flow and then immediately switched to a decreasing sequence of flows with the aim of detecting the effects of any possible disk displacement. This way, the position of the disk at the end of the test should be equal to or even more closed than that at the beginning, and consequently K_m should be greater or equal at the end of the test than at the beginning. A similar procedure was followed for the hydraulically operated seat globe valve, also to detect changes in position in the closing element.

For every orifice and for the two valves at every position of their closing element, the parameters K_m and σ_{1m} were obtained experimentally by minimizing the minimum relative squared error defined as

$$\varepsilon_r^2 = \sum_i \min\left[\left(\frac{K_i}{K_m} - 1\right)^2, \left(\frac{\sigma_{1i}}{\sigma_{1m}} - 1\right)^2\right] \tag{20}$$

where K_i and σ_{1i} were calculated from observed data using Eqs. (2) and (3). Values are given in the figures in the Results section with $K_m \pm \sigma_{\varepsilon Km}$ and $\sigma_{1m} \pm \sigma_{\varepsilon\sigma 1m}$, where the second terms are the corresponding part of the error standard deviations from Eq. (20).

Cavitation Limits. The cavitation limit studied so far is inadequate for pipeline design purposes, and other limits such as incipient and critical cavitation limits are used. These other limits, where cavitation does not take place across the whole contracted section, will occur under less severe boundary conditions and will be positioned to the right of the curve defined by Eq. (11) for sharp-edged orifices and by Eq. (14) for valves in the respective $K_m(\sigma_{1m})$ diagram. Turbulence regime-specific pressure fluctuations should play a role in the process under conditions where cavitation takes place but are not strong enough to reach the intensity corresponding to σ_{1m}. These cavitation limits can conceivably be related to σ_{1m}.

Turbulence regime-specific pressure fluctuations will produce points at which vapor pressure will approximately be reached during relatively short periods, even if the mean pressure throughout the contracted section is considerably bigger than the vapor pres-

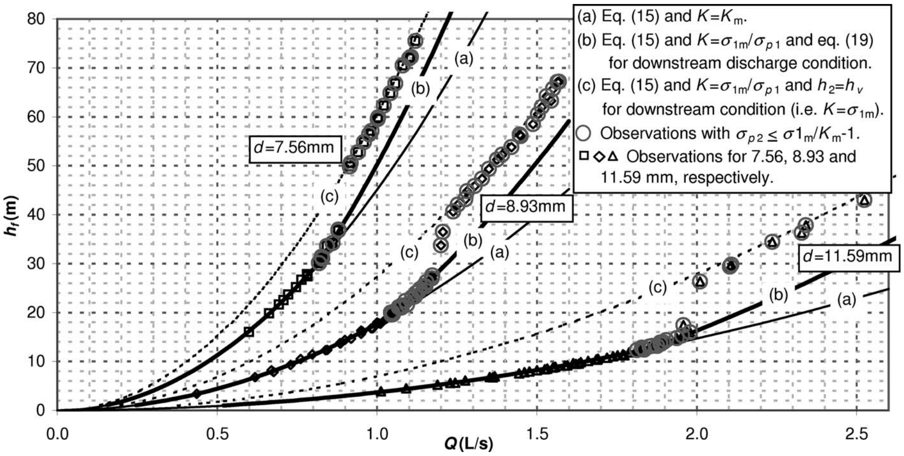

Fig. 5 Experimental and predicted results of head loss tests on sharp-edged orifices of diameter *d* in a pipe with an internal diameter $D=16$ mm

sure. In addition, although the root mean square values of pressure fluctuations do not vary with the jet speed, as noticed by Ran and Katz [20], the probability distribution changes significantly, causing a reduction in the incipient cavitation index with increasing velocity. However, considering that the pressure pulses close to the contracted section could be approximately proportional to the squared velocity pulses, as dictated by Bernoulli's equation for steady regime, for a pressure pulse intensity p', the relation between a cavitation limit σ_{1f} with pressure fluctuation p' and σ_{1m} would be

$$\sigma_{1f}=\frac{p_{1f}-p_v}{\rho\frac{U^2}{2}}=\frac{p_1-p_v+p'}{\rho\frac{U^2}{2}}=\sigma_{1m}+\frac{p'}{\rho\frac{U^2}{2}}=\sigma_{1m}+\frac{c'\cdot\rho\frac{U_c^2}{2}}{\rho\frac{U^2}{2}}$$

$$=\sigma_{1m}+\frac{c'}{\left(\frac{C_c\cdot\omega_e}{\omega}\right)^2} \tag{21}$$

In particular, for sharp-edged orifices, with the relations shown in Eqs. (7) and (8) between the section relation and the coefficients K_m and σ_{1m}, Eq. (19) expressed as a function of the latter coefficient is

$$\sigma_{1f}=\sigma_{1m}+c'\cdot(1+\sigma_{1m}) \tag{22}$$

The coefficient c' indicates the amplitude of the pressure fluctuation with respect to the velocity head at the contracted section for the value σ_{1f}.

Results and Discussion

The points in Fig. 5 show the experimental results for head losses as a function of flow in circular sharp-edged orifices placed in the 16 mm diameter pipe and with the fixed downstream boundary condition. Curves predicting the head losses according to Eq. (15) with $K=K_m$ (curves (a)) and with $K=\sigma_{1m}/\sigma_{p1}$ (curves (b) and (c)) have also been plotted. Curve (b) corresponds to the discharge condition according to Eq. (19), whereas (c) denotes the condition $h_2=h_v$. This approximates the minimum possible pressure head in the section where the downstream pressure is measured and is equivalent to $K=\sigma_{1m}$. Therefore, curve (c) is an unsurpassable limit, as these results also confirm. This curve has been obtained using $\sigma_{p1}=1$, which corresponds to the boundary condition $h_2=h_v$.

K_m and σ_{1m} values were obtained experimentally by minimizing the relative error, as shown in Eq. (20). We have circled the experimental observations in which the calculated value is $\sigma_{p1} \leqslant \sigma_{1m}/K_m$, indicating that cavitation should have a significant effect on h_f.

Points plotted in Fig. 6 show the calculated K and σ_1 values from the experimental observations shown in Fig. 5, and the solid lines indicate the result of Eqs. (15) and (17). Also, we have represented Eq. (11) and the experimental determinations of K_m and σ_{1m} by points alongside their coordinates. Being unique for all the boundary conditions, this representation can be used to get parameters K_m and σ_{1m}, meaning that, as far as head losses are concerned, the tested orifices have been characterized.

As shown in Fig. 5, the two parameters predict the operation of the orifices under the imposed boundary conditions, save that it is not possible to predict whether the possible vapor cavity will extend far enough to shift the downstream condition in the downstream testing pressure tap and, if it does, for what flow value it will do so.

Figure 7 shows additional experimental results carried out on the orifice of diameter $d=8.93$ mm, placed in a PVC pipe with a 16.2 mm internal diameter. Both the downstream and the upstream boundary conditions were manipulated, and we found that the theoretical curves plotted in Fig. 2(*b*) were confirmed experimentally. Apart from the observations and prediction curves for head losses, Fig. 7 also includes the imposed boundary conditions $h_1(Q)$ and $h_2(Q)$, and their difference $h_1-h_2(Q)$.

The results represented by solid points are similar to those al-

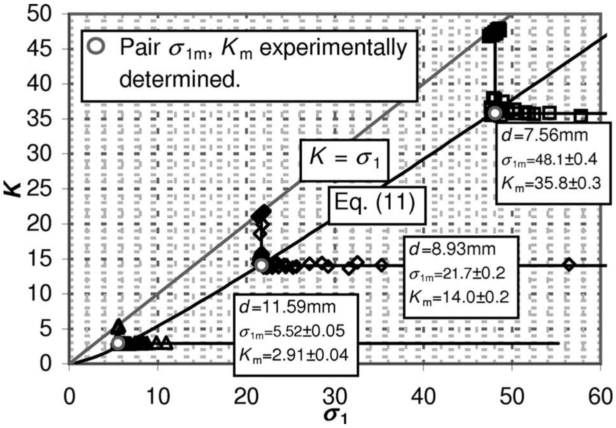

Fig. 6 Results of the proposed analysis applied to data from Fig. 5

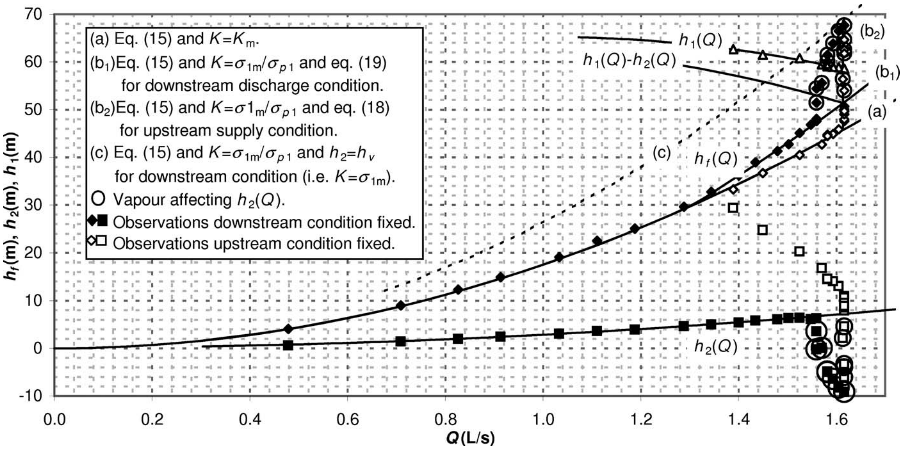

Fig. 7 Experimental results of head loss tests and predicted curves on the sharp-edged orifice of diameter $d=8.93$ mm in a pipe with an internal diameter $D=16.2$ mm

ready shown in Fig. 5, i.e., where the downstream boundary condition was constant and, particularly, V_2 was in a fully open position, whereas the empty points represent the results in which the upstream boundary condition was constant and, particularly, V_r was closed and V_1 was in a fully open position, meaning that $h_1-h_2(Q)$ was the maximum possible head loss. The meanings of curves (a), (b), and (c) are unchanged, although (b) is now split into two: curve (b_1) corresponds to the fixed downstream boundary condition and curve (b_2) corresponds to the fixed upstream boundary condition. The points that are below the line that corresponds to the imposed condition $h_2(Q)$ have been circled in Fig. 7. The explanation for this is that the vapor cavity has extended far enough to affect the measurement of the pressure difference with a manometer M_2. Note that the empty points corresponding to the fixed upstream boundary condition are still on the head loss predicting curves (a) and (b_2), whereas all the solid points are not positioned on curve (b_1). The circled observations do not exactly represent the head losses, as they are above the $h_1-h_2(Q)$ curve, i.e., line (b_1) does not predict that the experimental determinations do not match h_f. However, it is clear from Fig. 8 that this topic is no longer relevant in the analysis based on the $K(\sigma_1)$ representation, which simplifies and further specifies the determination of the parameters K_m and σ_{1m}. Also the points circled in Figs. 7 and 8 correspond to the same situation.

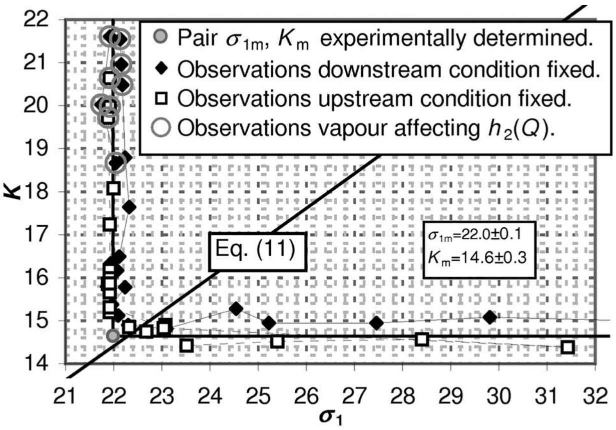

Fig. 8 Results of the proposed analysis applied to data from Fig. 7

The value of K_m obtained experimentally for the 8.93 mm diameter orifice in the 16 mm pipe was 14.0 ± 0.2, whereas it was 14.6 ± 0.3 for the 16.2 mm pipe. These results satisfy the Belanger–Borda expression shown in Eq. (8).

The points in Fig. 9 represent the experimental results of testing the butterfly valve with its round disk positioned at 45 deg. The points have been placed on two different curves, labeled as "*Q* increasing" and "*Q* decreasing," essentially obeying the fact that the position of the disk in the valve might change during the test. Figure 10 illustrates this more clearly. Similarly, we have plotted the curves that predict head losses according to Eq. (15) with $K=K_m$ (curves (a)) and with $K=\sigma_{1m}/\sigma_{p1}$ (curves (b)). The fitted

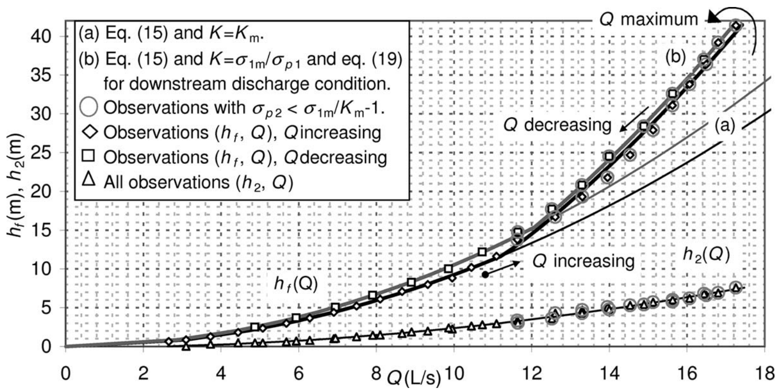

Fig. 9 Experimental and prediction results of head loss tests on a butterfly valve with a nominal diameter of 75 mm and a closing disk at 45 deg

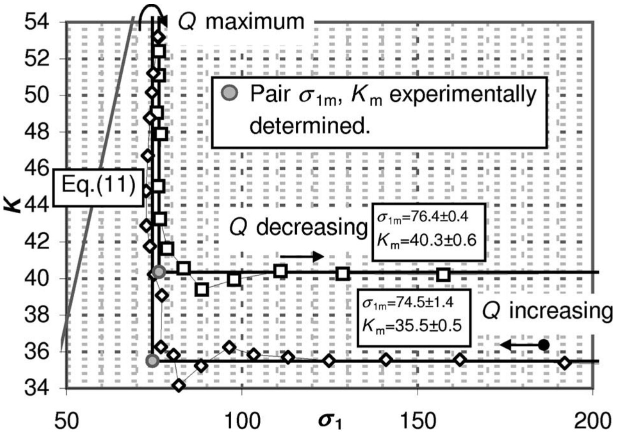

Fig. 10 Results of the proposed analysis applied to data from Fig. 9

discharge condition $h_2(Q)$ has also been represented, and unlike head losses, the observations are explained by a single curve.

As in the case of sharp-edged orifices, parameters K_m and σ_{1m} were fitted from the experimental determinations shown in Fig. 10 by minimizing the relative error shown in Eq. (20). In this case, two curves have been plotted to explain the observations for two disk positions. Accordingly, it can be said that the test started with the round disk in a position where $K=35.5 \pm 0.5$, and it ended with the disk in another where $K=40.3 \pm 0.6$. This change in position can be explained, bearing in mind the fact that the drag force on a disk tends to close it. Note also that according to the values of the σ_{1m} error standard deviations, the Q decreasing curve explains the respective experimental results slightly better than the Q increasing curve. This suggests that once the "Q maximum" has been reached, the position of the disk must have been unchanged, whereas during the flow increasing phase, it must have changed in position little by little several times. This is consistent with the fact that the force on the disk, which tends to close it, will be all the greater, the greater the flow is. When that force overcomes the static friction force that keeps the disk in its place, the disk must move.

Equation (17) was also used to predict and characterize head losses in the tested butterfly valve. We found that, as was foreseeable, Eq. (11) for sharp-edged orifices does not explain the determinations of K_m and σ_{1m}, as was already mentioned in the Materials and Methods section. Experimental results fell to the right of the curve of Eq. (11), which can be interpreted as the valve got into cavitation, as far as head losses are concerned, under less severe conditions than a sharp-edged orifice with the same K_m coefficient.

Figure 11 represents the experimental determinations of K_m and σ_{1m} for several positions of the butterfly valve and the seat globe valve. Note that they are all still to the right of Eq. (11) and that a value of $r=0.79$ with $K_0=0$, introduced in Eq. (14), would explain these values for the butterfly valve. Similarly, the coefficients $r=0.81$ and $K_0=5.46$ would explain the results in the case of the seat globe valve, and not all the points are now positioned to the right of Eq. (11).

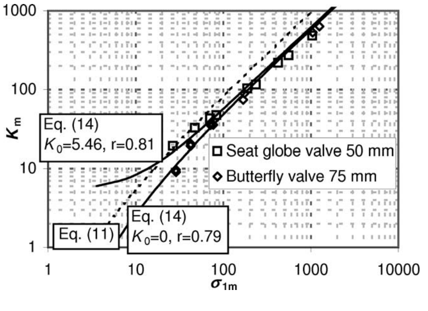

Fig. 11 Relations between experimentally determinated values of K_m and σ_{1m} on the two tested valves

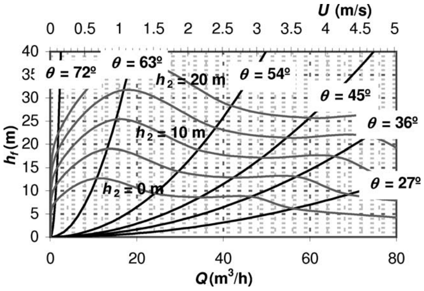

Fig. 12 Head loss curves in the tested butterfly valve for different valve positions and approximate validity bounds as a function of the downstream head pressure

The values of the characteristic parameters can be used to elaborate the information for practical or rather "immediate" valve use, as shown in Fig. 12 for the butterfly valve. The imposed conditions have been defined in this case as a function of the downstream pressure head h_2. One point of the graph $Q(h_f)$ would require a downstream value of h_2 equal to the one of the curve that goes through that point plus a safety margin.

To quantify this safety margin, Eq. (21) and its particular expression for sharp-edged orifices (Eq. (22)) reflect an attempt at approximating the magnitude of the pressure pulses through the intensity or continuity of cavitation. Taking Tullis' [3] experimental determinations about the critical and incipient cavitation limits for three sharp-edged orifices, Figs. 13 and 14 show a possible explanation based on Eq. (22). These results clearly show that as the author stated and as quantified by empirical equations, the effect of scale is patent. Besides, Arndt [21] suggested quantifying this effect of scale on incipient cavitation by studying semiempirically the pressure drop inside a vortex produced in the wake of a disk and expressed the incipient cavitation index as a function of geometrical dimensionless parameters, Strouhal number St and Re. Also, Katz and O'Hern's [22] results were consistent with the assumed trend of the cavitation inception index of sharp-edged bodies to increase with Re. Thus, we have adopted $c' \sim D^{0.5}$ since it has shown a reasonable agreement with the experimental results. If this approximation is accepted, apart from characterizing each singularity, the parameter σ_{1m} also serves as a reference for other less severe cavitation limits that are more useful for design purposes than σ_{1m} itself.

The above presented results for evaluating design cavitation limits are certainly limited and call for further research. In particular, it should be interesting to have at one's disposal the actual

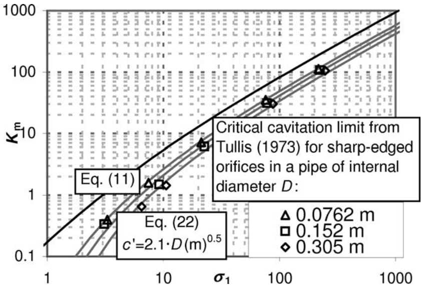

Fig. 13 Explanation of the relation between the critical cavitation limit values determined by Tullis [3] and the head loss coefficient based on the influence of the pressure fluctuation level

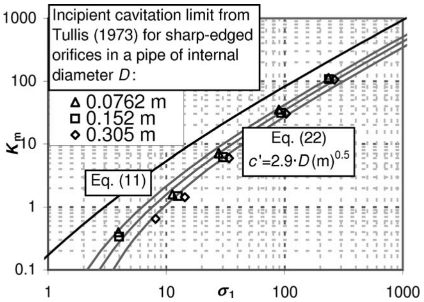

Fig. 14 Explanation of the relation between the incipient cavitation limit values determined by Tullis [3] and the head loss coefficient based on the influence of the pressure fluctuation level

values stated by the valve's manufacturers for contrasting the proposed expressions and evaluating the coefficient c'.

Conclusions

Head losses under cavitating flow conditions in sudden transitions, such as valves, can be predicted because they are characterized by the parameter σ_{1m}, in addition to the traditional head loss parameter K_m. The latter characterizes the flow pattern downstream of the section in which cavitation takes place, whereas σ_{1m} characterizes the flow pattern upstream of this section. In principle, both parameters must be determined experimentally. Head loss formulation under cavitation flow conditions is relatively simple, so it could become extensive in a distribution network calculation software improving its results.

The proposed head loss evaluation method splits the cavitation from other effects, including the displacement of valve closing elements due to the drag force. The influence of cavitation on the head loss coefficient has been quantified. As a consequence, uncertainties about whether or not cavitation has influenced local head losses during tests are removed. Even if the vapor phase extends to the downstream pressure tap of the transition, the determination of the two parameters that characterize and quantify such head losses is not conditioned.

If the parameter K_m for a singularity is known, it is possible to approximately estimate σ_{1m}, or vice versa. For design purposes, this last parameter can be used to determine the maximum flow for which head losses are not affected by cavitation under certain system-imposed boundary conditions. However, as cavitation can occur even if the flow does not surpass that maximum, it is worth taking into account a given safety margin to allow for pressure fluctuations in the flow. In this respect, σ_{1m} can be adopted as a reference value to estimate other cavitation levels on the basis of the pressure fluctuation-velocity head ratio.

Acknowledgment

We would like to thank the Spanish Interministry Science and Technology Board (CICYT) for its support of this work provided through Project No. AGL2004-01689/AGR.

Nomenclature

a_0, a_1, a_2 = fitting coefficients for the Q-H curve of a pump ($L, L^{-2}\cdot\mathrm{T}, L^{-5}\cdot\mathrm{T}^2$)
c' = fluctuation coefficient
C_c = contraction coefficient
C_D = discharge coefficient ($L^{5/2}\cdot\mathrm{T}^{-1}$)
g = gravitational acceleration ($L\cdot\mathrm{T}^{-2}$)
H = energy head (L)
h = pressure head (L)
h_f = head losses (L)
K = local head losses coefficient
K_0 = part of local head loss coefficient independent of the operation of the closing element in a valve
l, l', l'' = length inside the singularity (L)
p = pressure ($\mathrm{M}\cdot L^{-1}\cdot\mathrm{T}^{-2}$)
p' = pulse pressure ($\mathrm{M}\cdot L^{-1}\cdot\mathrm{T}^{-2}$)
Q = flow rate ($L^3\cdot\mathrm{T}^{-1}$)
r = axial-asymmetry coefficient
Re = Reynolds number
St = Strouhal number
U = mean water velocity at uniform pipe sections ($\mathrm{L}\cdot\mathrm{T}^{-1}$)
Δz = elevation difference (L)
ε_r = relative error
γ = specific weight ($\mathrm{M}\cdot\mathrm{L}^{-2}\cdot\mathrm{T}^{-2}$)
ρ = density ($\mathrm{M}\cdot\mathrm{L}^{-3}$)
σ, σ_p = cavitation numbers
ω = cross-sectional area (L^2)

Subscripts

1 = at upstream section
2 = at downstream section
c = contraction of flow
e = obstructed section
f = fluctuating
m = minimum
v = vapor

References

[1] Tullis, J. P., 1981, "Modeling Cavitation for Closed Conduit Flow," J. Hydr. Div., **107**(HY11), pp. 1335–1349.
[2] Ball, J. W., and Tullis, J. P., 1973, "Cavitation in Butterfly Valves," J. Hydr. Div., **99**(HY9), pp. 1303–1318.
[3] Tullis, J. P., 1973, "Cavitation Scale Effects for Valves," Inf. Sys., **99**(HY7), pp. 1109–1128.
[4] Testud, P., Moussou, P., Hirschberg, A., and Aurégan, Y., (2007), "Noise Generated by Cavitating Single-Hole and Multi-Hole Orifices in a Water Pipe," J. Fluids Struct., **23**, pp. 163–189.
[5] Zhang, Z., and Cai, J., 1999, "Compromise Orifice Geometry to Minimize Pressure Drop," J. Hydraul. Eng., **125**(11), pp. 1150–1153.
[6] Zhang, Q. Y., and Chai, B. Q., 2001, "Hydraulic Characteristics of Multistage Orifice Tunnels," J. Hydraul. Eng., **127**(8), pp. 663–668.
[7] ANSI/ISA, 2002, "Flow Equations for Sizing Control Valves," Report No. ANSI/ISA-75.01.01-2002.
[8] Idel'cik, I. E., 1999, *Memento des pertes de charge. Coefficients de pertes de charge singulières et de pertes de charge par frottement* (translated into French), Eyrolles, Paris (reprint of 1969 edition).
[9] Tullis, J. P., 1971, "Choking and Supercavitating Valves," J. Hydr. Div., **97**(HY12), pp. 1931–1945.
[10] Tullis, J. P., and Govindarajan, R., 1973, "Cavitation and Size Scale Effects for Orifices," J. Hydr. Div., **99**(HY3), pp. 417–430.
[11] Mishra, C. and Peles, Y., 2005, "Cavitation in Flow Through a Micro-Orifice Inside a Silicon Microchannel," Phys. Fluids, **17**(1), p. 013601.
[12] Sarpkaya, T., 1961, "Torque and Cavitation Characteristics of Butterfly Valves," ASME J. Appl. Mech., **28**, pp. 511–518.
[13] Nurick, W. H., 1976, "Orifice Cavitation and Its Effect on Spray Mixing." ASME Trans. J. Fluids Eng., **98**, pp. 681–687.
[14] Batchelor, G. K., 1967, *An Introduction to Fluid Dynamics*, Cambridge University Press, Cambridge, England.
[15] Rouse, H., and Jezdinsky, V., 1966, "Fluctuation of Pressure in Conduit Expansions," J. Hydr. Div., **92**(HY3), pp. 1–12.
[16] Sánchez, R., 2006, "Caracterización de Llaves Hidráulicas Automáticas y Modelación de su Funcionamiento en Sistemas de Riego," Ph.D. thesis (in Spanish), Technical University of Madrid (UPM), Madrid.
[17] ISA, 1995, "Considerations for Evaluating Control Valve Cavitation," Report No. ISA-RP75.23-1995.
[18] ASAE, 1999, "Procedure for Testing and Reporting Pressure Losses in Irrigation Valves," ASAE Standards, Report No. S447 DEC98.
[19] Tullis, J. P., and Skinner, M. M., 1968, "Reducing Cavitation in Valves," J. Hydr. Div., **94**(HY6), 1475–1488.
[20] Ran, B., and Katz, J., 1994, "Pressure Fluctuations and Their Effect on Cavitation Inception within Water Jets," J. Fluid Mech., **262**, pp. 223–263.
[21] Arndt, R. E. A., 1976, "Semiempirical Analysis of Cavitation in the Wake of a Sharp-Edged Disk," ASME Trans. J. Fluids Eng., **98**, pp. 560–562.
[22] Katz, J., and O'Hern, T. J., 1986, "Cavitation in Large Scale Shear Flows," ASME Trans. J. Fluids Eng., **108**, pp. 373–376.

Influence of Torque on the Lift and Drag of a Particle in an Oscillatory Flow

Paul F. Fischer

Gary K. Leaf

Mathematics and Computer Science Division,
Argonne National Laboratory,
Argonne, IL 60439

Juan M. Restrepo
Department of Mathematics,
and Physics Department,
University of Arizona,
Tucson, AZ 85721

In the work of Fischer et al. (2002, "Forces on Particles in an Oscillatory Boundary Layer," J. Fluid Mech., ***468****, pp. 327–347, 2005; "Influence of Wall Proximity on the Lift and Drag of a Particle in an Oscillatory Flow," ASME J. Fluids Eng.,* ***127****, pp. 583–594) we computed the lift and drag forces on a sphere, subjected to a wall-bounded oscillatory flow. The forces were found as a function of the Reynolds number, the forcing frequency, and the gap between the particle and the ideally smooth rigid bounding wall. Here we investigate how the forces change as a function of the above parameters and its moment of inertia if the particle is allowed to freely rotate. Allowing the particle to rotate does not change appreciably the drag force, as compared to the drag experienced by the particle when it is held fixed. Lift differences between the rotating and nonrotating cases are shown to be primarily dominated in the mean by the pressure component. The lift of the rotating particle varies significantly from the fixed-particle case and depends strongly on the Reynolds number, the forcing frequency, and the gap; much less so on the moment of inertia. Of special significance is that the lift is enhanced for small Reynolds numbers and suppressed for larger ones, with a clear transition point. We also examine how the torque changes when the particle is allowed to rotate as compared to when it is held fixed. As a function of the Reynolds number the torque of the fixed sphere is monotonically decreasing in the range* $Re=5$ *to* $Re=400$*. The rotating-sphere counterpart experiences a smaller and more complex torque, synchronized with the lift transition mentioned before. As a function of the gap, the torque is significantly larger in the fixed particle case.* [DOI: 10.1115/1.2969456]

1 Introduction

The experimental determination of the lift and drag on a particle in a wall-bounded flow is very challenging, as recounted by Rosenthal and Sleath [1]. In Refs. [2,3], hereafter referred to as FLR02 and FLR05, respectively, we used instead numerical means to obtain these forces. Our results, which were shown to be consistent with the fluid laboratory experiments of Rosenthal and Sleath, significantly extend the range of parameters for which the lift and drag are now known.

In FLR02 the particle was placed a small distance away from the wall and the forces were then characterized as a function of the forcing frequency and the Reynolds number. The dependence of lift and drag on the forcing frequency, or Keulegan–Carpenter number, was dramatic. The key findings were to show that the lift force is significantly enhanced by the choice of Keulegan–Carpenter number and that the lift, even when compared to a fairly wide range of buoyancy forces, is important in the physical setting. In FLR05 we added the gap number, or distance between the sphere and the bounding wall, to the parameter list. In doing so we found that the sphere experienced suction and repelling effects, depending on the gap number and the forcing frequency. We also found that the nature of the lift force changed from viscous-dominated to pressure-dominated when the Keulegan–Carpenter number, the nondimensional forcing period, is varied. We also showed that there are only a few degrees of freedom in the spectrum of the forces, suggesting that a reduced but fairly complete analytical model could be formulated for these forces, and such model be accurate for a large range of forcing frequencies.

In the present study we add a rotational degree of freedom to the particle and investigate how lift and drag are modified, as compared to the lift and drag of the same particle, held fixed. We will also quantify the changes in the torque. The primary focus, however, will be to characterize the lift, which we want to describe as a function of the Reynolds number, the forcing frequency, the gap between the sphere and the wall, and the moment of inertia of the particle; the near-term goal is to determine whether rotational freedom will change significantly the amount of lift experienced by a particle, a sensible possibility, at the outset. To suggest that allowing for rotation in the calculation of the lift and drag is of significance is inspired by the work that has been done on flow around circular cylinders. Oscillatory flow around a circular cylinder has been frequently studied: See Refs. [4–6] and the references contained in these works. However, as was demonstrated in FLR02 and FLR05, lift and drag estimates from cylinders in an oscillatory flow cannot be extrapolated to the spherical particle case, since the flow is fundamentally different.

The long term goals of this line of inquiry are to provide robust data and functional trends of the basic forces on ideal particles, with which to (1) infer the mechanics of particle dislodgement and suspension in oscillatory flows, such as those ocurring under the action of tidal motion, rhythmic sedimentation, and some industrial processes; and to (2) improve the parametric description of models for what are commonly referred to as "inertial particles" in the sedimentation literature. With regard to the first goal, it would seem that extrapolating sediment dynamic models from what occurs to a single particle is unrealistic. Yet, the basis of some of the most often cited models for the motion of sedimentary/erodible beds in these natural settings relies on a real or perceived understanding of how individual particles move under the influence of the surrounding fluid, how particles respond to fluid stresses, and how the energy dissipation balance plays out. Of note is that the lift and buoyancy forces enter in the parametrization of dislodgement and/or suspension of the sediment (see Ref. [7] and the

---

Contributed by the Fluids Engineering Division of ASME for publication in the JOURNAL OF FLUIDS ENGINEERING. Manuscript received October 21, 2007; final manuscript received June 5, 2008; published online September 4, 2008. Review conducted by Joseph Katz.

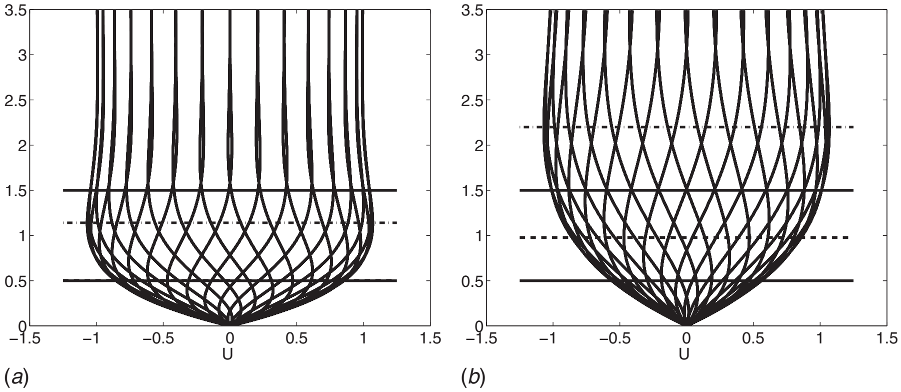

Fig. 1 Velocity profiles, given by Eq. (3), shown at equal intervals in time over the course of one period of oscillation. Re=100. (*a*) τ=80 and (*b*) τ=300. The horirontal lines depict the top and bottom positions of a unit-diameter sphere in (*a*) for gaps ϵ=0 (dashed) and ϵ=0.5 (solid), and in (*b*) for gaps ϵ=1 (dashed) and ϵ=0.5 (solid).

references contained therein; also see the original work of Bagnold [8] and the extension of this model to the oceanic setting by Bailard in Ref. [9]). In any event a thorough study of the single particle in an oscillating boundary layer bounded by an ideally smooth bounding wall, we feel, is a necessary first step in tackling the more physically relevant case of a bed of multidispersive particles subjected to oceanic/fluvial hydrodynamics. With regard to the second goal, inertial particle models depend critically on our understanding of how individual as well as finite collections of particles move and interact in a flow (see Ref. [10]; also, see Ref. [11] for references to the inertial particle literature).

Several studies have considered the forces on a sphere in a free flow. Of note are recent papers on flows over particles forced to rotate, for example, Refs. [12,13]; see also Ref. [14] for an experimental report on the matter. The results from these studies have important practical applications as well as popular interest, for example, the role played by forced spin on the trajectory of baseballs, tennis balls, and golf balls. In our study, however, we do not force the particle to spin, but rather, we allow it to freely spin in response to the shearing forces and we ask how the basic forces change by allowing for this degree of freedom.

In Refs. [15–17] the effect of free rotation on the motion of a solid sphere in an unbounded steady shear flow was examined (see also Ref. [18]). For flows with moderate Reynolds numbers, from 0.5 to 200, the results most relevant to our work were their findings as follows: (1) Rotation has a little effect on the drag. (2) There is a range of flows wherein the effect of allowing the particle to freely rotate leads to outcomes that are different from existing analytical estimates. (3) The effect of rotation on the lift is Reynolds-number (Re) dependent: For small Re the effect is very small, in accordance with Saffman's results [19,20]; beyond Re$\approx$200 the effect again becomes negligible. In the range Re $=5-100$, in particular, they found that the torque-free condition, i.e., steady state, generates a significant increase in the lift. This excess lift is attributed to a Magnus lift effect—of a sphere forced to spin at a rate $\Omega_{\rm st}=\mathcal{T}/8\pi\mu D^3$, the terminal value in a steady shear flow ($\mathcal{T}$ is the torque, D is the diameter of the sphere, and μ is the viscosity)—and that this excess is additive. (4) At moderate Re they observe that $\Omega_{\rm st}$ can be uniquely parametrized by Re alone, yielding a simple power law expression for $\Omega_{\rm st}$ as a function of Re.

We show in this study that the results obtained for a sphere that is freely rotating in a wall-bounded oscillatory flow are different from the results obtained in Ref. [15] for the steady shear flow case. Notably, we did not find an obvious way to decompose the forces into a fixed and rotational component, i.e., it could not be expressed as the sum of two fields, because the forces change qualitatively with parameters.

Wall-bounded forces on a rigid sphere were examined in Ref. [21]. They found that for flows with Reynolds number smaller than 100 the lift decreases with Reynolds number and increases for larger Reynolds-number flows. This is different from the oscillatory flow case we will present. However, the steady-flow case they considered and ours have a qualitative similarity with regard to the tendency of the lift to drop as the gap separating the sphere from the wall is increased.

2 Preliminaries

In order to calculate the forces as well as the flow we will be using a high-order spectral element time-dependent Navier–Stokes equations solver. The domain is infinite away from an ideally smooth rigid wall of infinite extent on which the no-slip boundary condition is applied. No-slip boundary conditions for the fluid are applied at the boundary of the sphere as well. The flow is forced to oscillate in time, so that in the absence of the sphere the velocity reverses direction smoothly. The sphere has a fixed diameter of 1 and the fluid has a density of $\rho_0 := 1$ in appropriate dimensional units.

As in FLR02 and FLR05 the Reynolds number is defined as

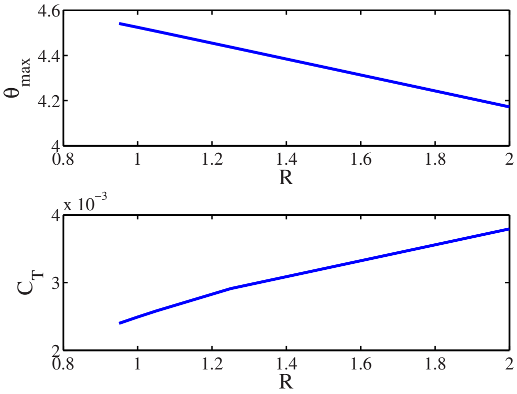

Fig. 2 Maximum rotation angle $\theta_{\max}$ (deg) and peak normalized torque C_T as a function of *R* for Re=100, ϵ=0.5, and τ =80

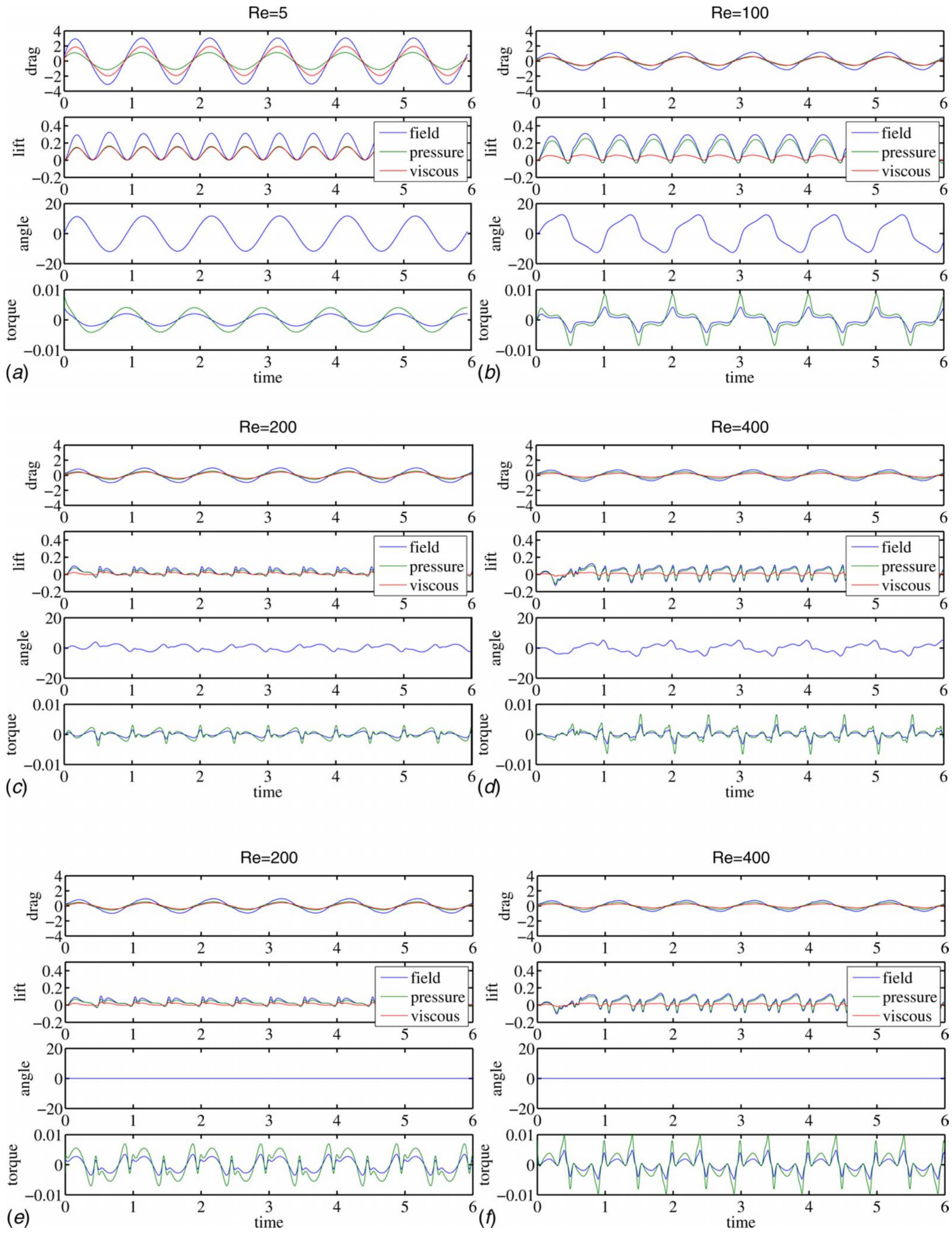

Fig. 3 Dependence on Reynolds number. $R=0.95$, $\tau=80$, and $\epsilon=0.25$. Time series of the drag, lift, torque, and angular deflection for a freely rotating particle: (*a*) Re=5, (*b*) Re=100, (*c*) Re=200, and (*d*) Re=400. For a nonrotating particle: (*e*) Re=200 and (*f*) Re=400.

$$\mathrm{Re} := UD/\nu$$

where the characteristic length-scale D is the particle diameter, and the convective time-scale is D/U. U is the amplitude of oscillation in the far-field velocity and ν is the kinematic viscosity. The nondimensional forcing period, otherwise known as the *Keulegan–Carpenter* number, is

$$\tau := TU/D$$

where T is the period of the forcing. The *gap* number is

$$\epsilon := d/D$$

and it represents the ratio of the distance between the edge of the sphere and the wall and D.

In adding a rotational degree of freedom to the particle the flow configuration is now characterized by four parameters: the Keulegan–Carpenter number, the Reynolds number, the gap, and the moment of inertia of the sphere (which in turn depends on the relative density for a given diameter D). The dependence of the forces on the relative density

$$R := \rho/\rho_0$$

will be briefly examined in this study. Here ρ_0 is the density of the fluid.

The computational scheme and parameters are described in FLR02 and FLR05. We thus only summarize how the original computational framework is modified to account for the rotating

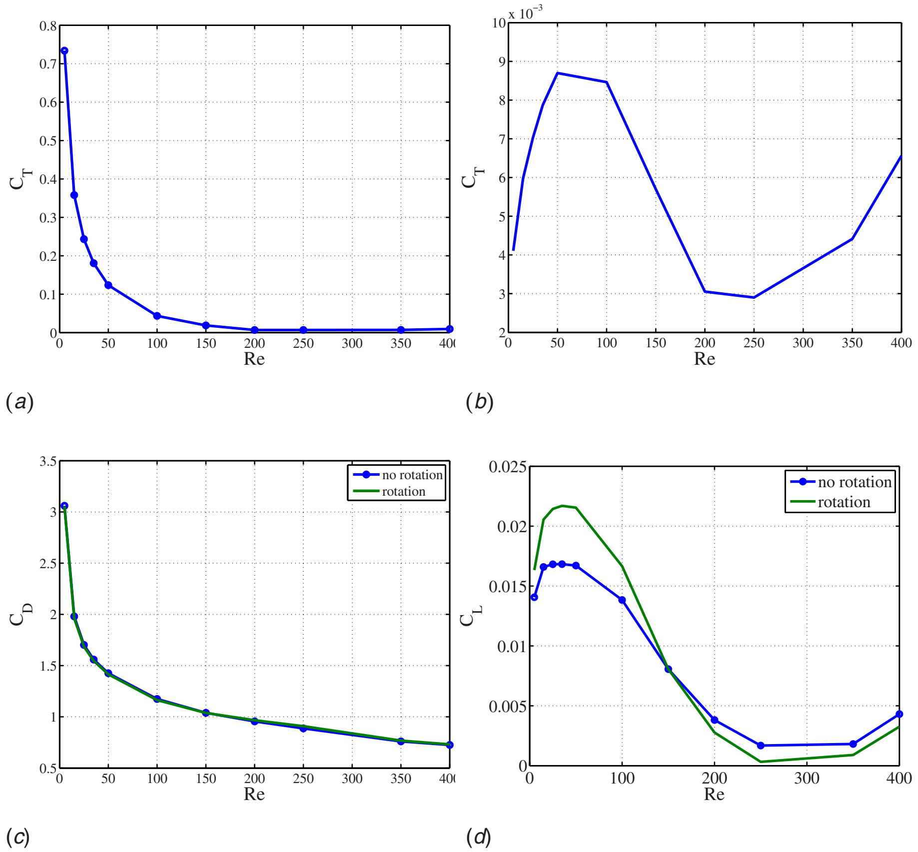

Fig. 4 Dependence on the Reynolds number. $R=0.95$, $\tau=80$, and $\epsilon=0.25$. (*a*) Maximum torque of the nonrotating particle and (*b*) maximum torque of the rotating particle. (*c*) Maximum drag, with and without rotational effects; (*d*) the mean lift of the freely rotating and nonrotating cases. The DML is the difference between the two curves in (*d*).

degree of freedom of the sphere. A no-slip boundary condition is enforced at the sphere's surface. The sphere's angular acceleration is derived from

$$\mathbf{T} = I\frac{d\Omega}{dt} \tag{1}$$

where the torque $\mathbf{T}$ is evaluated by integrating the contributions of the shear stress over the sphere and I is the moment of inertia of the sphere. A second-order Adams–Bashforth scheme

$$\Omega^n = \Omega^{n-1} + \frac{\Delta t}{I}\left(\frac{3}{2}\mathbf{T}^{n-1} - \frac{1}{2}\mathbf{T}^{n-2}\right) \tag{2}$$

is used to integrate the angular acceleration. For the density ratios and time step sizes considered (the latter governed by the standard Courant-Friedrichs-Lewey (CFL) condition restrictions arising from explicit treatment of the nonlinear terms in the Navier–Stokes equations) no additional stability restrictions on Eq. (2) were encountered (see Ref. [22]).

The dimensionless torque coefficient, hereon called the normalized torque, is reported as

$$C_T := \frac{2|\mathbf{T}|}{SD}$$

where

$$S := \tfrac{1}{2}\rho_0 A U^2$$

and $A=\pi D^2/4$. In what follows we mean by lift and drag the coefficients $C_L=F_z/S$ and $C_D=F_x/S$, respectively.

In the absence of the sphere the flow field is described analytically as

$$\mathbf{u}_b = \left(\sin\left(\frac{2\pi t}{\tau}\right) - e^{-z/\delta}\sin\left(\frac{2\pi t}{\tau} - z/\delta\right),0,0\right) \tag{3}$$

which corresponds to a unit-amplitude velocity field oscillating back and forth in the x-direction with nondimensional period τ. For viscous flows, this results in a time-periodic boundary layer with characteristic thickness

$$\delta = \sqrt{\frac{\tau}{\pi \mathrm{Re}}}$$

In this study the period is in the range $40 \leq \tau \leq 260$, and thus the Stokes layer range is $0.2 < \delta < 0.96$, for $\mathrm{Re}=100$, which overlaps somewhat with the range of the gap, $0.25 \leq \epsilon \leq 1.0$.

As in FLR02, we use $\mathbf{u}=\mathbf{0}$ as an initial condition in all cases. Mean quantities are reported once the flow has established periodicity in time. The base flow is established by specifying Dirichlet conditions on either end of the domain. When the far-field base flow is in the positive x-direction, we set $\mathbf{u}(-L_x,y,z,t)=\mathbf{u}_b$ and use a homogeneous Neumann condition at $x=+L_x$. When the far-field base flow is in the negative x-direction, we reverse these conditions. The Neumann condition corresponds to the usual outflow (natural) boundary condition associated with the Stokes subproblem that is solved in each step. Note that the required hydrostatic forcing results directly from application of the boundary conditions and that the auxiliary pressure p_0 is not needed.

3 Torque, Drag, and Lift

Figure 1 depicts the dimensionless velocity profiles (heavy lines) in the boundary layer at different times over the course of the forcing period for $\mathrm{Re}=100$. Figure 1(*a*) is representative of the

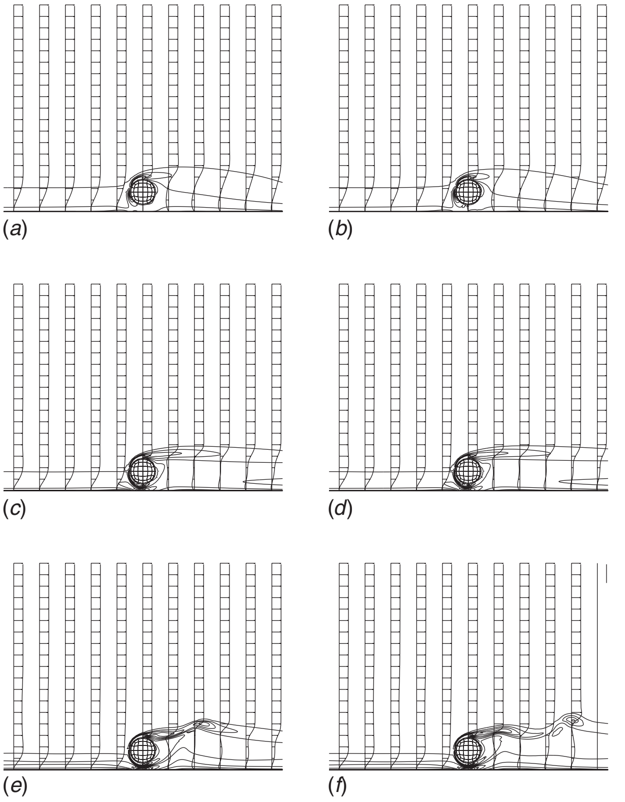

Fig. 5 Symmetry-plane velocity profiles and vorticity contours (unit spacing on [−5,5]) during deceleration: (*a*) Re=100, fixed; (*b*) Re=100, rotating; (*c*) Re=200, fixed; (*d*) Re=200, rotating; (*e*) Re=300, fixed; and (*f*) Re=300, rotating. *R*=0.95, τ=80, and ϵ=0.25.

flow for the smaller Keulegan–Carpenter number range; the figure corresponds to $\tau=80$. Figure 1(*b*), for $\tau=300$, is representative of the large τ situation. The horizontal lines superimposed on the flow indicate the top and bottom locations of a unit-diameter sphere for several values of the gap ϵ. The vertical scale is D. The size of the boundary layer is, by Eq. (3) and in terms of δ, directly proportional to the square root of the velocity amplitude and inversely to the square root of the period of oscillation. Some aspects of the forces on particles in steady flows (see Ref. [15] and references therein) are relevant to shearing flows near boundaries that are more generally time dependent: The time-mean lift force is insignificant if the particle is placed sufficiently far away from the bounding wall—many δ layer thicknesses away; that is to say, if the particle is located outside of the boundary layer, there is no shear and thus the lift is insignificant. By the same argument, the larger the boundary layer is relative to the diameter of the sphere provided the particle is close enough to the bounding wall, the higher the shear forces. The presence of the rigid wall also contributes to a Bernoulli effect, which as we shall show is still evident when the sphere is 1 diameter away from the wall, even if the bulk of the boundary layer is much smaller than the gap. There are fundamental differences between the steady flow and the oscillatory flow situation: The shear rate as inferred from the Fig. 1(*a*) flow should lead to a smaller lift than the one inferred from Fig. 1(*b*), by steady-flow arguments. Yet, the opposite is true. What is missing from consideration is the addition of a Bernoulli effect in the gap. As we will be showing in the following section, for the range of gaps considered and for large Reynolds numbers, the lift is pressure-dominated.

Bagchi and Balachandar [15] found that the lift of a freely rotating sphere in a steady shear flow will experience an additive lift associated with a Magnus effect. They established this by comparison of their numerical results to a theoretical estimate. When a particle is given a torque-free condition and the flow is oscillating it is not clear how the lift is modified by the added freedom in the motion of the particle. The two aspects that make the outcome hard to predict using prior knowledge about the steady shear case are as follows: (1) If the particle is in a rapidly oscillating shearing flow the particle may not achieve a torque-free condition before the flow reverses. (2) The flow may not be symmetric when there is a reversal in the direction of the force, for example, if vortical structures are generated during the course of the period and these persist beyond the time at which flow reversal takes place.

In what follows we shall define the *differential mean lift* (DML) as the difference between the mean lift of a particle allowed to rotate and the mean lift of the same particle held fixed. In most instances we will report on relative quantities. For an absolute reference we refer the reader to FLR02 and FLR05.

We describe now how the forces on a particle subjected to an oscillatory boundary layer flow in a torque-free situation depend on the moment of inertia (more specifically on the density ratio R), the Reynolds number Re, the Keulegan–Carpenter number τ, and the gap number ϵ.

3.1 Effect of the Density Ratio. We consider here a very small range of density ratios R because outside of this range we presume that the buoyancy force of a free particle would prevail in the dynamics of a particle in a fluid when compared to the lift force. The dependence of the torque on R was found to be weak. We tried $0.95 \leq R \leq 2$ for Re=100, $\epsilon=0.5$, and $\tau=80$. The maximum rotational angle $\theta_{\max}$ on R is negligible and the peak torque force dependence on R is nearly linear (see Fig. 2).

3.2 Sensitivity to the Reynolds Number. The dependence of the lift on the Reynolds number for steady flows was extensively investigated by Bagchi and Balachandar [15,16]. The definition of Reynolds number in their work is the same as the one adopted in the present study (see Ref. [21] for an investigation of the effect of a nearby wall on the lift and drag of a particle). Bagchi and Balachandar found that the lift was sensitive to rotational effects when the Reynolds number was intermediate, in the range $5 \leq \mathrm{Re} \leq 100$, approximately, but otherwise it was insensitive to changes in the Reynolds number. They also found that the difference between the fixed and free particles, with respect to the drag, was negligible across the whole range of the Reynolds number.

In Fig. 3 we show the time series of the drag and lift, the angle of deflection (in degrees), and the normalized torque, as a function of time, for several values of Re. Figures 3(*e*) and 3(*f*) can be contrasted with Figs. 3(*c*) and 3(*d*). The lift time series gets considerably more complex as the Reynolds number is increased, developing relatively large high frequency deflections. Comparison of Figs. 3(*c*) and 3(*e*), as well as Figs. 3(*d*) and 3(*f*), shows that the complexity in the lift and drag is not as much a function of whether the particle is fixed or torque-free, but primarily a function of Reynolds number. Examination of the fluid flow time series indicates that the complexity in the lift—and to a lesser extent in the drag—has something to do with the interactions of the sphere with its own vortical wake. Another feature of the flow is that, as the Reynolds number increases, more of the resulting lift and drag is created by the pressure contribution, as compared to the viscous component of the stresses.

It is apparent that the DML in the oscillatory wall-bounded flow case is sensitive in more complex ways to the Reynolds number than in the steady-flow case in Ref. [15]. Our results appear in Fig. 4. The difference between the torque of the nonrotating particle is much larger for small Re than of the rotating counterpart: Figures 4(*a*) and 4(*b*) show the torque dependence on the Reynolds number for the nonrotating and rotating cases, respectively. That it is much smaller in magnitude in the rotating case is not surprising; however, that it has a nonmonotonic structure is. In Fig. 7 we show the dependence of the maximum torque on the gap

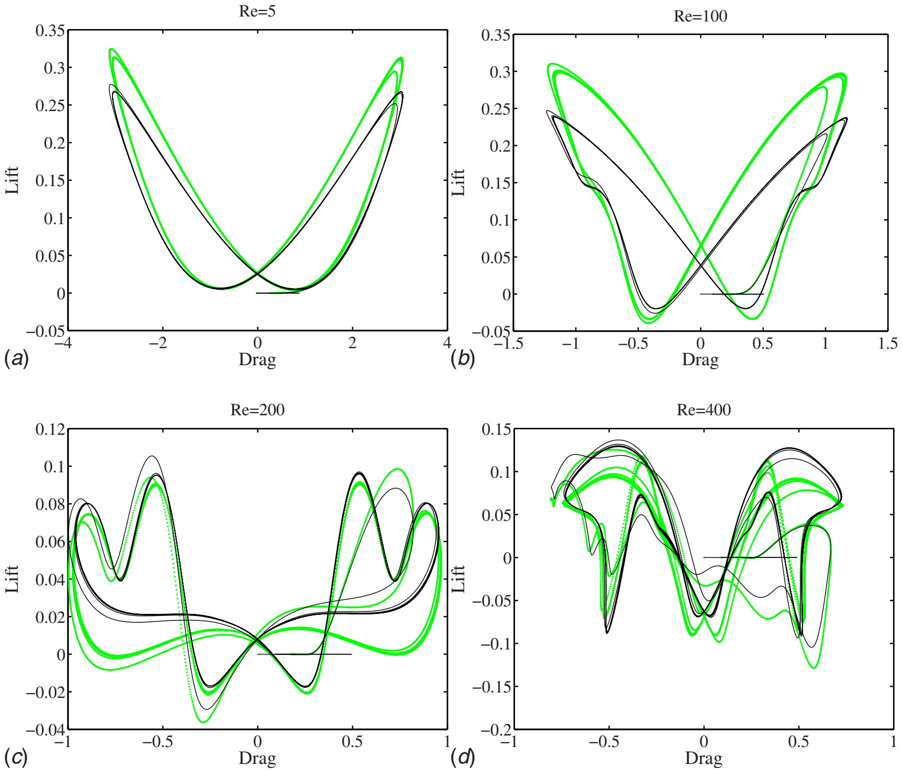

Fig. 6 Phase portrait for the instantaneous lift and drag. Dependence on Reynolds number. (*a*) Re=5, (*b*) Re=100, (*c*) Re=200, and (*d*) Re=400. Freely rotating (light); fixed (dark). $R=0.95$, $\tau=80$, and $\epsilon=0.25$.

width and the Keulegan–Carpenter parameter: The torque is small over a large range of Reynolds numbers and it appears to be true only because the gap was chosen to be large. Figure 4(*c*) shows that the drag is nearly equal in the rotating and nonrotating particle cases: Symmetry considerations dictate that if the flow is symmetric upon reversals then the maximum and minimum torque values for either the rotating or nonrotating particles should be the same in magnitude, and more importantly, that the difference of the mean drags of both cases should be zero. Figure 4(*d*) displays the lift, as a function of the Reynolds number, for the rotating and nonrotating cases: Lift is enhanced by rotation for Reynolds numbers below about 150 and depressed by rotation for Reynolds numbers above 150. Inspection of the vortex field showed that the fields are similar for the rotating and nonrotating cases below Re=200, roughly. In particular, the phase between the features in the vortical field and the forces is more complex; and when a comparison is made between the vorticity of the rotating and nonrotating cases well above Re=200 the fields are different from the lower Reynolds-number cases by the appearance of vortical structures (see Fig. 5). For Re≥300 we see that the sphere develops separating vortices on the top of the sphere. Examination of the structure for Re=300 shows two vortex structures separating from the sphere top when the sphere is not rotating. With rotation there are three vortex structures and these are less intense. This also explains why the time series is far more complicated for higher Re, as the passage of the vortices induces fluctuations in the lift and drag.

The change in the enhancing and depressing effects of rotation on the DML is not as apparent in the vortical plots, but they are in the plots of the phase of the lift and drag, as a function of time. Figure 6 shows the lift and drag, as a function of time and of the Reynolds number. These plots do not explain the underlying phenomenon but do point out that there is a significant portion of the phase tracks (see Fig. 6(*c*)) in which the lift is considerably smaller in the rotating case than in the fixed case in the range above Re=300.

Parenthetically, in Fig. 6(*d*) symmetry is significantly affected by the vortex shedding events.

3.3 Sensitivity to the Keulegan–Carpenter Number and the Gap.

The angle of deflection θ is more sensitive to changes in the gap ϵ than to the Keulegan–Carpenter number. This is shown in Fig. 7(*a*). The high frequency and larger gap cases produce smaller deflection angles. However, as seen from the figure of the maximum normalized torque, Fig. 7(*b*), the rate of change of the deflection angle is greater for high frequencies and small gaps, leading to higher torque force values. In Fig. 7(*c*) we plot the normalized torque for the rotating and nonrotating cases, as a function of τ for a fixed $\epsilon=0.125$. The difference between the the freely rotating and nonrotating cases for other ϵ is less pronounced.

Figure 8 shows how the DML depends on τ for various values of ϵ. For small gaps the DML is more important and nearly constant, as a function of τ. Its mean is positive, meaning that the rotation plays a role for small as well as large τ. As the gap is made larger the DML becomes more pronounced as τ increases. For large gaps and small τ the difference between the lift of the rotating and nonrotating cases is less pronounced. In fact, the DML disappears for a given ϵ and τ. The rightmost disappearance point is approximated by the equation $\tau_c=320\epsilon-100$. Below this value rotation adds suction. Above that line the DML is more prominent and gives an extra positive lift.

The DML and it pressure and the viscous components appear in Fig. 9. The plots indicate that the DML is nearly entirely captured by its pressure component, regardless of the gap and the period of forcing.

Phase portraits of the forces can be constructed by plotting the drag against the lift forces for all time. The phase portraits are shown in Fig. 10 for Re=100, $R=0.95$, and low, medium, and large τ. The phase portraits in Figs. 10(*a*)–10(*c*) correspond to τ

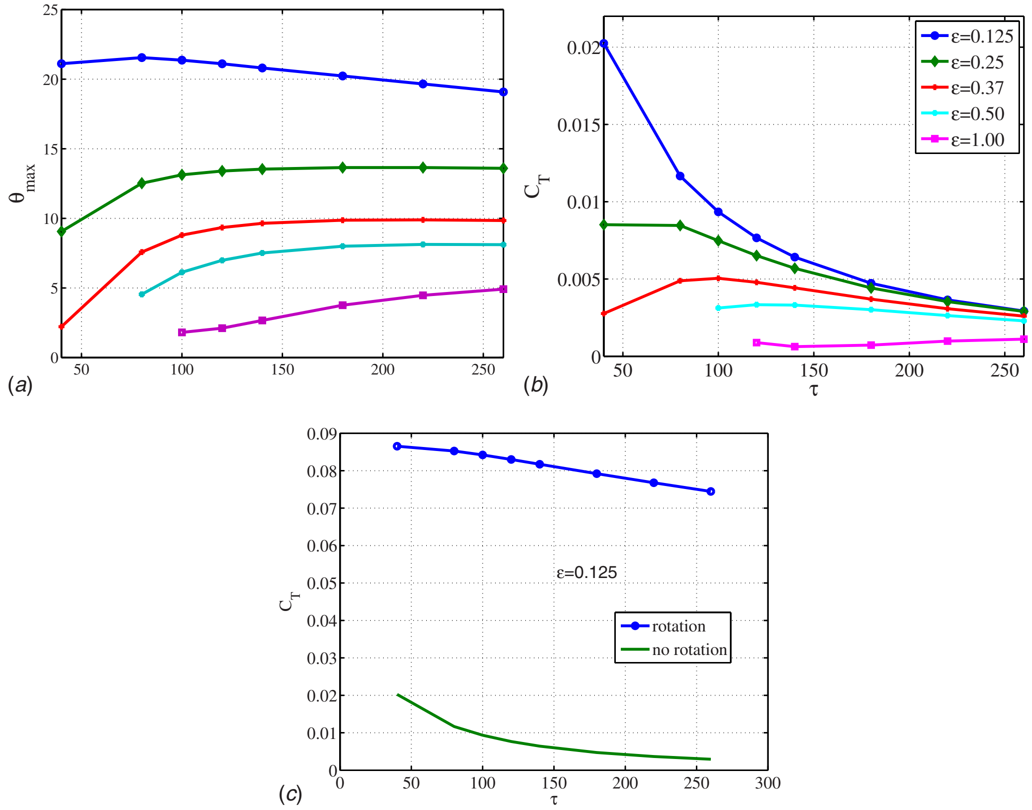

Fig. 7 (*a*) Maximum rotational angle (deg) and (*b*) peak normalized torque for the freely rotating sphere, as a function of ϵ and τ. (*c*) Peak normalized torque, comparing the rotating and nonrotating cases for $\epsilon=0.125$ for all τ. $R=0.95$ and $\text{Re}=100$.

$=40$, those in Figs. 10(*d*)–10(*f*) correspond to $\tau=120$, and those in Figs. 10(*g*)–10(*i*), to $\tau=220$. The plots include both the steady state and the transient history and thus are not expected to trace perfectly the same curve over every period. The overall lift decreases sharply with increased gap size and with increased period τ. As the gap gets larger the curves enclose less area and thus the forces are, overall, weaker. However, more importantly as the gap gets larger the force maxima go further out of phase and this effect is not dependent on whether the sphere is allowed to rotate or not. As the τ is increased the two minima in the lift are seen to flip above $\tau=120$. For small gap ϵ, the qualitative difference between the rotating and nonrotating cases, and the variation with τ are less pronounced. The smaller the gap the larger differences in the lift occur at the extremes of the drag. In the $\tau=220$ case we see that the difference between the rotating and nonrotating cases is not topologically different for small ϵ and below the τ_c. Figure 10(*h*) is below $\tau=\tau_c$. On the other hand, Fig. 10(*i*) is radically different and this case is sitting closely to where $\tau=\tau_c$, for this given gap case. For $\tau>\tau_c$ and $\epsilon=1$ the topology of the phase curve is similar to that of Fig. 10(*h*).

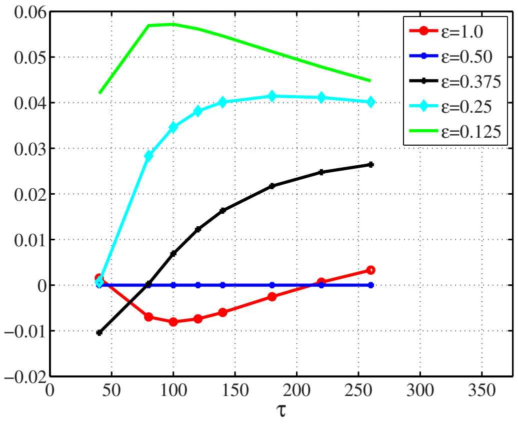

Fig. 8 For Re=100, Re=0.95, and the DML dependence on τ. From top to bottom: $\epsilon=0.125$, $\epsilon=0.375$, $\epsilon=0.5$, and $\epsilon=1.0$.

Bagchi and Balachandar [15] found negligible differences in the drag experienced by a freely rotating and a nonrotating sphere in a steady shear flow. We find the same type of behavior in the oscillatory shearing case. We thus refer the reader to FLR02 and FLR05 for a summary description on how the drag is affected by the choices in τ and ϵ.

4 Summary

The lift, drag, and torque on a spherical particle in an oscillatory wall-bounded flow were calculated, as a function of the particle density ratio, the Reynolds number, the Keulegan–Carpenter number, and the relative gap between the particle and the wall. The calculations were aimed at elucidating how a rotational degree of freedom affects these forces. In order to do so we calculate the forces on a particle that is held fixed and compare these to the forces obtained when the particle is allowed to freely rotate. These calculations, performed by solving the Navier–Stokes equations in three dimensions and time, complement the overall picture presented in Refs. [2,3], on the fundamental forces experienced by a particle in a wall-bounded oscillatory flow.

With regard to changes in the moment of inertia we found that the difference between the drag and lift of a fixed particle and one that is allowed to rotate was small. In contrast, the difference between a fixed and freely rotating particle with respect to torque was significant. The torque, not surprisingly, was larger for the fixed particle. The maximum normalized torque is most sensitive

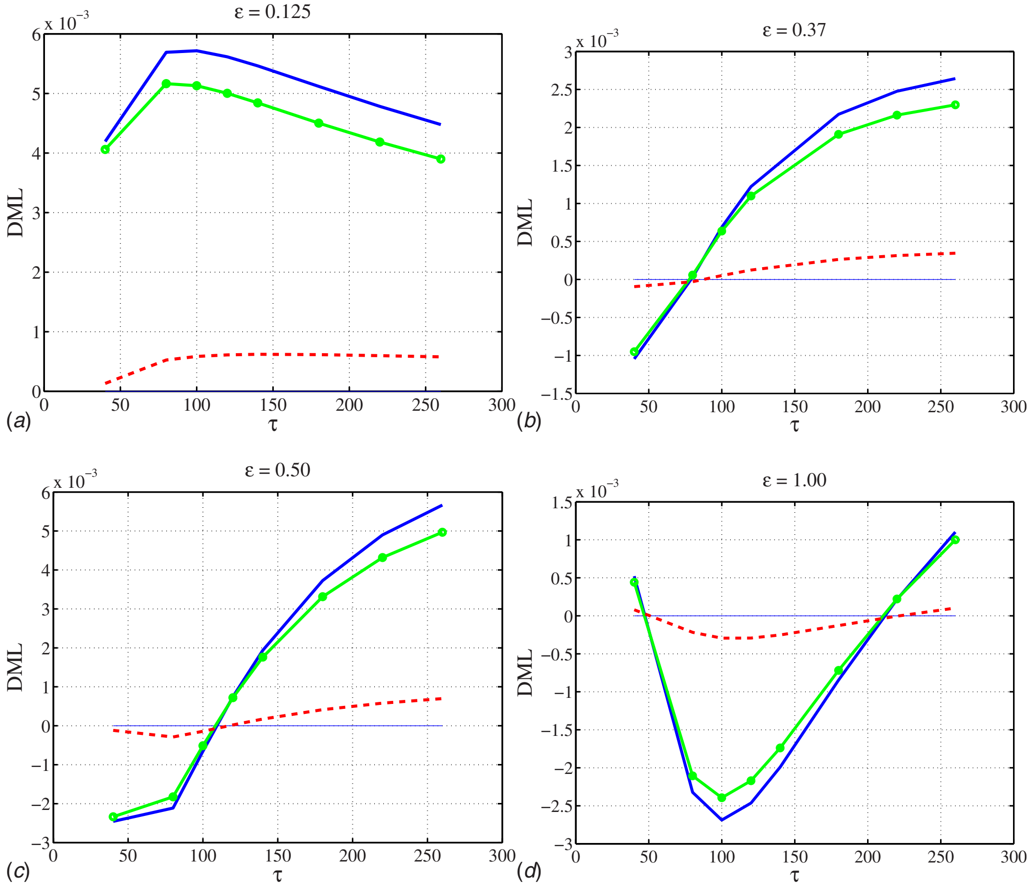

Fig. 9 For Re=100, DML (solid), its pressure (circles), and viscous (dashed) components as a function of τ; (*a*) ϵ=0.125, (*b*) ϵ=0.375, (*c*) ϵ=0.50, and (*d*) ϵ=1.00

to the closeness of the bounding wall when the forcing frequency is large, and is significant for Reynolds numbers smaller than 150, approximately. However, we found that the maximum torque, for low frequencies, is relatively insensitive to the gap size. The maximum normalized torque of a fixed particle was found to be a decreasing function of the Reynolds number. This is not the case for the rotating particle.

The drag forces of the freely rotating and the fixed particle are essentially the same, for small Reynolds numbers and variations of all parameters, and insignificantly different for larger Reynolds numbers.

The main focus of this study was the effect of rotation on the lift force. In order to characterize the effect of allowing the particle to freely rotate in response to the flow we focused on the difference between the mean lift of the rotating particle and the mean lift of the particle, fixed in place. This quantity we denoted here as the differential mean lift (DML). We found that the DML is positive for all forcing periods when the gap number is small. As the particle is placed farther away from the bounding wall we found that the effective lift is only positive for large Keulegan–Carpenter numbers. We also found that the maximal lift occurs nearly in phase with the maximum drag when the particle is placed close to the wall, but this phase difference increases as the particle is placed farther from the wall. Portraits of the drag and lift forces also indicate that the causal history of the forces is relatively insensitive to the forcing period when the particle is very close to the wall, but becomes sensitive when the particle is placed farther away. This last finding, however, is not a result of allowing the particle to rotate: The causal sensitivity is seen both in the rotating and nonrotating particle cases. The overall magnitude of the DML increases as the particle is placed closer to the wall. The DML is pressure-dominated throughout, the Bernoulli effect being significantly different when the particle is fixed as compared to when it is allowed to rotate.

As a function of the Reynolds number we found that for intermediate forcing periods allowing the particle to rotate produced an enhanced mean lift, when the Reynolds numbers was small, and a depressed mean lift in the large Reynolds-number regime. We found that this transition occurs approximately at Re=150. When examining the mean lift depression for larger Reynolds numbers we found that the Bernoulli effect alone could not account for the changes in the lift: The sphere induced more vortex shedding from the top of the sphere at high Reynolds numbers; however, the addition of rotation decreases their intensity but increases the number of vortex structures shed. This phenomenology leads to complex histories in the lift. At Reynolds numbers larger than 150 but not not significantly so, the forces of lift and drag are significantly different when the fixed and rotating cases are compared. Specifically, when the lift forces are averaged over the period of the forcing frequency the fact that for large Reynolds numbers the force is insignificant for larger fractions of the period when the particle is rotating is largely responsible for depressed values of the mean lift.

Acknowledgment

This work was carried out in part at the Argonne National Laboratory under the auspices of the Department of Energy under Contract No. W-31-109-Eng-38. J.M.R. wishes to thank the MCS Division at Argonne, as well as the support by DOE through Grant No. DE-FG02-03ER25577.

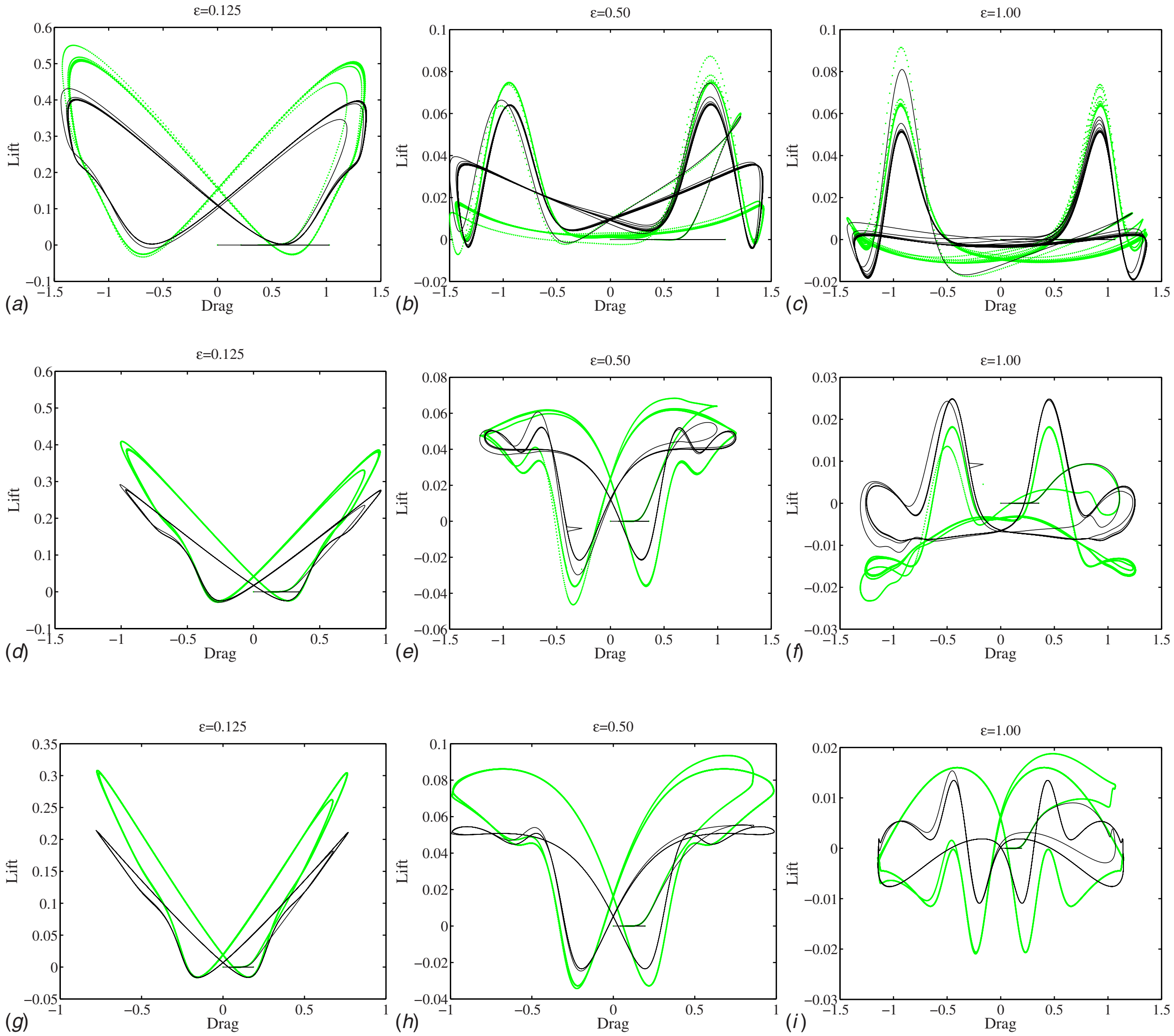

Fig. 10 Phase portraits for τ=40, Re=100, and R=0.95, and (*a*) ϵ=0.125, (*b*) ϵ=0.5, and (*c*) ϵ=1.00. Phase portraits for τ=120, (*d*) ϵ=0.125, (*e*) ϵ=0.5, and (*f*) ϵ=1.00. Phase portraits for τ=220, (*g*) ϵ=0.125, (*h*) ϵ=0.5, and (*i*) ϵ=1.00. (Light) freely rotating; (dark) fixed.

References

[1] Rosenthal, G., and Sleath, J., 1986, "Measurements of Lift in Oscillatory Flow," J. Fluid Mech., **146**, pp. 449–467.

[2] Fischer, P. F., Leaf, G. K., and Restrepo, J. M., 2002, "Forces on Particles in an Oscillatory Boundary Layer," J. Fluid Mech., **468**, pp. 327–347.

[3] Fischer, P. F., Leaf, G. K., and Restrepo, J. M., 2005, "Influence of Wall Proximity on the Lift and Drag of a Particle in an Oscillatory Flow," ASME J. Fluids Eng., **127**, pp. 583–594.

[4] Justesen, P., 1991, "A Numerical Study of Oscillating Flow Around a Circular Cylinder," J. Fluid Mech., **222**, pp. 157–196.

[5] Bearman, P. W., Downie, M. J., Graham, J. M. R., and Obajasu, E. D., 1985, "Forces on Cylinders in Viscous Oscillatory Flow at Low Keulegan–Carpenter Numbers," J. Fluid Mech., **154**, pp. 337–356.

[6] Obajasu, E. D., Bearman, P. W., and Graham, J. M. R., 1988, "A Study of Forces, Circulation and Vortex Patterns Around a Circular Cylinder in Oscillating Flow," J. Fluid Mech., **196**, pp. 467–494.

[7] Lane, E. M., and Restrepo, J. M., 2007, "Shoreface-Connected Ridges Under the Action of Waves and Currents," J. Fluid Mech., **582**, pp. 23–52.

[8] Bagnold, R. A., 1962, "Auto-Suspension of Transported Sediment; Turbidity," Proc. R. Soc. London, Ser. A, **265**, pp. 315–319.

[9] Bailard, J., 1981, "An Energetics Total Load Sediment Transport Model for a Plane Sloping Beach," J. Geophys. Res., **86**, pp. 10938–10954.

[10] Kelly, J. T., Asgharian, B., and Wong, B. A., 2005, "Inertial Particle Deposition in a Monkey Nasal Mold Compared With That in Human Nasal Replicas," Inhalation Toxicol., **17**, pp. 823–830.

[11] Benczik, I. J., Toroczkai, Z., and Teacute, T., 2003, "Advection of Finite-Size Particles in Open Flows," Phys. Rev. E, **67**, p. 036303.

[12] Kim, D., and Choi, H., 2002, "Laminar Flow Past a Sphere Rotating in the Streamwise Direction," J. Fluid Mech., **461**, pp. 365–386.

[13] Kurose, R., and Komori, S., 1999, "Drag and Lift Forces on a Rotating Sphere," J. Fluid Mech., **384**, pp. 183–206.

[14] Tsuji, Y., Morikawa, Y., and Mizuno, O., 1985, "Experimental Measurement of the Magnus Force on a Rotating Sphere at Low Reynolds Numbers," ASME J. Fluids Eng., **107**, pp. 484–488.

[15] Bagchi, P., and Balachandar, S., 2002, "Effect of Free Rotation on the Motion of a Solid Sphere in Linear Shear Flow at Moderate Re," Phys. Fluids, **14**, pp. 2719–2737.

[16] Bagchi, P., and Balachandar, S., 2002, "Shear Versus Vortex-Induced Lift Force on a Rigid Sphere at Moderate Re," J. Fluid Mech., **473**, pp. 379–388.

[17] Bagchi, P., and Balachandar, S., 2003, "Inertial and Viscous Forces on a Rigid Sphere in Straining Flows at Moderate Reynolds," J. Fluid Mech., **481**, pp. 105–148.

[18] Mikulencak, D. R., and Morris, J. F., 2004, "Stationary Shear Flow Around Fixed and Free Bodies at Finite Reynolds Number," J. Fluid Mech., **520**, pp. 215–242.

[19] Saffman, P. G., 1965, "The Lift on a Small Sphere in a Slow Shear Flow," J. Fluid Mech., **22**, pp. 385–400.

[20] Saffman, P. G., 1968, "(Corrigendum) The Lift on a Small Sphere in a Slow Shear Flow," J. Fluid Mech., **31**, p. 624.

[21] Zeng, L., Balachandar, S., and Fischer, P., 2005, "Wall-Induced Forces on a Rigid Sphere at Finite Reynolds Number," J. Fluid Mech., **536**, pp. 1–25.

[22] Fischer, P., Loth, F., Lee, S. W., Smith, D., and Bassiouny, H., 2007, "Simulation of High Reynolds Number Vascular Flows," Comput. Methods Appl. Mech. Eng., **196**, pp. 3049–3060.

Large Eddy Simulation of Flow Past Free Surface Piercing Circular Cylinders

G. Yu
e-mail: g.yu@qmul.ac.uk

E. J. Avital
e-mail: e.avital@qmul.ac.uk

J. J. R. Williams
e-mail: j.j.r.williams@qmul.ac.uk

Department of Engineering,
Queen Mary University of London,
Mile End Road,
London E1 4NS, UK

Flows past a free surface piercing cylinder are studied numerically by large eddy simulation at Froude numbers up to $Fr_D=3.0$ and Reynolds numbers up to $Re_D=1\times10^5$. A two-phase volume of fluid technique is employed to simulate the air-water flow and a flux corrected transport algorithm for transport of the interface. The effect of the free surface on the vortex structure in the near wake is investigated in detail together with the loadings on the cylinder at various Reynolds and Froude numbers. The computational results show that the free surface inhibits the vortex generation in the near wake, and as a result, reduces the vorticity and vortex shedding. At higher Froude numbers, this effect is stronger and vortex structures exhibit a 3D feature. However, the free surface effect is attenuated as Reynolds number increases. The time-averaged drag force on the unit height of a cylinder is shown to vary along the cylinder and the variation depends largely on Froude number. For flows at $Re_D=2.7\times10^4$, a negative pressure zone is developed in both the air and water regions near the free surface leading to a significant increase of drag force on the cylinder in the vicinity of the free surface at about $Fr_D=2.0$. The mean value of the overall drag force on the cylinder increases with Reynolds number and decreases with Froude number but the reduction is very small for $Fr_D=1.6$–2.0. The dominant Strouhal number of the lift oscillation decreases with Reynolds number but increases with Froude number. [DOI: 10.1115/1.2969462]

Keywords: free surface piercing cylinder, two-phase volume of fluid, large eddy simulation

Introduction

Flow past free surface piercing cylinders is of particular relevance to offshore structures and underwater vessels. The flow is known to show different complex structures in the vicinity of the cylinder; a bow wave appears at the front, which then spills over the cylinder to generate the near wake. The bow wave itself can break up and develop into a fountain at higher flow velocities. A Kelvin surface wake is generated behind the cylinder, which fans out to the far distance rear. The detailed hydrodynamics affecting this process are poorly understood and studies either by experimental tests or numerical simulations are rare. Wickramasinghe and Wilkinson [1] explored the possibilities of different methods, including practical tests, computational modeling, and theoretical analysis, that might be used for the study of the flow around a submarine mast. Inoue et al. [2] experimentally investigated cases with a vertical surface piercing cylinder at two Froude numbers, $\mathrm{Fr}_D=0.8$ and 1.0. Most previous numerical simulations had either been restricted to inviscid free surface flows (for example, in Ref. [3]) or neglected the free surface waves (for example, in Ref. [4]). Only recently have LES results been produced [5] for $\mathrm{Fr}_D\le0.8$ and subcritical Reynolds number of $\mathrm{Re}_D=2.7\times10^4$.

In this work, flows of low to high subcritical Reynolds number (up to $\mathrm{Re}_D=1\times10^5$) and Froude number higher than 1 (up to $\mathrm{Fr}_D=3.0$) are studied. The robust volume of fluid (VOF) method is used to simulate both the air and water phases. The primary objective is to investigate the effects of the free surface on flow structures near the cylinder, and to determine the force distribution along the cylinder for various Froude and Reynolds numbers.

Numerical Method

The flow is considered to be incompressible and to consist of two phases—water and air—with a clearly determined moving interface between them. Both phases are governed by the following two-phase nondimensional equations, which are then transformed into cylindrical coordinates:

$$\frac{\partial u_i}{\partial t}+\frac{\partial u_iu_j}{\partial x_j}=-\frac{1}{\rho}\frac{\partial p}{\partial x_i}+\frac{1}{\mathrm{Fr}_D^2}g_i+\frac{1}{\mathrm{We}}\frac{kc}{\rho}\frac{\partial c}{\partial x_i}+\frac{1}{\rho}\frac{\partial}{\partial x_j}\left[\left(\frac{\mu}{\mathrm{Re}_D}+\rho\nu_t\right)\times\left(\frac{\partial u_i}{\partial x_j}+\frac{\partial u_j}{\partial x_i}\right)\right] \tag{1}$$

$$\frac{\partial c}{\partial t}+\frac{\partial u_ic}{\partial x_i}=0 \tag{2}$$

$$\rho=c+(1-c)\frac{\rho_g^*}{\rho_l^*},\quad \mu=c+(1-c)\frac{\mu_g^*}{\mu_l^*} \tag{3}$$

$$\frac{\partial u_i}{\partial x_i}=0 \tag{4}$$

where u_i and p are the filtered velocity and pressure, x_i is the coordinate, t is the time, and $g_i=(0,0,-1)$ is a unit vector pointing in the direction of gravity. The color function c is a fractional volume scalar, which is 1 when the computational cell is full of water and 0 when occupied by air solely. The superscript * stands for a dimensional property, ρ_g^*, ρ_l^* and μ_g^*, μ_l^* represent the density and dynamic viscosity of air and water, respectively. The dimensionless parameters for the water are the Froude number, $\mathrm{Fr}_D=U/\sqrt{gD}$, and the Reynolds number, $\mathrm{Re}_D=\rho_l^*UD/\mu_l^*$ where D is the cylinder's diameter, U is the upstream velocity, and g is the gravitational acceleration. Based on the continuum surface force

---

Contributed by the Fluids Engineering Division of ASME for publication in the JOURNAL OF FLUIDS ENGINEERING. Manuscript received January 29, 2008; final manuscript received June 3, 2008; published online September 8, 2008. Assoc. Editor: Ugo Piomelli.

Table 1 Flows simulated and the size of the computational domain employed

	Re_D	Fr_D	Domain (radius × height)	Grid size (azimuthal × radial × height)
Case 1	27,000	0.8	$10D\times 6D$	$129\times 129\times 99$
Case 2	54,000	0.8	$10D\times 6D$	$129\times 129\times 99$
Case 3	100,000	0.8	$10D\times 6D$	$129\times 129\times 99$
Case 4	27,000	1.2	$15D\times 8D$	$129\times 157\times 131$
Case 5	27,000	1.6	$15D\times 8D$	$129\times 157\times 131$
Case 6	27,000	2.0	$15D\times 8D$	$129\times 157\times 131$
Case 7	27,000	2.5	$20D\times 10D$	$129\times 263\times 195$
Case 8	27,000	3.0	$20D\times 10D$	$129\times 263\times 195$

(CSF) method of Brackbill et al. [6], forces due to the interfacial tension can be expressed as surface volume forces and are written as

$$\boldsymbol{F}_s = \frac{1}{\mathrm{We}}\frac{kc}{\rho}\nabla c \tag{5}$$

where the nondimensionless Weber number is defined as $\mathrm{We} = \rho_l^* U^2 D/(2\sigma^*)$ and σ^* is the coefficient of surface tension between water and air. The interface curvature is calculated by

$$k = (1/|\boldsymbol{n}|)[(\hat{n}\cdot\nabla)|\boldsymbol{n}| - (\nabla\cdot\boldsymbol{n})] \tag{6}$$

where $\boldsymbol{n}=\nabla c$ is the normal direction of the air-water interface and $\hat{n}=\boldsymbol{n}/|\boldsymbol{n}|$. It is obvious that $\boldsymbol{F}_s$ is zero everywhere except for the cells containing the interface.

The Smagorinsky model [7] together with the Van Driest wall damping function [8] is used to model subgrid small scales. The eddy viscosity is given by

$$\nu_t = C_S^2\Delta^2(1-\exp(-y^+/A)^3)\sqrt{2S_{ij}S_{ij}} \tag{7}$$

As stated in Ref. [9], for a wake and jet flow the optimum value of Smagorinsky's constant C_S is around 0.2, which was also assigned to C_S by Kawamura et al. [5] to study the interaction between the turbulent wake and the free surface. In this study, the influence of C_S was investigated on overall drag coefficient $\bar{C}_d$; for Case 1 in Table 1, four values of C_S, 0.1, 0.15, 0.2, and 0.22, were considered. It was found that $C_S=0.1$ gave the lowest prediction of the mean value of $\bar{C}_d$, 0.5; it was around 0.7 for $C_S=0.15$. When $C_S=0.2$ the mean $\bar{C}_d$ was 0.84, which is the closest value to the experimental value of 1.2 in Ref. [10] for the same configuration but neglecting the free surface. The scheme became unstable if $C_S=0.22$. Δ is the cubic root of the volume of a computational cell, $S_{ij}=(1/2)(\partial u_i/\partial x_j+\partial u_j/\partial x_i)$ is the rate of strain tensor, and y^+ is the nondimensional distance from the wall defined by $y^+=(u_\tau y)/\nu$, where μ_τ is the wall shear velocity and $\nu=c+(1-c)\times(\mu_g^*/\mu_l^*)/(\rho_g^*/\rho_l^*)$, $A=25$ is the Van Driest constant.

The spatial discretization is based on the finite volume approach on a staggered grid; the QUICK scheme is used for the convection term and a second order central scheme for the diffusion term as in Ref. [5]. Breuer [11] investigated the effects of numerical schemes for the convection term and found that the QUICK scheme is not very suitable for flows past an infinite circular cylinder; instead a second order central scheme gives a better agreement with the experimental data. Nevertheless, this scheme failed to converge when applied to free surface flows past a piercing circular cylinder; it is probably due to the free surface deformation and the large density ratio of water and air. Equation (1) is solved by the projection method and is marched in time by a second order Runge–Kutta (RK) scheme. The Poisson equation for pressure resulting from the projection method is solved using the preconditioned biconjugate gradient stabilized (PBCGSTAB) method along with a polynomial preconditioner. Free surface motion is modeled using an air-water two-phase VOF model with the air initially on top of the water by Eq. (2), which is solved based on flux corrected transport (FCT) method of Rudman [12]. The coupling of Eqs. (1) and (2) at each RK stage is illustrated as follows in Cartesian forms.

1. Calculate the value of c at subtime level $n+1$ using the FCT method as follows:

$$c^{n+1} = c^n - \delta t\left(\frac{\partial u_i c}{\partial x_i}\right)^n \tag{8}$$

2. Find the densities and viscosities at the subtime level $n+1$ as follows:

$$\rho^{n+1} = c^{n+1} + (1-c^{n+1})\frac{\rho_g}{\rho_l}, \quad \mu^{n+1} = c^{n+1} + (1-c^{n+1})\frac{\mu_g}{\mu_l} \tag{9}$$

3. Estimate intermediate values of velocities at the subtime level $n+1$ as follows:

$$\begin{aligned}(u^{n+1})^* &= u^n - \delta t H^n \\ H^n &= -\frac{\partial u_i u_j}{\partial x_j} + \frac{1}{\mathrm{Fr}_D^2}g_i + \frac{1}{\mathrm{We}}\frac{kc}{\rho}\frac{\partial c}{\partial x_i} \\ &\quad + \frac{1}{\rho}\frac{\partial}{\partial x_j}\left[\left(\frac{\mu}{\mathrm{Re}_D}+\rho\nu_t\right)\left(\frac{\partial u_i}{\partial x_j}+\frac{\partial u_j}{\partial x_i}\right)\right]\end{aligned} \tag{10}$$

4. Solve the Poisson equation for pressure at the subtime level $n+1$ as follows:

$$\frac{\partial}{\partial x_i}(u^{n+1})^* = \frac{\partial}{\partial x_i}\left(\frac{\delta t}{\rho^{n+1}}\left(\frac{\partial p}{\partial x_i}\right)^{n+1}\right) \tag{11}$$

5. Update the velocities (divergence-free) at the subtime level $n+1$ as follows:

$$u^{n+1} = (u^{n+1})^* - \frac{\delta t}{\rho^{n+1}}\left(\frac{\partial p}{\partial x_i}\right)^{n+1} \tag{12}$$

A body fitted cylindrical grid is used to capture the form of the cylinder with the grid being stretched in the radial direction toward the outer edge of the computational domain, so that a finer grid can be used in the vicinity of the cylinder. The whole domain is composed of inflow and outflow regions along with a buffer zone ringed around the computational domain (see Fig. 1). The domain size for the cases studied and the corresponding grid points are shown in Table 1.

For all of the simulations in this study the still water height is $4D$ and a nonslip wall condition is imposed on the cylinder surface for the velocity. On the outer radial edge of the inflow side, the freestream water inflow velocity is perturbed by a small amplitude sinusoidal wave, $0.01\times\sin(2\pi ft)$. The frequency f was chosen to be of $\mathrm{St}_D=0.2$ ($\mathrm{St}_D=fD/U$), the preferred shedding mode for a cylinder, to encourage vortex shedding and thus reduce the computational time required to reach that stage; the air is taken as stationary. At the outlet a zero gradient velocity condition is applied in radial direction along with a buffer zone in which the computational scheme for the convection term is relaxed from the QUICK to a first order upwind scheme to dampen reflections. To eliminate reflections at an arbitrary outflow boundary, a convective outflow boundary condition proposed by Orlanski [13] is an effective and simple way for single phase flows. Nevertheless, applying Orlanski's method could not achieve converged results for the two-phase flow of this study. It was stated that the accuracy of the convective boundary depended largely on the local convective velocity by Heinrich et al. [14] who studied the effects of locations of the arbitrary outflow boundary and of the convective velocity. Heinrich et al. [14] also found that as the convective velocity became smaller, the singularity in the convection bound-

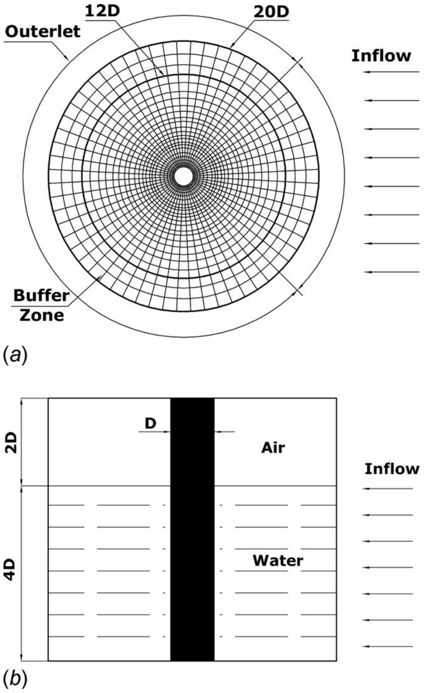

Fig. 1 Schematic description of the cylindrical coordinates (*a*) and the configurations of the computational domain (*b*). The inflow region covers an arc of 90 deg.

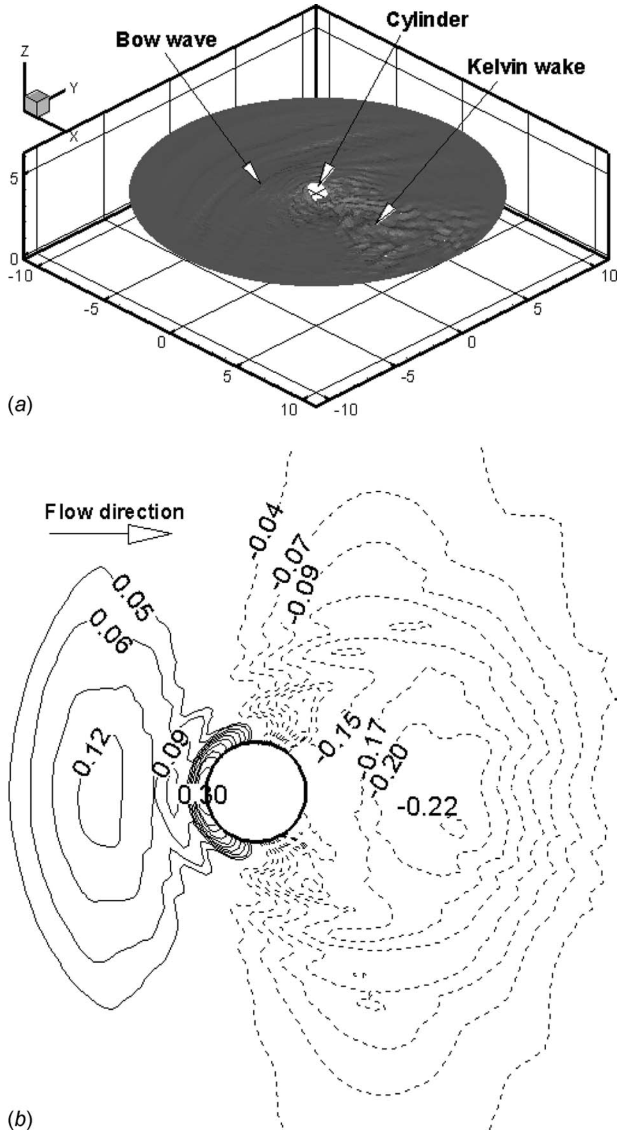

Fig. 2 (*a*) Instantaneous evolution of the interface surface (c =0.5), $\mathrm{Re}_D=2.7\times10^4$, and $\mathrm{Fr}_D=0.8$. (*b*) Contours of the time-averaged air-water interface height corresponding to c=0.5, $\mathrm{Re}_D=2.7\times10^4$, and $\mathrm{Fr}_D=0.8$.

ary condition became more evident. In this study of a two-phase flow problem, the air phase is initially stationary, and although there is some dynamic interaction between the air and water at the interface, farther away from it the air is almost undisturbed, its velocity at the outlet is close to zero, which may cause the divergence of the scheme with a convective boundary. At the bottom (water side) of the computational domain a free slip velocity condition is adopted, which means that no horseshoe vortex develops there; the same free slip condition is also applied on the top (air side). Pressure is set to zero on the top of the domain, while a zero gradient pressure is applied at the boundaries elsewhere.

It should be pointed out that in the PBCGSTAB method for the pressure and when calculating ∇c for the interface orientation, the color function c has been replaced with a smoothed color function $\tilde{c}$ as follows:

$$\tilde{c}(x,y,z)=\sum_{m=1}^{27} D(x-x_m)D(y-y_m)D(z-z_m)c(x_m,y_m,z_m) \quad (13)$$

where the smoothing function D is given by the function proposed by Peskin [15]; for example, in x direction, one has

$$D(x)=\frac{1}{2h}(1+\cos(\pi x)/h) \quad (14)$$

where $h=2\Delta_x$; Δ_x is the grid size in the x direction implying a 27-point computational stencil is used for the smoothening. It should also be stressed that this smoothed color function is only used in the situations mentioned above and not in the transport equation (2) of the material fluxes.

Validation of the Code

A parallel code was developed using FORTRAN 90 and the MPI message passing interface library. The computations were run on the HPCx at University of Edinburgh using 64 processors for production runs.

Figure 2(*a*) shows the instantaneous isosurface of the color function (c=0.5) for Case 1 in Table 1. The generation of bow waves in front of the cylinder and the subsequent generation of the Kelvin wake are clearly seen. The elevation variation is also seen in Fig. 2(*b*) where the time-averaged air-water interface height corresponding to the color function (c=0.5) is plotted for the same case. The interface height was converted from the VOF value assuming monotonically reducing color in vertical direction.

For validation, we first check if a turbulent flow is obtained in the near wake. An energy spectrum analysis at a point 2.5D away from the cylinder in the wake on the base plane (y=0) and 0.05D above the bottom of the domain was carried out over a period of $tU/D=60$; as can be seen in Fig. 3, Kolmogorov's $-5/3$ inertial subrange lasts more than one decade implying that the flow has reached turbulence. Therefore, the averaging time used for all cases to gather the statistical data started at $tU/D=60$ and finished at $tU/D=120$, which is 12 shedding cycles at a typical Strouhal shedding frequency, $\mathrm{St}_D=0.2$.

As mentioned earlier the most recent numerical and experimental investigation results on flows past a free surface piercing cylinder are available only for $\mathrm{Fr}_D\leq0.8$ and, as a consequence, the LES code is therefore validated against these. In Fig. 4 we com-

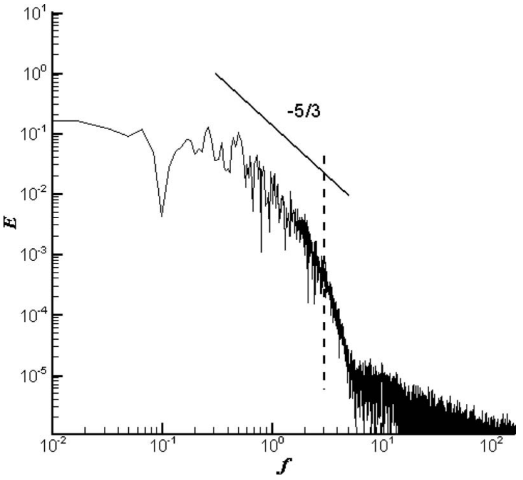

Fig. 3 Energy spectrum of the flow in the near wake of the cylinder; the solid straight line has a slope of −5/3; the dashed line represents the grid cutoff

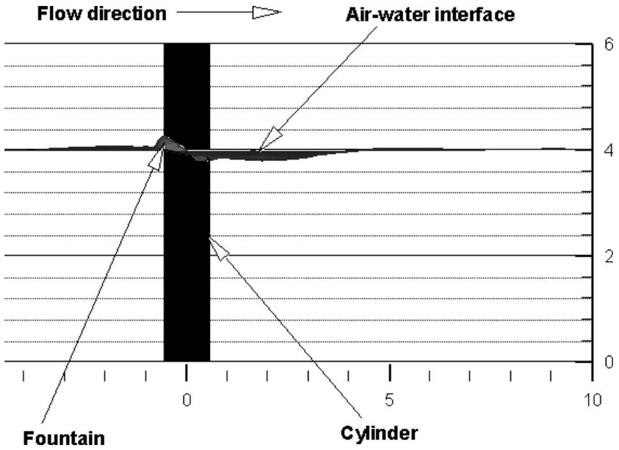

Fig. 5 Time-averaged air-water interface surface with a fountain generated in front of the cylinder; the initial still water height is 4*D*, $\mathrm{Re}_D=2.7\times10^4$, and $\mathrm{Fr}_D=0.8$

pare the time-averaged streamwise velocity profiles in the near wake along the vertical direction with published numerical and experimental results. The sample points were taken on the base plane of the wake ($y=0$) and 4.5*D* away from the cylinder. The figure shows the decrease of the streamwise velocity near the free surface and the agreement between our simulation with the velocity measurements and the computational results of Kawamura et al. [5]. It also shows that the difference between our computational results using different grid resolutions is small. The grid sizes used for cases studied in this paper are shown in Table 1.

We also compare the predicted fountain heights with the experimental observations of Wickramasinghe and Wilkinson [1] and the predictions of the hydrodynamic head model that was found by Wickramasinghe and Wilkinson [1] to predict reasonably well the experimentally measured bow wave heights up to about $\mathrm{Fr}_D=3$. The model states that the maximum possible surface elevation the flow could reach is the hydrostatic head, $U^2/2g$. Figure 5 shows the time-averaged air-water interface surface ($c=0.5$) on the plane of $y=0$; a maximum of bow wave height of about 0.3*D* above the still water level (4*D*) is seen in front of the cylinder (also see Fig. 2(*b*)), which agrees well with the experimental observation and the model prediction, 0.32*D*, as also shown in Fig. 6 where we compare the fountain heights predicted by our simulation with the experimental observations for flows at various Froude numbers. The figure shows that our model can predict the fountain height fairly accurately until $\mathrm{Fr}_D=2.0$; after this Froude number the model underpredicts the fountain height. This may be due to the fact that in our simulation a larger computational domain is adopted for higher Froude numbers; on the outer edge of the domain the azimuthal grid space is too big in an *O*-type cylindrical coordinate causing more numerical dissipation particularly at the inlet of the flow; thus, the code may underpredict the fountain height. Another possible reason is that at higher Froude numbers, surface tension and/or frictional processes in the thin film of water that flows up the cylinder may be significant in the fountain. Adding surface tension forces according to the CSF method (Eq. (5)) does not improve the prediction for $\mathrm{Fr}_D>2.0$; changing the color transport technique FCT-VOF to Youngs' 3D piecewise linear interface calculation (PLIC) method [16], PLIC-VOF, has shown only limited success in improving the prediction of the fountain height. This area certainly deserves more research with attention also given to the effect of the Smagorinsky subgrid scale (SGS) model. Therefore the following results and analysis concentrate on $\mathrm{Fr}_D\leq2.0$.

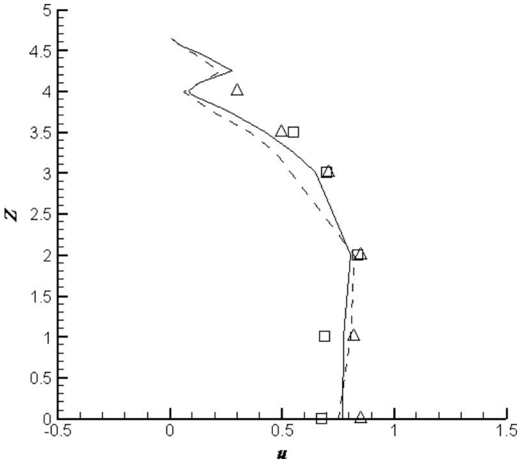

Fig. 4 Comparison of the time-averaged streamwise velocity profiles at $x=4.5D$, $y=0$ in the wake, $\mathrm{Re}_D=2.7\times10^4$, and $\mathrm{Fr}_D=0.8$. (□) Experimental results of Inoue et al. [2], (△) numerical simulation of Kawamura et al. [5], (—) current simulation with grid size of 161×161×131, and (---) current simulation with grid size of 129×129×99.

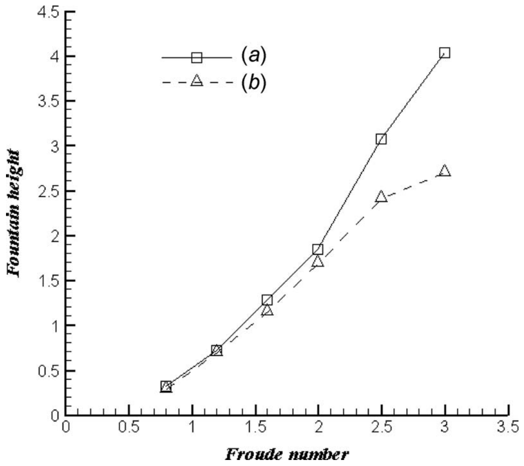

Fig. 6 Normalized fountain height by *D* versus Froude number. (*a*) Experimental observation of Wickramasinghe and Wilkinson [1] and (*b*) current simulation results.

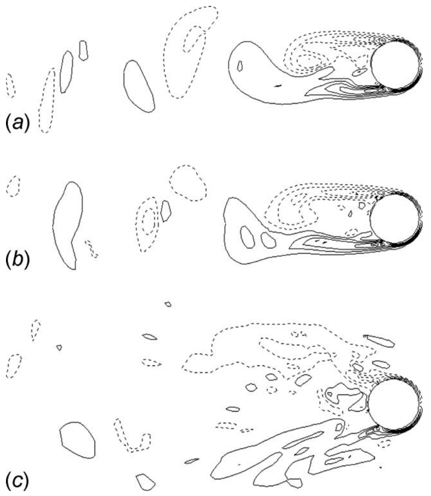

Fig. 7 Contours of the instantaneous vorticity magnitude for Case 1 in Table 1 on the plane adjacent to the bed (*a*), at the midplane (*b*), and near the free surface (*c*)

Free Surface Effect on Flow Structures in the Near Wake

It has been found that the free surface inhibits the vortex generation in the near wake and, as a result, the lift oscillation also bears this influence [5]. As can be seen in Fig. 7, a vortex street is observed below the midplane ($2D$ above the bed) and the corresponding lift oscillation is characterized by a dominant mode of $\mathrm{St}_D=0.23$; as the free surface is approached, the oscillation intensity is reduced; near the free surface oscillations with lower frequencies develop, and actually there is no dominant frequency and the oscillation becomes quite random (see Fig. 8).

Figure 9 presents the effects of the free surface on the time-averaged vorticity magnitude $\langle\omega\rangle$. There is no significant difference in the time-averaged vorticity magnitude below the midplane; the transverse spatial distance of each shear layer in the near wake is very narrow indicating a very high vorticity gradient of the shear layer; moreover, each layer is drawn toward the plane of symmetry of the base region; near the free surface each layer is deflected away from the symmetric plane and the vorticity in the shear layer is reduced. As described by Gerrard [17], vortex shedding occurs when the vorticity in the shear layer is strong enough to draw the opposing vortex across the wake to cut off further supply of vorticity from the shear layer. Below the midplane, the free surface effect on the vorticity is very weak and a regular vortex street is observed; near the free surface, due to the reduced vorticity in the shear layer by the free surface effect, no vortex shedding forms.

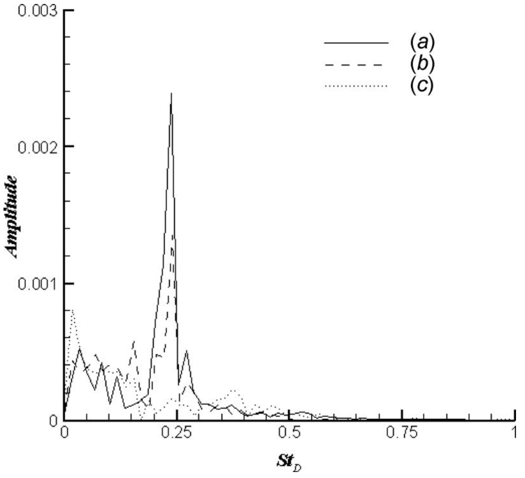

Fig. 8 Power spectral density of the lift for Case 1 in Table 1 on the plane adjacent to the bed (*a*), at the midplane (*b*), and near the free surface (*c*)

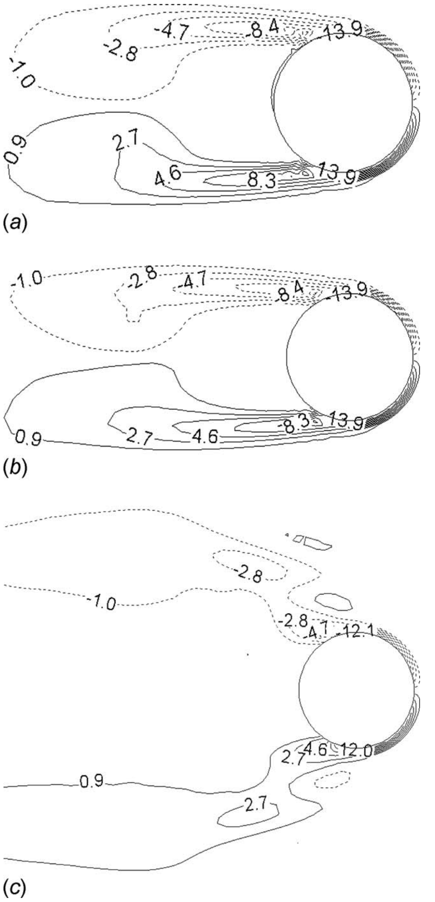

Fig. 9 Contours of time-averaged vorticity magnitude for Case 1 in Table 1 on the plane adjacent to the bed (*a*), at the midplane (*b*), and near the free surface (*c*)

It is also observed in Fig. 10 that the free surface reduces the Reynolds stress $\langle u'v'\rangle$ in the near wake, and that high concentration centers of $\langle u'v'\rangle$ are displaced further downstream as the free surface is approached. Furthermore, in the wake below the midplane an additional but weaker concentration pair occurs close to the base of the cylinder; this overall form of the Reynolds stress pattern qualitatively agrees with the experimental observation in the near wake of a cylinder with a larger spanwise extent as presented by Mittal and Balachandar [18].

By employing the λ-criterion defined by Jeong and Hussain [19], three dimensional coherent vortex structures can be identified in the near wake (λ is the second largest (negative) eigenvalue of the tensor related to the deformation rate tensor).

Figures 11 and 12 show the instantaneous vortex structure for flows at the same Reynolds number but with two different Froude numbers. At a Froude number of 0.8, few effects of the free surface can be felt in the deep wake resulting in a region where 2D flow features dominate and vortex tubes lie in horizontal planes; above the midplane the shedded vortex tubes slant and near the free surface they re-attach to the free surface exhibiting a strong 3D feature of the flow. The figure also shows that when the Froude number increases the vortex generation is further attenuated. At $\mathrm{Fr}_D=2.0$, the free surface effect has propagated throughout the wake and no regular vortex shedding is observed. With the

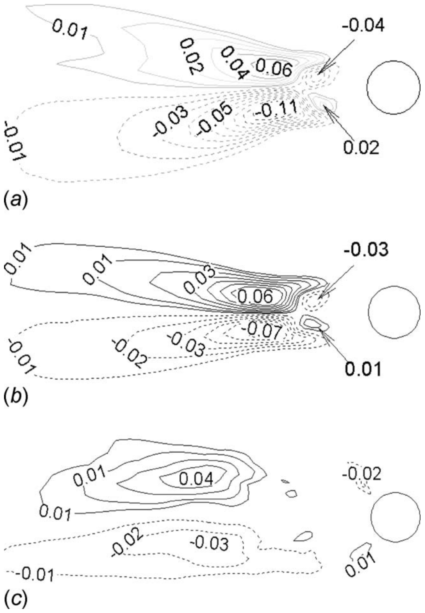

Fig. 10 Contours of the Reynolds stress $\langle u'v' \rangle$ for Case 1 in Table 1 on the plane adjacent to the bed (*a*), at the midplane (*b*), and near the free surface (*c*)

isosurface value of $\lambda = -5$, no vortex structure is seen well below the free surface implying vortices with less intensity dominate this region.

Vortex structures for flows at the same Froude number but two different Reynolds numbers are shown in Figs. 11 and 13. It is observed that at a higher Reynolds number, $\mathrm{Re}_D = 1.0 \times 10^5$, the 2D flow feature exists up to a position closer to the free surface than that at a lower Reynolds number, $\mathrm{Re}_D = 2.7 \times 10^4$, which implies that flows at a higher Reynolds number can swamp the free surface effect on the vortex structure in the near wake.

This feature can also be demonstrated by carrying out a spectrum analysis on the lift acting on the cylinder as shown in Fig. 14. It is well known that without a free surface the Strouhal number of the lift oscillation for a 2D flow past a horizontal cylinder is 0.2 by, e.g., observation of Roshko [20]. In the region adjacent to bed (see Fig. 14(*a*)), for $\mathrm{Re}_D = 1.0 \times 10^5$ the dominant St_D number of lift oscillation is identical to the typical value of 0.2, which indicates that this region is free of the free surface effect; whereas as Reynolds number decreases, the St_D number increases and the intensity of oscillation decreases indicating the free surface effect has spread further down from the air-water interface for flows with smaller Reynolds numbers. It is also shown in Fig. 14 that the oscillation intensity becomes stronger as the Reynolds number increases. For $\mathrm{Re}_D = 1.0 \times 10^5$, near the free surface, the oscillation is even not completely random and a relatively dominant frequency is observed. This confirms that flows at a higher Reynolds number have more resistance to the free surface effect.

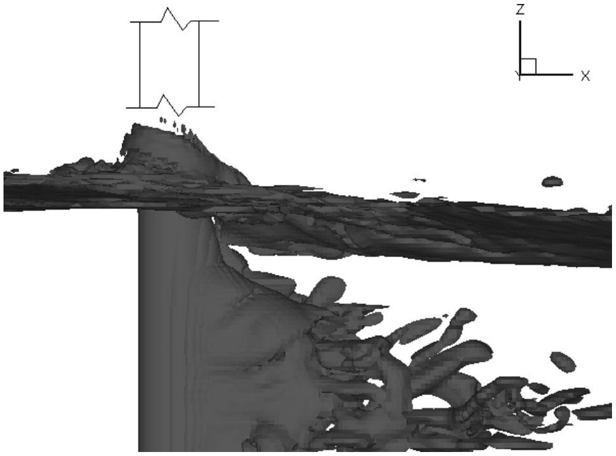

Fig. 12 Instantaneous vortex structure in the near wake at $\mathrm{Re}_D = 2.7 \times 10^4$ and $\mathrm{Fr}_D = 2.0$; the view is taken on the plane cross the cylinder center in the inflow direction ($\lambda = -5$)

Drag and Lift on the Cylinder

In this section we explore the drag distribution along the cylinder for various Reynolds and Froude numbers together with the overall mean drag coefficient. Spectrum analysis is applied to the lift to study its distribution at various Reynolds and Froude numbers.

The sectional drag coefficient C_d and lift coefficient C_l are defined, respectively, as

$$C_d = f_x / (\rho_l^* U^2 D / 2) \tag{15}$$

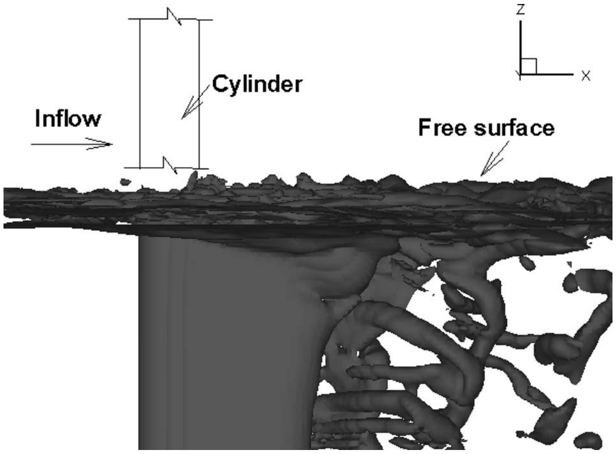

Fig. 11 Instantaneous vortex structure in the near wake at $\mathrm{Re}_D = 2.7 \times 10^4$ and $\mathrm{Fr}_D = 0.8$; the view is taken on the plane cross the cylinder center in the inflow direction ($\lambda = -5$)

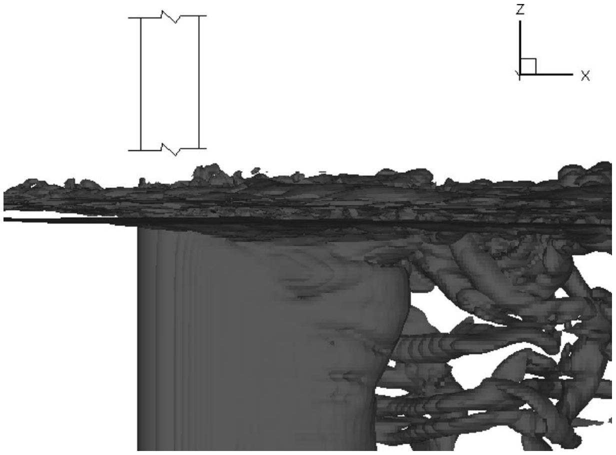

Fig. 13 Instantaneous vortex structure in the near wake at $\mathrm{Re}_D = 1.0 \times 10^5$ and $\mathrm{Fr}_D = 0.8$; the view is taken on the plane cross the cylinder center in the inflow direction ($\lambda = -5$)

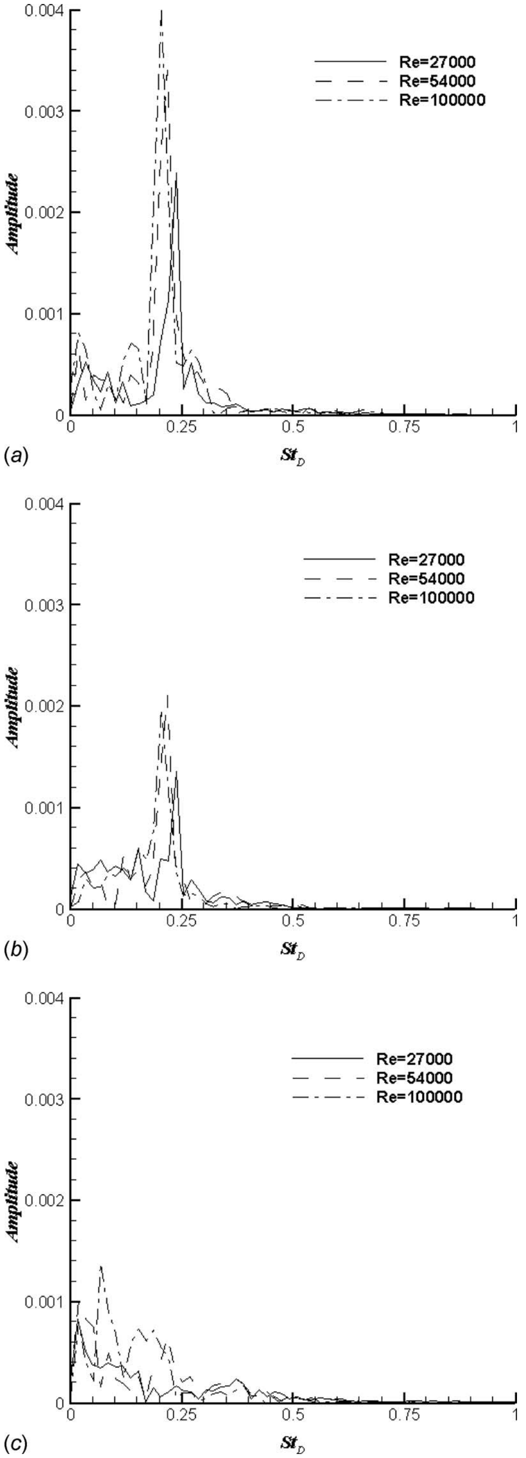

Fig. 14 Power spectral density of the lift at $Fr_D=0.8$, on the plane adjacent to the bed (*a*), at the midplane (*b*), and near the free surface (*c*)

$$C_l = f_y/(\rho_l^* U^2 D/2) \tag{16}$$

where f_x and f_y are the resultant forces per unit height of the cylinder in the flow and transverse directions, respectively. The flow consists of water and air with dynamic interaction, so the overall drag coefficient on the cylinder is calculated over the whole height of the cylinder by

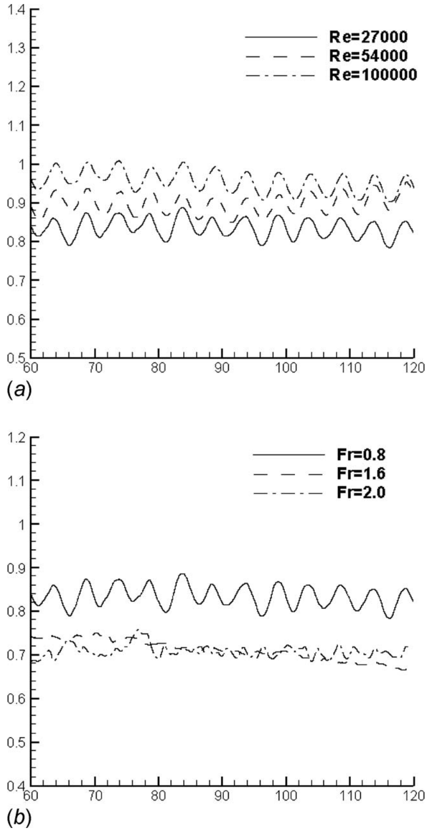

Fig. 15 Overall drag coefficient $\bar{C}_d$ as a function of time *tU/d* at the same $Fr_D=0.8$ but various Reynolds numbers (*a*) and the same Reynolds number $Re_D=2.7\times10^4$ but various Froude numbers (*b*)

$$\bar{C}_d = \left(\int_0^H f_x dz\right) \bigg/ (\rho_l^* U^2 D H_s/2) \tag{17}$$

where H is the cylinder height and H_s is the initially immersed height of the cylinder in water.

Figure 15(*a*) shows the time history of $\bar{C}_d$ for water height of $4D$ and $Fr_D=0.8$ with respect to various Reynolds numbers. It is seen that the mean value of $\bar{C}_d$ varies slightly with Reynolds number; however, it still reveals the effect of free surface. Without free surface, the mean $\bar{C}_d$ was measured by Wieselsberger [21] to be around 1.2 regardless of the Reynolds number for flows in subcritical region; therefore, the departure from this value reflects the extent of free surface effect. This reiterates our previous finding that flows at a higher Reynolds number are more capable of inhibiting the free surface effect. The profile of the time-averaged sectional drag coefficient, $\langle C_d\rangle$, along the cylinder is plotted in Fig. 16(*a*) for the same water height of $4D$ and $Fr_D=0.8$. As can be seen $\langle C_d\rangle$ is almost a constant below the midway ($2D$); the decrease of $\langle C_d\rangle$ above $2D$ implies the existence of the free surface.

Figures 15(*b*) and 16(*b*) display the time history of $\bar{C}_d$ and the profile of the time-averaged sectional drag coefficient $\langle C_d\rangle$, respectively, for the same water height of $4D$ and $Re_D=2.7\times10^4$ with respect to various Froude numbers. As the Froude number increases, the mean value of $\bar{C}_d$ decreases, the oscillation intensity reduces, and no dominant oscillation frequency is observed; however, the change is very small between $Fr_D=1.6$ and 2.0. It should also be noted that in Fig. 16(*b*), there is a big increase of $\langle C_d\rangle$ on the plane around $3.4D$ above the bed at $Fr_D=2.0$. The computa-

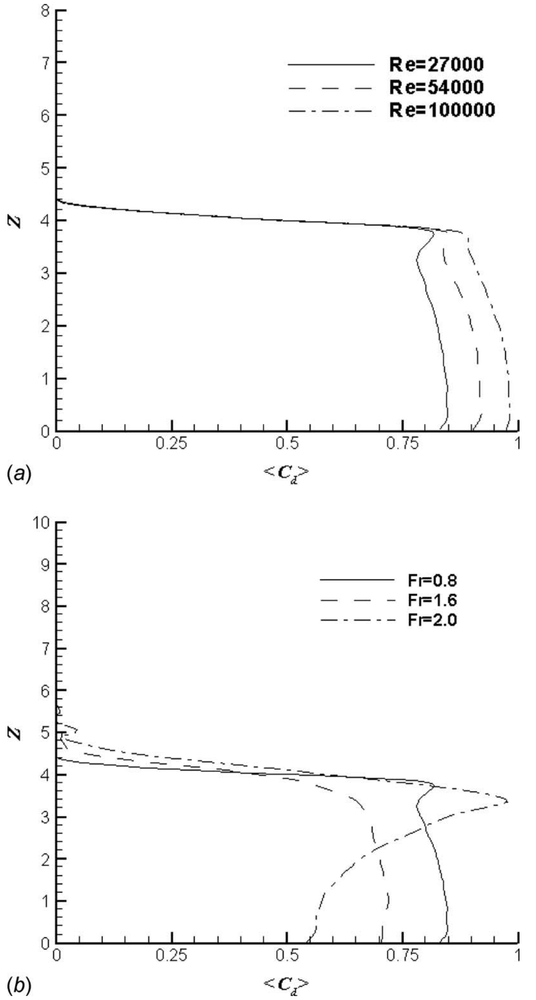

Fig. 16 Time-averaged sectional drag coefficient distribution along the cylinder at the same $Fr_D=0.8$ but various Reynolds numbers (*a*) and the same Reynolds number $Re_D=2.7\times10^4$ but various Froude numbers (*b*)

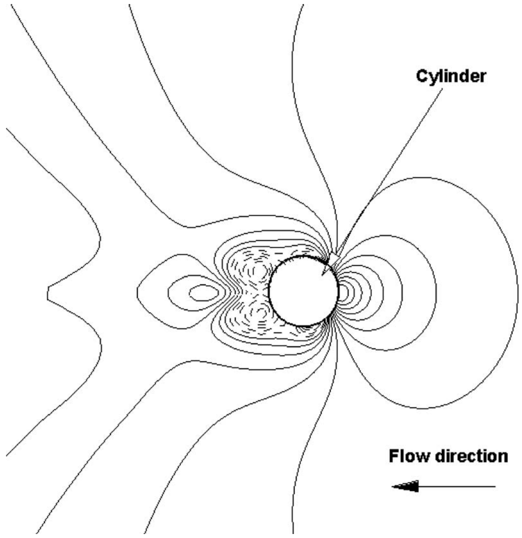

Fig. 18 Time-averaged pressure distribution on the plane 3.4*D* above the bed at $Re_D=2.7\times10^4$ and $Fr_D=2.0$. There are 20 levels between −0.34 and 0.59. The dashed lines represent negative values.

tional results show that the time-averaged drag force due to friction on the cylinder wall is trivial compared with the pressure contribution; this can therefore be explained by examining the pressure field in the area surrounding the cylinder. Figure 17 (*a*) shows the time-averaged air-water interface ($c=0.5$) at $Re_D=2.7\times10^4$ and $Fr_D=2.0$, and Fig. 17 (*b*) plots the time-averaged air-water interface for $Fr_D=0.8$ for comparison. Figure 18 illustrates the time-averaged pressure distribution on the plane 3.4*D* above the bed. It is seen that at $Fr_D=2.0$, a much deeper wake behind the cylinder, about 0.8*D* deep from the initial still water height (4*D*), and a more higher fountain in front of the cylinder, about 1.6*D* above the initial still water level, are generated. This as a consequence produces a negative pressure zone behind the cylinder, thus causing the jump of drag force. Computational results also reveal a negative pressure zone in both the air and water regions near the free surface, which demonstrates that for flows at a higher Froude number, i.e., $Fr_D=2.0$, the free surface in the wake near

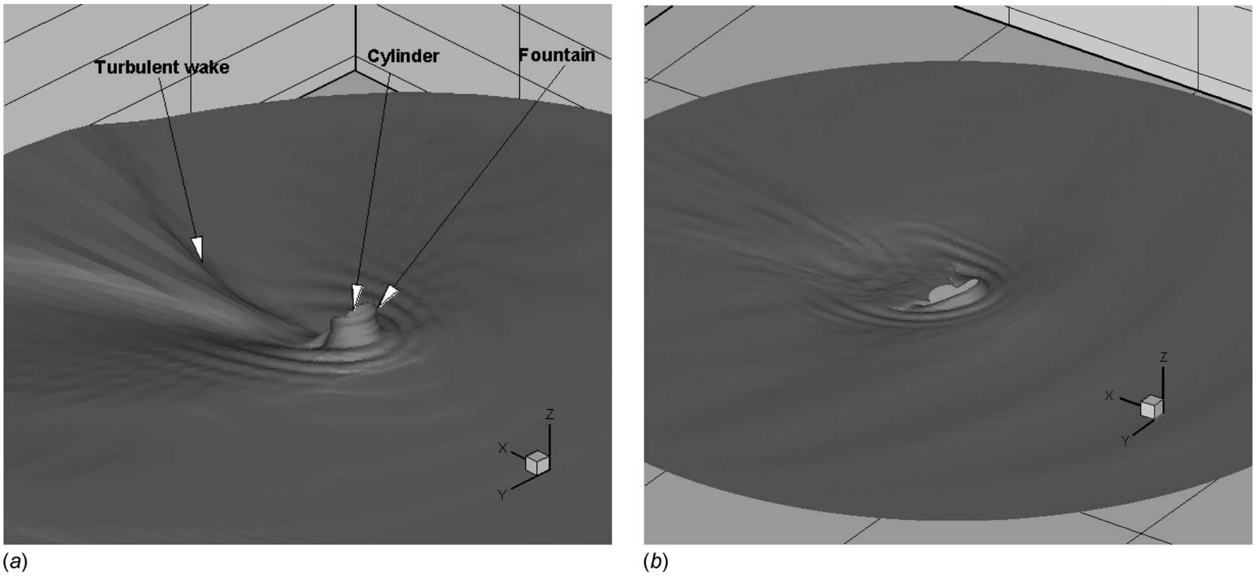

(*a*) (*b*)

Fig. 17 Time-averaged air-water interface ($c=0.5$) at $Re_D=2.7\times10^4$ and $Fr_D=2.0$ (*a*), and $Re_D=2.7\times10^4$ and $Fr_D=0.8$ (*b*). Water flows in the *x* direction.

the cylinder acts as a cavity leading to an abrupt force change on the cylinder near the free surface. Further down below the surface, a positive pressure zone builds up in the deep wake for $\mathrm{Fr}_D=2.0$; thus $\langle C_d \rangle$ decreases with Froude number (see Fig. 16(*b*)). This results in that the variation of overall drag force on the cylinder is insignificant between $\mathrm{Fr}_D=1.6$ and 2.0.

Summary and Conclusions

Flows at various Reynolds and Froude numbers are simulated by a two-phase LES model where the air-water interface is represented by volume of fluid (VOF) technique and a flux corrected transport (FCT) algorithm for transport of the interface. The focus is on the investigation of free surface effect on both flow structures in the near wake and the loadings on the cylinder.

This study has shown that the free surface attenuates the vortex generation in the near wake and, as a result, reduces the vorticity and vortex shedding. At a Froude number of 0.8, the flow in the deep wake has 2D vortex structures whereas near the free surface the vortex structures exhibit a strong 3D feature. At $\mathrm{Fr}_D=2.0$, the free surface effect has propagated throughout the wake and no regular vortex shedding is observed; vortices with less intensity dominate the region below the free surface. It has also been found that flows at a higher Reynolds number damp the free surface effect on the vortex structures in the near wake. At $\mathrm{Re}_D=1.0 \times 10^5$, 2D vortex structures prevail in the wake and the flow behaves like a 2D flow without a free surface.

For flows at the same Froude number, the mean value of the overall drag coefficient $\bar{C}_d$ increases with the Reynolds number; the time-averaged sectional drag coefficient $\langle C_d \rangle$ is almost invariant in the deep wake at a certain Reynolds number but this constant increases with the Reynolds number. The dominant St_D number of the lift oscillation in the deep wake decreases with the Reynolds number. For flows at the same Reynolds number, as the Froude number increases the mean value of $\bar{C}_d$ decreases, the oscillation intensity reduces, and the oscillation loses some of its period; however, the change is very small between $\mathrm{Fr}_D=1.6$ and 2.0. Although at $\mathrm{Fr}_D=2.0$ there is a big increase of $\langle C_d \rangle$ in the vicinity of the free surface, in the deep wake it decreases with the Froude number resulting in the variation of overall drag force acting on the cylinder to be insignificant.

Acknowledgment

The support of the EPSRC Grant No. GR/S46239/1 and the UK Turbulence Consortium for providing computing time are gratefully acknowledged.

Nomenclature

C_S = Smagorinsky constant
C_d = sectional drag coefficient
C_l = sectional lift coefficient
$\bar{C}_d$ = overall drag coefficient
$\langle C_d \rangle$ = time-averaged sectional drag coefficient
D = cylinder diameter
Fr_D = Froude number
$\boldsymbol{F}_s$ = surface tension force
H = cylinder height
H_s = initially immersed height of the cylinder in water
S_{ij} = rate of strain tensor
St_D = Strouhal number
U = inflow velocity
We = Weber number
c = color function
$\tilde{c}$ = smoothed color function
f_x = resultant forces per unit height of the cylinder in the flow direction
f_y = resultant forces per unit height of the cylinder in the transverse direction
g = gravitational acceleration
k = air-water interface curvature
p = pressure
t = time
u = velocity
x, y, z = coordinates
ρ = density
μ = dynamic viscosity
σ = coefficient of surface tension
ν_t = eddy viscosity
Δ = cubic root of the volume of a computational cell
μ_τ = wall shear velocity
λ = the second largest (negative) eigenvalue of the tensor related to S_{ij}

Superscripts

n = time level
$*$ = dimensional property

Subscripts

g = air
i,j = coordinate components
l = water

References

[1] Wickramasinghe, D., and Wilkinson, R. H., 1997, “Wakes and Waves Generated by Surface Piercing Cylinders,” DRA Study Report No. EX 3545.
[2] Inoue, M., Baba, N., and Himeno, Y., 1993, “Experimental and Numerical Study of Viscous Flow Field Around an Advancing Vertical Circular Cylinder Piercing a Free Surface,” J. Kansai Soc. Nav. Archit., **220**, pp. 57–64.
[3] Ferrant, P., and Guillern, P. E., 1998, “Interaction of Second Order Wave Packets With a Vertical Cylinder,” *Proceedings of the 8th International Offshore Polar Engineering Conference*, Montreal, Canada, May 24–29, Vol. III, pp. 340–347.
[4] Tseng, M. H., Yen, C. L., and Song, C. C. S., 2000, “Computation of Three-Dimensional Flow Around Square and Circular Piers,” Int. J. Numer. Methods Fluids, **34**, pp. 207–227.
[5] Kawamura, T., Mayer, S., Garapon, A., and Sorensen, L., 2002, “Large Eddy Simulation of a Flow Past a Free Surface Piercing Circular Cylinder,” ASME J. Fluids Eng., **124**, pp. 91–101.
[6] Brackbill, J. U., Kothe, D. B., and Zemach, C., 1992, “A Continuum Method for Modeling Surface Tension,” J. Comput. Phys., **100**, pp. 335–354.
[7] Smagorinsky, J., 1963, “General Circulation Experiments With the Primitive Equations I. The Basic Experiment,” Mon. Weather Rev., **91**, pp. 99–164.
[8] Van Driest, E. R., 1956, “On Turbulent Flow Near a Wall,” J. Aeronaut. Sci., **23**, pp. 1007–1011.
[9] Piomelli, U., Moin, P., and Ferziger, J. H., 1988, “Model Consistency in Large Eddy Simulation of Turbulent Channel Flows,” Phys. Fluids, **31**, pp. 1884–1891.
[10] Szepessy, S., and Bearman, P. W., 1992, “Aspect Ratio and End Effects on Vortex Shedding From a Circular Cylinder,” J. Fluid Mech., **234**, 191–217.
[11] Breuer, M., 1998, “Large Eddy Simulation of the Subcritical Flow Past a Circular Cylinder: Numerical and Modeling Aspects,” Int. J. Numer. Methods Fluids, **28**, pp. 1281–1302.
[12] Rudman, M., 1997, “Volume-Tracking Methods for Interfacial Flow Calculations,” Int. J. Numer. Methods Fluids, **24**, pp. 671–691.
[13] Orlanski, I., 1976, “Simple Boundary Condition for Unbounded Hyperbolic Flows,” J. Comput. Phys., **21**, pp. 251–269.
[14] Heinrich, J. C., Idelsohn, S. R., Oñate, E., and Vionnet, C. A., 1996, “Boundary Conditions for Finite Element Simulations of Convective Flows With Artificial Boundaries,” Int. J. Numer. Methods Fluids, **39**, pp. 1053–1071.
[15] Peskin, C. S., 1977, “Numerical Simulations of Blood Flow in the Heart,” J. Comput. Phys., **25**, pp. 220–252.
[16] Youngs, D. L., 1984, “An Interface Tracking Method for a 3D Eulerian Hydrodynamics Code,” AWRE, Technical Report No. 44/92/35.
[17] Gerrard, J. H., 1966, “The Mechanics of the Formation Region of Vortices Behind Bluff Bodies,” J. Fluid Mech., **25**, pp. 401–413.
[18] Mittal, R., and Balachandar, S., 1995, “Effect of Three-Dimensionality on the Lift and Drag of Nominally Two-Dimensional Cylinders,” Phys. Fluids, **7**(8), pp. 1841–1865.
[19] Jeong, J., and Hussain, F., 1995, “On the Identification of a Vortex,” J. Fluid Mech., **285**, pp. 69–94.
[20] Roshko, A., 1961, “Experiments on the Flow Past a Circular Cylinder at Very High Reynolds Numbers,” J. Fluid Mech., **10**, pp. 345–356.
[21] Wieselsberger, C., 1921, “Neuere Festellungen über die Gesetze des Flüssigkeits-und Luftwiderstands,” Phys. Z., **22**, pp. 321–328.

Extended Angular Range of a Three-Hole Cobra Pressure Probe for Incompressible Flow

Katia María Argüelles Díaz
e-mail: arguelleskatia@uniovi.es

Jesús Manuel Fernández Oro

Eduardo Blanco Marigorta

Fluid Mechanics Group,
University of Oviedo,
Campus de Viesques,
Gijón, 33271 Asturias, Spain

This paper analyzes the operative characteristics of a three-hole cobra type probe especially designed to attain an angular range higher than 180 deg for planar turbulent flows. A new calibration and data reduction method are also introduced, discriminating three different zones inside the angular range of the calibration. This methodology improves the probe performance, extending its operative angular range from the typical ±30 deg to ±105 deg. In addition, the transmission of the uncertainty—from the pressure measurements to the flow variables—is estimated, showing reasonably low levels for the whole angular range. Furthermore, the sensibility of the probe calibration to the Reynolds number and the pitch angle is considered, and the influence of the turbulence level is outlined. Regarding these factors, the probe precision in the extended angular range is found to be similar to that of the traditional range. Finally, the probe is tested in a flow field with large variations of the incidence angle, and the results obtained with the new method are compared to those given by the traditional calibration.

[DOI: 10.1115/1.2969457]

Introduction

The pressure and velocity of incompressible flows can be measured in a plane using three-hole pressure (THP) probes. Typically, these probes have angular ranges around ±30 deg, with slight variations depending on the probe type [1].

Recently, some procedures to extend the operative angular range of THP probes have been developed by the authors [2]. In that research, it was suggested that angular ranges higher than 180 deg could be attained using cobra type probes (Fig. 1), with construction angles between 30 deg and 40 deg. The present paper describes a calibration and a data reduction method employed with a probe of such characteristics in order to obtain the maximum possible angular range.

The cobra type probe operates with a "non-nulling" mode using a direct calibration method. The non-nulling mode keeps the probe position fixed and uses the pressure measured in the probe holes to obtain the velocity magnitude and the flow direction [3]. This method is less time-consuming than the "nulling" mode because there is no need to orientate the probe during the measurements. Also, using fast-response pressure transducers, it is possible to measure unsteady flows and even turbulence [4–6]. Moreover, the direct calibration procedure has the advantage to take into account the specific effects of the probe geometry [7].

Cobra type probes not only exhibit a higher angular range than cylindrical probes, but also they are unaffected by von Kárman's vortex shedding. However, they are less stable to variations in the Reynolds number than cylindrical geometries.

The maximum attainable angular range is limited by double points and duplicated zones in the data reduction equations. A complete description of this topic can be found in Refs. [2,8]. Double points compromise the unequivocal determination of the flow angle (α) and limit the maximum angular range for probes with construction angles higher than 35 deg. On the other hand, the emergence of duplicated zones implies that a single angular interval cannot be directly identified from the pressure measurements. The maximum angular range is limited by the appearance of duplicated zones for probes with construction angles under 35 deg.

Typically, THP probes are designed with a construction angle of 45 deg [9]. In a recent analysis [2], it was found that the highest angular range would be reached in the region where double points and duplicated zone boundaries overlap. To corroborate the theoretical analysis, a 35 deg cobra type probe has been built.

This paper analyzes the performance of the probe using a zone-based data reduction method to extend its operative angular range. Also, the uncertainty transmission and the other effects that influence the probe accuracy are addressed.

Probe Geometry

The geometry of the cobra type probe is shown in Fig. 2. The mechanical design is based on previous experiences in the construction of hot-wire anemometry probes [10].

The probe is composed of three aluminum tubes, with external and internal diameters of 2 mm and 1.5 mm. The frontal section of the probe is thus 6×2 mm^2. The flow Reynolds number is defined with a characteristic length of 6 mm. The construction angle (35 deg) corresponds to the angle between the faces of the central and each lateral hole. The probe holder, normal to the measurement plane, is 6 mm in diameter.

Calibration Method

In a typical calibration procedure, a THP probe is placed on a setup that provides a uniform flow. The probe is axially rotated to change the flow incidence angle [11]. For each position, the pressures in the probe holes (P_1, P_2, and P_3) are stored, together with the position angle (α) and the flow magnitude in the setup. The flow magnitude is usually defined through the static and dynamic pressures (P_s and P_d) at the measurement section with a Pitot-static probe.

The test rig used is a small wind tunnel with an open test section. The probe was positioned from −120 deg to 120 deg with a step-motor driven support, recording data every 5 deg. The base line calibration was conducted at 45 m/s, corresponding to a Reynolds number of 1.8×10^4.

Figure 3 shows the pressure distributions measured in the holes of the probe as a function of the flow angle. They have been

---

Contributed by the Fluids Engineering Division of ASME for publication in the JOURNAL OF FLUIDS ENGINEERING. Manuscript received December 19, 2007; final manuscript received July 2, 2008; published online September 4, 2008. Assoc. Editor Zvi Rusak.

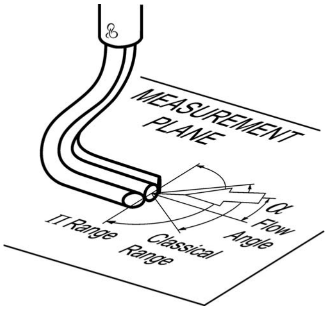

Fig. 1 Three-hole cobra type probe

normalized as typical pressure coefficients: $f_i=(P_i-P_s)/P_d$. Maximum values ($f_i=1$) are obtained for relative zero-incidence flow angles in each hole: 0 deg for the central and +35 deg and −35 deg for the right and left holes, respectively. Minimum values are found when the flow is aligned with the faces of the holes: ±90 deg for the central one ($f_1 \approx -0.8$) and +55 deg and −55 deg for the left and right, holes respectively.

The traditional calibration method defines normalized coefficients (angular coefficient C_α, total pressure coefficient C_{P_0}, and static pressure coefficient C_{P_s}), relating the values registered during the calibration [12].

$$C_\alpha = \frac{P_2 - P_3}{P_1 - 0.5(P_2 + P_3)}$$

$$C_{P_0} = \frac{P_0 - P_1}{P_1 - 0.5(P_2 + P_3)}$$

$$C_{P_s} = \frac{P_0 - P_s}{P_1 - 0.5(P_2 + P_3)} \tag{1}$$

where P_0 and P_s represent the total and static pressures in the setup, and P_1, P_2, and P_3 correspond to the pressures in the central, left, and right holes of the probe, respectively. With the value of these coefficients in each angular position, the calibration curves of the probe are constructed. Once the calibration is completed, those curves are employed to retrieve the direction and the velocity magnitude of the measured flow [13], according to the procedure shown in Fig. 4. In this data reduction procedure, the value of C_α is obtained for each measurement with the pressures recorded in the three holes, using the first expression in Eq. (1). From the C_α calibration curve, the flow angle α is determined (upper graphic in Fig. 4). Once α is known, the values of C_{P_0} and C_{P_S} for that particular angle are obtained from their own calibration curves (bottom graphic). Then, P_0 and P_s are calculated with the second and third expressions in Eq. (1). Finally, the difference between them, i.e., the dynamic pressure, provides the velocity magnitude of the flow.

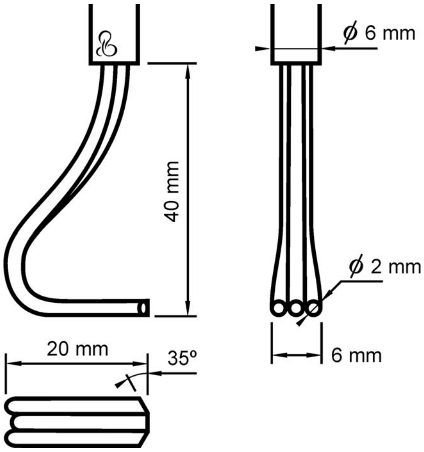

Fig. 2 Sketch of the cobra type probe

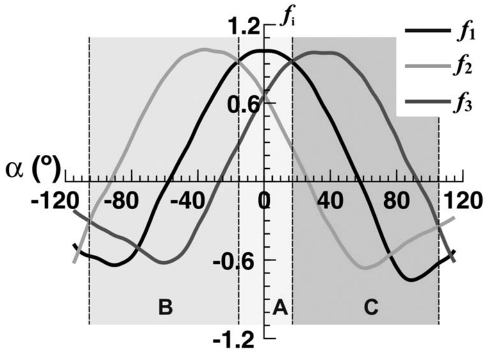

Fig. 3 Pressure coefficient distributions in the holes of the cobra type probe

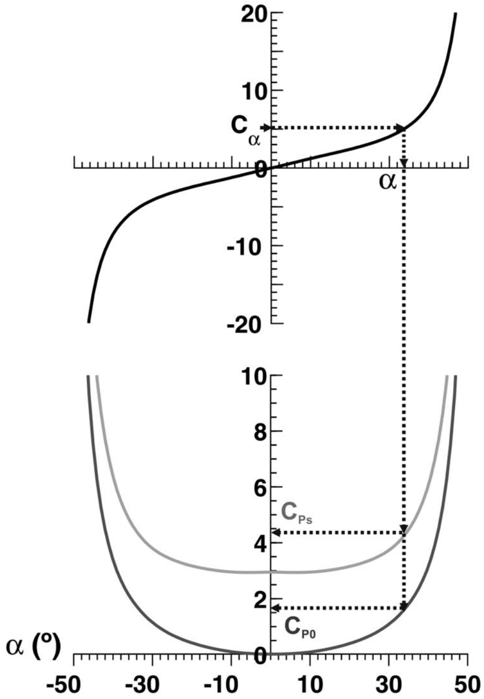

Fig. 4 Traditional calibration coefficients and data reduction procedure

With the traditional calibration, the operative angular range of the probe is about ±48 deg, due to the presence of singular points at −50 deg and +50 deg in the angular coefficient.

To avoid these singularities, a zone-based data reduction method has been defined. This method discriminates three different zones for the angular range of the calibration, which are identified using the pressures measured in the holes. In particular, each zone corresponds to the angular interval where one of the pressures in the holes is higher than the others. Figure 3 shows these three zones: A when P_1 is the highest pressure; B and C when P_2 and P_3 are the highest values, respectively. For each zone, a different angular coefficient is established.

$$C_\alpha = \frac{P_2 - P_3}{P_1 - 0.5(P_2 + P_3)} \quad \text{Zone A} \tag{2}$$

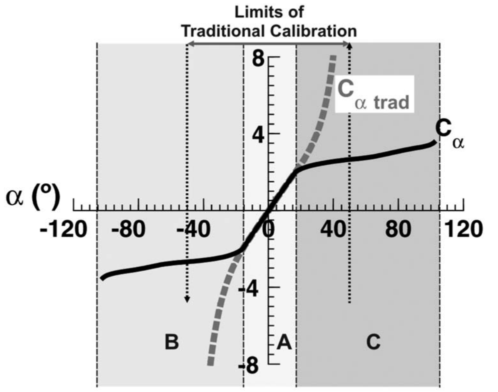

Fig. 5 Angular calibration coefficient: zone-based (solid) and traditional methods (dashed line)

$$C_\alpha = \frac{P_3 - P_2}{P_2 - 0.5(P_1 + P_3)} + 4 \quad \text{Zone B} \tag{3}$$

$$C_\alpha = \frac{P_3 - P_2}{P_3 - 0.5(P_1 + P_2)} - 4 \quad \text{Zone C} \tag{4}$$

Accordingly, both total and static pressure coefficients are also defined as

$$C_{P_0} = \frac{P_0 - P_1}{P_1 - 0.5(P_2 + P_3)} \quad \text{Zone A} \tag{5}$$

$$C_{P_0} = \frac{P_0 - P_1}{P_2 - 0.5(P_1 + P_3)} \quad \text{Zone B} \tag{6}$$

$$C_{P_0} = \frac{P_0 - P_1}{P_3 - 0.5(P_1 + P_2)} \quad \text{Zone C} \tag{7}$$

$$C_{P_s} = \frac{P_0 - P_s}{P_1 - 0.5(P_2 + P_3)} \quad \text{Zone A} \tag{8}$$

$$C_{P_s} = \frac{P_0 - P_s}{P_2 - 0.5(P_1 + P_3)} \quad \text{Zone B} \tag{9}$$

$$C_{P_s} = \frac{P_0 - P_s}{P_3 - 0.5(P_1 + P_2)} \quad \text{Zone C} \tag{10}$$

The angular coefficients (2)–(4) have no singular points in the zones where each one is defined. In addition, they are monotonous functions with the flow angle, allowing an extension of the operative angular range. Other expressions for the angular coefficient could be chosen [2], but the relations previously introduced have been selected because of the similarity to the traditional coefficients. Specifically, the +4 and −4 values in Eqs. (3) and (4) have been added to obtain a continuous function of the angular coefficient throughout the three zones, simplifying its graphic representation and the flow field determination.

Figure 5 compares the angular coefficient defined through Eqs. (2)–(4) (solid line) with the traditional one (dashed line). Obviously, both coefficients are equal in Zone A. It can be observed that, using the traditional calibration, this cobra type probe provides an important angular range (±48 deg), notably higher than typical ranges (±30 deg) found in the literature for THP probes. However, with the zone-based data reduction method, the angular range is extended up to ±105 deg. In this case, the limit is due to the appearance of duplicated zones and not to the emergence of double points. For instance, when the flow angle is higher than 105 deg, $P_2 > P_1 > P_3$, which is the same condition already fulfilled in Zone B. As a result, this external zone cannot be distinguished from the previous Zone B, and thus the angular range has to be limited to ±105 deg.

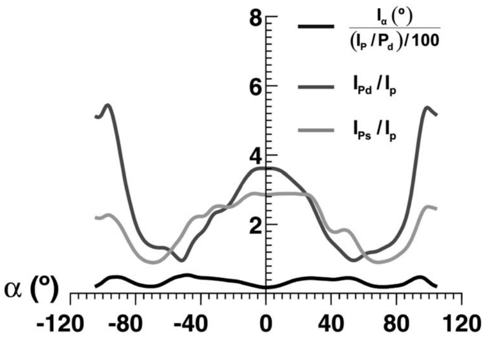

Fig. 6 Uncertainty of the flow variables

Uncertainty Transmission

In this section, the uncertainty transmitted from the pressures measured in the holes of the cobra type probe to the flow variables is estimated. This uncertainty is calculated based on the method proposed by Kline [14] (further details can be found in Ref. [2]):

$$I_\alpha = \frac{I_p}{P_d} \cdot \frac{\sqrt{(f_3 - f_2)^2 + (f_1 - f_3)^2 + (f_2 - f_1)^2}}{f_1'(f_3 - f_2) + f_2'(f_1 - f_3) + f_3'(f_2 - f_1)} \tag{11}$$

$$I_{P_d} = I_p \cdot \frac{\sqrt{(f_3' - f_2')^2 + (f_1' - f_3')^2 + (f_2' - f_1')^2}}{f_1'(f_3 - f_2) + f_2'(f_1 - f_3) + f_3'(f_2 - f_1)} \tag{12}$$

$$I_{P_s} = I_p \cdot \frac{\sqrt{(f_2 f_3' - f_3 f_2')^2 + (f_3 f_1' - f_1 f_3')^2 + (f_1 f_2' - f_2 f_1')^2}}{f_1'(f_3 - f_2) + f_2'(f_1 - f_3) + f_3'(f_2 - f_1)} \tag{13}$$

In these expressions, I_α denotes the uncertainty of the flow angle, while I_{P_d} and I_{P_s} are the uncertainties of the dynamic and static pressures, respectively. I_p is the uncertainty of the pressure measured by the transducers, which is supposed to be the same for the three holes of the probe. $f_i'(i=1,2,3)$ are the derivatives of the pressure coefficients f_i with respect to the flow angle. Equations (11)–(13) show that the uncertainty transmission to the final results depends only on the pressure coefficient distributions. Furthermore, it has been found that the uncertainty, although different for each specific geometry, is independent of the data reduction procedure employed.

Figure 6 shows the uncertainty results for this cobra type probe, estimated from expressions (11)–(13) with the pressure coefficients shown in Fig. 3. It represents the angle uncertainty (black line) and the uncertainties of the dynamic (dark gray line) and static (light gray line) pressures. The uncertainty of the flow angle is expressed as a percentage of the uncertainty in the pressure measurement I_p relative to the dynamic pressure P_d. Both dynamic and static pressure uncertainties are referenced to the uncertainty in the pressure measurement I_p. These latter uncertainties are from two to four times higher than in the case of cylindrical probes [2]. However, since the pressure uncertainty of typical transducers is quite low (from 0.1% to 0.25% of the nominal range), the absolute uncertainty levels are reasonably small. Moreover, the uncertainty distributions shown in Fig. 6 are the same as those of the traditional calibration in the common angular interval.

The angle uncertainty does not exceed 0.6 deg for every 1% of I_p/P_d in the whole angular range. In the case of zero-incidence flows, this uncertainty is barely 0.2 deg for every 1% of I_p/P_d. Also, the uncertainty levels for both dynamic and static pressures are, respectively, 3.6 and 2.8 times I_p. The dynamic pressure uncertainty reaches the maximum values around ±95 deg, while the

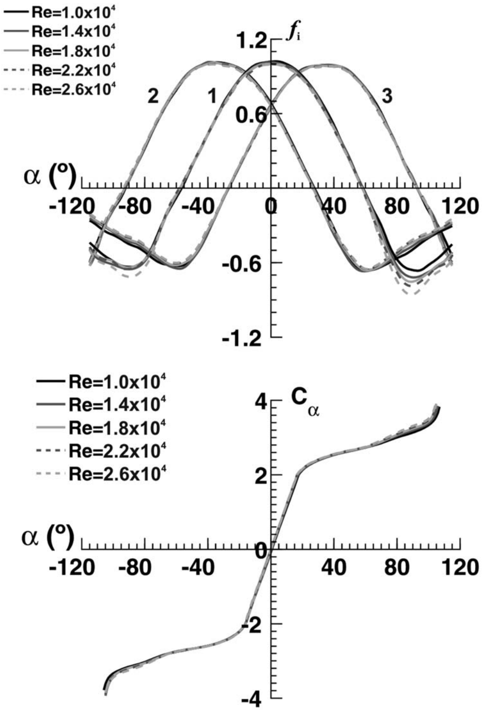

Fig. 7 Pressure and angular coefficients for different flow Reynolds numbers

minimum values are found at ±50 deg. The static pressure uncertainty has its maximum at zero-incidence flow, with the minimum values around ±70 deg, which are progressively increased toward the limits of the operating range.

Reynolds Number Effects

Previous sections described a zone-based procedure to improve the angular range of a cobra type probe. Also, the uncertainty transmission from the measurements to the results has been analyzed to characterize the probe accuracy. However, the major source of error for THP probes derives from the difference between the velocity adopted in the calibration and the measured velocity.

The analysis of the previous sections was conducted assuming that the pressure coefficient distributions are independent of the velocity magnitude, i.e., they are exclusively a function of the incidence angle α. Nevertheless, this is true only for a certain Reynolds number range, which even depends on the particular geometry of the probes. To outline the sensibility of the probe calibration to Reynolds number variations, different flow velocities were tested to obtain the pressure coefficients.

In the calibration setup, yaw angles ranging from −120 deg to 120 deg were considered every 5 deg. The measurements were obtained for five different velocities, from 25 m/s to 65 m/s, corresponding to Reynolds numbers from 1.0×10^4 to 2.6×10^4. Figure 7 shows the pressure coefficient distributions measured for the five Reynolds numbers. The figure includes all the angular coefficient distributions obtained with the zone-based method. The effect of the flow velocity is practically negligible for yaw angles within ±70 deg. The most significant variations are observed in the central hole pressure coefficient, when the yaw angle is beyond ±75 deg. For these external zones, the f_1 values decrease as the Reynolds number increases, with maximum variations around ±90 deg.

Data corresponding to Reynolds numbers of 1.0×10^4, 1.4×10^4, 2.2×10^4, and 2.6×10^4 were reduced with the zone-based method using the calibration of an intermediate Reynolds number

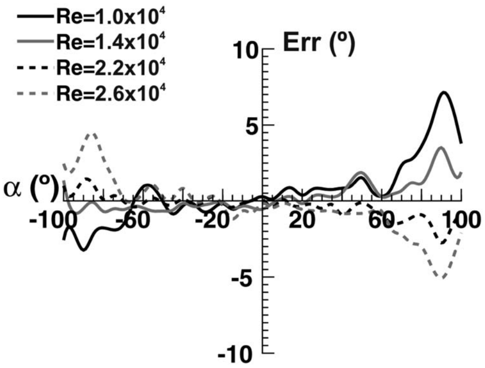

Fig. 8 Errors in the estimation of the flow angle using a reference calibration of Re=1.8×10^4

(1.8×10^4). The results have been compared with the real values to estimate the error introduced. Figure 8 represents the absolute error in the determination of the angle (Err) as a function of the real flow angle (α). As expected, the error increases with the difference between calibration and measured velocities. For centered intervals, ±40 deg, the error is less than 1 deg. It maintains reasonably low values (under 2.5 deg) from ±40 deg to ±75 deg, but it increases severely beyond that limit (where the largest variations of the pressure coefficients were observed in Fig. 7).

It is good practice to complete several calibrations for different Reynolds numbers when there is a large variation in the velocity magnitude (or high precision is required). Figure 8 shows a progressive enlargement of the errors, increasing with the deviation in the velocity magnitude from the base line calibration. Assuming a linear dependence between them (at least in averaged terms), an alternative methodology has been introduced, interpolating different calibrations in order to obtain more accuracy in the flow variables.

The results of this procedure are illustrated in Fig. 9. It shows the errors when the data reduction is done interpolating between calibrations at extreme Reynolds numbers: 1.0×10^4 and 2.6×10^4. In ±45 deg interval, the error is now reduced to values under 0.6 deg. External ranges present higher values but not exceeding 2 deg of absolute error. Moreover, the maximum relative error introduced for the determination of the velocity magnitude is 5%, with a 4% error in the static pressure measurement.

Pitch Angle and Turbulence Level Effects

Another error is caused by the deviation of the flow from the probe measurement plane. It is considered that THP probes provide accurate results if the pitch angle β (angle between the flow and the probe measurement plane) does not exceed 10 deg or

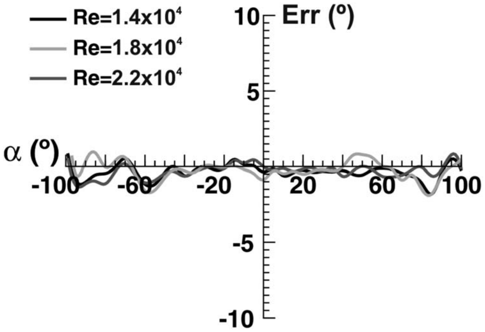

Fig. 9 Errors in the estimation of the flow angle when interpolating between two calibrations at different Reynolds numbers

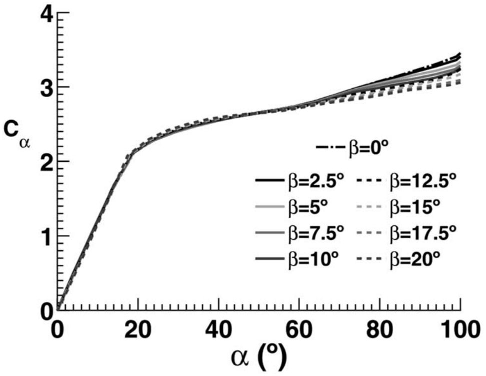

Fig. 10 Influence of the pitch angle β on the angular coefficient

12 deg (see Refs. [1,12]). In addition, it is to be expected that the pitch angle influence increases with the yaw angle. Then, its effect would be more evident in the extended range of the zone-based method.

A set of tests has been carried out to characterize this influence. The angular coefficient has been obtained for the whole calibration range varying the pitch angle from 0 deg to 20 deg every 2.5 deg. All the tests were conducted for the base line Reynolds number of 1.8×10^4.

Figure 10 shows these angular coefficients. Due to the symmetry of the results, only the positive values of the yaw angle have been plotted. From 0 deg to 60 deg, the angular coefficients reveal only small differences even for pitch angles as high as 20 deg. From 60 deg onwards, the difference becomes more evident, increasing with both pitch and yaw angles.

In order to quantify the effect of the pitch angle, these measurements have been used to determine the error introduced when the zero pitch calibration is employed with flows of nonzero pitch angle. Figure 11 shows, for each pitch series, the difference between the yaw angle obtained using the zone-based method and the real yaw angle set in the calibration setup. This allows a better appreciation of the pitch angle influence.

For yaw angles between 0 deg and 45 deg, the error remains below 1 deg if the pitch angle is smaller than 10 deg. For yaw angles above 45 deg, the pitch angle should be kept below 5 deg to obtain the same accuracy. Pitch angles above 15 deg give too much error even for low yaw angles, although up to 50 deg the error remains below 3 deg, for β as high as 20 deg.

The effect of the turbulence level is also closely related to the pitch angle influence. Cobra type probes are less sensitive to turbulence than the three-hole cylindrical probes, because they develop bluff-body separations instead of a boundary-layer detachment over a convex surface. Nevertheless, there are two effects of the turbulence level over the probe accuracy: the error induced over the pressure value and the flow angle deviation (see Refs. [9,15]). The first effect is considered low if the turbulence intensity is not too high; Chue [15] reported a total pressure change of only 2% with a turbulence intensity of 20%. Also, this effect can be taken into account using fast-response transducers (a correction of the line-cavity system can be needed [4–6]). On the other hand, the flow angle deviation can only be partially determined with fast-response transducers because fluctuations occur in both yaw and pitch angles.

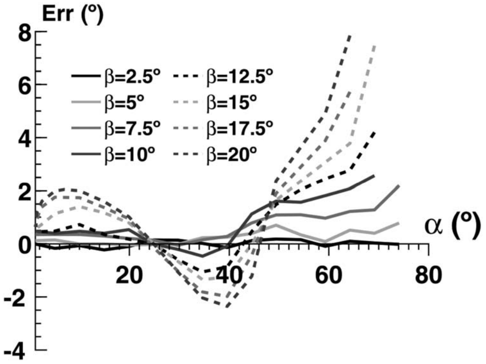

Fig. 11 Errors in the yaw angle determination with different pitch angles

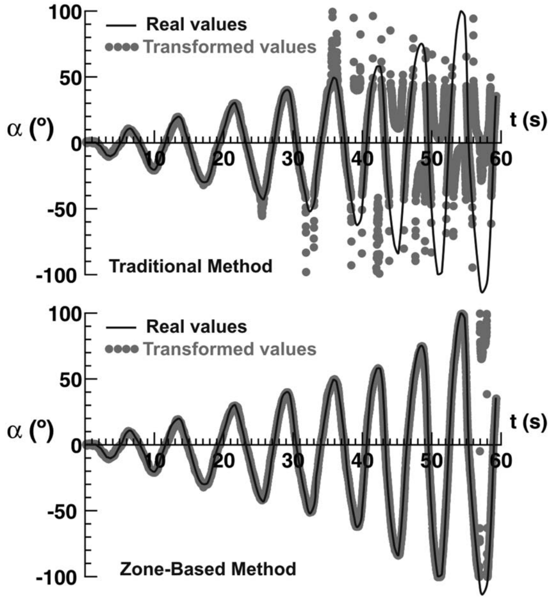

Fig. 12 Flow angle measurements obtained with the traditional calibration and with the zone-based data reduction method

No specific tests have been carried out to analyze the influence of the turbulence level on this cobra type probe. However, concerning the deviation of the flow angle, a relation could be assumed between the turbulence intensity and a certain amplitude of angular oscillations. In particular, Walsche et al. [16] argued that 15 deg correspond to quite a strong intensity, about 40%. Therefore, it is expected for the probe to be rather insensitive to turbulence in the range of the traditional calibration: An amplitude of 10 deg has been analogous to a turbulence level around 25%. On the other hand, if good accuracy has to be maintained for the whole extended angular range, the turbulence level of the flow should be lower (an amplitude of 5 deg, about 10%).

Measurement Test

The performance of the cobra type probe has been tested in a flow field with large variations of the incidence angle.

The probe was mounted in the calibration setup on a support able to generate an oscillating angular motion. The flow velocity, maintained constant, was measured with a Pitot-static probe. The angular oscillation was continuously measured using a goniometer of 0.25 deg precision. The amplitude of the oscillations was progressively increased from 0 deg to ±120 deg. The pressure values of the probe holes were acquired with a frequency of 100 Hz during 60 s, together with the angular position and the flow velocity. The flow variables were calculated using both traditional and zone-based data reduction methods.

The retrieved flow angles are shown in Fig. 12 compared to the real values. Fluctuations in the flow direction within ±40 deg are accurately described by both methods. When the variations are beyond those angles, the traditional calibration fails, providing an incorrect value of the flow angle. On the contrary, the zone-based method measures correctly the variations of the flow angle of up to ±100 deg. Beyond this limit, erratic values are also obtained.

Conclusions

A three-hole cobra type probe with a construction angle of 35 deg has been designed and built to measure flow fields with strong variations of the incidence angle.

A zone-based method has been defined for the data reduction procedure, extending the operative angular range from the ±48 deg of the traditional calibration to ±105 deg. The uncertainty transmission has been analyzed, and the values in the extended angular range have been found to be similar to those in the traditional range.

The effect of the Reynolds number on the probe performance has also been studied. A methodology, based on the interpolation between two calibrations for different Reynolds numbers, was proposed. It has been shown that this strategy reduces the errors even in the extended angular range, to 2 deg in the angle, 5% in the velocity magnitude, and 4% in the static pressure.

In addition, the influence of pitch angle deviations has been tested. The results show that pitch angles below 10 deg are acceptable in the traditional range, while 5 deg is the maximum admissible deviation to obtain the same accuracy in the extended range.

Finally, a measurement test was conducted in a flow with large variations in the incidence angle. It is shown that the traditional calibration provides accurate results of up to ±40 deg, while the zone-based method enlarges the attainable span more than two times, reaching up to ±100 deg.

Acknowledgment

This work was supported by the Research Project "Effect of the volute geometry of centrifugal pumps on the fluid-dynamic perturbations due to rotor-stator interaction," Ref. No. DPI-2006-15638-C02-01, MEC.

Nomenclature

C_α = angular coefficient
C_{P_0} = total pressure coefficient
C_{P_s} = static pressure coefficient
Err = absolute error (deg)
f_i = pressure coefficient, $i=1,2,3$
I_α = angle uncertainty (deg)
I_P = pressure uncertainty (Pa)
I_{P_d} = dynamic pressure uncertainty (Pa)
I_{P_s} = static pressure uncertainty (Pa)
P_1 = central hole pressure measurement (Pa)
P_2 = left hole pressure measurement (Pa)
P_3 = right hole pressure measurement (Pa)
P_d = dynamic pressure (Pa)
P_0 = total pressure (Pa)
P_s = static pressure (Pa)
Re = Reynolds number
t = time (s)

Greek Letters

α = flow angle (yaw angle) (deg)
β = pitch angle (deg)
δ = construction angle of the probe (deg)

References

[1] Dudziniski, T. J., and Krause, L. N., 1969, "Flow-Direction Measurement With Fixed-Position Probes," NASA TM X-1904.

[2] Argüelles Díaz, K. M., Fernández Oro, J. M., and Blanco Marigorta, E., 2008, "Direct Calibration Framework of Triple-Hole Pressure Probes for Incompressible Flow," Meas. Sci. Technol., **19**, 075401.

[3] Wuest, W., 1967, "Measurement of Flow Speed and Flow Direction by Aerodynamic Probes and Vanes," AGARD Conf. Proc., **32**, pp. 373–426.

[4] Hooper, J. D., and Musgrove, A. R., 1997, "Reynolds Stress, Mean Velocity, and Dynamic and Static Pressure Measurement by a Four-Hole Pressure Probe," Exp. Therm. Fluid Sci., **15**, pp. 375–383.

[5] Guo, Y., and Wood, D. H., 2001, "Instantaneous Velocity and Pressure Measurements in Turbulent Mixing Layers," Exp. Therm. Fluid Sci., **24**, pp. 139–150.

[6] Chen, J., Haynes, B. S., and Fletcher, D. F., 2000, "Cobra Probe Measurements of Mean Velocities, Reynolds Stresses and Higher-Order Velocity Correlations in Pipe Flow," Exp. Therm. Fluid Sci., **21**, pp. 206–217

[7] Treaster, A. L., and Yocum, A. M., 1979, "The Calibration and Application of Five-Hole Probes," ISA Trans., **18**, pp. 23–34.

[8] Argüelles Díaz, K. M., Fernández Oro, J. M., and Blanco Marigorta, E., 2008, "Three-Hole Pressure Probes at Large," *Proceedings of the 19th Symposium on Measuring Techniques for Transonic and Supersonic Flows in Cascades and Turbomachines*, Belgium.

[9] 2007, *Springer Handbook of Experimental Fluid Mechanics*, C. Tropea, A. L. Yarin, and J. F. Foss, eds., Springer-Verlag, Berlin.

[10] Blanco, E., Ballesteros, R., and Santolaria, C., 1998, "Angular Range and Uncertainty Analysis of Non-Orthogonal Crossed Hot Wire Probes," ASME J. Fluids Eng., **120**, pp. 90–94.

[11] Lewis, W. E., 1966, "Fixed-Direction Probes for Aerodynamic Measurements," Proc. Inst. Mech. Eng., **180**, pp. 141–152.

[12] Bryer, D. W., and Pankhurst, R. C., 1971, "Pressure-Probe Methods for Determining Wind Speed and Flow Direction," National Physical Laboratory, Her Majesty's Stationary Office (HMSO), Teddington (London), England.

[13] Sumner, D., 2002, "A Comparison of Data-Reduction Methods for a Seven-Hole Probe," ASME J. Fluids Eng., **124**, pp. 523–527.

[14] Kline, S. J., and McClintock, F. A., 1953, "Describing Uncertainties in Single Sample Experiments," Mech. Eng. (Am. Soc. Mech. Eng.), **75** pp. 3–8.

[15] Chue, S. H., 1975, "Pressure Probes for Fluid Measurement," Prog. Aerosp. Sci., **16**(2), pp. 147–223.

[16] Walsche, D. E., and Garner, H. C., 1960, "Usefulness of Various Pressure Probes in Fluctuating Low Speed Flows," Brit. ARC 21714.

Pressure Drop Through Anisotropic Porous Mediumlike Cylinder Bundles in Turbulent Flow Regime

Tongbeum Kim
Assistant Professor
Thermofluid Division of MOE Key Laboratory for Strength and Vibration,
School of Aerospace,
Xi'an Jiaotong University,
28 West Xianning Road, Xi'an 710049, P.R.C.
e-mail: tongbeum@gmail.com

Tian Jian Lu
Professor
MOE Key Laboratory for Strength and Vibration,
Xi'an Jiaotong University,
28 West Xianning Road,
Xi'an 710049, P.R.C.

Pressure drop through anisotropic porous mediumlike cylinder bundles is experimentally examined in turbulent flow regime. Three porosities, $\varepsilon=0.66$, 0.82, and 0.90, are considered. The flow blockage by the cylinder bundles is varied, with the yaw angle (α) used as an anisotropic measure. When the yaw angle is fixed while the porosity is varied, the pressure drop behaves as predicted by the force balance model, consistent with the classic observation: The pressure drop is proportional to the square of the flow velocity with the empirical proportionality as a function of $(1-\varepsilon^{1/2})/\varepsilon^2$ obtained from the force balance model compared to that of $(1-\varepsilon)/\varepsilon^3$ from the hydraulic radius theory. On the other hand, for a given porosity, topological anisotropy of the cylinder bundles causes the sinusoidal response of the pressure drop to the variation of yaw angle. At $\alpha=0$ deg with a 60 deg period, the lowest pressure drop occurs from the most open configuration of the cylinder bundle whereas the largest flow blockage at $\alpha=30$ deg causes the highest pressure drop. This variation appears to result from an increase in the drag coefficient of each cylinder element in a harmonic manner.
[DOI: 10.1115/1.2969454]

Introduction

Analyzing pressure drop in porous media has long been a popular research subject for its importance in civil and chemical engineering applications including flow through soil grains and various filters [1–6]. Typically, the porous media are assumed to be isotropic. At the microscopic level, the size of individual pores often differs spatially. However, at the macroscopic level, the pores are assumed to be statistically and volumetrically isotropic. This assumption may be reasonable if the pores are randomly distributed within the bulk of the porous media.

Numerous efforts made hitherto have led to a multitude of comprehensive studies on pressure drop across porous media (see, e.g., Trussell and Chang [1]). Following the well-known Darcy experiment in 1856 for pressure drop through a unidirectional (isotropic) porous medium, the so-called "Darcy flow" has been extended for higher flow velocity regimes such as Forchheimer, transitional, and turbulent regimes. This is due to the fact that Darcy's empirical correlation is only valid in a very low flow velocity (creeping flow) regime, i.e., $\mathrm{Re}_{\mathrm{dp}}<1$, where dp is representative pore diameter.

It has been well established that pressure drop through an isotropic porous medium is dependent on the porosity of the medium and its representative pore size. Moreover, the pressure drop is proportional to flow velocity in the Darcy flow regime and its square in the turbulent flow regime. For isotropic porous media, it is nonetheless not a function of flow orientation to the porous medium. Reynolds numbers for flow through porous media such as soil and sand are often inhibited by low porosity values, resulting in, therefore, Darcy flow. On the other hand, flow through highly porous media (e.g., open-celled metallic foams with random cellular structures and lattice-frame materials having periodic topologies) with porosity values as high as 0.9 falls typically in the turbulent regime. For turbulent flow, with viscous contribution neglected, pressure drop ΔP through length ΔL of an isotropic porous medium can be expressed as

$$\frac{\Delta P}{\Delta L}=\beta V^2 \tag{1}$$

where V is the discharge velocity through the porous medium and β is an empirical constant.

When flow through anisotropic porous media such as a high porosity lattice-frame material at high Reynolds numbers is of concern [7], the orientation of flow plays an important role in determining pressure drop and heat transfer characteristics. Depending on the flow orientation, up to 200% more pressure drop was caused from the most closed configuration compared to the most open one [7]. However, a literature search reveals that there exists no study on the systematic variation of flow orientation and its influence on pressure drop.

The present study aims to study experimentally the effect of flow orientation on pressure drop through high porosity anisotropic media in turbulent regime. To this end, flow through banks of cylinders (assumed to be a porous medium) whose flow orientation is allowed to systematically change for three selected porosities, $\varepsilon=0.66$, 0.82, and 0.90, is considered with Reynolds number (Re_d) based on cylinder element diameter varying from 5.0×10^2 to 5.0×10^3. In addition, information regarding the pressure drop in circular bundles composed of cylinder banks as a function of cross flow orientation is applicable to many heat exchanger applications. Traditionally, the flow direction of the cross flow to such heat exchangers is assumed to be known and invariant. However, in many cases, it may vary, leading to the change of pressure drop patterns across the heat exchangers. This paper also addresses this problem.

Experimental Details

Test Facility and Models. Banks of cylinder models were fabricated using parallel and periodically arranged Perspex tubes glued onto two circular disks as endwalls. Figure 1(*a*) shows schematically the cylinder bundle and its unit cell. The unit cell has an equilateral triangular configuration, with S_X, S_Y, and S_{XY} denoting the longitudinal, transverse, and equilateral pitches, respectively.

As argued by Fowler and Bejan [8] and Kim et al. [9], for a given flow orientation, the use of porosity may provide a better parametrized view of the pressure drop behavior in the cylinder bundle (as a porous medium) if the porosity is varied by changing the cylinder diameter while the spacing between the cylinder elements is fixed. Under this condition, the porosity can thence be used as a reference parameter, even though the idea of porosity stems from volumetric considerations. The porosity, ε (void fraction), is defined based on the configuration of Fig. 1(*a*) as

---

Contributed by the Fluids Engineering Division of ASME for publication in the JOURNAL OF FLUIDS ENGINEERING. Manuscript received October 17, 2007; final manuscript received June 10, 2008; published online September 4, 2008. Assoc. Editor: James A. Liburdy.

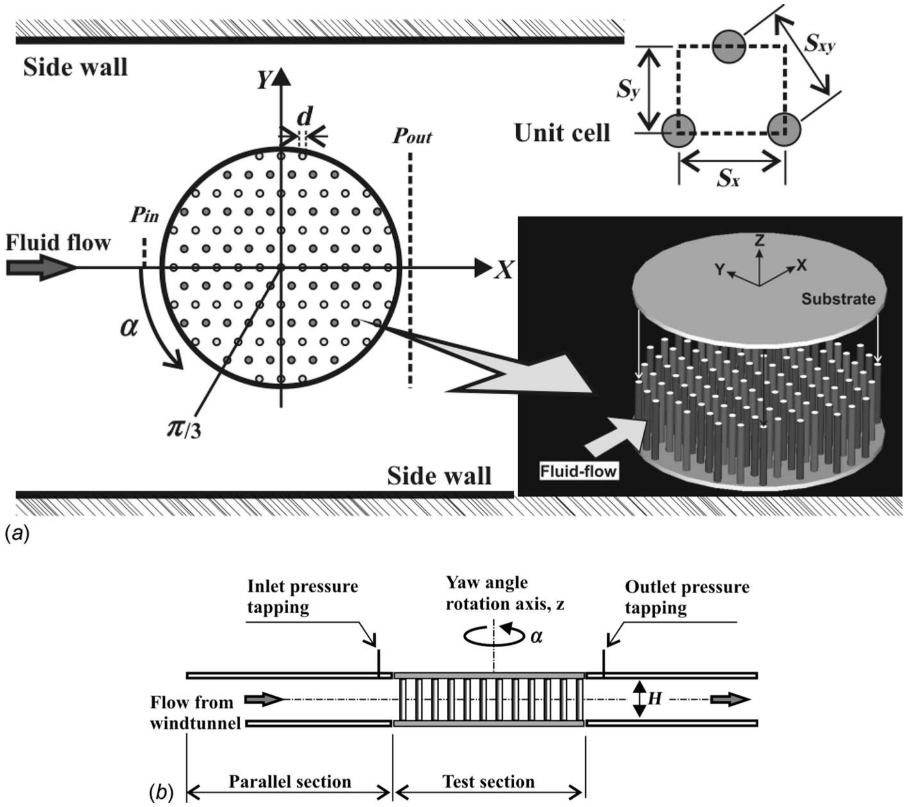

Fig. 1 Schematics of test rig used for pressure drop measurement: (*a*) plan view; (*b*) side view

$$\varepsilon = 1 - \frac{\pi}{4\cos(\pi/6)}\left(\frac{d}{S_{XY}}\right)^2 \approx 1 - 0.907\left(\frac{d}{S_{XY}}\right)^2 \tag{2}$$

where d is the cylinder diameter and S_{XY} is the centerline distance between cylinders (equilateral pitch). To change the porosity, S_{XY} is set to be constant while the diameter of the cylinder elements is varied. Three test samples with different porosities (0.66, 0.82, and 0.90) were fabricated. The geometrical parameters of each test sample are summarized in Table 1.

A side view of the test rig is presented in Fig. 1(*b*). Flow in the test section is supplied by a blowdown wind tunnel (not shown in Fig. 1(*b*)). The cylinder bundle disk consisting of 110 cylinder elements distributed according to the parameters in Table 1 is placed at the center of a rectangular flow channel (0.2 m (width) × 0.026 m (height)), with its diameter equal to half of the channel width. The disk axis coinciding with the z-axis is connected to a rotary table, so that the yaw angle (α) of the cylinder bundle can be systematically varied.

Velocity and Pressure Measurements. For pressure drop measurement, pneumatic pressure tappings were installed at both the inlet and outlet of the cylinder bundle. Two tappings were used to measure the inlet pressure (averaged later) while another ten tappings were transversely distributed at the outlet of the test sample with 1.0Sy interval, as illustrated in Fig. 1(*a*). The pressure tappings were then connected to a differential pressure transducer.

Reynolds number is defined based on the cylinder diameter d as

$$\mathrm{Re}_d = \frac{\rho U_m d}{\mu} \tag{3}$$

where U_m is the mean inlet flow velocity, ρ is the air density, and μ is the air viscosity.

The uncertainties associated with the measurements of static pressure and flow velocity were estimated using a method reported in Coleman and Steele [10] (based on 20:1 odds) and found to be within 2.9% and 1.8%, respectively. Note that only random errors were considered and it was assumed that, with careful calibrations, the bias (systematic) errors could be minimized.

Force Balance in Cylinder Bundles

Analytically, for flow passing through a cylinder bundle, the drag force experienced by each cylinder element may be expressed by considering force balance in a control volume (Fig. 2). Consideration of force balance between flow and cylinder elements in the control volume ($=l_x l_y l_z$) leads to [1]

Table 1 Detailed parameters of cylinder bank models

Porosity (ε)	Yaw angle (α, deg)	Cylinder diameter (d, mm)	Cylinder length (H, mm)	Aspect ratio (H/d)	Cell pitches (mm) S_X	S_Y	S_{XY}	Spacing ratio (S_{XY}/d)
0.90	0 deg ≤ α ≤ 60 deg with 5 deg increment	3.0	26	8.67	7.79	9.0	9.0	3.0
0.82		4.0		6.5				2.25
0.66		5.5		4.7				1.64

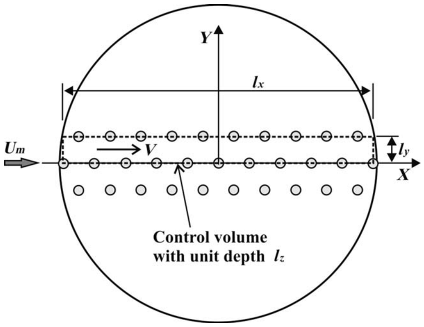

Fig. 2 Control volume at the central part of the circular cylinder bank for the force balance analysis

$$-\frac{\partial p}{\partial x}l_x l_y l_z - C_d\frac{1}{2}\rho V^2 A N = 0 \tag{4}$$

where C_d is the drag coefficient, V is the discharge velocity in the control volume, A is the frontal area of each cylinder element, and N is the number of cylinders in the control volume. The discharge velocity (V) takes account for the reduced flow area by the increased flow velocity due to the cylinder elements in the control volume as $V=U_m/\varepsilon$, where ε is the porosity defined in Eq. (2). The frontal area of each cylinder element and the number of cylinder elements in the control volume are $A=l_z d$ and $N=((4/(\pi d^2))(1-\varepsilon)l_x l_y$, respectively.

Substitution of these into Eq. (4) yields

$$-\frac{\partial p}{\partial x} = C_d\frac{2\rho}{\pi d}\left(\frac{1-\varepsilon}{\varepsilon^2}\right)U_m^2 \tag{5}$$

Let

$$\beta' = C_d\frac{2\rho}{\pi d}\left(\frac{1-\varepsilon}{\varepsilon^2}\right) \tag{6}$$

denote the proportionality coefficient, Equation (5) for pressure drop across a cylinder bundle can then be rewritten as

$$-\frac{\partial p}{\partial x} = \beta' U_m^2 \tag{7}$$

which has the same format as Eq. (1) but for the detailed expression of β' relative to β. It should also be noted that the effect of porosity on the empirical constants in quadratic terms (nonlinearity factor) obtained from the hydraulic radius theory (see Ref. [1]) and from the force balance model are distinguished: $(1-\varepsilon)/\varepsilon^3$ versus $(1-\varepsilon)/\varepsilon^2$, respectively.

Discussion of Results

Overall Pressure Drop Behavior With Porosity Variation at High Reynolds Numbers. Figure 3(*a*) plots pressure drop through the porous mediumlike cylinder bundle as a function of flow velocity. Three different porosity cases (ε=0.66, 0.82, and 0.90) are included for α=0 deg (as configured in Fig. 2). Clearly, as the pressure drop is proportional to the square of flow velocity, the flow is in the turbulent regime.

At a fixed Reynolds number, a higher pressure drop is observed from a lower porosity sample, indicating a larger value of the proportional constant (slope (β') in Eq. (7)). Based on the force balance model, the proportional constant is calculated for each sample and plotted in Fig. 3(*b*) as a function of Reynolds numbers. The proportional constant increases in value as the porosity is decreased but is approximately independent of the Reynolds number in the turbulent range of $1.0\times10^3 \leqslant \mathrm{Re}_d \leqslant 5.0\times10^3$. On the other hand, when $\mathrm{Re}_d \sim 1.0\times10^3$ in the present study, transition from laminar flow appears to take place. This transitional Reynolds number is consistent with the data reported in Refs. [9,11].

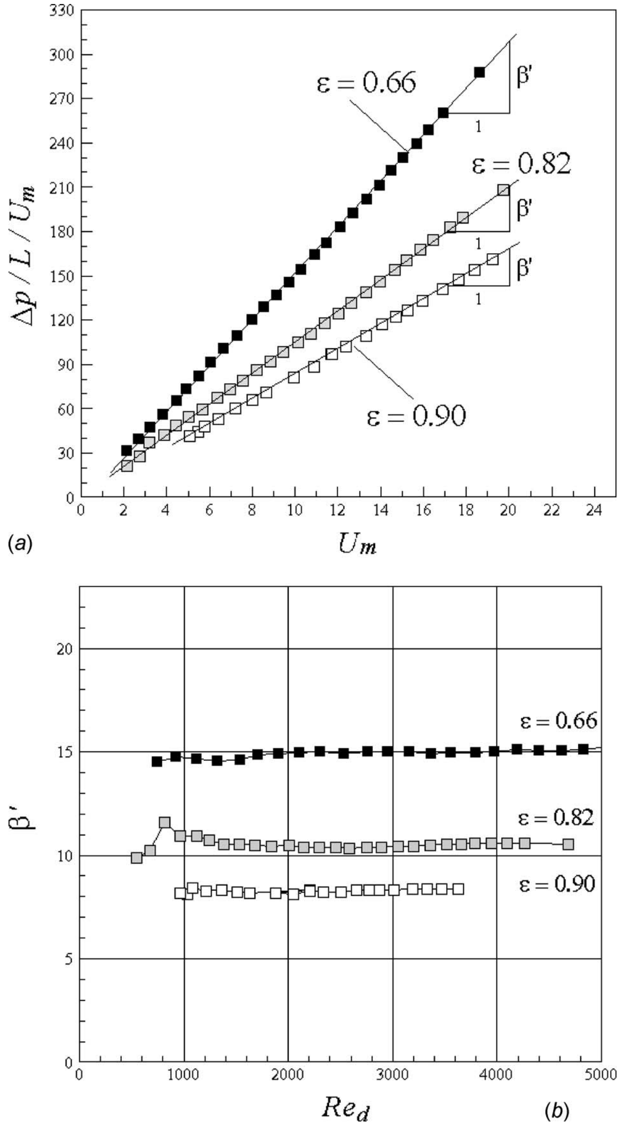

Fig. 3 Measured pressure drop and empirical constants in Eq. (6) for three porosities: (*a*) U_m versus $\Delta p/L/U_m$; (*b*) Re_d versus β'

Applicability of Force Balance Based Model. Equation (6) suggests that the proportionality constant β' depends on the porosity of the cylinder bank according to $(1-\varepsilon)/\varepsilon^2$. However, in Eq. (6), β' is a function of not only porosity ε but also cylinder diameter d, which changes as ε is varied. In the present experiment, to decrease porosity, the cylinder diameter was increased while the equilateral pitch, S_{XY} remained unchanged. Hence, with Eq. (2), the empirical constant β' can be rewritten as

$$\beta' = C_d\left(\frac{\rho}{\sqrt{\pi\cos(\pi/6)}}\Big/ S_{XY}\right)\left(\frac{(1-\varepsilon)^{1/2}}{\varepsilon^2}\right) \tag{8}$$

With S_{XY} fixed, Eq. (8) confirms that the proportional constant is mainly a function of the porosity of each sample, showing a linear trend with the porosity product, $(1-\varepsilon^{1/2})/\varepsilon^2$ (Fig. 4), with a least squares deviation of R^2=0.9953. This implies that the drag coefficient C_d of individual cylinder elements is constant regardless of the difference in porosity amongst different samples. Ac-

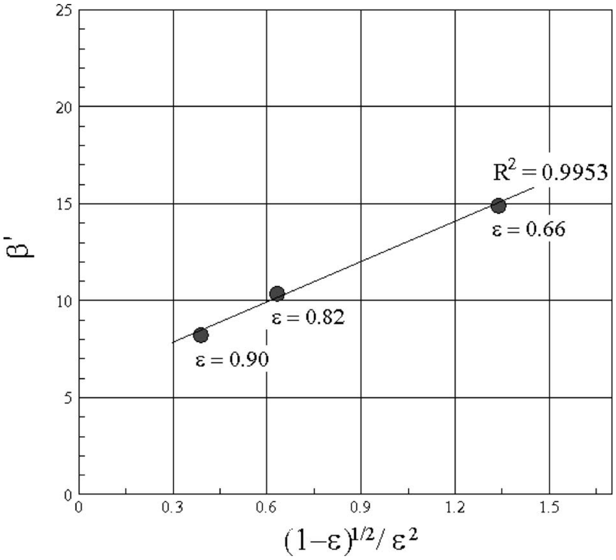

Fig. 4 Applicability of the force balance based model

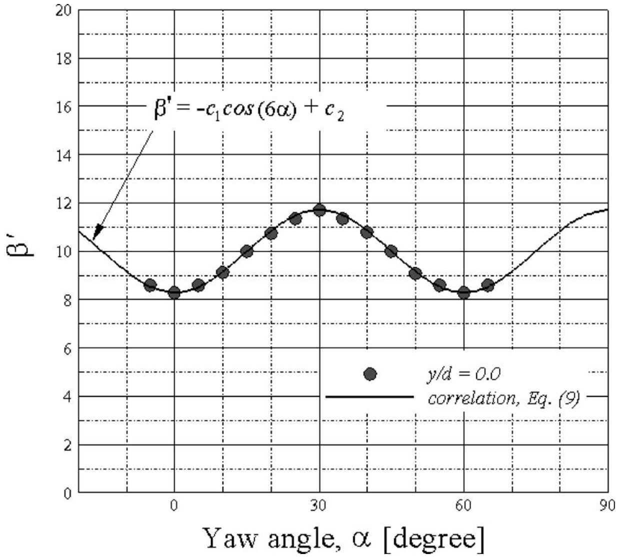

Fig. 5 Variation of empirical constant (β') with yaw angle of the cylinder bundles for $\varepsilon=0.90$ at $Re_d=2.5\times10^3$

cording to Gu and Sun [12] who classified flow pattern on three circular cylinders arranged in equilateral triangular configuration, the three cases in the present study fall separately into small spacing $S_{XY}/d=1.7$ (for $\varepsilon=0.66$), transition spacing $S_{XY}/d=2.2$ (for $\varepsilon=0.82$), and medium spacing $S_{XY}/d=2.5$ (for $\varepsilon=0.90$). Test data on drag coefficient at "zero" yaw angle [12] showed that cylinder elements experiencing wake shed from upstream cylinders had similar values regardless of the range of spacing, supporting the present observation.

Observation of Pressure Drop Variation With Yaw Angle. Systematic rotation of the cylinder bundle disk relative to the z-axis (Fig. 1) results in different cylinder configurations seen by the incoming flow. While rotation at every 90 deg leads to four different configurations, only two configurations are distinctive in terms of projection area in streamwise view. For example, aerodynamically, $\alpha=0$ deg and $\alpha=60$ deg are identical and have the most open flow passage to the flow whereas at $\alpha=30$ deg and $\alpha=90$ deg, the flow passage is the most closed.

As a measure of anisotropy for a given Reynolds number, this section aims to examine experimentally how the observed pressure drop is affected by the variation of cylinder yaw angle. To this end, the cylinder bundles were rotated with respect to the geometrical center of the bundles as illustrated in Fig. 1. The variation of yaw angle (α) ranges from −5° to +65°, with the Reynolds number fixed at $Re_d=2.5\times10^3$.

To examine the effect of yaw angle on empirical constant β', pressure drop at $y/d=0$ is considered. Figure 5 plots the variation of β' with yaw angle α for $\varepsilon=0.90$, from which it is seen that its overall response to yaw angle variation obeys a harmonic function. With curve fitting, this can be expressed as

$$\beta' = -c_1\cos(6\alpha) + c_2 \qquad (9)$$

where $c_1=(\beta'_{\max}-\beta'_{\min})$ and $c_2=(\beta'_{\max}+\beta'_{\min})/2$.

The measurement data of Fig. 5 show excellent agreement with Eq. (9). To investigate what causes such harmonic variation, Eq. (6) derived from force balance consideration is revisited. When both the porosity and Reynolds number are fixed, the only source to affect the empirical constant β' is the drag coefficient C_d. There is an indication of the harmoniclike variation of C_d with yaw angle reported by Gu and Sun [12]: Inside the cylinder bundles (except a couple of unit cells from the entry region), reattachment patterns of wake shed from upstream cylinders on subsequent downstream cylinders are varied with the yaw angle. As a result, the drag coefficient on each cylinder element is varied in a harmonic fashion. This may lead to the bulk harmonic response of the drag coefficient to yaw angle variation as observed in the present study (Fig. 5).

Conclusions

Pressure drop characteristics through anisotropic porous mediumlike cylinder bundles are experimentally examined, with the results interpreted using a force balance flow model. Three porosity cases ($\varepsilon=0.66$, 0.82, and 0.90) are considered in the turbulent flow regime ($5.0\times10^2\leqslant Re_d\leqslant5.0\times10^3$). The following conclusions are drawn:

(1) Following the conventional relation of the pressure drop through a variety of porous media, the pressure drop through the porous mediumlike cylinder bundles is proportional to the square of the flow velocity.
(2) For the particular configuration used in this study when varying porosity, the empirical constant (β') is linearly proportional to $(1-\varepsilon^{1/2})/\varepsilon^2$ obtained from the force balance flow model compared to that to $(1-\varepsilon)/\varepsilon^3$ from the hydraulic radius theory.
(3) With varying the yaw angle as a measure of the anisotropy of the cylinder bundle, the pressure drop responds in a harmonic manner with a 60 deg period for a given porosity as a result of the varied drag coefficient of each cylinder element (and the bulk of the cylinder bundles).

Acknowledgment

This work is supported by the National Basic Research Program of China (2006CB601203), the National Natural Science Foundation of China (50676075, 10328203, 10572111, 10632060), and the National 111 Project of China (B06024).

Nomenclature

a, b, a', b' = empirical constants
β' = empirical constant
c_1, c_2 = empirical constants
C_d = drag coefficient
d = cylinder element diameter, m
dp = representative pore diameter, m

H = length of cylinder elements (and channel height), m

l_x, l_y, l_z = length of each side of control volume

L = test sample length along the flow direction, m

p_{in} = inlet static pressure, Pa

p_{out} = outlet static pressure, Pa

S_X, S_Y, S_{XY} = longitudinal, transverse, diagonal pitches of a unit cell, m

U_m = mean inlet flow velocity, m/s

V = discharge flow velocity ($=U_m/\varepsilon$), m/s

X, Y, Z = Cartesian coordinates

Greek Symbols

α = yaw angle, deg

ε = porosity

μ = viscosity, kg/ms

ρ = density, kg/m^3

References

[1] Trussell, R. R., and Chang, M., 1999, "Review of Flow Through Porous Media as Applied to Head Loss in Water Filters," J. Environ. Eng., **125**, pp. 998–1006.

[2] Burcharth, H. F., and Andersen., O. H., 1995, "On the One-Dimensional Steady and Unsteady Porous Flow Equations," Coastal Eng., **24**, pp. 233–257.

[3] Lage, J. L., and Antohe, B. V., 2000, "Darcy's Experiments and the Deviation to Non-Linear Flow Regime," ASME J. Fluids Eng., **122**, pp. 619–625.

[4] Sabiri, N.-E., and Comiti, J., 1995, "Pressure Drop in Non-Newtonian Purely Viscous Fluid Flow Through Porous Media," Chem. Eng. Sci., **50**, pp. 1193–1201.

[5] Venkataraman, P., and Rao, P. R. M., 1998, "Darcian, Transitional, and Turbulent Flow Through Porous Media," J. Hydraul. Eng., **124**, pp. 840–846.

[6] Legrand, J., 2002, "Revisited Analysis of Pressure Drop in Flow Through Crushed Rocks," J. Hydraul. Eng., **128**, pp. 1027–1031.

[7] Kim, T., Hodson, H. P., and Lu, T. J., 2004, "Fluid-Flow and Endwall Heat-Transfer Characteristics of an Ultralight Lattice-Frame Material," Int. J. Heat Mass Transfer, **47**, pp. 1129–1140.

[8] Fowler, A. J., and Bejan, A., 1994, "Forced Convection in Banks of Inclined Cylinders at Low Reynolds Numbers," Int. J. Heat Fluid Flow, **15**, pp. 90–99.

[9] Kim, T., Hodson, H. P., and Lu, T. J., 2006, "On the Prediction of Pressure Drop Across Banks of Inclined Cylinders," Int. J. Heat Fluid Flow, **27**, pp. 311–318.

[10] Coleman, H. W., and Steele, W. G., 1999, *Experimentation and Uncertainty Analysis for Engineers*, 2nd ed., Wiley, New York.

[11] Zukauskas, A., 1987, "Heat Transfer From Tubes in Crossflow," Adv. Heat Transfer, **18**, pp. 87–159.

[12] Gu, Z., and Sun, T., 2001, "Classifications of Flow Pattern on Three Circular Cylinders in Equilateral-Triangular Arrangements," J. Wind. Eng. Ind. Aerodyn., **89**, pp. 553–568.

Benchmark Experimental Data for Fully Stalled Wide-Angled Diffusers

K Kibicho
Department of Mechanical Engineering,
Jomo Kenyatta University of Agriculture and Technology,
P. O. Box 62000,
Nairobi 00200, Kenya

A. T. Sayers
Department of Mechanical Engineering,
University of Cape Town,
Rondebosch 7701, South Africa

Due to adverse pressure gradient along the diverging walls of wide-angled diffusers, the attached flow separates from one wall and remains attached permanently to the other wall in a process called stalling. Separated diffuser flows provide a classical case of pressure driven flow separation. Such flows present a very serious challenge to fluid dynamics modelers. This paper provides a data bank contribution for the streamwise mean velocity field and pressure recovery data in wide-angled diffusers. Turbulent mean flow measurements were carried out at Reynolds numbers between 1.07×10^5 *and* 2.14×10^5 *based on inlet hydraulic diameter and centerline velocity for diffusers whose divergence angles were between 30 deg and 50 deg. The results presented provide a reliable validation data bank for computational fluid dynamics studies for pressure driven flow separation studies.*

[DOI: 10.1115/1.2969270]

1 Introduction

In many engineering applications, diffusers are used to convert kinetic energy into pressure energy. In the last few decades, a lot of experimental and computational research have been devoted to this subject. Unfortunately, even the usually turbulent flows in two-dimensional diffusers are extremely complicated, and our understanding of the details of energy transfer and dissipative losses inside a diffuser is still incomplete.

In wide-angled diffusers, the attached flow separates from one wall and remains attached permanently to the other wall in a process known as "stalling." This flow separation is caused mainly by the adverse pressure gradient along the walls of the diffuser, causing a back-flow region within the diffuser. The back-flow behavior of stalled diffusers is uniquely related to the diffuser geometry as described in the flow regime chart of Fox and Kline [1]. In the fully stalled regime, a stalled diffuser provides a classical case of steady flow separation that is pressure driven. Furthermore, due to the simplicity of construction and experimentation, wide-angled two-dimensional diffuser data are suitable for benchmarking computational fluid dynamics (CFD) codes.

Positive directions of x, y, and z were measured relative to the center of the diffuser entry plane according to the frame of reference shown in Fig. 1 that also shows the convention commonly used in two-dimensional diffusers.

The relationship between diffuser geometry and performance is mainly covered by Reneau et al. [2] and Kline et al. [3], among others. The work of Reneau et al. [2] is however widely used in the design and mapping of two-dimensional diffusers.

Once a diffuser flow is stalled, most theoretical work relies on correlations of actual experimental data and on the semiempirical performance prediction methods derived from these data. The reason why there is scarce numerical work on wide-angled diffusers is because reliable experimental data and especially data that cover the velocity flow-field are lacking. Contrary to this, flows in narrow plane asymmetric diffusers have been extensively studied experimentally by many researchers, among them, Obi et al. [4] and, Buice and Eaton [5].

It is against this background that the data provided in this paper become a useful benchmark for validating CFD codes.

2 Experimental Apparatus and Instrumentation

The experimental apparatus is shown in Fig. 2. Air was delivered by a radial flow fan into a 1.9 m long rectangular-circular transition duct, which was connected to a 600 mm inner diameter, 3.7 m long circular duct. A 1 m long circular-rectangular transition duct transferred the air to a 400 mm × 100 mm × 1 m long straight inlet duct before its entry into the diffuser proper. After flowing through the diffuser, the air was discharged back into the atmosphere.

All the plates for the straight inlet section and diffuser were machined from 10 mm thick transparent thermoplastic resin (Perspex). The details of the complete design of the flow facility, instrumentation, and uncertainty analysis can be found in Ref. [6].

Due to the manufacturing difficulties of drilling static pressure holes at the exact diffuser entry, a set of eight holes of 1.8 mm diameter were drilled at a location 2 mm upstream of the diffuser entry. The entry static pressure was averaged by connecting the eight static tubes to a common ring tube. The output of the common ring tube was the inlet static pressure P_1.

The roof of the diffuser was constructed from six 150 mm wide strips and two strips of widths 15 mm and 85 mm installed as the first and last strip at the entry and exit of the diffuser, respectively. A 2 m long by 150 mm wide Perspex probing strip was used to move a three-tube yaw meter in the y direction for measuring the velocity profiles across the diffuser test section. All the 150 mm wide roof strips were removed, in turn, and replaced with the probing strip.

The pressure recovery coefficient C_{pr} was evaluated according to the definition given by

$$C_{\mathrm{pr}} = \frac{P_x - P_1}{\frac{1}{2}\rho U_1^2} \tag{1}$$

where P_x is the pressure measured along the walls of the diffuser.

Streamwise velocity profiles were measured using a three-tube yaw meter. The probe was calibrated against a hot-wire anemometer in a low-turbulence intensity (0.4% turbulence intensity) wind tunnel flow-field. Nondimensional calibration parameters were calculated in terms of pressures and resultant flow velocity q similar to those specified by Yajnik and Gupta [7], and Rhagava et al. [8] and are given by

$$f(\psi) = \frac{P_l - P_r}{P_c - P_m} \tag{2}$$

$$Q_p = \frac{P_c - P_m}{\rho q^2/2} \tag{3}$$

where P_l and P_r are the pressures sensed by the off-center tubes, $P_m=(P_l+P_r)/2$ is the mean pressure for the off-center pressures, and P_c is the pressure measured by the central tube.

The reference probe null-position was selected as the direction of the centerline of the probe tip in line with the main flow direction when the pressures recorded from the off-center tubes were equal to each other. At this reference direction, $\psi=0$ deg. The pressure measured at the central tube of the probe at this position

---

Contributed by the Fluids Engineering Division of ASME for publication in the JOURNAL OF FLUIDS ENGINEERING. Manuscript received November 21, 2006; final manuscript received June 27, 2008; published online September 8, 2008. Review conducted by Phillip M. Ligrani.

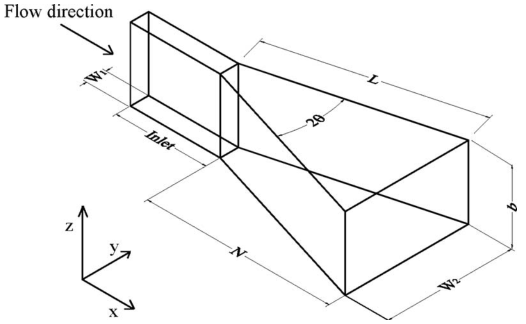

Fig. 1 Two-dimensional diffuser geometry and the frame of reference

was the total (stagnation) pressure of the flow P_t. These functions can be established directly and are known to be independent of Reynolds number. Thus, once established at one Reynolds number, they can be applied to a range of Reynolds numbers. The calibration of the probe was done at 15 m/s. The calibration charts of $f(\psi)$ and Q_p against ψ were therefore generated.

By using Eq. (2) to get $f(\psi)$, the flow angle ψ was established at every measurement point from the charts. Thus, knowing ψ, Q_p was also read off the charts and Eq. (3) was used to evaluate the flow velocity q. The velocity components u and v with respect to the x and y directions of the pressure probe, respectively, were then calculated according to

$$u = q \cos \psi$$

$$v = q \sin \psi \tag{4}$$

The results obtained by using these equations were tested at several locations within the diffuser test section against the null-reading technique. The average error in measuring the flow angle was 0.81 deg. The root mean square (rms) error in velocity measurement was 1.37%.

3 Results and Discussion

3.1 Tunnel Qualification

3.1.1 Uniformity of Inlet Channel Flow. A measure of the nonuniformity of the flow λ was evaluated as the percentage overall discrepancy of axial velocities u_i, measured at corresponding points to the right and left of the x-axis. It is known that once a flow is stalled, the velocity profile at the inlet of the diffuser considerably distorts. At an upstream location of $(x/W_1)=-2.35$, the nonuniformity had a maximum value of 0.23% for all diffusers, and therefore the inlet velocity U_1 was taken at this point.

It still remains unclear why stalling in the two-dimensional fully stalled regime in diffusers occurs on a particular wall. Great care was taken to manufacture highly symmetrical diffusers. Tests to rule out the possibility of a bias toward the flow attaching to a particular wall whenever the fan was switched on were carried out. In this regard, for all diffusers and before any measurements were taken, a start-stop check was done whereby the fan was started, the wall to which the flow was attached noted, the fan switched off and started again, and the process repeated. These tests were done at an inlet duct velocity of 15 m/s. An intermittency parameter γ_s was then defined as a ratio of the number of times the flow remained attached to a given wall to the total number of start-stop cycles. γ_s was measured to have a maximum value of 0.60 in favor of the left hand wall for the 50 deg diffuser.

3.1.2 Reproducibility and Replication. Flows in wide-angled diffusers are inherently unsteady. In order to reduce the effect of the unsteadiness in the experimental results, the pressure transducer differential voltages were averaged over long durations. Due to the large number of data points obtained especially when measuring the velocity profiles, it was found adequate to take readings at each point three times and then average their discrepancies for all the data points. In any case, the statement of overall uncertainties is all that is required. The reproducibility seemed to worsen as both Reynolds number and divergence angles increased, the maximum discrepancy for both velocity profiles and static pressure recovery at 1.88% indicated fairly reproducible experiments of these physically complex flows.

As has already been observed, the wall to which the flow attached was quite random. However, since the data acquisition system was placed on the left side of the diffuser, the flow was always manually "switched" to the left wall in instances when it attached to the right wall. With this in mind, it was important to confirm that both the pressure and velocity fields were independent of the wall to which flow was attached (replication). To verify this requirement, the flow-field was measured with the flow first attached to the left wall and second with the flow attached to the right wall. The discrepancies of the velocities at corresponding points when the flow was attached to either left or right wall could be established. The maximum replication discrepancy obtained for both velocity profiles and static pressure recovery was 2.13%.

3.1.3 Reynolds Number Dependence. Results showed that by changing the velocity from 10 m/s to 20 m/s, the static pressure recovery increased by 8.31%, 10.15%, and 9.35% for 30 deg,

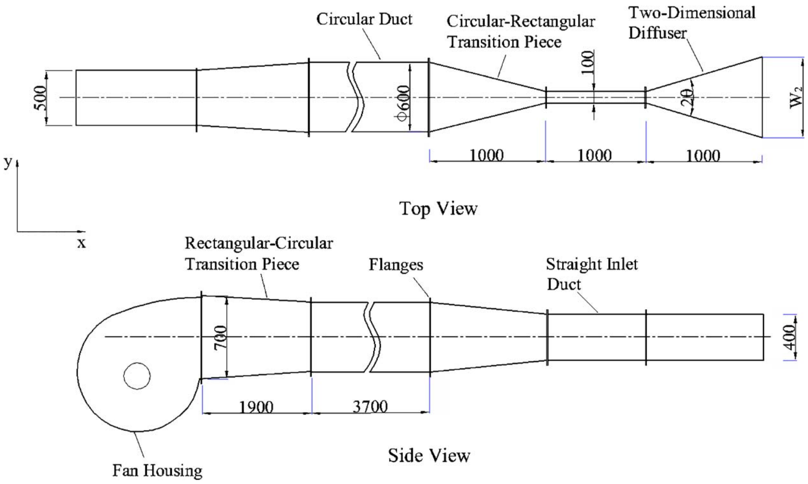

Fig. 2 Experimental apparatus

40 deg, and 50 deg diffusers, respectively. A similar increase in Reynolds number for the velocity profiles showed that the increase in the normalized velocities was 1.37%, 1.57%, and 1.60% for 30 deg, 40 deg, and 50 deg diffusers, respectively. Evidently, the static pressure was influenced by the Reynolds number at values that are outside the overall experimental uncertainties of about 2% in this work.

Results from the limited number of flow cases in this study cannot be considered adequate to provide a reasonable correlation. Bearing this in mind and in order to focus on the primary objectives of this research, it was decided that from this point onwards, the Reynolds number be held constant at 1.63×10^5 corresponding to an inlet duct velocity of 15 m/s.

3.1.4 Two-Dimensionality. Traditionally, proof of two-dimensionality of a flow is carried out by measuring axial velocity profiles at two different planes, one below the midplane, and another above the midplane. Thus, for a given location within the diffuser, axial velocity profiles were measured in three planes, namely: Upper, mid, and lower planes. The upper and lower planes were both at a 100 mm distance from the roof and the floor of the diffuser, respectively. For all diffusers in this study, the two-dimensionality of the flow was verified using this procedure, with the velocity profiles being measured at three locations downstream of the diffuser inlet located at $(x/W)_1=0.9$, 3.9, and 8.4. With the midplane held as the datum, the overall deviations from this plane for the lower and the upper planes produced a maximum deviation of 0.3% meaning that the two-dimensionality was well within the uncertainties of the experimental data in this research.

4 Data Bank Contribution

In the interest of clarity while discussing the experimental results, only representative cases of extensive experimental data have been presented. However, the same rigorous checks and experimental procedures, as discussed in Sec. 3.1, were performed for all flow cases. These results are presented in the Appendix as a data bank contribution. The results presented in the data bank include the axial velocity profiles, (u/U_1), and the wall static pressure recovery C_{pr}.

5 Conclusions

In this study, experimental investigations of separated flows in fully stalled wide-angled diffusers have been carried out. Due to the adverse pressure gradient along the diffuser walls, flow separated from one diverging wall and became attached to the other wall, thus forming a region of steady stall within the diffusers. It was not possible to determine, in advance, the wall to which the flow would attach. Tests to determine the wall to which the flow remains attached led to the conclusion that the wall of preference was totally random and was probably caused by a slight upstream disturbance that was impossible to detect. However, it was possible to switch the flow from one wall to the other by introducing an inlet disturbance. It was found that once switched to a wall, the flow remained attached to that wall permanently. Experimental results showed that regardless of the wall to which the flow was attached, both the velocity and pressure flow-fields were replicated with discrepancies below 2%.

Although current literature states that for a given geometry, the Reynolds number has little influence on the static pressure recovery, it was found in this study that by increasing the velocity from 10 m/s to 20 m/s, the static pressure recovery for the 30 deg diffuser increased by 8.31%. However, as the divergence angle was increased, a similar increase in Reynolds number resulted in a higher percentage of pressure recovery. The limited range of Reynolds numbers investigated in this study could not allow a rational correlation between the Reynolds number and the C_{pr} profiles. This range was limited by the physical constraints imposed by the wind tunnel and fan speed. For instance, a change in velocity from 10 m/s to 80 m/s would not change the Reynolds number by even one order of magnitude.

The experimental uncertainties in this research were approximately 2%. Within these uncertainties, a reliable data bank contribution has been provided for unvaned fully stalled wide-angled diffusers.

Appendix

Experimental results are presented as data bank contributions. Figures 3–5 show coefficients of static pressures for 30 deg, 40 deg, and 50 deg diffusers. Figures 6–8 show axial velocity profiles for 30 deg, 40 deg, and 50 deg diffusers.

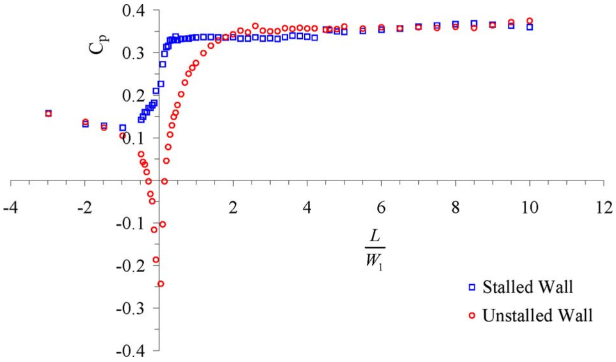

Fig. 3 Coefficient of static pressure for the 30 deg diffuser

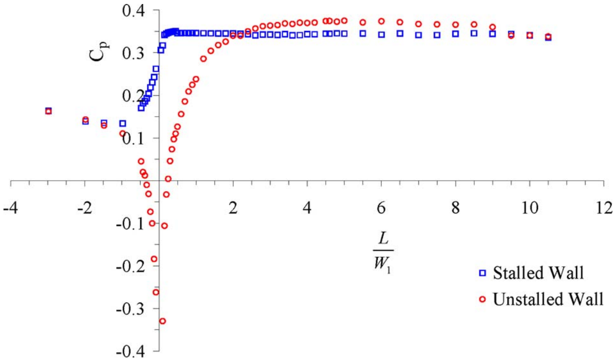

Fig. 4 Coefficient of static pressure for the 40 deg diffuser

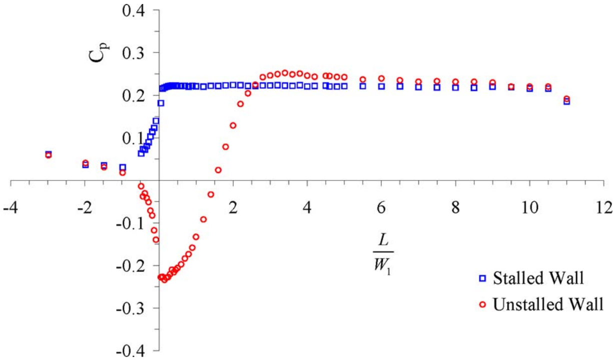

Fig. 5 Coefficient of static pressure for the 50 deg diffuser

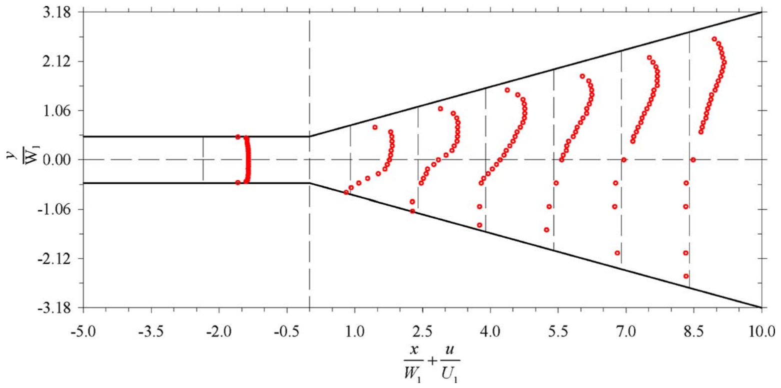

Fig. 6 Axial velocity profiles for the 30 deg diffuser

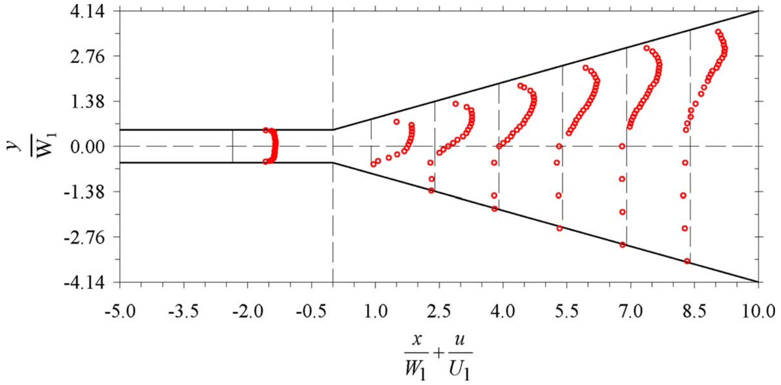

Fig. 7 Axial velocity profiles for the 40 deg diffuser

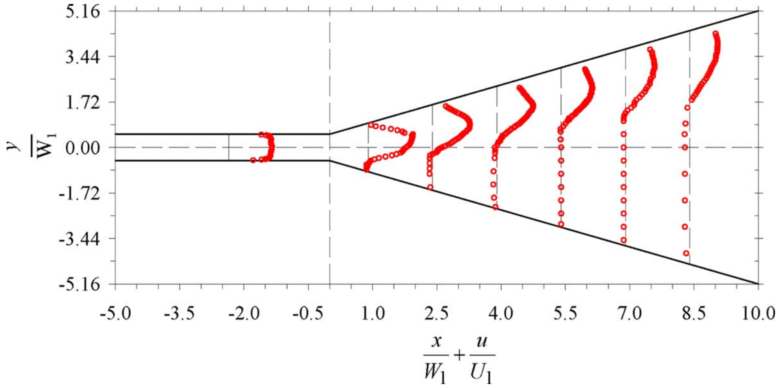

Fig. 8 Axial velocity profiles for the 50 deg diffuser

References

[1] Fox, R., and Kline, S., 1962, "Flow Regime Data and Design Methods for Curved Subsonic Diffusers," ASME J. Basic Eng., **84**, pp. 303–312.

[2] Reneau, L., Johnston, J., and Kline, S., 1967, "Performance and Design of Straight, Two-Dimensional Diffusers," ASME J. Basic Eng., **89**(1), pp. 141–150.

[3] Kline, S., Abbort, D., and Fox, R., 1959, "Optimum Design of Straight-Walled Diffusers," ASME J. Basic Eng., **81**, pp. 321–331.

[4] Obi, S., Aoki, K., and Masuda, S., 1993, "Experimental and Computational Study of Separating Flow in an Asymmetric Planar Diffuser," *Proceedings of the Ninth Symposium on Turbulent Shear Flows*, Kyoto, Japan, Aug. 16–18, Vol. 305, pp. 1–4.

[5] Buice, C., and Eaton, J., 1997, "Experimental Investigation of Flow Through an Asymmetric Plane Diffuser," Center for Turbulence Research, Stanford University, Report No. TSD 107.

[6] Kibicho, K., 2006, "Flow-Field Structure in Wide-Angled Diffusers," Ph.D. thesis, University of Cape Town, South Africa.

[7] Yajnik, K., and Gupta, R., 1973, "A New Probe for Measurement of Velocity and Flow Direction in Separated Flows," J. Phys. E, **6**, pp. 82–86.

[8] Rhagava, A., Kumar, K., Malhotra, R., and Agrawal, D., 1979, "A Probe for the Measurement of Velocity Field," ASME Trans. J. Fluids Eng., **11**(1), pp. 143–146.